UNIVERSITY OF CALIFORNIA

Santa Barbara

Instrument development towards understanding the spin dynamics of radical heterogeneity and clusters in dynamic nuclear polarization

A dissertation submitted in partial satisfaction of the

requirements for the degree Doctor of Philosophy

in Chemistry

by

Alisa A. Leavesley

Committee in charge:

Professor Songi Han, Chair

Professor Mark Sherwin

Professor Frederick Dahlquist

Professor Bernard Kirtman

June 2018

The dissertation of Alisa A. Leavesley is approved.

_____

Mark Sherwin

_____

Frederick Dahlquist

_____

Bernard Kirtman

_____

Songi Han, Committee Chair

June 2018

Instrument development towards understanding the spin dynamics of radical heterogeneity and clusters in dynamic nuclear polarization

Alisa A. Leavesley

ACKNOWLEDGEMENTS

Alisa would like to recognize the enormous support she has received from her group members, friends, and family. In special recognition of their help in the lab is Ilia Kaminker for his continued advice and problem-solving skills, Ting Ann Siaw for showing me the ropes around the lab, Alicia Lund for being an awesome office mate and her general advice, Daphna Shimon for helping me through that first paper, Blake Wilson, Sheetal Jain, and Asif Equbal for great discussions, and finally Songi Han for her unerring support and guidance through this whole process. Partial financial support was provided by the CPS technologies fellowship. Alisa must recognize her trivia team (Andre, Will, John, Nate, and Annie), Erin Morgan, Victoria Steffes, and Matt Downy for keeping her sane with fun adventures that usually involved laughter, food, and wine or beer. Hearts Therapeutic Equestrian Center also needs a shout-out for providing an extra incentive to be outdoors at least once a week and gave its own version of therapy to her by helping out and by being around horses. Finally, Alisa must recognize the support of her family: Susan & Peter and Tina & Drew who helped listen to her highs and lows through the whole doctoral journey (including a bit of proof reading for applications). It was the combined efforts and support of these and many more who have helped Alisa complete this doctoral degree.

VITA OF ALISA A. LEAVESLEY
June 2014

EDUCATION

Doctor of Philosophy, Department of Chemistry and Biochemistry, University of California, Santa Barbara, June 2018 (expected), concentration: Physical Chemistry
Bachelor of Chemistry, James Madison University, May 2013 (summa cum laude)

RESEARCH EXPERIENCE

- **Graduate Student Researcher**, University of California, Santa Barbara, (January 2014 – June 2018), Advisor: Professor Song-I Han
  - Investigating dynamic nuclear polarization (DNP) mechanisms and efficiency via high field cwEPR, electron and nuclear relaxation, electron depolarization, DNP measurements, and computer simulations in collaboration with Mark Sherwin (UCSB) and Daniella Goldfarb and Shimon Vega (Weizmann Institute of Science)
  - Researching the impact of electron spectral diffusion, glassing conditions, and local radical clustering on DNP through analysis of electron depolarization, DNP profiles, and DNP build-up curves in collaboration with Andrzej Rajca (University of Nebraska)
  - Developing high field dual DNP/EPR instrumentation with home-built inductively coupled NMR coils and cw-, pulsed, and pump-probe microwave capabilities via a quasi optic microwave bridge with super-heterodyne EPR detection
  - Trouble shooting, diagnosing, and fixing poor instrument performance and experimental data sets
- **Undergraduate Research Assistant**, James Madison University, (January 2010-May 2013)
  Advisor: Professor Debra L. Mohler
  - Synthesized isotopically labeled bisphenol-A and BPA polycarbonate with high yield on the mg scale
  - Developed synthesis and characterization of an organic siRNA analog through ROMP
- **Amgen Scholar**, University of California Berkeley, Berkeley, CA, (May-August 2012)
  Advisor: Professor Felix R. Fischer
  - Synthesized precursor ligands, worked towards the development of a ROAMP catalyst, and fully characterized compounds synthesized during the internship
  - Optimized ROAMP polymerization reactions and analyzed products
- **Undergraduate Research Assistant**, University of Florida International REU program, (May-August 2011), Host: Universidad de Buenos Aires, Buenos Aires, Argentina
  Advisors: Professor Fabio Cukiernik and Dr. Florencia Cecchi
  - Synthesized and characterized liquid crystal polymers
  - Synthesized and analyzed multivalent Ru(II)/Ru(III) coordination compounds
- **Research Intern**, Center for Research in Contraceptive and Reproductive Health, University of Virginia, Charlottesville, VA, (June-August 2009)
  Advisors: Dr. John C. Herr and Dr. Jagathpala Shetty
  - Expressed and isolated soluble proteins for crystallization as potential male contraceptive targets

TEACHING EXPERIENCE

- **Teaching Assistant**, University of California, Santa Barbara, (September 2013-December 2017 - quarterly)
  - Instructed General and Physical Chemistry labs
  - Lead discussion sections for Physical Chemistry: statistical and quantum mechanics
- **Peer Assisted Study Session (PASS) Leader for Organic Chemistry**, James Madison University, (August 2011-May 2013)
  Supervisors: Dr. Alicia James and Professor Scott Lewis
  - Presented review lectures and developed alternative explanations of lecture concepts, though demonstrations and worksheets to develop students' problem solving skills

PUBLICATIONS

11. **Leavesley, A.,** Thicklin, R., Malay, T., Kaminker, I., Han, S. *Development of a sample exchanger for a versatile dual DNP/EPR instrument at 200 GHz.* Manuscript in preparation.
10. Kundu, K.; **Leavesley, A.**; Vega, S.; Goldfarb, D.; Han, S. *Influence of microwave power on electron depolarization and dynamic nuclear polarization.* Manuscript in preparation.
9. Siaw, T.A., Jain, S., **Leavesley, A.,** Jenkins, I., Han, S. *Inductively coupled single resonance nuclear magnetic resonance coils for cryogenic temperatures.* Manuscript in preparation.
8. Equbal, A., **Leavesley, A.**, Han, S. *Cross Effect Dynamic Nuclear Polarization Reexamined.* Manuscript in preparation.
7. **Leavesley, A.,** Wang, X., Long, J., Gan, Z., Han, S. *Gd3@C80 boosts signal enhancement by 25-fold.* Manuscript in preparation.
6. **Leavesley, A.,** Jain, S., Rajca, A.; Han, S. *Three spin e-e-n cross effect modulate the nuclear spin T_{1n} and DNP build-up time.* Manuscript submitted to Chemical Science.
5. **Leavesley, A.**, Kaminker, I., Han, S. *Versatile dynamic nuclear polarization hardware with integrated electron paramagnetic resonance capabilities.* Manuscript Accepted. DNP Handbook, ed. Vega, S., Michaels, V., Griffin, R., Corzilius, B. 2018
4. Equbal, A., Li, A., **Leavesley**, **A.**, Huang, S., Rajca, S., Rajca, A., Han, S. *Truncated Cross Effect Dynamic Nuclear Polarization: An Overhauser Effect Doppelgänger*. **J. Phys. Chem. Lett.** 9 (2018) 2175-2180. doi: 10.1021/acs.jpclett.8b00751
3. **Leavesley, A.**, Wilson, C.B., Sherwin, M.; Han, S. *Effect of water/glycerol polymorphism on dynamic nuclear polarization*. **Phys. Chem. Chem. Phys.** 20 (2018) 9897-9903. doi:10.1039/c8cp00358k
2. **Leavesley, A.**; Shimon, D.; Siaw, T.A.; Feintuch, A.; Kaminker, A.; Goldfarb, D.; Vega, S.; Han, S. *Effect of electron spectral diffusion on static dynamic nuclear polarization at 7 Tesla.* **Phys. Chem. Chem. Phys.** *19* (2017) 3596–3605. doi:10.1039/C6CP06893F.
1. Siaw, T.A.; **Leavesley, A.;** Lund, A.; Kaminker, I.; Han, S. *A versatile and modular quasi optics-based 200 GHz dual dynamic nuclear polarization and electron paramagnetic resonance instrument*, **J. Magn. Reson.** *264* (2016) 131–153. doi:10.1016/j.jmr.2015.12.012.

CONFERENCE PRESENTATIONS:

- *Influence of radical clustering on dynamic nuclear polarization.* 6th Chemical Science Student Seminar Series, UCSB, Santa Barbara, CA, November 6, 2017 (oral presentation).
- *Insights into DNP by probing electron depolarization via ELDOR experiments at 7T*. 20th International Society of Magnetic Resonance Conference, Quebec City, Canada, July 23-28, 2017 (poster 63).
- *Impact of radical clustering on electron spin depolarization and DNP performance*. 58th Experimental NMR Conference, Pacific Grove, CA, March 26-31, 2017 (poster 155)
- *Electron spectral diffusion measured via ELDOR for DNP at 7 T*, 58th Rocky Mountain Conference, Breckenridge, CO, July 17-21, 2016 (oral EPR150/SSNMR335)
- *Analysis of Frozen Water Glasses for Consistent DNP Performance*. 57th Experimental NMR Conference, Pittsburg, PA, April 10-15, 2016 (poster 358)
- *Versatile 200 GHz solid state microwave source as an optimal platform for ssDNP mechanistic studies*. Southampton, UK, June21-26, 2015, EU-COST Summer School on Nuclear Spin Hyperpolarization Techniques (poster).
- *Instrument Development for Coherence-Spectroscopy Approach to DNP at 200 GHz.* Pacific Grove, CA, April 19-24, 2015, 56th Experimental NMR Conference (poster 464)
- *Development of an Air Stable and Selective Molybdenum Catalyst for Ring-Opening Alkyne Metathesis Polymerization*. Amgen Scholars Symposium, University of California, Berkeley, Berkeley, CA, July 30, 2012 and August 2, 2012 (poster and oral presentations), and Chemistry Department Seminar, James Madison University, Harrisonburg, VA, September 28, 2012 (oral presentation).
- *Synthesis and Purification of 2,7,-Acetyloxy-3,6,10,11-tetrahexyloxy triphenylene copolymer*. 243rd National Meeting of the American Chemical Society, San Diego, CA, March 25-29, 2012 (poster presentation, CHED 1361), and Chemistry Department Seminar, James Madison University, Harrisonburg, VA, September 9, 2011 (oral presentation).
- *High Yield Synthesis of Isotopically Labeled Bisphenol A and its Polycarbonate.* 36th Annual Spring Undergraduate Research Symposium, James Madison University, Harrisonburg, VA, March 24, 2011 (poster presentation), and REU Research Symposium, James Madison University, Harrisonburg, VA, July 30, 2010 (poster presentation).

AWARDS

- **Travel award for International Society of Magnetic Resonance (ISMAR) conference,** Recipient (2017)
- **Travel award for Experimental NMR Conference (ENC)**, Recipient (2016)
- **Travel award for Rocky Mountain Conference on EPR (RMC)**, Recipient (2016)
- **Outstanding Service Award**, Chemistry Department, UC Santa Barbara (2015 & 2016)
- **CSP Technologies Fellowship**, Recipient (2014)
- **National Science Foundation, Graduate Research Fellowship**, Honorable Mention (2013)
- **Barry M. Goldwater Scholarship**, Honorable Mention (2012)
- **Frances Pitts Memorial Scholarship**, James Madison University (2010-2013)

ABSTRACT

Instrument development towards understanding the spin dynamics of heterogenous and clustered radicals in dynamic nuclear polarization

by

Alisa A. Leavesley

Dynamic nuclear polarization (DNP) has re-emerged as a method to increase NMR signal by orders of magnitude in the past two decades. The recent developments in high frequency microwave (μw) sources, instrumentation, and radical synthesis have substantially enhanced the NMR signal at standard NMR fields via polarization transfer from unpaired electron spins to their coupled nuclei. Since the re-emergence of DNP, there has been a four-fold increase in publications associated with DNP compared to its initial discovery in 1953. This immense interest in understanding and optimizing the DNP mechanisms has led to numerous biological-, materials-, and imaging-based applications. However, only a limited set of sample formulations result in reliable and significant enhancement of the NMR signal – primarily nitroxide-based radicals in aqueous solvents. Furthermore, with recent technological developments, NMR spectrometers at magnetic fields > 20 T are now operational, where the standard DNP mechanisms governed by continuous wave μw irradiation, namely the solid-effect and cross-effect become less efficient. In order to broaden the scope of sample formulations and develop DNP methods for high magnetic fields, the underlying electron-

nuclear spin dynamics must be better understood. However, there are limited instruments that can simultaneously acquire the spin dynamics of both the electron and nuclear spins under identical experimental conditions due to the instrumental challenges associated with acquiring these spin dynamics. Therefore, the aim of this work is to implement developments on our home-built static 194 GHz DNP system to allow for dual NMR and EPR detection, 2-source electron-electron double resonance, and arbitrary waveform generation. With these improvements, we can gain insight into the DNP mechanisms, how experimental conditions affect them, and explain odd phenomenon in experimental results.

Here this dual-purpose instrument is specifically used to investigate the impact electron-electron (*e*-*e*) interactions have on DNP and the underlying spin dynamics. It has previously been assumed that the radicals containing the unpaired electron necessary for DNP were homogeneously distributed through the sample volume; however, we have found that both the solvents' propensity to form glass polymorphs and the radical type can significantly alter the distribution of mono-radicals throughout the sample. Subsequently, the heterogeneity and clustering of the electron spins will significantly alter the *e*-*e* interactions, and therefore, the DNP enhancement and spin dynamics. We find that many *e*-*e* interactions (even if they are relatively weak) can cause a significant reduction in nuclear relaxation due to *e*-*e*-*n* mediated relaxation, which allows for a faster build-up of hyperpolarized NMR signal and can decrease acquisition times.

TABLE OF CONTENTS

1. Introduction to dynamic nuclear polarization and electron paramagnetic resonance

Magnetic resonance is a common technique in the physical sciences to understand the structure and dynamics of species containing active nuclear spins and unpaired electron spins – paramagnetic species. It has applications ranging from structural determinations at the molecular level for organic and inorganic materials and biological samples,[1–5] to molecular dynamic studies of diffusion processes,[6–8] and magnetic resonance imaging (MRI).[9] The driving force behind magnetic resonance is the inherent angular momentum of electron and nuclear spins that causes them to precess at a specific frequency when inside a static magnetic field. This characteristic precession frequency is dependent on the local environment surrounding the spin and can be used to identify different types of electrons or nuclei, such as differentiating between a carbonyl ^{13}C and a methyl ^{13}C. The energy levels of the electron and nuclear spins will also split in the magnetic field based on their spin angular momentum quantum number, m_I, where the resulting number of energy levels is $2m_I+1$. It is the difference in populations between theses energy levels that produces the signal for magnetic resonance, where electron and nuclear spins were first observed, respectively, via electron paramagnetic resonance (EPR) in 1944 by Zavoisky[10] and nuclear magnetic resonance (NMR) in 1946 by Bloch and Purcell.[11,12]

Although NMR has become a ubiquitous characterization technique across the physical sciences, it suffers from poor signal sensitivity. At standard operating conditions, the population difference between energy levels (or polarization) of 100% abundant ^{1}H at 298 K and at 7 T is 0.01 %, where this effect is worse for low-γ nuclei, such as ^{13}C, which only has a 35 ppm polarization. For ^{13}C, the total NMR signal will further suffer due to its poor natural

abundance of 1.1 %. Attempts to improve the NMR signal include using larger magnetic fields (an expensive endeavor as a new instrument is required) and lowering the experimental temperature. The populations of the energy levels are dictated by Boltzmann statistics, which is temperature dependent; thus, lowering the temperature from 298 K to 4 K increases the ^{1}H and ^{13}C polarizations to 1.1% and 0.03%, respectively. Further NMR signal gains can be achieved via hyperpolarization of the nuclear spins, where the hyperpolarization method that has the most potential to be applicable across a wide range of sample architypes is dynamic nuclear polarization.

Dynamic nuclear polarization (DNP) is a hyperpolarization technique that enhances the NMR signal by the transfer of polarization from unpaired electron spins to nearby nuclear spins, most prominently ^{1}H, in frozen aqueous glasses containing free radicals. The polarization is transferred from electron spins upon irradiation with microwaves (μw) corresponding to the EPR frequency.[13–16] Hyperpolarized nuclei can be detected directly or via cross polarization (CP) from ^{1}H in the solvent to other low-γ nuclei.[17] NMR signal enhancement via DNP was originally proposed by Overhauser in 1953 and was confirmed experimentally by Slichter in the same year with metallic ^{7}Li.[18,19] Over the following decades DNP-based research focused primarily on polarized targets for high energy physics, inorganic materials with inherent paramagnetic species, and by doping polymers with paramagnetic species.[20–23] It was only in 1997 that DNP was successfully applied to a biological sample by the Griffin group.[24] The development of DNP between its origin and the 21st century was inhibited by the limited hardware capabilities at the time, where a 10 GHz EPR spectrometer was not commercially available until the early 1960's, while a 94 GHz EPR spectrometer was not available until 1996. The continued improvement of μw-sources for EPR detection and

the ability to dope biological samples with paramagnetic species has unlocked the field of DNP-based research. The resulting explosion of research in this field has led to the introduction of a commercial DNP spectrometer in 2013. Some key examples of biological-based DNP applications include protein structure determination,[24–26] doping of micelles,[27] ^{17}O detection,[28,29] and entrapped enzymes for heterogeneous catalysis.[30,31] On the other hand, materials applications of DNP include studying nanoparticle structures,[32,33] surface modifications to nanoparticles and mesostructured materials,[34–38] polymeric local and supramolecular structures,[39,40] and catalytic species.[35,38,41,42]

Solid-state (ss) DNP is generally conducted at cryogenic temperatures, either under static conditions or under magic angle spinning (MAS)[1].[24,37,43] Although research to achieve DNP at room temperature is underway,[44,45] the commercial DNP spectrometer typically operates at 90 K under MAS conditions. There are many benefits to operating at cryogenic temperatures, including the thermal induced 10^1-10^2-fold gain in nuclear spin polarization, and to obtain high electron Zeeman energies for DNP, where the DNP process will cause a further 10^1-10^3-fold gain to nuclear spin polarization. The combined gain in nuclear spin polarization between cryogenic temperatures and DNP allows for the wide practical application of DNP; however, some systems that would highly benefit from DNP (and have not yet been achieved) are thin films, extended surfaces, interfacial species in bio- and inorganic materials, and low-γ nuclei in technologically important materials. DNP has the potential to transform NMR into a staple materials and biosolids characterization tool, when considering NMR experimental time saving corresponds to the square of the signal gain. This enables studies of NMR-sensitive

[1] MAS is a process in NMR, where rotating a sample at an angle of 54.7° can reduce dipolar and quadrupolar interactions that will narrow the linewidth of NMR spectra.

nuclei at concentrations and conditions that were conventionally inaccessible to NMR, given the experimental times that would span weeks or months of signal averaging. The acquisition of natural abundance heteronuclear correlation measurements for catalytic materials is a clear example of the advantage DNP presents to materials-based applications.[38,46,47]

The NMR signal enhancement that results from DNP motivates this work to better understand the electron and nuclear spin dynamics that govern the DNP process. However, the spin evolution during static- and MAS-DNP experiments differ significantly enough that the two experiment types have to be considered separately when designing and evaluating models of DNP mechanisms.[13,15,48–50] As such the rest of this dissertation will focus solely on static DNP. Although the majority of the previously mentioned examples of biological and materials applications of DNP were under MAS conditions, static DNP is the basis of dissolution DNP (dDNP), where continuous-wave (cw) μw irradiation hyperpolarizes the nuclear spins typically at 1-2 K and at 3-7 T. After the nuclear spins are polarized, the sample is rapidly dissolved and/or melted. The solution-state hyperpolarized sample can then be used for kinetic reaction experiments, metabolic tracking, and/or for molecular MRI upon injection into a sample or living subject.[31,51–54] Furthermore, static DNP is of importance to ultra-wideline NMR, which is characteristically employed for enhancing quadrupolar nuclei or nuclei subject to paramagnetic broadening to extract the chemical shift anisotropy, in cases where MAS is unable to achieve effective line narrowing for high-resolution NMR spectroscopy.[55,56] An example of this is the identification of active agent formulations in solid pharmaceuticals via solid-state ^{35}Cl DNP.[57–59]

The remaining parts of chapter 1 will introduce the DNP mechanisms and some of the characteristic properties of electron spin relaxation that will influence DNP. This chapter will

also illustrate how the electron spin dynamics can provide key clues to help elucidate the mechanisms and relaxation processes that occur in DNP. Finally, I will touch on some of the instrument requirements that are necessary to understand the electron and nuclear spin dynamics.

1.1. DNP mechanisms

There are two primary ss-DNP mechanisms: the solid effect (SE) and the cross effect (CE), where SE is based on a two-spin effect (one electron and one nuclei)[60–62] and CE is based on a three-spin effect (two electrons and one nuclei) for the polarization transfer from the electron spin(s) to the nuclear spin.[21,63–65] Extensive work has been done to described these mechanism explicitly by quantum mechanics, with notable contributions by the Vega group,[14,15,66–68] the Griffin group,[13,69,70] Tycko et al.,[49,71,72] and Köckenberger et al.[73–75] Both of these DNP mechanisms can be described by quantum mechanics with the following Hamiltonian:

$$\mathcal{H} = \mathcal{H}_Z + \mathcal{H}_D + \mathcal{H}_{hfi} + \mathcal{H}_d + \mathcal{H}_{\mu w} \tag{1.1}$$

where $\mathcal{H}_{\mathrm{Z}}$ is the Zeeman interaction for electron and nuclear spins (energies associated with putting a spin in a magnetic field), $\mathcal{H}_{\mathrm{D}}$ is the electron-electron (*e*-*e*) dipolar interaction, $\mathcal{H}_{\mathrm{hfi}}$ is the hyperfine interaction between dipolar coupled electron-nuclear (*e*-*n*) spins, $\mathcal{H}_{\mathrm{d}}$ is the nuclear-nuclear (*n*-*n*) dipolar interaction, and $\mathcal{H}_{\mu\mathrm{w}}$ is the effect of μw irradiation. The $\mathcal{H}_{\mathrm{Z}}$, $\mathcal{H}_{\mathrm{hfi}}$, and $\mathcal{H}_{\mu\mathrm{w}}$ terms are dependent on which DNP mechanism is active, while the remaining terms are defined below:

$$H_D = \sum_{a<b} D_{ab}(3S_{z,a}S_{z,b} - \overline{S_a}\ \overline{S_b}) \quad (1.2)$$

$$H_d = \sum_{i<j} d_{ij}(3I_{z,i}I_{z,j} - \overline{I_i}\ \overline{I_j}) \quad (1.3)$$

Here a and b are indices defining the electron spins, while i and j define nuclear spins, D and d represent the dipolar interaction coefficients, and S and I are the electron and nuclear spin angular momentum vectors, respectively. In SE DNP, monochromatic cw-μw irradiation excites the "forbidden" zero-quantum (ZQ, |↓↑› to |↑↓›) and double-quantum (DQ, |↓↓› to |↑↑›) transitions of a single *e-n* spin system, and induces a polarization transfer from the electron spin to its hyperfine coupled nuclei.[14,76] A schematic of the mixed nuclear and electron spin energy levels that result from an *e-n* system and SE DNP is shown in figure 1.1, where excitation of the DQ transition will result in positive enhancement by equalizing the nuclear spin populations of |2> and |3>, which preferentially populates the lower nuclear spin energy levels (α_n). On the other hand, irradiation on the ZQ transition will cause negative enhancement by equalizing the populations of |1> and |4>, which increases the population of the β_n states. The $\mathcal{H}_Z$, $\mathcal{H}_{hfi}$, and $\mathcal{H}_{\mu w}$ terms for SE DNP are shown below

$$H_Z = \sum_{a=1,\dots,N_e} \Delta\omega_a S_{z,a} - \omega_n \sum_{i=1,\dots,N_n} I_{z,i} \quad (1.4)$$

$$H_{hfi} = \sum_{\substack{a=1,\dots,N_e \\ i=1,\dots,N_n}} A_{z,ai}S_{z,a}I_{z,i} + \frac{1}{2}(B_{ai}^{+}S_{z,a}I_i^{+} + B_{ai}^{-}S_{z,a}I_i^{-}) \quad (1.5)$$

$$H_{\mu w} = \omega_1 \sum_{a=1,\dots,N_e} S_{x,a} \quad (1.6)$$

where angular frequencies, ω, are used instead of linear frequencies, ν, with ν=ω/2π, A and $B^{\pm}$ represent the secular and pseudo-secular coefficients of the *e-n* hyperfine interaction tensor,[77] respectively, and the μw irradiation strength is denoted by ω_1.

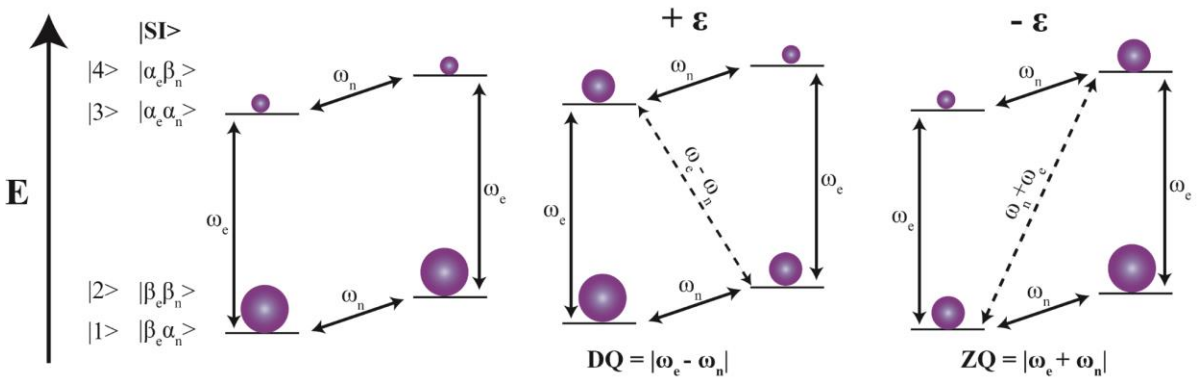

Figure 1.1. Schematic of SE DNP. The leftmost diagram is the nuclear spin populations resulting from a S=1/2 spin system interacting with a I=1/2 spin system with no μw irradiation. The middle diagram shows the effect of μw irradiation on the DQ forbidden transition to the nuclear spin populations – note how the α_n states are more populated, which results in positive ε. The rightmost diagram shows the effect of μw irradiation on the ZQ forbidden transition to the nuclear spin populations – note how the β_n states are more populated, which results in negative ε. The spin states for each energy level is shown on the far left, where α_n and β_e are the lower energy states corresponding to parallel alignment of nuclear spins and antiparallel electron spins relative to B_0, due to their gyromagnetic ratios. The size of the balls corresponds to nuclear spin populations, where the difference in populations between the α_n and β_n states yields NMR signal. Solid lines represent allowed transitions, while dashed lines represent forbidden transitions.

CE DNP occurs when the Zeeman energies of two dipolar coupled electron spins differ by the Zeeman energy of a nuclear spin ($|v_{e1} - v_{e2}| = v_n$), where the electron spins have unequal hyperfine coupling interactions with the nuclear spin.[78] This requirement is termed the CE condition, and when it is fulfilled, polarization is transferred from electron spins to nuclei as a result of strong *e-n* state mixing as shown by the schematic of CE DNP in figure 1.2.[15,76] In this schematic, the CE condition is met when |4> and |5> are degenerate. When this occurs and ω_{e2} is irradiated, the nuclear spin populations are equalized between |2>, |4>, |5>, and |7>, and via ω_n the α_n states are preferentially populated, resulting in positive NMR signal enhancement. Similarly, when the CE condition is fulfilled and ω_{e1} is irradiated, the

populations of |1>, |4>, |5>, and |8> are equalized, where μw irradiation drives the nuclear spins into β_n states, resulting in negative enhancement. For the CE to result in polarization transfer, a polarization difference between the CE-fulfilling electron spins is required, which dictates the maximum polarization that can be transferred to the nuclei. The polarization difference can be induced from direct μw irradiation of one of the electron spins (direct CE) or may come from inherent equilibrium polarization differences between the two electron spins (indirect CE).[79] However, I will only refer to the combined effects of both processes and will thus not differentiate between CE. The $\mathcal{H}_Z$, $\mathcal{H}_{hfi}$, and $\mathcal{H}_{\mu w}$ terms for 3-spin CE DNP are shown below:

$$H_Z = \Delta\omega_a S_{z,a} + \Delta\omega_b S_{z,b} - \omega_n \sum_{i=1,\dots,N_n} I_{z,i} \tag{1.7}$$

$$H_{hfi} = \sum_{\substack{\varepsilon=a,b \\ i=1,\dots,N_n}} A_{z,\varepsilon i} S_{z,\varepsilon} I_{z,i} + \frac{1}{2}\left(B^{+}_{\varepsilon i} S_{z,\varepsilon} I^{+}_{i} + B^{-}_{\varepsilon i} S_{z,\varepsilon} I^{-}_{i}\right) \tag{1.8}$$

$$H_{\mu w} = \omega_1 (S_{x,a} + S_{x,b}) \tag{1.9}$$

where the effect of electron spin pairs is considered for the secular and pseudo-secular terms of the hyperfine interaction tensor and when irradiating the sample. A fourth term also needs to be considered for the CE that accounts for frequency differences between the μw irradiation and ω_e, which is called $\mathcal{H}_{offset}$,

$$\mathcal{H}_{offset} = \sum_{\varepsilon} \Delta\omega_{\varepsilon,\mu w} S_{z,\varepsilon} \tag{1.10}$$

where $\Delta\omega_{\varepsilon,\mu w}$ is the frequency difference between the electron spins and the μw irradiation.

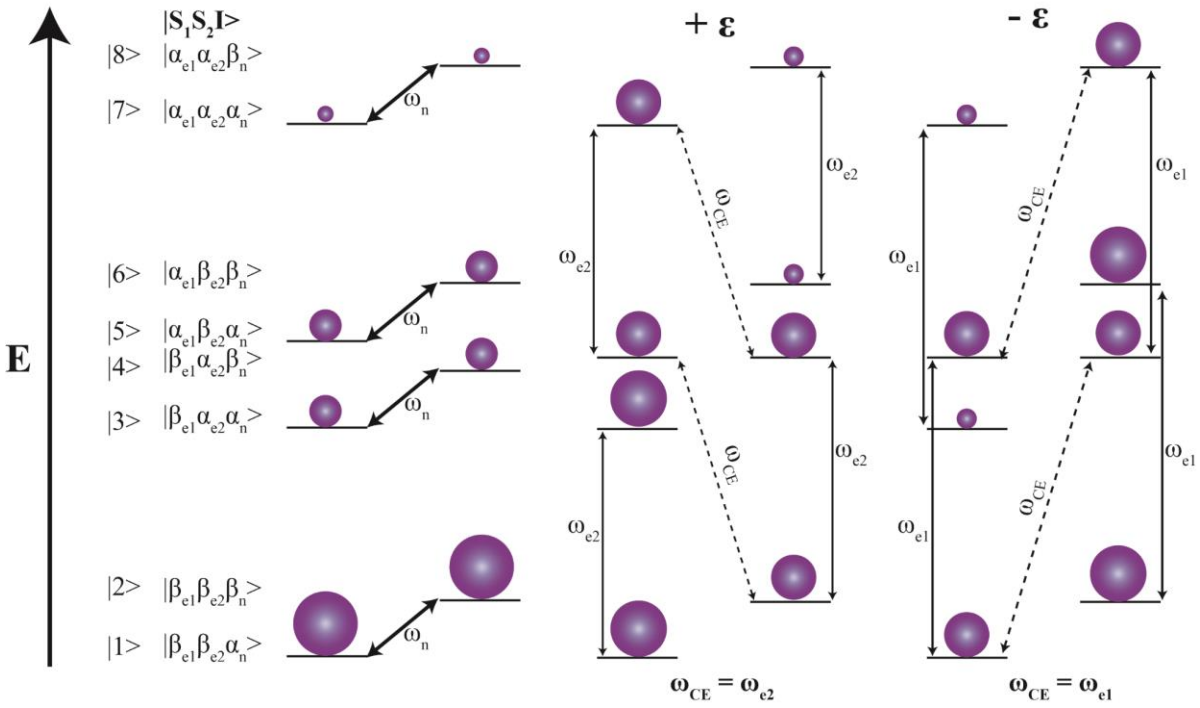

Figure 1.2. Schematic of CE DNP. The leftmost diagram is the nuclear spin populations that result from a three-spin system composed of two coupled electron spins (S=1/2) and one nuclear spin (I=1/2). The middle diagram illustrates the nuclear spin populations that result from irradiation of ω_{e2}, when states |4> and |5> are degenerate (i.e. meet the CE condition) – note how the α_n states are more populated, which results in positive ε. The nuclear spin populations of the two degenerate states become equalized. The rightmost diagram shows the effect of μw irradiation on ω_{e1} to the nuclear spin populations, when |4> and |5> are degenerate – note how the nuclear spin populations of |4> and |5> have equalized and the β_n states are more populated, which results in negative ε. The spin states for each energy level is shown on the far left, where α_n and β_e are the lower energy states corresponding to parallel alignment of nuclear spins and antiparallel electron spins relative to B_0 due to their gyromagnetic ratios. The size of the balls corresponds to nuclear spin populations, where the difference in populations between the α_n and β_n states yields NMR signal. Solid lines indicate allowed transitions, while dashed lines refer to forbidden transitions.

If the difference between the electron spin polarizations is generated directly by selective saturation of one of the electron spin populations by μw irradiation, then the resulting hole burnt into the EPR spectrum is expected to have a width dictated by electron spin relaxation via the lattice phonons, T_{1e}, and phase decoherence of the electron spins, T_{2e}. If this hole burnt into the EPR spectrum is smaller than the frequency difference between the electron spins at

the CE condition, then an electron spin polarization differential exists between these electron spins, which can then be transferred to the hyperfine coupled nuclei. If the EPR spectrum is inhomogeneously broadened, as occurs for nitroxide-based radicals, which are the most commonly used radical type for DNP applications, then electron spectral diffusion (eSD) can broaden the hole burnt into the EPR spectrum. An inhomogeneously broadened EPR spectrum occurs when the radical interacts anisotropically with the magnetic field, B_0. This can be observed by the orientation of the p_z-orbital of the nitroxide moiety with respect to the magnetic field, where the z-axis aligns with B_0, which correspond to different g-factors – i.e. molecular orientation in the magnetic field. The nitroxide EPR spectrum is further broadened by anisotropic *e-n* hyperfine interactions, where the S=1/2 spin system of the electron spin interacts with the I=1 spin system of ^{14}N. This causes the energy levels of the spin system to split into six states that can undergo three degenerate transitions as indicated in figure 1.3a. The anisotropic hyperfine splitting is largest for the z-component, which is the only observed hyperfine splitting at high fields (>140 GHz) as shown by the nitroxide EPR spectra of figure 1.3b, where the orientation dependent g-factors are labeled as g_{xx}, g_{yy}, and g_{zz} and correspond to the principle axis system of the g-factor tensor. The hyperfine z-component, A_{zz}, causes the three bumps in the g_{zz} segment of the nitroxide EPR spectrum at 194 GHz.

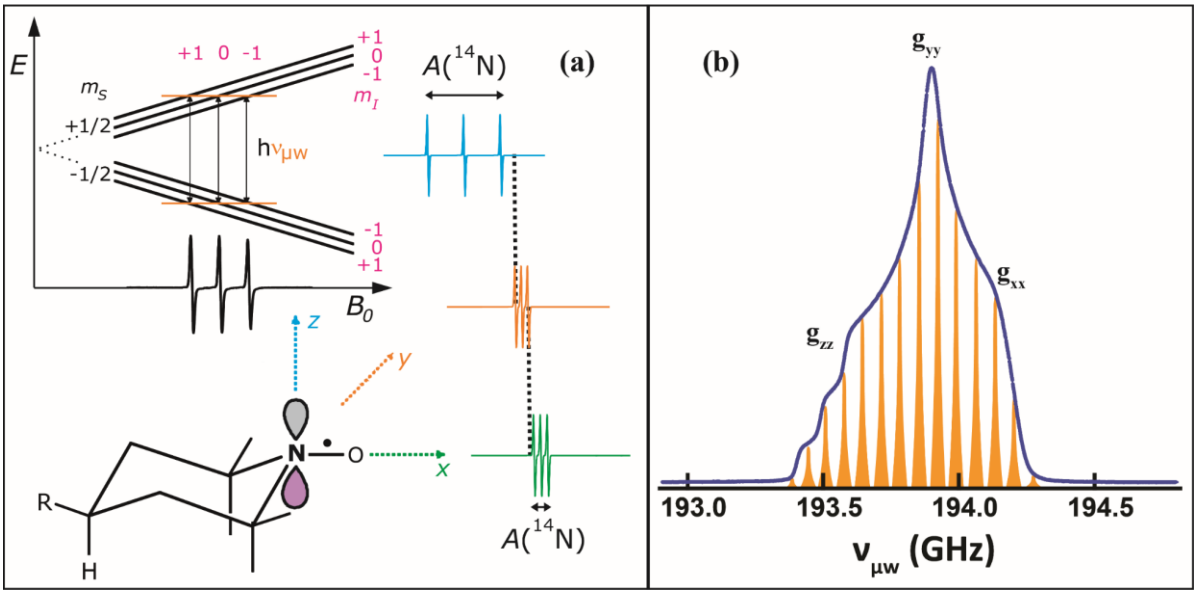

Figure 1.3. Illustrations of the nitroxide EPR hyperfine interactions that result from a spin-1/2 system (m_S) and a spin-1 system (m_I), resulting in three degenerate electron transitions. (a) The nitroxide radical is shown with its p_z-orbital, which is the cause of anisotropic hyperfine interactions, A. The x-, y-, and z- components of a low field nitroxide EPR spectrum (10 GHz) resulting from solely the hyperfine interactions are shown in blue, gold, and green in (a). An example nitroxide spectrum at 194 GHz is shown in (b), where the inhomogeneously broadened EPR spectrum is composed of homogeneously broadened spin packets, represented by the gold Lorentzian distributions. At higher fields the, resolution of different g-factors improves, as annotated in (b). This occurs to such an extent that weak hyperfine interactions are challenging to distinguish in these spectra. Therefore, only the z-component of the hyperfine interaction for nitroxides are easily visible – as seen by the three bumps in g_{zz}.

In general, we say that an inhomogeneously broadened EPR spectrum is composed of spin packets that correspond to homogeneously broadened spins that result from a single orientation of both the molecule in the magnetic field and the hyperfine interaction. This concept is illustrated in figure 1.3b. If the homogeneous line-broadening of individual spin packets overlap, then eSD occurs, where polarization is transferred from one spin packet to another. eSD can also occur between non-overlapping spin packets if the electron spins are spatially close enough to dipolar couple – this process is sometimes defined separately from eSD as electron spin diffusion, but for the purposes of this dissertation, eSD will refer to both

processes. It should be noted that larger $\Delta\nu_e$ ($\Delta\nu_e=|\nu_{e1}-\nu_{e2}|$) and weaker dipolar interaction strengths will result in less efficient polarization transfers between spin packets. The concept of eSD is illustrated in figure 1.4, where ν_{excite} defines the frequency of μw irradiation and Δ_{bin} defines the width of the spin packet.

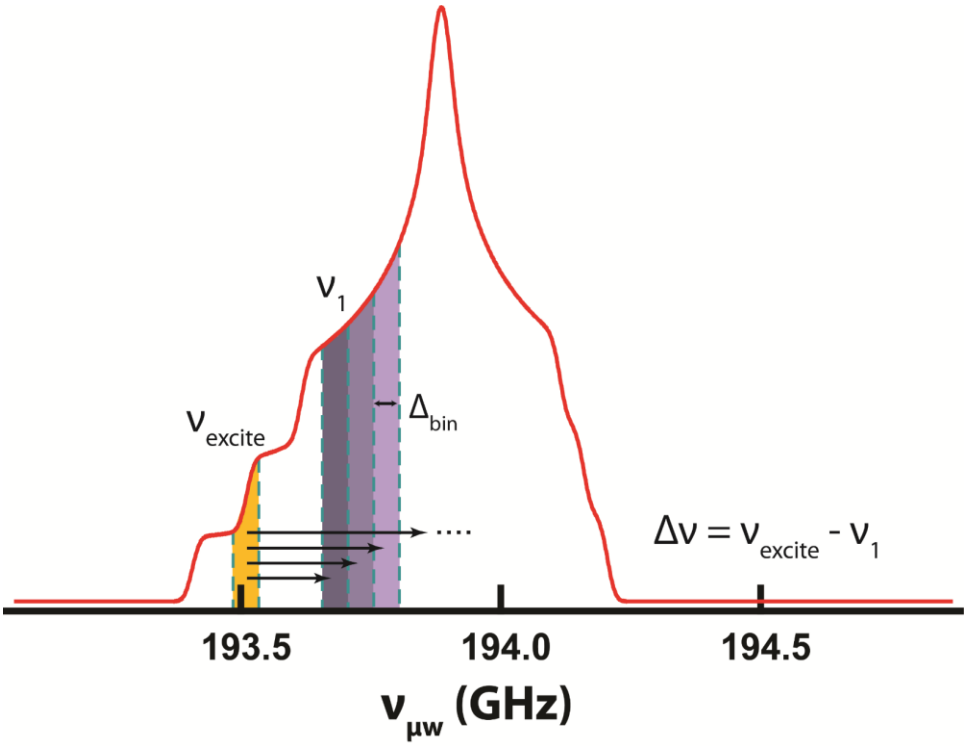

Figure 1.4. Pictorial description of electron spectral diffusion, where the spin packet directly irradiated by μw, ν_{excite}, (gold) transfers polarization to other spin packets at different resonant frequencies, ν_1 (purple). As $\Delta\nu$ increases the polarization transfer efficiency decreases, as shown by the lighter purple tones. The width of the spin packets is denoted by Δ_{bin}.

In both DNP mechanisms, the polarization of the bulk nuclei that are not directly hyperfine coupled to the electron(s) is possible due to efficient nuclear spin diffusion processes.[66,70] The nuclei that are directly hyperpolarized by an electron spin are termed core nuclei, while those hyperpolarized via *n*-*n* spin diffusion are termed bulk nuclei. The nuclei that are in close

proximity to the electron spins will have very fast relaxation rates, due to paramagnetic relaxation enhancement (PRE) effects,[80,81] which results in these nuclei being "invisible" to NMR detection – also known as bleached. This results in the bulk nuclei generating the majority of the detectable NMR signal. However, not all core nuclei are close enough to the electron spin(s) to be invisible; therefore, it is a combination of the unbleached core nuclei and bulk nuclei hyperpolarized via *n*-*n* spin diffusion that generate the detectable hyperpolarized NMR signal.[14,70,82] The spin diffusion process to bulk nuclei from a single electron spin and a single core nucleus can be described by the following Hamiltonians

$$\mathcal{H} = \mathcal{H}_Z + \mathcal{H}_b + \mathcal{H}_{e-c} + \mathcal{H}_{c-b} + \mathcal{H}_{b-b} \tag{1.11}$$

$$\mathcal{H}_Z = \Delta\omega_e S_z + \omega_n I_{z,c} \tag{1.12}$$

$$\mathcal{H}_b = -\sum_{b=1,\ldots,N_b} \omega_n I_{z,b} \tag{1.13}$$

$$\mathcal{H}_{e-c} = A_z S_z I_{z,c} + \frac{1}{2}[B^+ S_z I_c^+ + B^- S_z I_c^-] \tag{1.14}$$

$$\mathcal{H}_{c-b} = \sum_{b=1,..,N_b} d_{cb} \left\{ 2I_{z,c} I_{z,b} - \frac{1}{2}(I_c^+ I_b^- + I_c^- I_b^+) \right\} \tag{1.15}$$

$$\mathcal{H}_{b-b} = \sum_{b<b'=1,..,N_b} d_{ij} \left\{ 2I_{z,b} I_{z,b'} - \frac{1}{2}(I_b^+ I_{b'}^- + I_b^- I_{b'}^+) \right\} \tag{1.16}.$$

Here *b*, *c*, and *e*, denote bulk nuclei, core nuclei, and electrons respectively, $\mathcal{H}_Z$ represents the Zeeman energies of the single electron spin and the core nuclear spin used in this model, while $\mathcal{H}_b$ is the Zeeman energies of all bulk nuclei. $\mathcal{H}_{e-c}$ is the hyperfine interaction between the electron spin and the core nucleus, which represents the *e*-*n* polarization transfer process, while $\mathcal{H}_{c-b}$ and $\mathcal{H}_{b-b}$ represent the spin diffusion processes from core to bulk nuclei and between bulk nuclei respectively.

These two DNP mechanisms and the spin diffusion process only consider a limited number of spins in the system, when in reality a sample will have orders of magnitude more spins per sample. Therefore, a third mechanism called thermal mixing (TM), used primarily in dDNP, attempts to describe the multi-electron and multi-nuclei spin system present in *real* samples utilizing a spin temperature formalism.[22,83–90] However, a full quantum mechanics based theory of a multi-electron and multi-nuclei system, representative of a realistic sample is still lacking.[83] In recent years, it has become apparent that the commonly accepted theoretical framework of TM for static conditions at very low temperatures (< 5 K) may not be consistent with experimental DNP observations, in particular the lineshapes of DNP spectra and the underlying saturation profile of the EPR spectrum.[68,83,91–93] As such we will focus on the previously described CE and SE DNP mechanisms.

1.2. Importance of understanding spin dynamics

While the quantum mechanical-based SE and CE DNP models can fit DNP spectral lineshapes,[50,94,95] they do not fully describe or easily predict the outcome of DNP experiments, such as the shape of the DNP spectrum or the DNP enhancement, mainly because critical experimental parameters are usually unknown, and thus are estimated when modeling DNP. These include electron relaxation rates, electron spectral diffusion rates, EPR saturation profiles, and nuclear spin diffusion properties under operational DNP conditions. Therefore, the only current viable method to optimize DNP conditions is through empirical determination of these operating parameters. However, the design for reliable DNP experiments is still limited primarily to a proven set of experimental conditions and sample types that produce effective signal enhancements and consistent DNP performance. A rational design of DNP experiments will benefit from the analysis of the DNP mechanisms under a variety of sample

formulations, requiring the study of both the nuclear and electron spin dynamics in the system – ideally under identical experimental conditions.

As DNP is the transfer of polarization from the electrons to the hyperfine coupled nuclei in a system, it is imperative to understand the electron and nuclear behaviors individually and how they interact with each other, under conditions relevant for DNP. Thus, EPR can help elucidate surprising DNP results and refine our understanding of the mechanisms that drive DNP processes. Therefore, selected examples of how studying EPR improved our understanding of DNP results or enhanced the DNP performance are presented to illustrate the importance of acquiring the whole picture of the spin system. This is especially important when presented with odd or puzzling experimental results and to expand the scope of viable samples that can be studied via DNP. The study of the electron (de)polarization profile has helped identify the DNP mechanism(s) in a system,[96] such as differentiating between a truncated CE that has the appearance of the Overhauser effect,[97] evaluating the contributions of CE and SE DNP,[66,98] and contributed to the development of new DNP theory, such as the heteronuclear-CE.[92] Careful analysis of the DNP polarization profile and the electron spin relaxation properties revealed that glass polymorphism generated by specific solvent mixtures induced radical clustering, as identified by altered electron spin phase memory time (T_m).[99] The measurement of T_m also helped determine that the incoherent term of the *e*-*n* hyperfine coupling is suppressed when the electron spins are saturated under DNP conditions, which reduces the NMR linewidth.[100] These studies exemplify the benefits of a dual DNP/EPR spectrometer that yield mechanistic insight and unravel experimental misunderstandings.

Thus, a dual DNP/EPR spectrometer needs to be intelligently designed to effectively detect and analyze the electron and nuclear spins in the system. This understanding is not

new.[30,96,101–103] However, high field instrumentation with dual DNP/EPR capabilities is scarce, with only a few setups available to date, including custom instrumentation at 95 GHz at the Weizmann Institute and Nottingham University,[104–107] 140 GHz at MIT,[108,109] and 200 GHz at UCSB.[110,111] A versatile dual DNP/EPR instrument requires broad-band μw capabilities to select for multiple paramagnetic species, allow for μw manipulation through an arbitrary waveform generator (AWG), and be capable of pump-probe, multi-frequency, EPR experiments. Solid-state (ss) μw sources are an essential feature to achieve this type of versatility. However, only in recent years have ss-μw sources become powerful enough for DNP and pulsed EPR experiments. A number of ss-μw source-based high-field EPR spectrometers operational at > 95 GHz have led the way, including that of van Tol and coworkers at the National High Magnetic Field Lab (110-395 GHz),[112,113] Takahashi at USC (115 and 230 GHz),[114,115] Griffin at MIT (140 GHz),[116] Britt at Davis (263 GHz), Prisner at the Goethe University in Frankfurt (180 GHz),[117] Sherwin at UCSB (240 GHz),[118,119] Lubitz at the Max Planck Institute (122 and 244 GHz),[120] Freed at Cornell University (250 GHz),[121] the commercial Bruker pulsed EPR system, the E780 (263 GHz),[122] Schmidt at Leiden University (275 GHz),[123,124] and Möbius at the Free University Berlin (360 GHz).[125,126] Tycko and Thurber at the National Institute of Health (264 GHz) have demonstrated the use of a ss-μw source for MAS DNP operation,[127–129] while Zilm and coworkers at Yale University (200 GHz) have debuted at the 2017 ISMAR a dual MAS DNP/EPR instrument operational at room temperature using diamond P1 center signal.[130] A summary of available DNP spectrometers and their capabilities are provided in Appendix A. We forecast for MAS and static experiments, that dual DNP/EPR will become a critical capability for advancing the field of DNP, by rationally improving DNP performance and increasing the application scope of DNP.

1.3. Summary

The combined importance of needing a versatile instrument platform to study DNP – in terms of both unique sample formulations and basic spin physics – has motivated our development of hardware for a high field dual DNP/EPR spectrometer. The improvement of the instrumental capabilities has enabled us to probe both the electron and nuclear spin dynamics in the system at various experimental conditions to better understand the underlying spin physics for the DNP process in general and for unique or exotic samples or radicals. The NMR signal enhancement (ε) depends on the underlying DNP mechanism that is dictated by the radical design, radical concentration, solvent property, and nuclear spin type, as well as other factors such as the μw power and operating temperature that influence the electron and nuclear relaxation and polarization transfer rates; all of these components must be considered to fully understand the DNP process. Therefore, the following chapters will address the hardware developments I have made to the Han group's 194 GHz dual DNP/EPR spectrometer as well as the resulting studies towards understanding the underlying spin physics that occur during the DNP process. The EPR capabilities of the instrument are presented in chapter 3, with selected examples that showcase the range of data that can be acquired. Chapter 3 also explains how to interpret this data in terms of the sample and with respect to DNP. The influence experimental conditions such as radical concentration, temperature, and μw power have on the DNP mechanism and efficiency are discussed in chapter 4. A key assumption made in DNP experiments is that the radicals, which are crucial to hyperpolarize the nuclear spins as they are the source of the unpaired electrons, are homogeneously distributed throughout the sample; however, in chapter 5, I provide illustrative examples that this is a poor assumption, and in fact, the radicals can cluster. With

this in mind, chapter 6 delves into the impact local *e*-*e* interactions have on the DNP process in general and specifically on the nuclear relaxation rates. Finally, chapter 7 provides a short summary of the findings discussed throughout this work and provides a perspective on interesting future research opportunities that remain for DNP instrument development, DNP mechanistic research and the underlying spin dynamics associated with it, as well as potential applications of DNP to materials science.

2. Hardware developments

A versatile dual DNP/EPR spectrometer benefits from a modular design, so that modifications for specific experiments and hardware developments can be easily incorporated. Designing for modularity requires a particular eye for the type of experiments one wants to achieve with the instrument. The type of DNP to be performed will alter the required components for the spectrometer, where dissolution DNP will need a rapid melting apparatus and generally cryogenic handling capabilities down to ~1 K, magic angle spinning (MAS) DNP requires a stator and other associated hardware for MAS, while static DNP may require wider microwave (μw) bandwidths or a cavity for easy conversion between DNP and EPR. However, all dual DNP/EPR instruments require at least an NMR console and a superconducting magnet corresponding to the magnetic field of choice, sample temperature control, μw source and manipulation stage for transmission, a probe to direct the μw to the sample and support the sample, and detection capabilities for the EPR signal. In this section we will review some of the options available for each of these essential components for dual DNP/EPR instruments, while describing specific examples for the 194 GHz static dual DNP/EPR system installed in the Han lab at UCSB, where the general schematics of the instrument, as previously described by Siaw et al,[110] is shown in figure 2.1a and a picture of the actual instrument in figure 2.1b.[131] In this chapter, detailed descriptions of recent advances to integrate arbitrary waveform generators (AWG) and 2-μw source capabilities will be provided, among others.[131,132] In the following sections we detail the components and design of the different modules in the dual DNP/EPR instrument with shaped pulse capabilities for μw transmission, pump-probe electron spin experiments, and synchronized radio frequency (rf)- and μw- pulsing capabilities, which were recently published.[131]

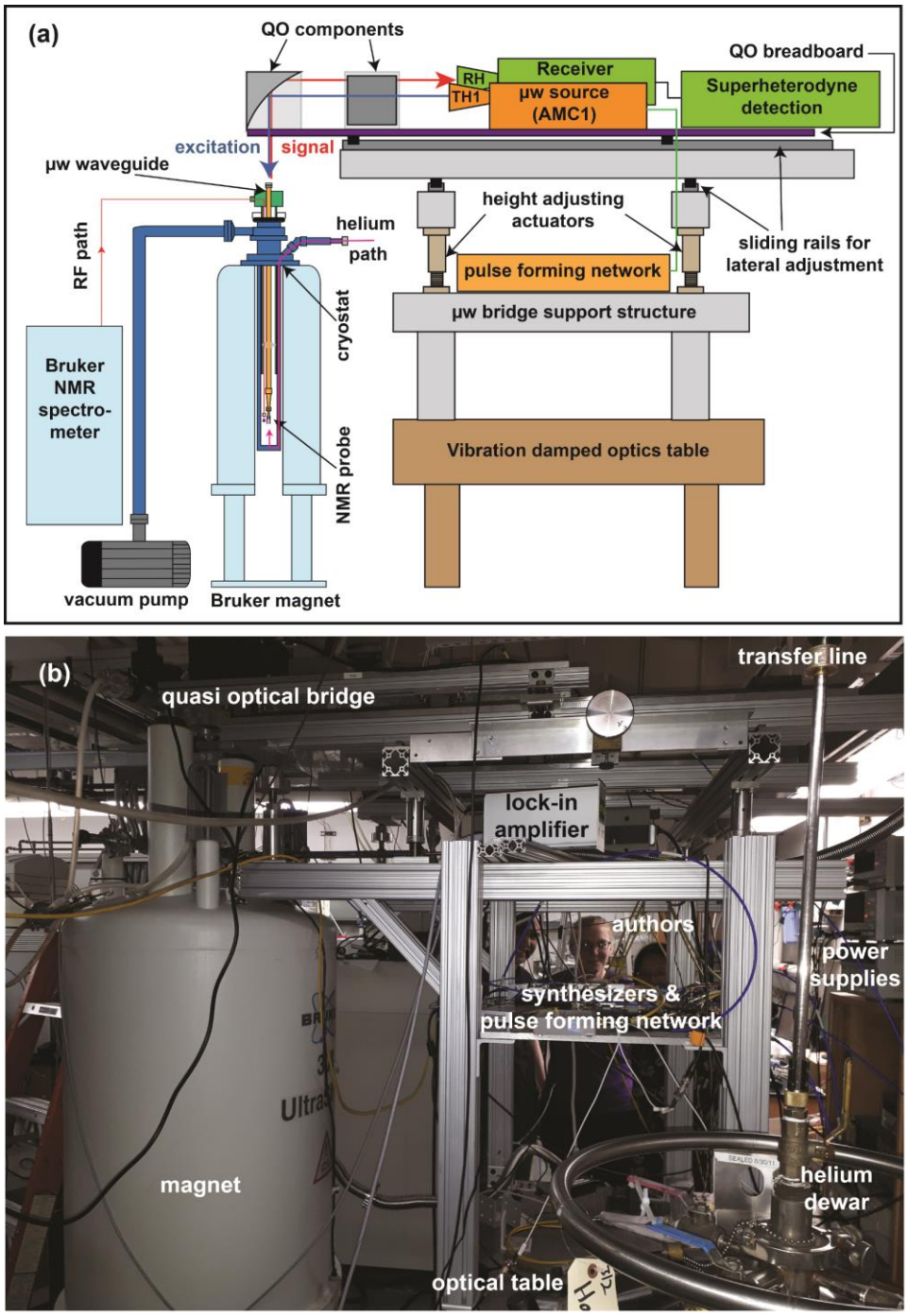

Figure 2.1. Instrument overview schematic (a) and picture (b) of the dual 194 GHz DNP/EPR spectrometer at UCSB.

2.1. High field magnet

A dual DNP/EPR instrument is capable of acquiring both NMR and EPR data. For MAS DNP operation, particularly biological samples, where achieving sub-ppm resolution is important, a static-field NMR magnet with 10^{-7} – 10^{-8} field homogeneity is a necessary prerequisite. An alternative for static NMR/DNP and d-DNP is a variable-field EPR magnet, where a ~10 ppm homogeneity can be achieved and the magnetic field easily adjusted and swept by changing the current in the superconducting coil. There are other important parameters to consider when choosing the best magnet for a given system – cryogen-free versus a wet design, bore size, type and number of cryogenic shims, and the presence of a dedicated superconducting and/or room temperature sweep coil. All of these choices will affect the cost of the magnet itself but have added benefits; a cryogen-free system will decrease helium consumption, while the majority of the magnet operating costs will be electricity. Variable field and sweep coils in the magnet allow for traditional field-swept EPR experiments, and consequently avoid some of the problems associated with frequency swept EPR experiments, such as standing waves in the quasi optics and frequency dependent source output power. A variable-field magnet also increases the scope of paramagnetic species that can be employed as polarizing agents in DNP by meeting the resonance conditions for species with $g \neq 2$. In our example system a commercial, wide-bore (89 mm) NMR magnet at 7 Tesla from Bruker (Avance D300WB) was used.

2.2. NMR console

An NMR console can be home-built or purchased commercially. Hilty and Takeda provide two different bases for building-your-own NMR consoles.[133,134] In the example systems that we discuss here, a commercial Bruker Avance DSX console with 1 kW ^{1}H and X channel

amplifiers was used. Due to the large difference in NMR signal intensity between DNP enhanced and unenhanced signals, the dynamic range of the commercial analog to digital convertor (ADC) was insufficient. If the receiver gain of the spectrometer was adjusted for the unenhanced NMR signal intensity the enhanced signal under DNP conditions saturated the ADC. Alternatively, if the receiver gain was adjusted for the intensity of the DNP-enhanced signal the signal to noise ratio of the unenhanced signal became unsatisfactory. Varying receiver gain throughout the experiment was precluded by non-linear variations in the gain, which resulted in large errors in the absolute NMR signal intensity, even after a calibration procedure. Implementation of a set of calibrated variable attenuators (Pasternack) between the pre-amplifier and the console allowed for operation with a high receiver gain setting and prevented saturation of the ADC for DNP-enhanced signals, which has been standard operating procedure for the Han lab UCSB instrument for routine operation. The unattenuated signal is then calculated according to $V_{in} = V_{out}10^{0.05A}$, where A is the applied attenuation in dB, V_{in} is the voltage input, and V_{out} is the voltage output after the attenuator(s), which is a standard dB to voltage calculation. The integrals of the NMR peaks scale linearly with the signal voltage.

2.3. Cryostat and temperature control

DNP at temperatures above 200 K have been successfully demonstrated at high magnetic fields (> 5 T) for BDPA and TEKPol radicals dissolved in *ortho*-terphenyl;[135] however, other examples of DNP performed at high temperatures and high magnetic fields are limited.[45,136] Freezing a sample to cryogenic temperatures with liquid helium or nitrogen significantly improves the electron spin Boltzmann statistics and prolongs the electron spin relaxation times, which subsequently increases the achievable NMR signal under DNP. Thus, operation

at a low (≤100 K) and stable temperatures is typically desired for most DNP experiments. For MAS-DNP, there are three current designs for spinning and cooling the sample: nitrogen only (> 90 K),[137] a hybrid nitrogen (spinning) and helium (cooling) system (>20 K),[35,127] and a helium-only design (> 6 K).[138,139] For static DNP/NMR, dDNP, and EPR systems, a cryostat is used to cool the sample to low temperatures – typically either using a continuous-flow or a cryogen-free design. A decision must be made if the cryostat will be top- or bottom-loaded, whether an optical window is needed, and if a cryogen-free cryostat will be used or not – the latter option can significantly reduce the operational costs. The Han lab UCSB system uses a custom Janis STVP-200-NMR continuous-flow cryostat (Janis Research Co. LLC) designed for operation from <3 K to 325 K, with a 50 W voltage controlled resistive heater for temperature control that outputs 0-35 V with a 15 A power supply. A Cernox temperature sensor (LakeShore Cryogenics) near the cryogen inlet for the cryostat acts as the detector for a Labview proportional-integral-derivative (PID) algorithm to control the voltage for the heater, maintaining stable temperatures (±0.05 K) over long experimental times. Liquid helium from a slightly pressurized, 3 psi, liquid helium dewar (Praxair) is supplied to the cryostat with a flow-controlled liquid helium transfer line (Janis Research Co LLC). The cryostat outlet is maintained at atmospheric pressures for operation at temperatures > 5 K and reaches a stable temperature in less than an hour. For operations < 5 K, a Sogevac SV65B rotary cane pump (Oerlikon Leybold Vacuum) is used to evacuate the sample chamber of the cryostat, while still flowing the liquid helium to depress the boiling point of the helium, allowing for operation down to ~3 K. The cryostat itself is top-loaded into the 89 mm bore of the NMR magnet (room temperature shims are removed) with a hollow 52 mm bore for a top-loaded dual DNP/EPR probe (Figure 2.1a).

2.4. Microwave bridge support

The support structure can be constructed in any form and from any non-magnetic material that allows for precise vertical, horizontal, and angular position adjustment of the μw bridge relative to the orientation of the μw waveguide. To minimize vibrations, we recommend that the support structure for the μw bridge is mounted on top of an optical table (RS 1000^{TM}, Newport Corp.) (although this is not crucial for μw in the mm-wave regime, so the optical table can be omitted to minimize costs). The support structure for the 194 GHz system is constructed using T-slotted aluminum extrusions (McMaster-Carr), equipped with sliding rails (McMaster-Carr), to enable lateral movement of the bridge positioned above the superconducting magnet. This is for easy removal of the cryostat and/or DNP probe and to align the μw beam from the μw bridge with the waveguide for optimal coupling. Four custom machined actuators mounted on the corners of the support structure are used for fine adjustment of the height and relative angle between the μw bridge and the waveguide of the probe insert.

2.5. Microwave source and bridge control

The μw source is the heart of a dual DNP/EPR spectrometer. The requirements for μw power vary significantly between different DNP experiments, with few millliWatts being sufficient for d-DNP at very low ~1.2 K temperatures to several Watts or tens of Watts needed for MAS DNP performed at ≥ 100 K. The required frequency range depends on the choice of the operating magnetic field, and typically varies between 95 GHz (3.3 T) for d-DNP and DNP/EPR instruments to 527 GHz (17 T, 800 MHz ^{1}H) for high-resolution MAS DNP. Another important consideration is whether continuous wave (cw) μw are sufficient as used in d-DNP and MAS DNP systems, or whether a more sophisticated manipulation of the μw is

required for pulsed operation, frequency, phase, and/or amplitude modulation. If shaping of the μw is desired, the conventional approach utilized in pulsed EPR at ~9-35 GHz, is to pre-form and shape the pulses at X-band (8-12 GHz) and low power (mW), potentially multiply to higher frequencies, and amplify the power output to hundreds of Watts or a few kiloWatts, before guiding the microwave beam to the sample. This approach works well up to ~140 GHz,[105,140–143] but has limited utility at 150 – 300 GHz, with current state of the art extended interaction klystron amplifiers (EIK) providing only a few watts of power.[144–146] Above 300 GHz, this design becomes obsolete, since high power amplifiers are not available for these frequencies. The commercially available DNP spectrometer made by Bruker relies on a different design concept: a gyrotron source is used,[147] which inherently limits the operation to cw, but allows for tens of Watts of power output up to 527 GHz (800 MHz ^{1}H).[148] However, if low μw power is sufficient, typically when operating at liquid helium temperatures below 50 K, as found in ultra-low temperature MAS-, static-, and d-DNP, a solid state (ss) μw source can be used.[106,110,129] In addition to being the cheapest option, a ss-μw source is significantly more agile than either a klystron or a gyrotron, and thus, it is an ideal μw source for a versatile dual DNP/EPR instrument. Besides simply considering the output power of the μw source, the ss-μw source is easier and faster to manipulate, where modulation of the μw, beyond changing the frequency in cw operation, significantly increases the scope of potential DNP and EPR experiments that the instrument can perform. Examples of these will be provided with case studies.

2.5.1. Sold-state microwave sources

Solid state-MW sources can have large operational bandwidths; but suffer from relatively low power outputs of ≤ 500 mW at high fields (>150 GHz). Only in recent years have ss-μw

sources in the 100 GHz – 200 GHz range matured enough to be effectively utilized for EPR and DNP experiments without further amplification, with generally ~150 mW produced at 200 GHz and tens of milliWatts at higher frequencies. High field ss-μw synthesizers come in a variety of forms, as gunn diodes, metal-oxide semiconductor (CMOS) chips, or low frequency synthesizers that are amplified and multiplied to the desired high-field frequency. The later type of sources generally rely on a crystal that will produce oscillatory irradiation in the tens of GHz range when a voltage is applied, which is then multiplied to the desired frequency through a series of doublers and amplifiers collectively referred to as amplification-multiplication chains (AMCs). Virginia Diodes Inc (VDI) and Elva-1 produce sources at frequencies ranging from 40 GHz to 3.2 THz, and from 26 GHz to 180 GHz, respectively.[149,150] In our example system, ~ 12 GHz cw-irradiation is produced with a yttrium iron garnet (YIG) crystal (Microlambda and VDI) and is multiplied x16 by a VDI AMC to reach ~140 mW at 200 GHz, with a bandwidth of 190-201 GHz. The resultant linearly polarized 200 GHz μw are transmitted through a corrugated WR4.3UG to 12.7 mm i.d. transmission horn (Thomas Keating Ltd) to generate a Gaussian beam suitable for quasi-optical transmission to the sample (see section 2.10.2.). In the last year we have acquired from VDI a 500 mW, 194 GHz source that combines a W-band (~95 GHz) amplifier with a custom AMC to boost the output power to > 400 mW over 188-196 GHz. Similar developments were initially conceived by A. I. Smirnov and A. A. Nevzorov at NC State.[151] All of the synthesizers have 1 Hz frequency resolution and a ~10 ms response time to changing frequencies. μw amplitude modulation is integrated into the AMCs through an analog voltage (0-5 V) control, which has a response time of ≤ 0.5 ms. The frequency and amplitude modulation are paramount features for agile μw manipulation that are necessary for accurate DNP and EPR

experiments, where elevating μw irradiation beyond the cw mode will improve the versatility of the system by allowing for pulsed-DNP and pulsed-EPR experiments, especially for coherent control of the electron spin systems. However, the slow response times of the YIG synthesizer (~10 ms frequency switching time) and the integrated amplitude modulation control for the AMCs limit the instrument's capabilities for electron spin manipulation that require manipulations on a faster (ns – μs) timescale. To allow for greater flexibility in system performance and to overcome the above limitations, a two-source system with AWG capabilities was implemented.

2.5.2. Synthesizer selection

Our strategy to reduce the frequency switching time in two-frequency experiments, e.g. for ELectron-electron DOuble Resonance (ELDOR) measurements, is to employ two separate YIG-based synthesizers. The selection between the two cw- μw synthesizers is done with solid-state switches (SWM-DJV-1DT-2ATT, American Microwave Corp.) that have a short, < 10 ns, response time (shown in figure 2.2a/b - orange block), followed by a power combiner (Narda). Selecting which switch is open or closed will determine which synthesizer is used to direct the ~12 GHz μw signal to the AMCs, and so acts as the first cut for generating, and defining the length of, μw pulses. If cw-irradiation is desired, the switches are simply opened for entire duration of the experiment. If two different synthesizers are used in the spectrometer, it is important to ensure that the input power to the pulse forming network module (teal block in figure 2.2b) is the same, regardless of which synthesizer is selected. This avoids saturating some of the components in the pulse forming network module when using one synthesizer versus the other and is typically achieved by adding attenuators after the synthesizer with the higher output power.

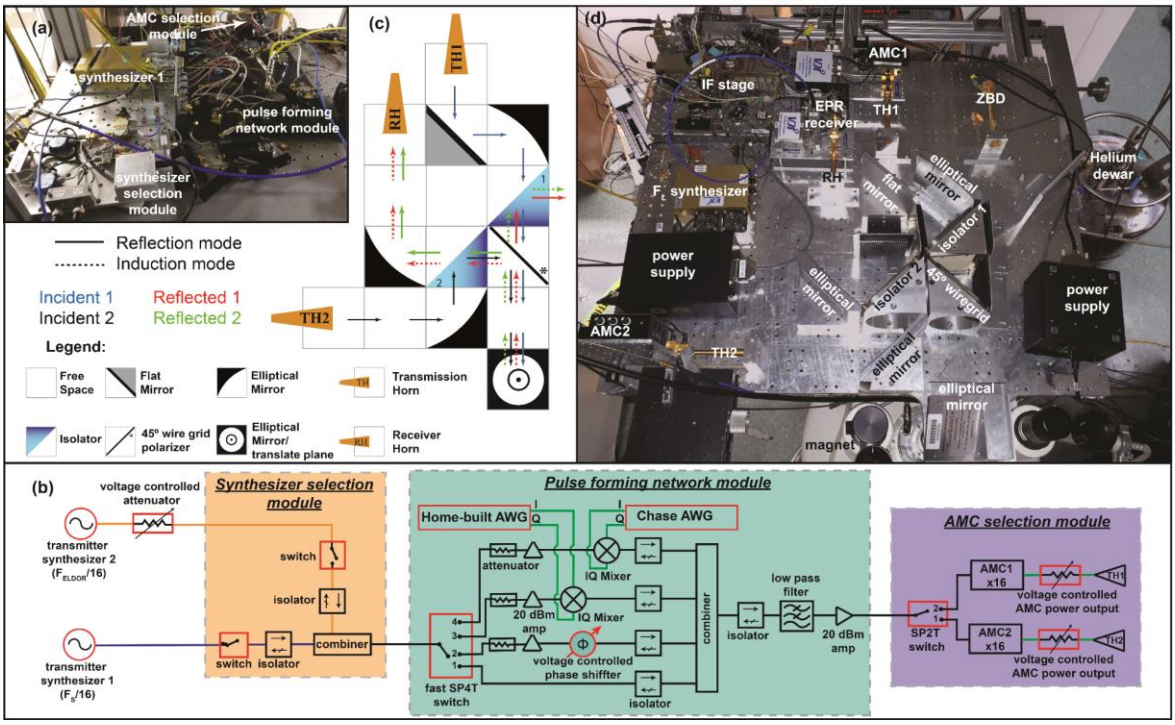

Figure 2.2. Picture (a) and schematic (b) of the μw manipulation capabilities at 12 GHz for the dual DNP/EPR spectrometer. Orange block denotes synthesizer selection module; teal block details the components of the homemade pulse forming unit with phase cycling, bypass, home-built AWG, and Chase AWG channels available (left to right); purple block denotes the AMC selection module. Components shown in red are computer controlled by Specman4EPR software. Blue line denotes the path of 12 GHz signal at main (F_S) frequency generated by transmitter source 1. Orange line denotes the path the 12 GHz signal at 2nd (F_{ELDOR}) frequency generated by transmitter source 2. Green line denotes the path of signal mixed with the AWGs. Black lines denote the paths shared by both F_S and F_{ELDOR} signals. (c) Quasi-optical design for a 2-source system. Each tile represents a distance of 125 mm or f/2. The dark part of the isolator indicates where the Faraday rotator is located. TH1 (transmission horn 1) results in induction mode EPR detection, TH2 results in reflection mode detection, and RH (receiver horn) captures the EPR signal for detection. Arrows indicate the μw pathway in free space through the quasi-optics as defined by color and solid vs dashed in the figure. (d) Picture of the μw bridge supporting the quasi optics, AMC1, AMC2, and the EPR detector (EPR receiver system and intermediate frequency (IF) stage).

2.5.3. Pulse forming network with AWG capabilities

A pulse forming network further develops the pulse from the initial cut provided by the source selection module. This is where phase, frequency, and amplitude manipulations can be performed to shape the pulse to the desired outcome. Various components can be incorporated

to manipulate the 12 GHz signal in the pulse forming network prior to passing through the AMCs to reach 194 GHz, which is a significant advantage of the ss-μw source-based system compared to a gyrotron-based system. The schematics for the example system's pulse forming unit are shown in figure 2.2b – in the teal block. The signal from the synthesizer selection module is sent to a four-way SP4T switch (F9140AH, General Microwave) with a 10 ns response time to select the type of pulse manipulation. The 1st "bypass" channel is used if no other manipulations are necessary, such as in straightforward cw-DNP or cw-EPR experiments. The 2nd channel is equipped with a voltage-controlled phase shifter (SLPS-122-25V, Spacek Labs) that shifts the phase of the μw pulse by an arbitrary value relative to the "bypass" channel, as needed by two-step phase cycling for pulsed EPR. As the response of the voltage-controlled phase shifters is frequency dependent, a calibration of the phase shift per applied voltage as a function of irradiation frequency is necessary to optimize the pulse phases to ensure ideal 0°/180° phase cycling. Since the AMC will multiple the phase by 16x, the phase is shifted by 180°/16 = 11.25° at 12 GHz for 0°/180° two-step phase cycling.

Channels 3 and 4 are used for arbitrary shaping of the μw pulse by mixing, via an IQ mixer (IQ0618LXP, Marki microwaves), the 12GHz cw source with an arbitrary waveform produced by the AWG. In the Han lab UCSB system, two AWGs are installed: one is a home-built AWG developed with the Martinis group at UCSB,[152] with 16 kB of memory and clock frequency of 1 GHz, which allows for 1 ns temporal resolution at a maximum pulse length of 15 μs.[153] The second AWG is commercial (DAx22000-8M, Chase Wavepond) with 8 MB of memory and a 2.5 GHz clock frequency; this increases the length of the shaped pulses to ~3.3 ms with 400 ps time resolution. Two AWGs may be required for pulse sequences where the total length of the sequence is longer than 3.3 ms, and thus exceeds the memory of the AWG

– this is typical for DNP experiments. In many cases, the seconds long irradiation for DNP experiments consists of a repeating unit of < 3 ms. In this case one AWG is programmed to generate the repeating unit and produces the waveform upon receiving an external trigger, which is supplied repeatedly for the length of the experiment. The 2nd AWG can be used for a different set of shaped pulses, for example, detection pulses in an ELDOR experiment. Another notable advantage of AWGs is that to the first order the phases generated by mixing the pulse with the AWG waveform are independent of the pulse frequency. This allows for frequency-independent phase cycling and no calibration table that is inherent to the traditional phase shifter-based approach. Since the AMCs will multiply all phase and frequency manipulations by 16x, this should be accommodated in the programming of the AWG waveform.

Under normal operating conditions AMCs are operated under saturating conditions to minimize the amplitude modulation (AM) noise. If amplitude modulation is required, it is possible to reduce the output power of the AMC by reducing the amplitude of the input signal to the AMC. To achieve these types of amplitude modulations, a voltage-controlled attenuator can be applied to the synthesizer(s) to reduce the amplitude of the 12 GHz signal, or AM can be applied to the pulse using the AWG(s), such that the AMCs run under non-saturating conditions. There is a very narrow dynamic range over which amplitude modulations at 12 GHz are carried over to 194 GHz, < 0.5 dB, but more significantly hysteresis effects and increased AM noise makes reproducible operation of AMC under these conditions challenging. The successful implementation, as well as the challenges and pitfalls, of amplitude modulated AWG pulsed for pulsed EPR at 200 GHz have been recently reported by Kaminker et al.[153]

Following the four channels: bypass, phase shifter, and two AWGs, a combiner (Narda) is used to allow all four channels to be directed to either of our two AMCs. Note that special care was taken to ensure that the power is the same (within 1dB) after the combiner regardless of the channel used. Note that the AWG channels are calibrated for waveforms at maximum intensity. After the combiner, the manipulated 12 GHz signal is sent through an isolator (Quest) and a low pass filter (Marki microwave) to remove leaked second harmonics of the carrier frequency from the IQ mixer for AWG operations. The resultant signal is then amplified (ZVA-183-S+, Mini-circuits) and sent to the AMC selection module.

2.5.4. AMC selection

As described later we find that in order to minimize the hysteresis effects of switching amplitude and/or frequency within a single AMC, pump-probe type experiments are best performed with two AMCs. The selection module that controls which AMC will receive the manipulated 12 GHz signal from the pulse forming network is depicted in the purple block of figure 2.2b. This configuration utilizes a SP2T switch (F9120AH, General Microwaves) with a 10 ns time resolution after the pulse forming module to direct the manipulated μw to the desired AMC. After the signal has been selected for either of the two AMC, attenuators are used to set the input power for each AMC to ensure operation under saturating, but safe, conditions when a full amplitude input pulse is generated. We will refer to the two AMCs by AMC1/TH1 and AMC2/TH2 in the following sections, where TH is the transmission horn.

2.5.5. Spectrometer control

The control of all μw switches in the pulse forming unit and the superheterodyne receiver system (see section 2.8), triggering of AWGs, and synchronization with the NMR

spectrometer are performed by a 24-channel pulse generator with 3.3 ns time resolution (PulseBlaster ESR-PRO SpinCore). The voltages to the voltage-controlled attenuator and voltage-controlled phase shifter are provided by a DAC board (USB-6001 National Instruments). All the spectrometer control electronics are controlled by a SpecMan4EPR software as described in section 2.9.

2.6. Quasi-optics design for transmission and EPR detection

After the AMCs have produced the 194 GHz waveform, quasi-optics are used to direct the μw through free space on the μw bridge to the sample in the magnet, and for EPR experiments guide the EPR signal back out from the sample to the EPR detector located on the μw bridge. At lower frequencies, waveguides are generally used for low-loss transmission from source to sample; however, the losses associated with waveguide transmission become prohibitively high at sub-THz frequencies. At these frequencies quasi-optics is an effective solution to manipulate the μw and minimize power losses. The first demonstrated use of quasi optics for high field EPR was by Freed and co-workers.[154] The schematic representation of the quasi-optical design for two-source operation is shown in figure 2.2.c with the picture of the actual quasi-optical bridge in figure 2.2d. In figure 2.2c each square represents half of the 250 mm focal length, *f*, of the elliptical mirrors used in the system. All quasi-optical components were purchased from Thomas Keating Ltd. A corrugated WR4.3UG to 12.7 mm i.d. horn translates the 194 GHz μw irradiation from the AMC to free space, producing a linearly polarized Gaussian beam with a beam diameter of 8 mm (=12.7*0.64). Once the μw beam leaves the horn it will begin to diverge. Thus, a combination of two elliptical mirrors is used to refocus the beam following a *f-2f-f* configuration between the horn, mirrors, and waveguide to prevent image effects such as parity inversion, and to maximize the quality of the beam waist at the

top of the waveguide. Isolators are used to protect the AMCs from reflected power and reduce the standing waves in the system. An isolator is a combination of a wiregrid polarizer, a Faraday rotator that rotates the beam polarization by 45°, and an absorber mounted on a half cube in a triangular configuration. Two isolators are used in the Han lab UCSB quasi-optical μw bridge as shown in figure 2.2c and are labeled as 1 and 2.

The transmission pathways through the quasi-optics from both AMCs will now be described for the example system. Following the μw beam with vertical polarization from AMC1/TH1, a flat mirror 125 mm away from the horn is used to change the direction of the beam without altering the divergence of the beam due to limited space on the quasi-optical bread board. An elliptical mirror placed 250 mm away from the horn (125 mm from the flat mirror) is then used to refocus the beam through isolator 1, which contains a horizontal wiregrid. In a wiregrid polarizer, the electric field polarization is transmitted if it is perpendicular to the wires of the wiregrid polarizer and is reflected if it is parallel. The Faraday rotator in the beam rotates the electric field polarization by 45° counter-clockwise to 135°. The now 135° polarized beam is then transmitted through the 45° wiregrid (E-field is perpendicular) to the second elliptical mirror spaced *2f* from the first elliptical mirror, which refocuses and translates the beam onto the waveguide 250 mm below the second elliptical mirror (the corrugated waveguide will be discussed in Section 2.6.). After the μw beam has interacted with the sample, the polarization is no longer linear, but elliptical. As a result, the returning beam will be split by the 45° wiregrid; the component orthogonal to the incident beam, is reflected by the 45° wiregrid (commonly referred to as the induction mode EPR signal). The other component with the same polarization as the incident beam (commonly referred to as reflection mode EPR signal) is transmitted through the 45° wiregrid and rotated

a further 45° counter-clockwise by the Faraday rotator, resulting in a horizontal E-field polarization, which is reflected off the horizontal wiregrid in isolator 1 and sent to the absorber. The induction mode EPR signal from AMC1/TH1 passes through a second Faraday rotator and is converted to vertical polarization that will be transmitted through the horizontal wiregrid in isolator 2. The beam will then be refocused with an elliptical mirror *2f* from the first elliptical mirror after the waveguide to the receiver horn for EPR detection positioned 250 mm after the last elliptical mirror.

Next, we consider the path of the μw beams produced from AMC2/TH2 that have horizontal electric field polarization. The first elliptical mirror is placed 250 mm from the horn and refocuses the beam towards isolator 2, which has a horizontal wiregrid. As the polarization is horizontal, the beam will be completely reflected by the wiregrid and sent through the Faraday rotator. This beam has 455° polarization after isolator 2 that will be parallel to the 455° wiregrid, and thus will also be reflected towards the second elliptical mirror, placed *2f* from the first elliptical mirror on the AMC2/TH2 beam path and refocused on the waveguide below. After interacting with the sample, the returning signal will similarly be elliptical and split by the 45° wiregrid; however, in the opposite fashion compared to the reflected beam / signal originating from AMC1/TH1, since the polarization of the incident beam from AMC2/TH2 is perpendicular to that of AMC1/TH1. Therefore, the induction mode EPR signal will be transmitted through the 45°-degree wiregrid and sent into the absorber of isolator 1, while the reflection mode EPR signal will be reflected by the 5° wiregrid and sent to the receive horn for EPR detection. In other words, the receiver detects the induction mode EPR signal from AMC1/TH1, and the reflection mode EPR signal from AMC2/TH2. It is important to note that if the absorber in isolator 1 was removed and another elliptical mirror

was placed to allow for the *f-2f-f* configuration to a second EPR detector, then induction and reflection mode EPR signals could be read for both AMCs, depending on which EPR receiver was used. An important consideration is that the reflection mode EPR signal has significantly more power (reflected incident beam plus EPR signal) than induction mode EPR signal (only EPR signal). The higher power of the reflection mode EPR signal could damage the EPR detection scheme. As such, precautions to prevent EPR detector damage should be taken when operating in reflection mode. In our system, the detector can only safely withstand reflected pulses, if pulse lengths do not exceed 2 μs and a 0.5% duty cycle; this is ensured by the spectrometer control software (section 2.9). If cw-irradiation from AMC2/TH2 is required, these experiments cannot be combined with EPR detection as an absorber must be placed before the receiver horn to protect the EPR detector (EPR detection schemes will be discusses in section 2.8). It is important to note that this same quasi optical bridge is compatible with alternative μw sources, e.g. Klystron oscillators or high-power gyrotron sources; therefore, up-grades to the μw sources can be performed without changing the quasi optics.

2.7. Dual DNP/EPR probe

A dual DNP/EPR probe needs two primary components for effective dual operation: NMR circuitry (i.e. NMR coil/tuning/matching circuit) and EPR circuitry (i.e. waveguide and optionally a resonant cavity). A commercial low-temperature NMR probe can be coupled with a waveguide to direct the μw to the sample. However, the example system uses a home-built probe that is top-loaded into the cryostat with inductively coupled NMR circuitry and a waveguide with no cavity to direct the μw for DNP and EPR operation. The waveguide is a 0.9 m long corrugated waveguide supplied by Thomas Keating Ltd with an ID of 12.7 mm that is tapered down to a 5.3 mm ID to concentrate the μw onto the sample. A 42 mm long,

smooth walled, copper extension with a 5.3 mm ID is used to reach the sweet spot of the magnetic field and helps support the NMR circuitry. The corrugations of the main waveguide and taper allow for low-loss power transmission of the microwaves from free space in the quasi-optics to the sample, as a 1 m long waveguide causes < 0.5 dB of loss. The waveguide is capped at the top with a transparent polymethylpentene (TPX®) window to allow for a complete vacuum seal. For complete transmission of the MW beam, the window must be a multiple of $\lambda/2$ thick – here 3.55 mm.[155] The corrugated waveguide transmits the HE_{11} mode of the μw beam, which has a 98% coupling efficiency from free space (TEM_{00}) into the waveguide, for which the beam waist needs to be 0.64 times that of the corrugated waveguide inner radius for ideal coupling. A potential alternative to an expensive corrugated waveguide that is yet to be attempted in a DNP or high field EPR instrument is a smooth walled waveguide, which can be implemented with three stipulations: there is only a 91% ideal coupling efficiency from free space to the waveguide, the waveguide will transmit the TE_{11} mode, and the waveguide i.d. needs to be 0.76 times of the beam waist for optimal transmission. The loss of MW power through the coupling efficiency for both smooth-walled and corrugated waveguides is due to higher order mode conversions. Additional loss of ~1% will result with smooth-walled waveguides due to resistive wall losses, while this effect is negligible for corrugated waveguides. Thus, a smooth-walled waveguide may be a low-cost alternative that should be considered if μw power is not a limiting factor. However, smooth-walled waveguides have not been systematically studied for quasi-optical DNP and EPR systems at high magnetic fields, and thus further investigations are necessary before a final judgment can be made.

The NMR circuitry utilizes inductive coupling to improve the circuit filling factor (see Appendix B.1 for more details on the theory behind inductively coupled NMR coils).[156,157] Each individual nuclei has its own NMR coil tuned to its resonance frequency, where resonances > 200 MHz are generated with an Alderman-Grant type coil design with a ±7 MHz tuning range, while nuclei with resonances below < 200 MHz are made with saddle coils that have a ±2 MHz tuning range at room temperature (^{13}C, ^{27}Al, ^{7}Li, ect.). The NMR coils have a copper skirt extending beyond the basic coil for tuning of the circuit at cryogenic temperatures. The copper skirt in conjunction with the copper extension of the waveguide and the tuning ring (see figure 2.3a) with sapphire between each layer acts as a capacitor, where the degree of overlap between the tuning ring and the NMR coil skirt will change the resonant frequency of the NMR coil, allowing the NMR coil to have tuning capabilities from room temperature to 4 K.[156] Detailed descriptions of how to construct these inductively coupled NMR coils can be found in Appendix B.2. NMR signal and rf-pulses are transmitted and received between the NMR coil and the console via a pick-up loop. The pick-up loop is inductively coupled to the NMR coil; this was done to minimize the number of grounding loops in the system, increase the coil's filling factor, and allow for greater experimental versatility, since different nuclei simply need the NMR coil to be exchanged for operation (private communication, Toby Zens). Matching is accomplished in these inductively coupled NMR coils by adjusting the distance between the window in the NMR coil and the pick-up loop, where larger distances result in poorer couplings and a reduction in the Ohmic match. Adjusting the distance between the pick-up loop and the coil can be done either manually at room temperature or with a matching mechanism as depicted in figure 3a for cryogenic manipulations. For pulsed-EPR operations, no modifications to the probe are necessary, while cw-EPR needs a modulation

coil to modulate the B_0 for lock-in based acquisition, which consists of 30 AWG magnet wire wound 100 turns around a 11 mm OD quartz tube. This configuration is depicted in figure 2.3b.

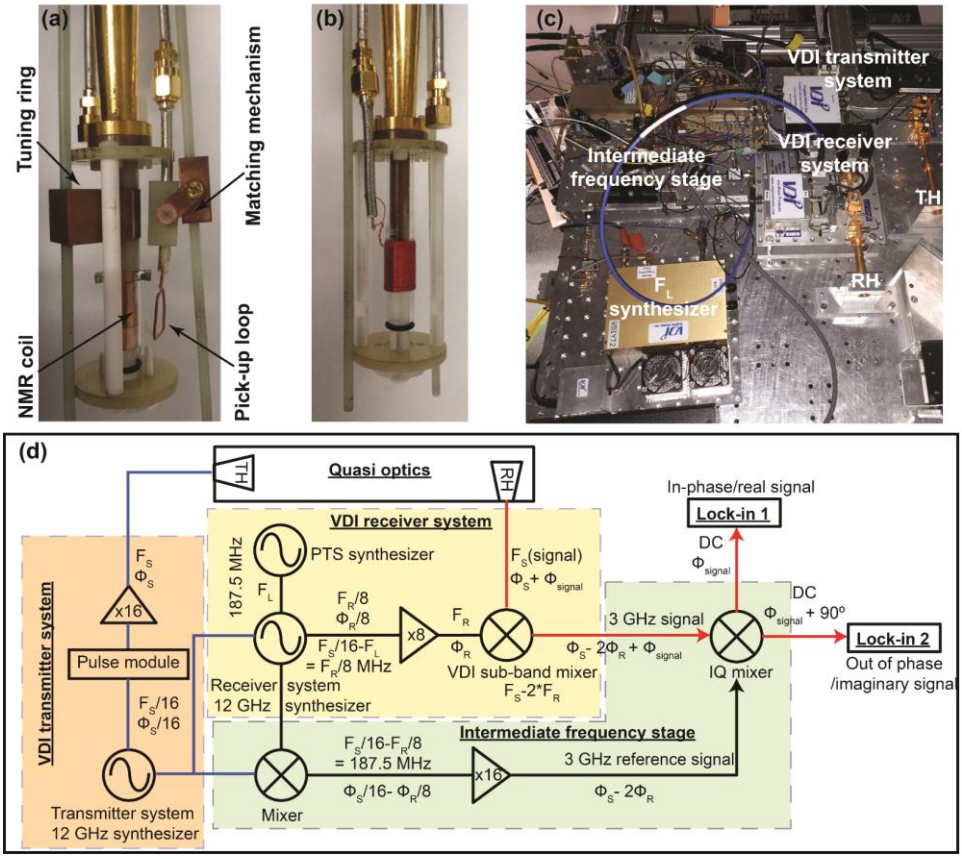

Figure 2.3. (a) Close up of the probe in NMR / pulsed EPR configuration with an inductively coupled 1H Alderman-Grant coil. (b) The probe in the cw-EPR configuration with the modulation coil in place. Picture (c) and schematic (d) of the superheterodyne EPR detection used in the UCSB dual 194 GHz instrument. The orange block denotes the primary VDI transmitter, where all MW manipulations are abbreviated to pulse module. The yellow block denotes the VDI receiver system and dedicated synthesizer. The green block denotes an abbreviated IF stage. Incident μw are shown as blue lines, while μw carrying EPR signal are shown in red. Reference frequencies are shown as black.

2.8. EPR detection hardware and methods

To enable EPR detection the spectrometer should include a sensitive detector for the relevant frequency range, e.g. 190 - 200 GHz for the Han lab UCSB system. Several of detector options are available: direct magnitude detection of the signal amplitude is possible with a zero-biased Schottky diode (ZBD) (Virginia Diodes Inc). If phase-sensitive detection is required, a homodyne or heterodyne detection schemes should be implemented. A ZBD is a good starter detector for initial tests of the system due to its simplicity, as it converts the amplitude of the μw to a voltage that can be directly detected; however, a ZBD has limited sensitivity that in practice makes it only suitable for lock-in amplifier based cw-EPR detection, but difficult for pulsed EPR detection. Lock-in based cw-EPR detection using ZBD requires modulation of the magnetic field B_0, usually in the form $B_0 = B_0^0 + \sin(\omega_{mod} t) * B_{mod}$, where B_0^0 is the central magnetic field of the superconducting magnet, ω_{mod} is the modulation frequency, and B_{mod} is the amplitude of the magnetic field modulation. The resulting cw-EPR signal is then modulated by $\sin(\omega_{mod} t)$ and is demodulated with a lock-in amplifier (Stanford Research Systems – SR830). A lock-in amplifier acquires quadrature signal, where a zero-order phase correction can be used to convert all of the signal into a single trace. The modulation-demodulation process results in the acquisition of the derivative EPR signal. In the Han lab UCSB system, the B_0 modulation at 20 kHz is achieved by the modulation coil (see figure 2.3b) mounted on the EPR/NMR probe, where a current is passed through the wire that is wrapped around the sample holder of the probe to provide the B_0 modulation required for cw-EPR detection. If the system is equipped with a variable field magnet or a sweep coil, then the magnetic field can be swept to acquire the EPR spectrum while keeping the microwave frequency constant. However, if changing the magnetic field is not feasible such

as when a conventional NMR magnet is used, then the EPR spectra can be acquired by sweeping the μw frequency, as demonstrated with the Han lab UCSB DNP/EPR system (see section 3.1).[110]

For high sensitivity EPR detection and/or if phase information is of interest a heterodyne detection method is recommended. While a homodyne detection is also possible (reference and signal at the same carrier frequency are mixed to DC), this method is not recommended because of the large 1/f noise associated with a homodyne detection scheme. Therefore, a heterodyne detection scheme with an intermediate frequency is the method of choice. In this scheme, the sub-THz EPR signal is initially down-converted to an intermediate frequency using a sub-band mixer. When the intermediate frequency signal is mixed with the local oscillator, the 1/f noise is significantly reduced for the final down-conversion to DC with an IQ mixer. The Han lab UCSB DNP/EPR system utilizes a heterodyne detection scheme with a 3 GHz intermediate frequency (see Appendix B.3 for details on the intermediate stage), which was chosen given the readily, commercially available and affordable μw components needed for the intermediate frequency stage of the heterodyne EPR detection scheme, as depicted in figure 2.3c/d. To detect the 194 GHz EPR signal (F_S), the Gaussian beam is collected by a receiver horn connected to a sub-band mixer (Rx-143, Virginia Diode Inc.) with a local oscillator reference frequency (F_R) of 95.5 GHz, which results in the signal being down-converted to 3 GHz (3 GHz = F_S-2F_R). To accommodate changes in the F_S (for frequency stepped echo detected or frequency swept cw-EPR experiments), the F_R should be set such that after the sub-band mixer the down converted signal is always at 3GHz. The LO of the sub-band mixer is produced by an AMC (Rx-143, Virginia Diodes Inc.) by multiplying the signal from a dedicated synthesizer operating at F_R/8 by 8-fold (receiver synthesizer in

figure 2.3d). This dedicated synthesizer from VDI is a special YIG synthesizer designed to output the frequency difference between two analog inputs (i) the transmitter synthesizer frequency ($F_S/16$) and (ii) an offset frequency, F_L, set to 187.5 MHz (3 GHz / 16 = 187.5 MHz) generated by a rf-source (Programmed Test Sources Inc.). The output frequency of the receiver synthesizer becomes $F_R/8 = F_S/16\text{-}F_L$. This enables F_S and $2F_R$ to always be 3 GHz apart and ensures that the EPR signal after the sub-band mixer is exactly at 3 GHz, independent of the F_S. The 3 GHz EPR signal then passes through a low noise amplifier (S020040M4601, Lucix), an isolator (ATM), and a filter (K&L microwave) before being mixed with a 3 GHz reference signal in an IQ mixer (IQ0255LMP, Marki microwaves) to produce the EPR signal at DC. The 3 GHz reference signal is mixed (M10616NA, Marki microwaves) down from the primary synthesizers to 187.5 MHz. and subsequently multiplied 16x (WFM-T-187.5-3000, Wilmanco) to 3 GHz. The IQ mixer produces two quadrature EPR signals at DC: absorption and dispersion mode. For cw-EPR, each quadrature from the IQ mixer would need to be sent to a synchronized lock-in amplifier to demodulate the cw-EPR signal. For pulsed EPR echo-detected experiments the signal is directly digitized with a 1 GHz dual-channel digital-to-analog converter (AP240, Keysight, formerly ACQIRIS). A full detailed description of the heterodyne EPR detection scheme and intermediate frequency stage are presented by Siaw et al.[110]

2.9. Integrated software control

An integrated software system is useful so that one program can be used to control all the components of the instrument. In practice, it is convenient to retain control of the NMR part of the instrument with a commercial software that was supplied with the NMR spectrometer (e.g. TOPSPIN 1.3 in the Han lab UCSB system). In this case one only needs to take care of

the synchronization between the NMR rf-pulses and DNP/EPR MW pulses. In the Han lab UCSB system, this has been achieved with Specman4EPR (Femi Instruments LLC) software package.[158] Specman4EPR directly controls the μw components, either via the DAC (USB-6001, National Instruments) for voltage-controlled components or by programming the 24 channel digital pulse generator (PulseBlaster ESR-PRO SpinCore) that controls all of the four μw switches in the system. Specman4EPR software also controls the frequency of the two transmitter synthesizers (synthesizer 1 and synthesizer 2 in figure 2.2b) and programs the waveforms into the AWGs (Home-built and Chase. In addition, the EPR signal is recorded from either ADCs in pulsed EPR experiments, or from the lock-in amplifiers in cw-EPR or power calibration experiments. The synchronization with the NMR software (TOPSPIN 1.3) is achieved by providing a TTL trigger(s) to the NMR spectrometer, with NMR pulses sequence that are designed to advance to the next step upon receiving the trigger. This ensures that all the timings in the experiment are set in the SpecMan4EPR software.

2.10. Performance diagnostics

Power loss analyses of the different components in the instrument should be performed to accurately measure the μw power at the sample position, and to aid in diagnosing instrument performance issues that arise. A combination frequency counter and power meter (EIP 548A, EIP Microwave Inc) can be used to characterize the various components at 12 GHz from the synthesizer to the many parts of the AMC selection module, as well as the 3 GHz components of the heterodyne detection scheme. The insertion loss of each component was measured and tabulated, so that if performance declines, then measurement of the power after key components such as amplifiers and mixers can be used to determine if a component has become faulty. This streamlines the process of diagnosing poor μw performance. An

oscilloscope (Agilent MS071048) is helpful for the analysis of the AWG outputs at 12 GHz. A photoacoustic absolute power meter (Thomas Keating) was used to determine the power loses through the quasi optical components at ~ 200 GHz, of which the Faraday rotators cause the largest power loss of 2 dB per pass through a rotator. A detailed description of how μw source performance is characterized and quasi optical power loss analyses can be performed are provided in Appendices C.1 and C.2, respectively and Siaw et al.[110] A pyroelectric (ELTEC Instruments Inc.) detector equipped with a 0.177" x 0.177" square lithium tantalate sensing element mounted at the sample position inside the magnet is used for aligning the μw beam path from the bridge, with the waveguide in the probe insert—this aligning is done regularly (see Appendix C.3). Once calibrated in reference to the absolute power meter, the pyroelectric detector can act as a pseudo-power meter for the complete system. Another way to analyze the system's μw performance is by monitoring the EPR echo intensity of a standard sample – diamond is a good standard to choose because it does not degrade with time and has a large room temperature EPR signal of its P1 centers. A network analyzer (Hewlett Packard – 8753A) is used to check the performance of the various home-built NMR coils for each nuclei regarding their Q-factor, resonance frequency tuning range, and matching to the 50 Ohm rf-output from the NMR console.

2.10.1. Echo intensities to quantify μw B_1

The echo intensity of a standard sample can be used to characterize the total μw performance at the sample position through all 12 GHz and 194 GHz μw manipulations. An ideal standard sample should provide large echo intensities at room temperature; examples of good standard samples include: diamond, BDPA crystals or BDPA dispersed in polystyrene, and Gd_3Cl in 1:1 DMSO:H_2O. In general, larger echo intensities correlate with more incident

μw power on the sample. EPR signal echoes are formed by combining two pulses spaced τ apart. The EPR signal will refocus at a time, τ, after the second pulse. For traditional Hanh echo experiments, the first pulse is 90°, while the second pulse is 180°.[159] Echoes can also be formed efficiently if two 135° pulses (3/4*180° t_p) are used. In this work, the method utilizing 135° pulses are used, unless otherwise noted.

One way to quantify the μw irradiation strength, B_1, at the sample position is with a nutation curve. In a nutation curve, the length of pulses that form echoes are varied at a set μw power (really it is a set attenuation level for the AMC). The nutation curve determines the 180° pulse length, which occurs at the pulse length, t_p, that minimizes the electron echo intensity. This type of analysis was used to compare the μw B_1 from the low power (~120 mW) and high power (~500 mW) AMCs with a sample of Gd_3Cl in 1:1 DMSO:H_2O as shown in figure 2.4. The high power AMC has a 180° time that is approximately half that of the low power AMC. Since the nutation time is related to the square of the B_1, the high power AMC has approximately 4-fold larger B_1 than the low power AMC. This comparison agrees with the μw power outputs measured from the photoacoustic absolute Thomas Keating power meter. It should be noted that Gd^{3+} has a spin-7/2, which will shorten the nutation time (180° pulse length) by a factor of 3 compared to a spin-1/2 system, thus the 180° t_p from the low power AMC for a spin-1/2 system will be ~1 μs, compared to ~340 ns for a spin-7/2 system.

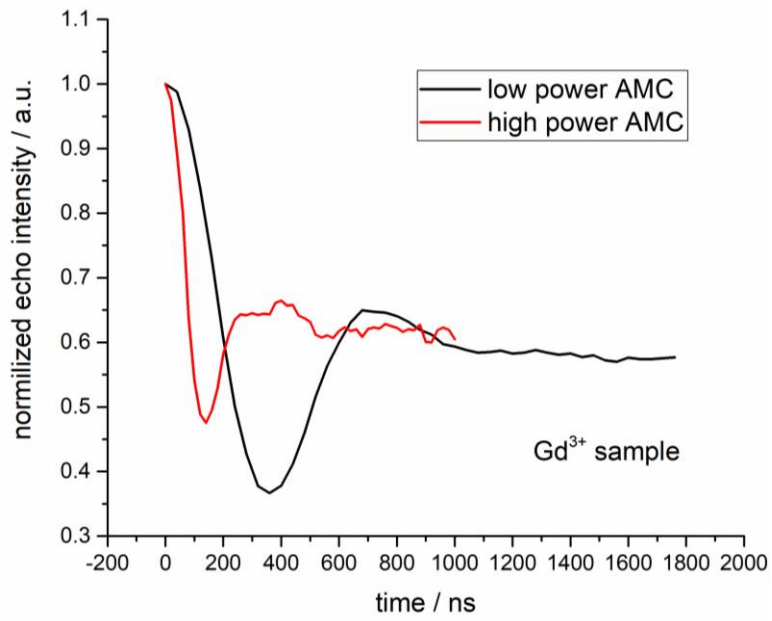

Figure 2.4. Nutation curves for the high (red) and low (black) power AMCs as measured with a standard sample of Gd_3Cl in 1:1 DMSO:H_2O.

2.10.2. Martin-Puplett based DNP: a diagnostic example

The Martin-Puplett based DNP circuit was from a previous setup of the UCSB DNP instrument, which was first presented by Armstrong et. al.[111] A Martin-Puplett interferometer in the quasi optics can convert the linearly polarized μw beam to circular polarized. This is advantageous because paramagnetic species can only absorb one type of circularly polarized μw; thus the conversion from linearly to circularly polarized μw enables the μw power B_1 to be effectively increased by 41%.[111] Note that circularly polarized μw are incompatible with induction mode EPR experiments; therefore, this quasi optical circuit can only be used for DNP and reflection mode EPR. The quasi optical circuit for this Martin-Puplett based DNP is shown in figure 2.5a and the transmission of the μw beam is explained in detail in Appendix C.4. While the use of circularly polarized μw leads to an increased absorption of μw by the

sample,[111] theoretically generating 41% higher μw B_1, and therefore higher DNP enhancement (experimentally measured to increase by 28%),[111] the recorded μw power transmitted through the quasi optics was inconsistent and reduced by ~ 50% after the instrument was moved between facilities. In order to determine the cause of this power loss simulations of Gaussian beam propagation were conducted. Paraxial analysis based on the 3D model of the Martin-Puplett based DNP quasi optical circuit in SolidWorks and beam waist calculations for the fundamental Gaussian free space mode[160] demonstrated absence of significant vignetting of the 99% encircled energy beam for all of the components. The physical optics option of ZEMAX® EE, a commercial optical design software, was used for more detailed analysis of the setup. System efficiency was determined at 99.8% (1.2% energy losses) up to the waveguide, where system efficiency is defined as the transmission energy through the circuit. The coupling coefficient for ideal optics positions was determined by the overlap integral between the incoming μw wavefront and the waveguide fundamental mode to be 88.6%. The coupling coefficient has a maximum value of 1, where some of the causes for reductions in the coupling coefficient are vignetting, absorption, and mismatching of the μw beam and waveguide amplitude and/or phase. The total power coupling coefficient is the product of the system efficiency and the coupling coefficient, which yielded 88.4 %. Additionally, the transition between HE_{11} and Gaussian modes typically has a 2% conversion loss,[161,162] resulting in a total ideal coupling efficiency between the source and waveguide of 86.4% for an idealized Martin-Puplett interferometer circuit. The equations used to calculate the total power coupling efficiency can be found in the ZEMAX® EE e-manual under the subsection of single mode coupling.

One possible source of misalignment was identified as a tilt of the moving roof mirror in the interferometer as suggested by Gaussian beam image analysis. The wavefront caused by the tilted roof mirror will have distorted phases, decreasing the coupling coefficient to the HE_{11} mode of the waveguide. In addition, higher order modes will be excited by the tilted wavefront, according to the following equation:

$$\frac{P(\Delta\theta)}{P_0} = 4.2 \cdot \left(\frac{a \cdot \Delta\theta}{\lambda_0} \right)^2 \qquad \text{Eqn. 2.1}$$

where $\Delta\theta$ is the wavefront tilt in radians, a is the radius of the waveguide, and λ_0 is the wavelength of the μw beam [163]. For a ~200 GHz beam coupled to our 12.5 mm waveguide, a tilt of the wavefront by 1° (0.5° tilt of the roof mirror) will cause 2.2 % of the μw beam to be coupled to higher order modes. For this same 1° vertical tilt of the wavefront, the calculated system loss was 57.2% (due to the energy vignetting at the waveguide), and the coupling integral was 61.3%, resulting in a total system efficiency of 36.1% - more than 50% less compared to the ideal optics arrangement – similar losses to those measured experimentally. Additional loss in DNP efficiency would result from the interference fringes produced by the two tilted wavefronts after the interferometer (not calculated in ZEMAX® EE).

In order to confirm that the tilt of the moveable roof mirror was the cause of power losses for the Martin-Puplett based DNP quasi optical circuit, an array detector, Pyrocam III (Ophir Photonics), was used to perform Gaussian beam image analyses. Immediately after the transmission horn the μw beam was circular with a Gaussian profile (figure 2.5b). At the position of the waveguide (after the Martin-Puplett interferometer) a distorted beam of linearly

polarized μw was observed (figure 2.5c-d), and the use of an additional polarizer (labeled with a †) confirmed the presence of two wavefronts as shown in figure 2.5e-f. Two linearly polarized μw beams are chosen via the interferometer (parallel – 135° and perpendicular – 45° to the added polarizer) to show the distortions to the Gaussian beam profile in overall shape and polarization that occur from a tilted roof mirror. The polarizer added after the interferometer helped to isolate the divergent wavefronts according to their polarization. This indicated that the movable roof mirror was indeed tilted and the cause of poor DNP performance. Upon adjustment of the roof mirror tilt, an improved Gaussian shape and polarization of the beam and a significant increase of μw power was observed as predicted by the simulations and shown in figure 2.5g-h.

A similar Gaussian beam image analysis was performed for the quasi optical circuit used for dual DNP/EPR operation. The Gaussian profile observed immediately following the transmission horn is maintained for the entire path of the μw for the dual-purpose circuit, as verified with the focused μw beam at the position of the waveguide as shown in figure 2.5b. These results show how crucial the integrity of the Gaussian μw beam is for the polarization of the μw beam to be manipulated correctly by the quasi optics, minimization of the power losses, and spatially even excitation of the sample by the μw beam. The Gaussian fidelity of the μw beam, characterized by the size, Gaussian shape, and relative power of the μw beam, can be imaged by an array detector to ensure optimal performance.

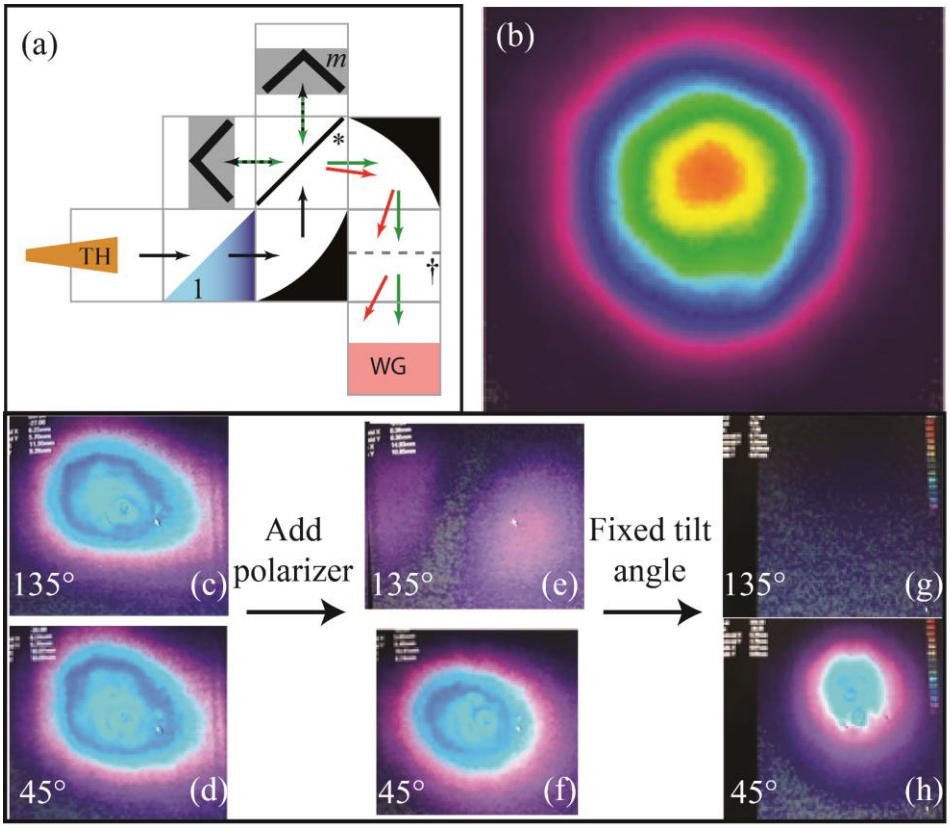

*Figure 2.5. (a) Schematic of the Martin-Puplett interferometer-based DNP quasi optical circuit. The isolator (1) contains a 45° polarizer and the polarizer labeled with * is a vertical polarizer. The roof mirror labeled m is the moveable roof mirror. The green arrows indicate polarization that has passed through the interferometer, while the red arrows indicate polarization resulting from a tilted roof mirror. The polarizer indicated by the dashed line and † represented the added 135° polarizer to diagnose power loses in this circuit. (b) Gaussian beam profile image immediately after the transmission horn as imaged by the Pyrocam III. The same beam profile was observed immediately prior to the waveguide with the dual DNP/EPR quasi optical circuit. Gaussian beam profile images with a polarization of 135° (c,e,g) and 45° (d,f,h) after the interferometer (c-d), after the interferometer with an added polarizer of 135° (e-f), and after the interferometer once the tilt of the movable roof mirror was fixed (g-h).*

2.11. Summary

Versatile and agile dual DNP/EPR spectrometers are necessary to broaden the scope of DNP experiments for a broader range of applications, and to understand the underlying physics and mechanisms for DNP processes, especially when new sample formulations or odd results are to be explored. The instrument and experimental designs outlined here enables the reader to build a modular two ss-μw source design for an AWG-capable dual DNP/EPR instrument. The advantage of a modular design allows the instrument to be easily modified to accommodate exactly what is needed for the desired experiments or available budget, while also providing easy access for up-grading one module at a time or adding new modules. Although alternative μw sources were mentioned, the ss-μw source is the heart of a versatile dual capability instrument owing to its wide bandwidths (~10 GHz) and tunability that allows the user to access a range of g-factors found with atypical radicals or paramagnetic transition metals for DNP and EPR experiments. The AWG capability provides the agility necessary for precise μw pulse shaping and broadening the excitation bandwidth for DNP and EPR, while the addition of a second μw source increases the performance and eliminates artifacts for pump-probe type ELDOR experiments.

3. ELECTRON DEPOLARIZATION VIA ELECTRON-ELECTRON DOBLE RESONANCE (ELDOR)

3.1. Electron relaxation rates

In order to qualitatively determine the electron depolarization, the electron relaxation rates must also be known for the particular sample in addition to the systems' EPR spectrum. Generalized EPR spectra for subsets of paramagnetic species can be used, such as most nitroxide-based radicals have similar spectra; however, specific EPR spectra should be acquired for exotic and unique paramagnetic species, especially where the atomic structure resulting in the unpaired electron spin is directly altered. Example pulsed and cw-EPR spectra acquired on our system are shown in figure 3.1a/b for two standard samples: Mn^{2+} (S=1/2, I=5/2) in modeling clay for cw-EPR (a) and P1 (nitrogen) centers of a type 1b diamond for pulsed EPR (b). In both cases the spectra acquired on our system are *frequency stepped*, which are then compared with *field swept* EPR spectra acquired at 240 GHz in the laboratory of Professor Mark Sherwin (UCSB). The field swept spectra were converted to frequency units and inverted relative to the center frequency. For the modeling clay the zero-biased detector was used for magnitude mode acquisition of the EPR signal at room temperature. There is good agreement between both spectra, where the position of the typical Mn^{2+} sextet, resulting from the hyperfine interactions between the electron spin and the ^{55}Mn (I=5/2), is the same for both field-swept and frequency-stepped spectra. There are slight differences in amplitudes that has been attributed to variations in power output with irradiation frequency and residual standing waves in the quasi optics.

The P1 center was acquired with the heterodyne detection scheme at room temperature. The two spectra show the characteristic triplet due to the hyperfine interactions of the unpaired

electron in the P1 center with ^{14}N. Similar to what was previously observed in the cw-EPR spectra comparison (figure 3.1a) between the two systems, the line positions and linewidth are consistent between the two, while the line intensities are not. Again, this is attributed to the presence of frequency dependent standing waves in the 200 GHz system and to variations of incident power across the frequency range used to acquire the EPR spectrum.

The electron relaxation rates were also acquired for the P1 centers to demonstrate these standard data acquisitions. The phase memory time, T_m, (figure 3.1c) was measured by using a two-pulse (t_p-τ-t_p-τ-echo) spin echo pulse sequence (see inset) where τ was varied. On the other hand, the electron spin-lattice relaxation time, T_{1e}, (figure 3.1d) was acquired with a three-pulse saturation recovery (t_{sat}-t_d-t_p-τ-t_p-τ-echo) pulse sequence (see inset), where t_d was varied. Both experiments were acquired on the central line of the P1 center triplet of the diamond sample at room temperature (290 K). Both curves could be satisfactorily fitted with a single exponential, and the obtained values of T_m = 965 ns and T_{1e} = 1.6 ms are in good agreement with measurements performed using the 240 GHz EPR setup in the Sherwin group at UCSB on the same diamond sample. It should be noted that although T_m and T_{1e} should ideally be fitted with a single exponential as they are here, this is not always possible. Frequently T_{1e} must be fitted with a bi-exponential, where there is a fast and a slow relaxing component. Frequently only the slow component is reported in literature.[96,164,165] T_m similarly can be fitted with either a bi-exponential or a stretched exponential.[118,165]

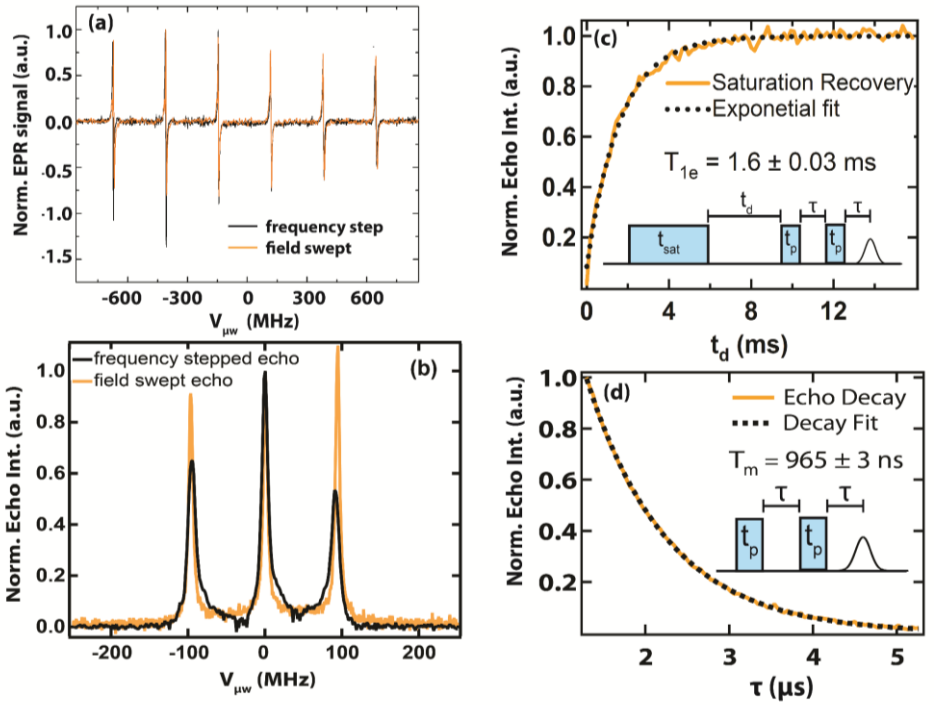

Figure 3.1. (a) 200 GHz frequency stepped cw-EPR magnitude spectra of Mn^{2+} in modeling clay (black) compared to field swept cw-EPR magnitude spectra (gold) at 240 GHz. (b) 200 GHz frequency stepped echo detected spectrum (black) and 240GHz field swept echo detected EPR spectra (gold) of P1 centers in diamond. (c) Two pulse echo decay (gold) and mono-exponential fit (black). (d) Saturation recovery experiment using the t_{sat} - t_d - t_p-τ-t_p-τ-*echo pulse sequence (insert of d) varying the* t_{sat} *(gold) and mono-exponential fit (black). The pulse sequence* t_p-τ-t_p-τ-*echo (insert of c) was used in (b) and (c); Experimental parameters (a,black) modulation frequency 20 kHz, modulation amplitude 0.26 mT, time constant = 30 ms,* $P_{\mu w}$ *= 22 mW, 10 scans, frequency stepping rate 10 Hz acquired with a ZBD detection scheme. (a,gold) Pμw = 0.5 mW, field swept rate = 0.1 mT/s, modulation frequency = 20 kHz, modulation amplitude = 0.1 mT, time constant = 200 ms, 1 scan acquired with a heterodyne detection scheme. (b, black):* ν_{detect} *= 197.3 GHz – 197.8 GHz;* t_p *= 300 ns; τ =500 ns; repetition time 2 ms; no phase cycling. (b, gold): magnetic field 8.578 T – 8.589 T;* t_p *= 500 ns; τ =900 ns; repetition time 10 ms; no phase cycling (c)* t_p *= 300 ns; varying τ = 500 ns – 2600 ns; repetition time = 2 ms; no phase cycling. (d)* t_{sat} *= 20 ms;* t_p *= 300 ns; τ = 900 ns; varying* t_d *= 1 μs – 16000 μs; repetition time = 40 ms; no phase cycling. For all experiments the magnetic field was set to 7.05 T.*

3.2. Hole-burning ELDOR and ED-NMR

The basic electron-electron double resonance (ELDOR) experiment carried out with the pulse sequence shown in figure 3.3a can be delineated into two distinct regimes

characterized by the length of the excitation pulse, t_{excite}: (i) hole burning ELDOR—if t_{excite} is longer than the time required for the whole electron spin system to reach steady state, typically on the order of T_{1e}, then the effects observed in the ELDOR spectra are characteristic of electron spectral diffusion (eSD), and (ii) ELDOR-detected NMR (ED-NMR)—if t_{excite} is short ($<< T_{1e}$) the ELDOR spectra are dominated by signals originating from the excitation of forbidden electron-nuclear transitions of proximal hyperfine coupled nuclei (ED-NMR). The hole burning ELDOR is relevant for the study of DNP mechanisms and probing the state of the electron spins under DNP conditions, since the long t_{excite} pulse mimics the prolonged irradiation found in DNP experiments. ELDOR measurements were first used in relation to DNP by the Köckenberger group at 94 GHz in 2007.[107]

3.2.1. Hole burning ELDOR

In hole burning ELDOR experiments, strong μw irradiation (t_{excite}) is applied for sufficient time to saturate the electron spins resonant with the irradiation frequency. A saturated or perturbed electron spin system will have a reduced or eliminated EPR signal. In the absence of spin-spin interactions, the shape of the hole "burnt" into the EPR spectrum will have a Lorentzian lineshape with the width depending on the strength of the μw irradiation, the electron spin lattice relaxation time (T_{1e}), and the electron phase memory time (T_m) – a measure of transverse relaxation. The presence of eSD resulting from electron spin-spin dipolar interactions will manifest itself as a deviation from the Lorentzian lineshape, where the strength of eSD can be extracted through analysis of ELDOR spectra, as has been previously demonstrated and as illustrated by figure 3.2.[79,96]

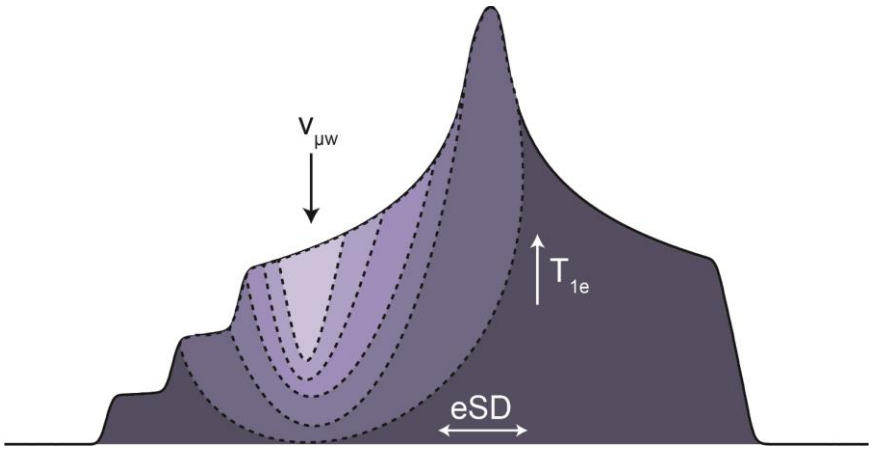

Figure 3.2. Cartoon depicting the deviation from a Lorentzian lineshape of a hole burnt into the electron spin spectral density of a nitroxide. The T_{1e} will relax the hole burnt into the EPR spectrum back towards equilibrium, while eSD will broaden said hole, where stronger or longer duration μw irradiation will burn a larger hole into the EPR spectrum until a steady state is reached amongst the electron spins.

To acquire a 1-D ELDOR/ED-NMR spectrum a constant field technique is used, where the magnetic field and detection frequency (ν_{detect}) are held constant while the excitation frequency (ν_{excite}) is sampled across the EPR spectrum, as shown by the pulse sequence in the inset of figure 3.3a. A complete (2D) set of ELDOR/ED-NMR spectra can be acquired by either stepping ν_{detect} across the whole EPR spectrum, or if the spectrometer is equipped with a variable field magnet or a sweep coil, by changing the magnetic field.[98,166] In a DNP experiment the length of μw irradiation (typically minutes at low temperatures) is long enough for the electron spin system to reach steady state. In ELDOR experiments minutes long irradiation is impractical because the acquisition of a 2D ELDOR dataset will become unrealistically long. Instead t_{excite} is set for the shortest time required for the electron spin system to reach steady state. This can be done either by taking complete ELDOR profiles at several t_{excite}, or by acquiring ELDOR experiments as function of t_{excite} at only a few ν_{excite} values. The advantage of the latter approach is that it is a less time-consuming method to

determine a t_{excite} that is representative of DNP conditions, compared to acquiring the complete ELDOR dataset for each t_{excite} value. Typically, we find that the longest time to reach a steady state occurs near the edges of the EPR spectrum, and therefore, the ν_{excite} values should be extended to cover the whole EPR spectrum. Four of these ELDOR vs. t_{excite} measurements are shown in figure 3.3a for 10 mM TOTAPOL. These rates show that if $\nu_{excite} = \nu_{detect}$, then the electron spins will become saturated at approximately 10 ms, while if $\nu_{detect} \neq \nu_{excite}$, then the process takes about an order of magnitude longer. The reduction of EPR signal intensity at $\nu_{detect} \neq \nu_{excite}$ is a result of polarization transferred between two electron spins with different resonant frequencies via eSD. The efficiency of polarization transfer decreases with the increase in the frequency separation between the electron spins and is proportional to the relative spin populations of the two frequencies. Therefore, excitation in the middle of the EPR spectrum will take the longest time to reach a steady state on either side of the spectra, where frequency separation between ν_{excite} and ν_{detect} is large, and spin population is low. Besides determining representative DNP t_{excite}'s, the rate of electron depolarization between ν_{excite} and ν_{detect} can be extracted by fitting the ELDOR vs. t_{excite} data to $y = Ae^{-t/t_{eSD}} + C$, where t_{eSD} is the rate of spectral diffusion between electrons at ν_{excite} and ν_{detect}. The extracted t_{eSD} were found to be 1 ms for ν_{detect} = 193.67 GHz ($\nu_{excite} = \nu_{detect}$, $\Delta\nu = 0$ MHz), 17 ms for ν_{detect} = 193.887 GHz (center of the nitroxide EPR spectrum, $\Delta\nu = 217$ MHz), 25 ms for ν_{detect} = 193.52 GHz (edge of the EPR spectrum $\Delta\nu = -150$ MHz), and 18 ms for ν_{detect} = 194.06 GHz (intermediate position on EPR spectrum, $\Delta\nu = 390$ MHz). It is clear that the extracted t_{eSD} values correlate better with the relative spin populations between the two electron spin frequencies than with the frequency separation, $\Delta\nu$.

After determining t_{excite}, hole burning ELDOR spectra can be acquired, where the hole burning ELDOR profiles for 5 mM (green) and 10 mM (red) TOTAPOL in 6:3:1 d_8-glycerol:D_2O:H_2O at 4K are shown in figure 3.3b. Both spectra have a sharp peak at $\nu_{detect}=\nu_{excite}$, corresponding to the allowed EPR transition, which is denoted by *. The weaker, sharp features correspond to forbidden transitions between the electron and its hyperfine coupled nuclei, where the ^{14}N and ^{1}H forbidden electron-nuclear transitions are annotated in figure 3.3b. These forbidden transitions are the basis for ED-NMR and will be discussed further in section 3.2.2. A simulation of the hole-burning experiment without any eSD effects is shown in black in figure 3.3b. The inability of this simulation to capture the broad depolarization at the center of the EPR spectrum at 197.85 GHz that is especially pronounced in the 40mM sample suggests that this feature is caused by eSD. The eSD process is driven by electron-electron dipolar interactions that propagate the μw-induced electron spin depolarization to the off-resonance electron spins. Therefore we expect the eSD induced depolarization to be more pronounced in the samples with higher electron spin concentrations. In addition, as was discussed previously, eSD is proportional to the relative spin population and is thus most pronounced in the ELDOR spectra at the frequency corresponding to the center of the EPR spectrum. The 40 mM 4-amino TEMPO sample has significantly larger eSD effects compared to the 10 mM sample as seen by the larger depolarization feature at the center of the EPR spectrum at 193.92 GHz (marked with dashed line in figure 3.3b).

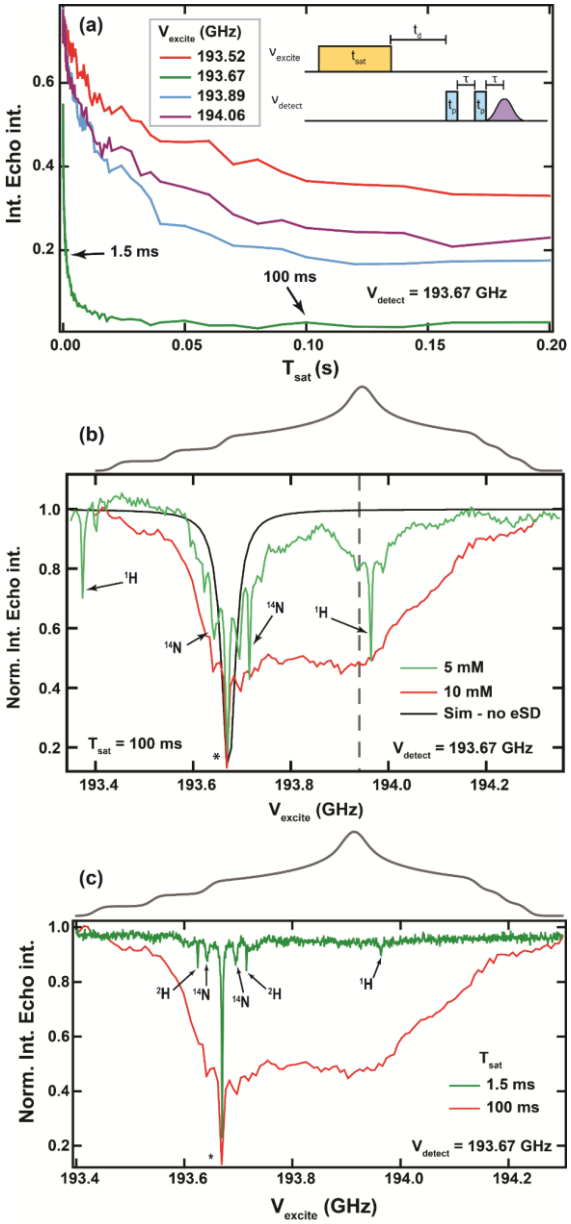

Figure 3.3. (a) Electron excitation rates for 10 mM TOTAPOL in 6:3:1 d_8-glycerol:D_2O:H_2O at 4 K at ν_{detect} = 193.67 GHz for various ν_{excite} as denoted in the figure. The inset is the ELDOR pulse sequence used here. (b) Experimental ELDOR spectrum of 5 mM (green) and 10 mM (red) TOTAPOL in 6:3:1 d_8-glycerol:D_2O:H_2O at 4 K overlaid with an ELDOR simulation without eSD (black), with t_{sat} = 100 ms. The nitroxide EPR spectrum is shown as reference in gray above the ELDOR spectrum. The hyperfine forbidden transitions are annotated in the figure, and the allowed EPR transition is annotated by "". (c) ELDOR spectra taken with 1.5 ms (green) and 100 ms (red) t_{excite} for10 mM TOTAPOL in 6:3:1 d_8-glycerol:D_2O:H_2O at 4 K at ν_{detect} = 193.67 GHz. The simulated EPR spectrum for is shown above, based on an experimental EPR spectrum acquired at 8.56 T and 4.5 K with traditional field-sweeping capabilities.[119] Experimental parameters for all spectra: repetition time = 500 ms, t_p = 750 ns, tau = 500 ns, and t_d = 10 μs.*

3.2.2. ELDOR Detected-NMR

The hole burnt into the electron spin system is dominated by the allowed EPR transitions excited with the saturation pulse. However, if electron – nuclear hyperfine interactions are present in the system, additional holes due to excitation of forbidden electron-nuclear transitions can be detected as well — this is the basis for the ED-NMR experiment. These holes originate from electron spin depolarization due to simultaneous electron-nuclear spin flip-flops when the μw irradiation matches the difference in energy between the electron-nuclear mixed states from the forbidden transitions.[167] ED-NMR can be thought of as detecting the solid effect (SE) for *all* the different NMR active nuclei that are weakly hyperfine coupled to the unpaired electrons in the system, with symmetric peaks centered about the allowed EPR transition. The frequency difference between the symmetric peaks and the allowed EPR transition correspond to the nuclear Larmor frequency of the hyperfine coupled nuclei. ED-NMR to detect hyperfine coupling fingerprints was first proposed by Schossler, Wacker, and Schweiger in the mid 1990's.[168]

1-D and 2-D ED-NMR spectra are acquired in the same manner as those for hole-burning ELDOR; however, the length and/or power of the excitation pulse needs to be adjusted to prevent broadening of the allowed EPR transition, which can mask the forbidden hyperfine transitions of low γ-nuclei. This sharp depolarization due to the allowed EPR transition when $\nu_{excite} = \nu_{detect}$ is termed the central peak blindness. For ED-NMR, the detection pulses to form an echo can be used to selectively enhance the observation of specific types of forbidden transitions, such as selecting for differences in the microenvironment (via detection of multiple A_{zz}) versus detecting double quantum forbidden transitions.[169,170] The echo detection method shown in figure 4a can be substituted with FID detection; however, recent

research has significantly favored the echo over FID detection for ELDOR-based experiments.[168,171] Finally, the delay between the excitation and the detection pulses for both DNP-relevant hole burning and the ED-NMR experiments, t_d, needs to be sufficiently long to eliminate unwanted electron spin transverse coherences – i.e. longer than T_m.[172]

ED-NMR with short excitation pulses is of particular interest because it can detect the nuclei that are hyperfine coupled to a paramagnetic spin, which is extremely beneficial in determining the identity, structure, and spatial relations of nuclei immediately surrounding an unpaired electron. A comparison of ED-NMR data (green trace) and hole-burning ELDOR data (red trace) of the same 10 mM TOTAPOL sample in 6:3:1 d_8-glycerol:D_2O:H_2O at 4 K, 7 T and with ν_{detect} = 193.67 GHz are shown in figure 3.3c. As forecasted, the only difference between the ED-NMR and hole burning ELDOR acquisitions lies in t_{excite}, with t_{excite}=1.5 ms for the former and t_{excite}=100 ms for the latter. The nuclei that are hyperfine coupled to the TOTAPOL are denoted for the resolved ED-NMR resonance in figure 3.3c, where it should be noted no eSD is observed. In the hole burning ELDOR spectrum representing DNP conditions, it is difficult to identify which nuclei are hyperfine coupled to the electron given the extensive depolarization across the EPR spectrum due to eSD.[96]

3.3. Two-source ELDOR

As described in section 3.2.1, in order to acquire ELDOR profiles, ν_{excite} is stepped across the entire EPR spectrum – ideally with the same μw power across the whole frequency range. However, the power output from the AMCs *is* frequency dependent; thus, to get (DNP and EPR) frequency-dependent data with the same nominal power across the frequency range, a power calibration for the relevant frequency range (for the UCSB DNP system: 192 to 195 GHz) is required to acquire DNP and EPR spectra for commonly used DNP radicals. For

AMCs operating under saturating conditions, the power variation across the typical frequency range for nitroxides is approximately 10-15%, which is acceptable, but this variation becomes significantly worse for AMCs operating in non-saturating conditions. As was discussed in section 3.2.2, to prevent central peak blindness, a two-frequency ELDOR experiment may require the pulses at each frequency to be produced with different output powers. The slow, on the EPR timescale, response time of the built-in AMC amplitude control (section 2.5.1 and section 2.5.4) of ~0.5 ms prohibit directly manipulating the AMCs amplitude in the course of single EPR pulse sequence. This makes acquiring ELDOR electron depolarization profiles with a single AMC challenging when different power levels are required for the excitation and detection pulses.

In the following, we provide an illustrative example on the importance of power calibration and a benefit of using the 2-AMC setup for acquiring ELDOR spectra with power-dependent t_{excite} pulses.[131] When power-dependent electron depolarization profiles are obtained for a 40 mM 4-hydroxy TEMPO (4HT) sample in 1:1 DMSO:H_2O at 4 K with a single AMC and without power calibration, clear distortions of the background signal are observed, as shown in figure 3.4a. For this dataset, a single AMC was used, and the μw power level ($P_{\mu w}$) was varied for the entire ELDOR pulse sequence, i.e. both excitation and detection pulses. Lowering the intensity of the detection pulses results in a lower echo intensity and requires more signal averaging to acquire data with a similar SNR as the ELDOR spectra acquired with higher $P_{\mu w}$. The distortions in the background of the ELDOR profiles are due to variations in the power output as a function of frequency, and are most noticeable for intermediate irradiation powers, as the distortion effects are minimized at the maximum AMC

output where the performance is optimal, and at low powers where frequency-dependent power variation is minimal.

In an effort to obtain reliable power-dependent ELDOR data without sacrificing SNR for the lower power level experiments and to overcome the slow response time of the AMC amplitude control we attempted to modulate the output power of the AMC by changing the power of the input (~12 GHz) signal to the AMC. This was achieved by adding a voltage-controlled attenuator between synthesizer 2 (F_{ELDOR}) and the pulse forming network. This allows the synthesizer used for the excitation pulse to be attenuated at each ν_{excite} in an ELDOR experiment and leaves the detection pulses, generated from synthesizer 1 ($F_S/16$), to be at full power. As the AMC is designed to operate under saturating conditions, the AMC will be forced to run under the less-ideal non-saturating conditions, which results in higher AM noise for the excitation pulses. The response of the AMC to changes in $P_{\mu w}$ of the input signal are highly non-linear under non-saturation conditions. Therefore, a calibration of the output at high frequency (~194 GHz) as a function of the input $P_{\mu w}$ at ~12 GHz is required for this method to work. However, the very narrow dynamic range where the AMC performs under non-saturating conditions limits the precision that the μw power can achieve with this methodology. Nevertheless, when this power calibration was carried out the resulting power dependent ELDOR spectra were significantly improved, yet some artifacts were still clearly visible in the ELDOR spectra. These artifacts could be traced to the "heating (memory) effects" of the AMC, where the detection pulses were dependent on the frequency and power of the preceding excitation pulse.

The use of a second AMC to completely separate the excitation and detection channels eliminates these "memory" effects, since the detection and excitation pulses are now

generated by separate AMCs. The more robust built-in amplitude modulation can now also be used to control the power level of the excitation pulses, as each AMC only requires a single power level in a given ELDOR experiment. Note that as detailed in section 2.8 our sub-band mixer EPR detector detects induction mode EPR signal from AMC1/TH1, and reflection mode EPR signal from AMC2/TH2, as shown in figure 2.2c. In the reflection mode EPR configuration, the signal and the reflected excitation pulses are both transmitted into the detector; thus, the excitation pulses must be short (2 μs with 5% duty cycle) in order to prevent damage to the sub-band mixer. Therefore, AMC1/TH1 was used for the long excitation pulses and AMC2/TH2 for the shorter detection pulses. Power-dependent ELDOR profiles of the 40 mM 4-hydroxy TEMPO (4HT) sample in 1:1 DMSO:H_2O at 4 K were acquired using the just introduced two-source configuration by solely varying the power of the excitation pulses and are shown in figure 3.4b. Notably, the previously observed distortions to the background signal in the ELDOR acquired with a single AMC (figure 5a) are eliminated. Thus, the implementation of a second source for two-source ELDOR improves the quality of power-dependent electron depolarization profiles and allows for acquisitions of highly reproducible electron depolarization profiles with clean baselines.

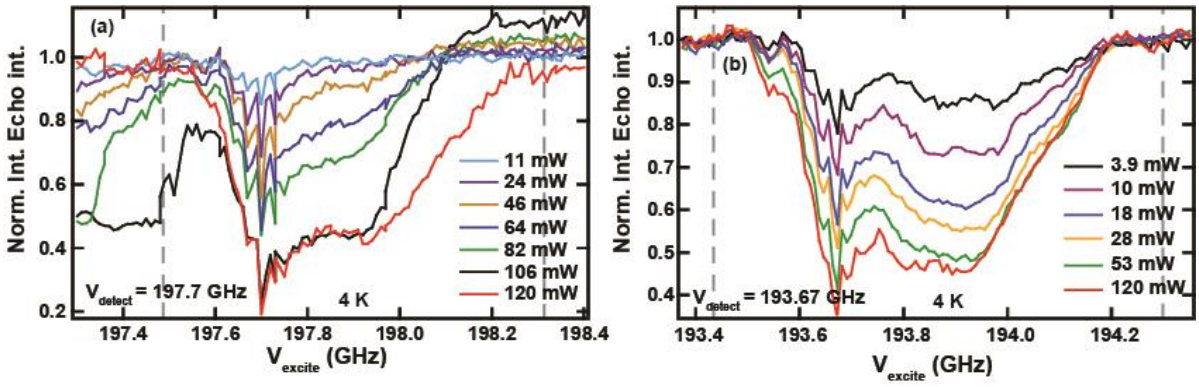

Figure 3.4. Electron depolarization profiles of 40 mM 4-hydorxy TEMPO in 1:1 DMSO:H_2O at 4 K and at 7 T with attenuation of AMC power output for the whole pulse sequence (a) and with 2-source ELDOR (b). For each the applied $P_{\mu w}$ during the saturation pulse was varied and is depicted inside the figure. The dashed gray lines correspond to the width of the EPR line. Experimental parameters: (a) repetition time = 400 ms, t_{excite} = 100 ms, ν_{excite}=197.7 GHz, t_p = 500 ns, tau = 500 ns, and t_d = 10 μs. (b): repetition time = 500 ms, t_{excite} = 100 ms, ν_{excite}=193.67 GHz, t_p = 750 ns, tau = 500 ns, and t_d = 10 μs.

3.4. Arbitrary waveform shaped pulses for EPR

Integration of an AWG allows for enhanced control over the pulse amplitude, frequency, and phases for more elaborate spin manipulations than is possible with rectangular pulses. AWG has been utilized by NMR for decades,[173–175] but only in the last few years has the technology became mature enough, reaching sub-ns time resolution, for AWGs to shape μw pulses in EPR experiments, mainly at X-band (9.5GHz) and Q-band (35GHz) frequencies.[176–182] We have recently integrated AWG capabilities in our 200 GHz DNP/EPR spectrometer.[153] An AWG can be used as a convenient way to provide phase cycling capabilities for rectangular pulse experiments, beyond what is possible with a traditional two-channel spectrometer design, as the AWG phase manipulation is frequency independent to the first order. But more importantly, phase and amplitude modulated pulses can be used to enhance the performance of the system relative to a rectangular pulse, for example by extending the bandwidth of a

pulse to much beyond >> ω_1 of a rectangular pulse. This is beneficial for systems where the available source technology is power limited (see section 2.5.1), yielding low ω_1 of order 0.5 MHz for EPR and DNP experiments. The solution to enhance ω_1 through the use of a resonant cavity as is commonly employed for EPR is not compatible with high frequency DNP experiments, given the relatively large sample volumes (30-50 μl) frequently used for DNP experiments. Therefore, AWG-enhanced shaped pulses become a very attractive approach to address the ω_1 limitations, as they allow for fine control of the spin dynamics and spin manipulation over the bandwidth that can exceed the available ω_1 by orders of magnitude.

Due to the nonlinear nature of the AMC and small dynamic range of the input signal when operating under non-saturating conditions, amplitude modulation becomes challenging.[153] As such we will limit our discussion of AWG functionality to frequency and phase modulations. Fortunately, under power limiting conditions, phase-shaped full amplitude pulses typically provide the best performance.[183–185] One common frequency modulated pulse used to increase the bandwidth of a pulse is the chirp pulse, where the frequency is changed in a linear fashion over the duration of the pulse. The chirp pulse is defined by the following parameters: (i) the chirp pulse bandwidth $\Delta\omega_{chirp}$, (ii) the rate at which the instantaneous frequency is swept across this bandwidth, k, and (iii) its amplitude. Since the instantaneous frequency of the chirp pulse is changing linearly from $\omega_{mw} - \frac{\Delta\omega_{chirp}}{2}$ to $\omega_{mw} + \frac{\Delta\omega_{chirp}}{2}$ during the chirp pulse duration, t_{chirp}, the chirp rate is given by $k = \frac{\Delta\omega_{chirp}}{t_{chirp}}$. The phase profile of the chirp pulse, $\Theta_{pulse}(t)$, is: $\Theta_{pulse}(t) = \left(\left(-\frac{\Delta\omega_{chirp}}{2}\right)t + \frac{kt^2}{2}\right)$.

The pulse sequence for measuring the inversion profile of a saturation pulse is shown in Figure 3.5a. Here, the intensity of the echo formed by the two t_p pulses (here chosen to be 90°

pulses) was monitored as a function of the offset frequency of the t_{chirp} inversion pulse. The advantage of using the phase modulated chirp pulses is illustrated in figure 3.5b. An inversion efficiency of three different chirp pulses with $\Delta\nu_{chirp}$ of 2, 6, and 10 MHz clearly exceed that of a rectangular-π pulse (dashed blue line). Notably for this sample of 1% BDPA in o-terphenyl, the inversion bandwidth of the shaped pulses exceeds that of the rectangular pulse by more than a factor of ten.

The gain in performance by using chirp pulses was also demonstrated for coherent EPR experiments with a refocused echo pulse sequence, where the rectangular pulses (Figure 3.5c) are replaced with a pair of refocusing chirp pulses (Figure 3.5d). Figure 3.5e clearly shows the enhanced performance for a 3.4 nm Gd^{3+} ruler molecule, as the echo intensity is two times higher when the chirp refocusing pulses were used. These examples illustrate the improved electron spin control that is enabled by using AWG phase shaped pulses.

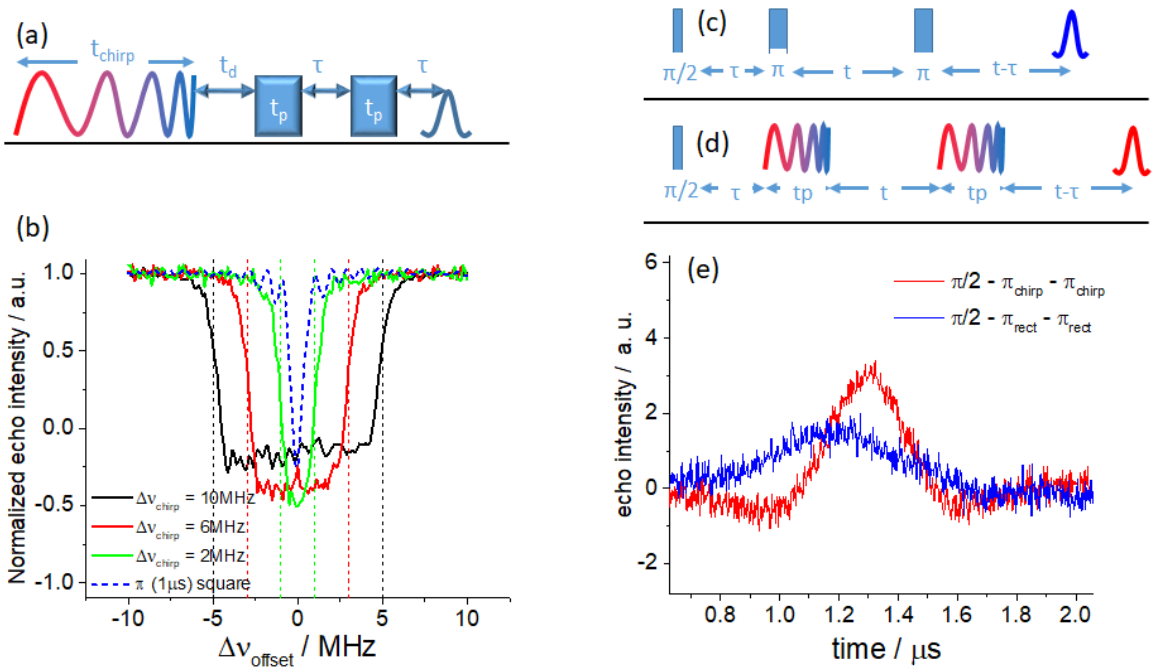

Figure 3.5. (a) Pulse sequence used for measuring inversion profile of a chirp pulse. (b) Experimental inversion profiles of a 10μs chirp pulse for BDPA in o-terphenyl sample. Refocused echo pulse sequence with (c) all rectangular pulses and (d) chirp refocusing pulses. (e)Refocused echoes as measured on the 3.4 nm Gd^{3+} ruler molecule using pulse sequences in (c) blue trace and pulse sequence in (d) red trace. Experimental parameters BDPA sample: t_p = 500 ns; τ = 800 ns; t_d = 2.4 μs; k = 1MHz / μs; Gd^{3+} sample: π/2 = 187.5 ns; π = 375 ns; π_{chirp} = 1 μs; $\Delta\omega_{chirp}$ = 4MHz; τ = 1 μs; t = 6 μs; t_p = 1 μs; repetition time 100 μs.

3.5. Summary

This chapter showcases the possible μw manipulation (including AWG) and electron detection techniques currently available with our 194 GHz dual DNP/EPR instrument at UCSB from electron spin relaxation processes to electron depolarization. Example spectra and their experimental parameters for these techniques were presented, and we discussed the analytical procedures used to understand these types of datasets. Overall there is good agreement between frequency-stepped and traditional field-swept EPR spectra, confirming the performance of the electron spin detection aspect of the 194 GHz instrument presented in

chapter 2. The acquisition parameters and the theory behind hole-burning (DNP relevant) ELDOR spectra versus ELDOR detected NMR (ED-NMR) is compared to illustrate how differences in the electron spin relaxation dynamics and μw manipulation can drastically influence the degree of electron spin depolarization.

4. EFFECT OF RADICAL CONCENTRATION, TEMPERATURE, AND MICROWAVES ON HOMOGENEOUS RADICAL DISTRIBUTIONS

The characteristic lineshape of the DNP spectrum, which is the NMR signal enhancement as a function of the μw irradiation frequency, $\nu_{\mu w}$, can provide information regarding the active DP mechanisms present in a given sample. This has been successfully achieved under static conditions, where analyses yielded the relative contributions of simultaneously active DNP mechanisms.[79] However, even for the simple case of static DNP (as compared to MAS-DNP), no model to date comprehensively captures all multi-electron and multi-nuclei effects on the DNP enhancement mechanisms.[15,16,76,79,186–189] Static DNP studies at 95 GHz have shown that parameters such as the radical concentration, the spin-lattice relaxation rates of the electron and nuclear spins, as well as the applied μw B_1 field (μw power, $P_{\mu w}$) must be considered in order to analyze the DNP spectral lineshape. Specifically, Hovav et al. introduced a phenomenological eSD model for evaluating electron depolarization profiles as a function of different $\nu_{\mu w}$ using these parameters.[79,98] This model relies on fitting simulated electron-electron double resonance (ELDOR) curves to experimental ones, measured at several ν_{detect}, and converting the resultant electron depolarization profiles to represent the depolarization at fixed ν_{excite}. At 3.4 T, they showed that these simulated electron depolarization profiles can be used to simulate basic SE- and iCE-DNP spectra, which were then used to analyze their contribution to the experimental DNP spectra.[98] The occurrence and validity of the eSD effect at higher magnetic fields, and its influence on DNP at these fields have not yet been explored. Specifically, the effects of electron spin concentration, temperature, and $P_{\mu w}$ on the eSD process and DNP spectra have not been studied to date at high fields.

This chapter explores the effect of the radical concentration, temperature, and $P_{\mu w}$ on DNP spectra of a model water/glycerol glass containing mono-nitroxide radicals, specifically 4-amino TEMPO (4AT), at 7 T. Variations in the DNP lineshapes are interpreted through simulations based on the SE- and iCE-DNP models. In particular this chapter will focus on the experimental conditions where the eSD process strongly affects the DNP lineshape. Under these conditions, the electron spin depolarization profile is influenced by many-electron spin dipolar couplings and dynamics, which must be considered to accurately model the DNP data.

As such, ELDOR spectra obtained from 10 mM and 40 mM 4-amino TEMPO (4AT) samples in a water-glycerol glass at 4 K and at 7 T are presented in figure 4.1 to show that eSD does occur under these conditions. Discussion of the ELDOR spectra and their acquisition can be found in chapter 3, where the ν_{excite} for these ELDOR spectra was incremented from 197.4 to 198.3 GHz. The sharp negative peak at the detection frequency of 197.55 GHz, where $\nu_{excite} = \nu_{detect}$ is a result of direct μw saturation of the electron spins, corresponding to an allowed EPR transition (annotated as "3"). The sharp peaks near the allowed EPR transition (annotated as "1" in figure 4.1) are due to the single quantum forbidden EPR transitions resulting from hyperfine interactions with the ^{14}N atoms on the nitroxide radicals, as described by Florent et al.[169] A third sharp peak at 197.85 GHz (annotated as "2") can be assigned to the forbidden EPR transition resulting from hyperfine interactions with the ^{1}H nuclei; this peak is more prominent in the 10 mM sample than the 40 mM sample. The broad negative peak seen around ν_{excite}=197.85 GHz in the 40 mM sample, and to a small degree in the 10 mM sample, is a manifestation of the eSD process resulting from the electron-electron (*e*-*e*) dipolar interactions that cause the exchange of polarization between coupled electron spin pairs. These electron spin pairs can have significantly different

resonant frequencies and different probabilities of occurrence in a sample; however, the probability of nearby spins being spatially close enough to dipolar couple to an electron spin that was directly excited by μw irradiation is largest for those electron spins with resonant frequencies near the center of the EPR line due to their higher relative population. The increase in eSD induced depolarization in the ELDOR spectra from 10 mM to 40 mM demonstrate the need to include eSD effects in DNP simulations, as the electron depolarization has a direct impact on the resultant DNP spectra, as has been observed at 3.5 T.[30,79]

As the ELDOR profile lineshape is dependent on the radical concentration, the electron spin couplings and dynamics, and the shape of the EPR spectrum, the profile lineshape will reflect the density distribution of strongly interacting spin pairs, which is non-uniform along the EPR spectrum. Given this, the broad negative peak at ν_{excite}=197.85 GHz is a consequence of the relatively high concentration of coupled spin pairs at that frequency, which coincidentally happens to be 300 MHz off-resonance from ν_{detect}. This depolarization effect observed near the center of the EPR line is not due to ^{1}H-electron spin forbidden transitions, as the broad negative peak is observed approximately at ν_{excite}=197.85 GHz independent of ν_{detect} for the 40 mM sample, while the depolarization would always have to be 300 MHz offset from ν_{detect}, if it was induced by the ^{1}H forbidden transition as observed for the 10 mM sample (Appendix E.1). Additionally, this frequency off-set is well beyond the width of the hole burnt into the EPR spectrum solely due to spin relaxation effects (T_{1e}, T_{2e}), as reflected in the simulated ELDOR spectral width in the absence of eSD effects (black trace, figure 4.1b). Therefore, it is clear from the experimental ELDOR spectra that eSD under the aforementioned conditions has a very large effect and dramatically broadens or alters the shape of the ELDOR profiles. These results at 7 T agree with previous work at 3.5 T that

found eSD determined from ELDOR spectra to be directly reflected in the DNP spectra.[8,30,33] The ELDOR spectra in figure 4.1 was acquired at 7 T, and are used solely to demonstrate the need to incorporate eSD in the DNP simulations under the relevant experimental conditions; however, we showcase how the theoretical model that incorporate eSD can be used to effectively simulate DNP spectra without requiring the acquisition of ELDOR profiles, when considering the radical concentration (section 4.2), temperature (section 4.3), and $P_{\mu w}$ (section 4.4). The measurement and analysis of the ELDOR curves, and their dependence on various experimental conditions is discussed in chapters 3 and 6, while the influence of $P_{\mu w}$ on DNP, while considering electron depolarization profiles will be discussed in section 4.3.2.

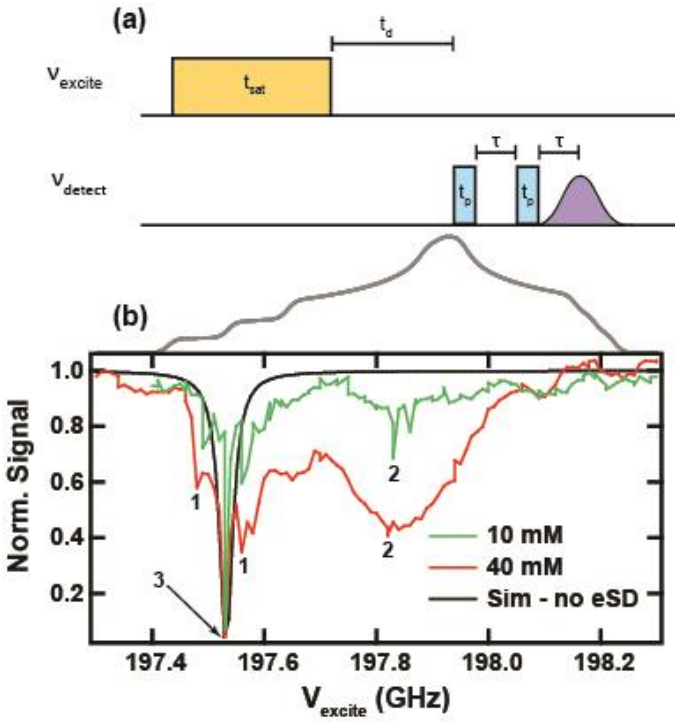

Figure 4.1. (a) ELDOR pulse sequence applied to obtain the experimental data presented here, where t_{sat} = 100 ms, t_p = 500 ns, τ = 500 ns, t_d = 10 μs, and v_{detect}=197.55 GHz. (b) Experimental ELDOR spectrum of 10 mM (green) and 40 mM (red) 4-amino TEMPO in a 5:4:1 d-glycerol:D_2O:H_2O glass at 4 K overlaid with an ELDOR simulation without eSD (solid line). The nitroxide EPR spectrum is shown as reference in gray above the ELDOR spectrum. Annotations "1" mark ^{14}N hyperfine forbidden transitions, "2" mark ^{1}H hyperfine forbidden transitions and "3" mark allowed EPR transitions. ELDOR spectra of 10 mM (c) and 40 mM (d) 4AT at 4K and 7 T for varying v_{detect} as defined inside the figure. The nitroxide EPR line is above the ELDOR spectra as a reference of the relative electron populations.

4.1. Simulation theory for DNP profiles and electron depolarization

Before we can test the eSD-based model developed by Hovav et al to determine the active DNP mechanisms for a sample formulation at high magnetic fields, we first need to introduce the method.[79,98,191] In the following, a brief summary of the eSD model is presented and how to calculate DNP spectra from contributions corresponding to the SE and the CE mechanisms from the electron spin-polarization profiles. The electron spin depolarization

profile $P_e(\nu_{detect};\nu_{excite})$ is derived from ELDOR experiments, where the spins are observed at one frequency, ν_{detect}, in the EPR spectrum as a function of μw irradiation at another frequency, ν_{excite}. The pulse sequence used to obtain the ELDOR data is shown in figure 4.1a, where the long pump (excite)-pulse saturates the EPR transitions around ν_{excite} and the probe (detect) pulses form an echo for detection at ν_{detect} . $P_e(\nu_{detect};\nu_{excite})$ is the normalized electron spin polarization at ν_{detect} and ν_{excite}. In a previous study by collaborators, it was showed that these $P_e(\nu_{detect};\nu_{excite})$ can be simulated by the eSD model, accounting for the EPR line shape, here composed only of the allowed EPR transitions (with the forbidden transitions constituting negligible overall intensities).[98] This is done by partitioning the electron spins forming the EPR line into a fixed number of frequency bins, *j* (electron spin packets), with average frequencies, $\nu_{e,j}$, and a constant bin width, Δ_{bin}. The model assumes that each bin contains a relative number of electrons, f_j , reflected by the normalized EPR lineshape. All of the electrons in each bin are assumed to have the same polarization, $P_e(\nu_j)$. The polarization dynamics of the bins are evaluated by solving a set of coupled rate equations for the $P_e(\nu_j)$'s and the polarization of a single nucleus.[79] This nucleus is representative of the nuclei that are influenced by the μw irradiation on the forbidden transitions of the electron spins during the SE process. The rate constants in these equations are a function of the μw irradiation frequency (ν_{excite}) and amplitude (ν_1), the electron spin-lattice relaxation time (T_{1e}), the electron spin-spin relaxation time (T_{2e}), an eSD exchange constant (Λ^{eSD}) defining the polarization exchange rate between the bins, and the effective pseudo-hyperfine (electron-

nuclear hyperfine) coupling constant ($A^{\pm}$) that all together determine the effective ZQ and DQ μw irradiation rates causing the polarization depletions via the SE-DNP mechanism. In samples containing high ^{1}H concentrations, as is the case in our studies, the $A^{\pm}$ constant represents some average electron-proton hyperfine interaction responsible for ^{1}H-SE-DNP. The ^{1}H-dCE and ^{1}H-iCE DNP processes are conventionally assumed not to influence the electron depolarization profile, given the low concentration of electrons fulfilling the CE conditions.[98] In order to derive the simulated $P_e(\nu_{excite},\nu_{detect})$ profiles from the solution of the coupled rate equations, and to compare them to the experimental ELDOR results, values for the three unknown parameters must be chosen: T_{2e}, $\bar{A}^{\pm}$, and Λ^{eSD}, while inserting into the equations the experimentally determined f_j, T_{1e} values and the radical concentration. After the construction of $P_e(\nu_{detect};\nu_{excite})$ profiles with the chosen T_{2e}, $\bar{A}^{\pm}$, and Λ^{eSD} values for experimental or estimated ELDOR data, the basic DNP lineshapes can be simulated from the ^{1}H-SE and the ^{1}H-iCE DNP mechanisms (respectively $S_{SE}(\nu_{excite})$ and $S_{iCE}(\nu_{excite})$), using the method described by Hovav et al.:[79]

$$S_{SE}(\nu_{excite}) = N_{SE}^{-1}\{f_{e-}P(\nu_{excite}-\nu_{1H};\nu_{excite}) - f_{e+}P(\nu_{excite}+\nu_{1H};\nu_{excite})\} \qquad (4.1)$$

$$S_{iCE}(\nu_{excite}) = N_{iCE}^{-1}\sum_j f_j f_{j-}\frac{P_e(\nu_{e,j};\nu_{excite}) - P_e(\nu_{e,j}-\nu_{1H};\nu_{excite})}{1-P_e(\nu_{e,j};\nu_{excite})\times P_e(\nu_{e,j}-\nu_{1H};\nu_{excite})} \qquad (4.2)$$

Here $f_{e\pm} = f(\nu_{excite}\pm\nu_{1H})$ are the relative intensities of the electron packets ν_{1H} away from ν_{excite}, $f_j = f(\nu_j)$ and $f_{j-} = f(\nu_j - \nu_{^1H})$ are the intensities at ν_j and at $\nu_j - \nu_{^1H}$. N_{SE}^{-1}

and N_{iCE}^{-1} are normalization factors for the basic ^{1}H-SE and ^{1}H-iCE DNP spectra, respectively.

The steady state ^{1}H-DNP spectra can then be expressed as

$$E_{1H}(\nu_{excite}) = k_{SE}S_{SE}(\nu_{excite}) + k_{iCE}(S_{iCE}(\nu_{excite}) - S_{iCE,0}) + c_{eq},$$

(4.3)

where the k_{SE} and k_{iCE} coefficients express the relative contributions of the two mechanisms and c_{eq} is added to account for thermal equilibrium. The subtraction of the iCE thermal equilibrium value, $S_{iCE,0}$, from the ^{1}H-iCE spectrum is explained in the work of Shimon et al.[190] Following previous work from collaborators, the dCE-DNP spectrum is not accounted for, as the steady state nuclear polarization resulting from the polarization differences of the dCE electron pairs are included in the calculation of the iCE DNP spectrum expressed in equation 4.2.[98] Note that $P_e(\nu_{detect};\nu_{excite})$ for the iCE mechanism are calculated by including irradiation on electron-nuclear DQ/ZQ transitions. The excitation of these transitions results in a depletion of the electron polarization corresponding to the SE mechanism. Consequently, the SE-derived electron spin polarization depletion process changes the profile of $P_e(\nu_{detect};\nu_{excite})$, and hence influences the iCE DNP spectrum, $S_{iCE}(\nu_{excite})$. This indirect SE mechanism does not disturb the presence of the direct SE enhancement process that results in the SE-DNP spectrum. Thus, the shape $S_{SE}(\nu_{excite})$ must

be calculated separately from $S_{iCE}(\nu_{excite})$ and when necessary combine them as presented in equation 4.3.

In cases where no experimental ELDOR data is available, as in the current DNP study at 200 GHz, the basic DNP spectra must be calculated by assuming values for T_{2e}, $A^{\pm}$, and Λ^{eSD} and then compare them to the experimentally obtained DNP spectra. The parameters chosen to simulate the electron spin polarization profiles, $P_e(\nu_{detect};\nu_{excite})$), are also used to calculate the basic DNP spectra for the SE or iCE mechanism. In the present study, the values for the parameters used are in the vicinity of the fitting parameters for T_{2e}, $\bar{A}^{\pm}$, and Λ^{eSD}, derived from EPR and ELDOR data of a similar sample – an aqueous glass containing 40 mM of 4-hydroxy-TEMPO, as measured at 95 GHz.[79]

4.2. Global radical concentration

The first experimental parameter that we tested this model on is the radical concentration, since the eSD polarization transfer process, which is driven by *e*-*e* dipolar interactions and resulting cross relaxations, is expected to be strongly dependent on the radical concentration. The radical concentration will determine the average distance between electron spins, and thus the strength of dipolar interactions between them, particularly when using monoradicals, assuming a homogeneous radical distribution throughout the sample.

4.2.1. Experimental concentration dependent DNP profiles

Four radical concentrations, C_e, ranging from 1.7 to 40 mM of 4AT (Cambridge Isotopes) were used for this study. Normalized DNP profiles for each radical concentration are shown in figure 4.2, where a representative nitroxide EPR spectrum is provided above.

For the 1.7 mM sample, the DNP spectrum spanned a frequency range wider than the EPR spectrum, with a peak-to-peak (positive-to-negative) frequency difference, Δ_{DNP}, of 600 MHz, i.e. twice the proton Larmor frequency, ν_{1H}, which is characteristic of SE-DNP.[14] As the electron spin concentration is increased, this Δ_{DNP} reduces by about 50%, and the full DNP spectrum falls completely within the EPR spectrum. This is consistent with a gradual change from a dominant SE-DNP mechanism at 1.7mM to a dominant iCE-DNP mechanism at 40 mM. At 10 mM, the Δ_{DNP} of less than $2\nu_{1H}$ indicates the onset of iCE, while the overall span of the DNP spectrum, especially near the baseline, is still broader than that of the EPR spectrum, implying contributions from SE effects. The lineshape of DNP spectra at radical concentrations > 10 mM suggest that the iCE mechanism is dominant – i.e. $\Delta_{DNP}<2\nu_{1H}$ and the full DNP profile falls within the allowed EPR spectrum, as indicated by the dashed lines in figure 4.2.

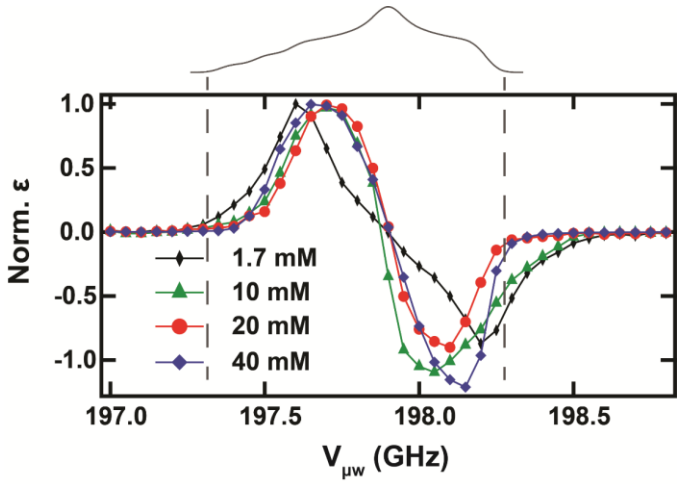

Figure 4.2. Experimental ^1H DNP profiles of 4-amino TEMPO at 4 K for different concentrations as indicated. The vertical dashed lines are drawn to represent the edges of the EPR spectrum.

4.2.2. Simulating concentration dependent DNP profiles

The concentration-dependent DNP spectra were compared with simulated spectra obtained by the procedure discussed in section 4.1. To simplify the fitting procedure, the analysis of the 10, 20, and 40 mM samples was restricted by considering only an iCE-DNP profile, $s_{iCE}(\nu_{excite})$ of equation 4.2 by setting $k_{SE} = 0$ in equation 4.3, and the 1.7 mM sample by considering only a SE-DNP profile, $s_{SE}(\nu_{excite})$ of equation 4.1 by setting $k_{iCE} = 0$ in equation 4.3. Here it is noted again that the model used to simulate iCE spectra takes the SE-induced electron depletion into account due to the partial saturation of the ZQ/DQ transitions in the presence of a pseudo-hyperfine coupling constant between the electron and the nuclei, $A^{\pm} \neq 0$. Consequently, in the presence of an efficient spectral diffusion mechanism, irradiation of ZQ/DQ transitions outside of the EPR spectrum will result in iCE-DNP lineshapes that are broader than the EPR line, while here the EPR spectrum is only referring to allowed transitions.[79] Our best fitting results determined by eye are shown in figure 4.3, where the values used for the spin-spin relaxation time, $T_{2e,}$ the effective hyperfine coupling constant, $A^{\pm}$, and the electron spectral diffusion constant, Λ^{eSD}, for evaluating $P_e(\nu_{detect};\nu_{excite})$ profiles, are given in table 4.1. The T_{1e} values were determined experimentally as previously published, where a bi-exponential curve was fit to experimental data and the longer time constant defined as the effective T_{1e}.[43] In order to narrow the parameter space for the fitting procedure to within an order of magnitude, since systematic ELDOR data at 200 GHz is not yet available, the fitting parameters found by Hovav et al. for a 40 mM 4-hydroxy-TEMPO sample at 95 GHz and 6 K were chosen as a starting point.[98] Assuming that the eSD process is largely determined by *e-e* spin dipolar interactions and temperature, this choice is reasonable. Currently only simulations of normalized DNP lineshapes are possible, since a

quantitative model predicting absolute DNP enhancements that depend on many-nuclear spin interactions and dynamics, including nuclear spin diffusion processes, is not available.

The simulated data for each of the concentrations agree reasonably well with the experimental data (figure 4.3), suggesting that the selection of the SE-DNP mechanism for 1.7 mM and the iCE-DNP mechanism for 10-40 mM was appropriate. The best fits were achieved for the 1.7 mM and 40 mM DNP spectra, i.e. under conditions that are unambiguously in the SE- or iCE-DNP regime, respectively. To fit the DNP spectra with increasing radical concentrations ≥10 mM, the value of Λ^{eSD} had to be increased accordingly (table 4.1). The significant increase in Λ^{eSD} from C_e = 10 mM to C_e = 40 mM can be attributed to the increase in the average dipolar interactions between the electrons, manifesting itself as a broadening of the intrinsic homogeneous linewidths around each μw frequency. Increasing the radical concentration also increases the absolute number of electron spin pairs fulfilling the CE condition through mutual dipolar interaction.[67]

Table 4.1. Concentration dependent simulation parameters, where T_{2e} is the estimated electron spin-spin relaxation time, $A^{\pm}$ is the effective hyperfine coupling constant, T_{1e} is the electron spin-lattice relaxation time, ν_1 is the μw irradiation strength, Λ^{eSD} is the phenomenological eSD parameter and $T_{\max}^{eSD}$ is the maximal eSD timescale in the system.

C_e (mM)	T_{2e} (μs)	$A^{\pm}$ (MHz)	Λ^{eSD} (μs^{-3})	$T_{\max}^{eSD}$ (ms)	T_{1e} (ms)	ν_1 (MHz)
40	10	0.5	800	0.04	30	0.3
20	20	0.5	100	0.3	93	0.3
10	30	0.5	50	0.7	198	0.3
1.7	100	0.5	0.5	67.6	500*	0.3

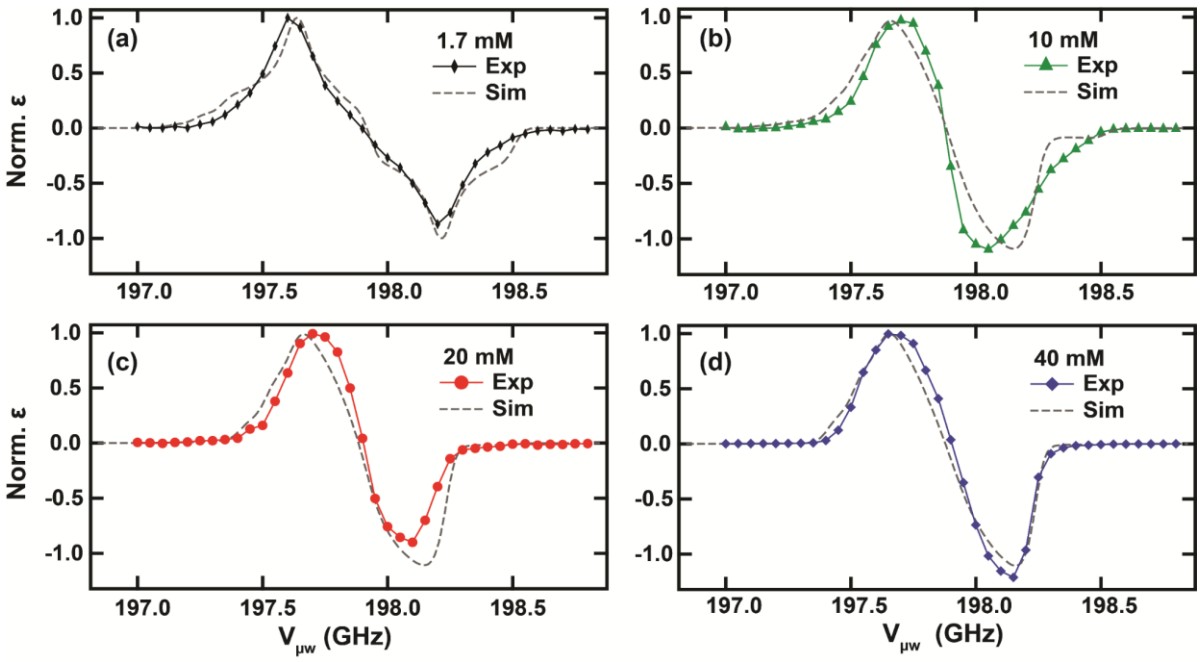

Figure 4.3. Normalized experimental (dots) and simulated (solid lines) DNP profiles of 4-amino TEMPO at 4 K, using t_{excite} = 60 s with radical concentrations of 1.7 mM (a), 10 mM (b), 20 mM (c), and 40 mM (d). The parameters used in the simulations are given in Table 1 and Δ_{bin}=2MHz.

4.2.3. Analysis of C_e-based simulations

After simulating the C_e-dependent DNP profiles, we will now analyze the quality of these simulations relative to the experimental results. At 1.7 mM radical concentration, the SE-DNP is the dominant mechanism since the average inter-radical distance is sufficiently large to minimize the average dipolar interaction between the electrons, and thus reduce eSD effects and suppress the CE-DNP mechanism. As such it is not surprising that the simulated SE-DNP profile at 1.7 mM reproduces all main features of the experimental profile. The fitting of the 10 mM DNP spectrum is less successful, particularly in the high frequency regime. The origin of the deviation between the experimental and simulated spectra is not clear at this point. Possibly, additional SE-DNP contributions need to be considered for the simulation of

the 10 mM data. Quantitative analysis of experimental ELDOR spectra is expected to further improve the accuracy of the simulated DNP spectra; however, the goal of was simulate DNP spectra without acquiring ELDOR spectra. The simulated DNP spectra of the C_e = 20 and C_e = 40 mM samples fit qualitatively well with their experimental counterparts, indicating that the fitting parameters describe the eSD process reasonably well. The sensitivity of the simulations to variations in T_{2e} and Λ^{eSD} can be evaluated by introducing an overall quality parameter, σ_{DNP}, that scales with the variance between the values of the experimental and simulated enhancements.[92] This σ_{DNP} parameter is not very sensitive to local variations in the DNP spectral lineshape. As a result, the sensitivity of σ_{DNP} to variations in T_{2e} is negligible for all of the radical concentrations studied here, and decreases with lower radical concentrations with respect to Λ^{eSD} (figure 4.4). The general insensitivity of the simulated DNP spectra to T_{2e} and Λ^{eSD} made it difficult to unambiguously fit the data. Thus, only qualitative trends for Λ^{eSD} values were derived from the concentration dependence of the DNP spectral lineshapes.

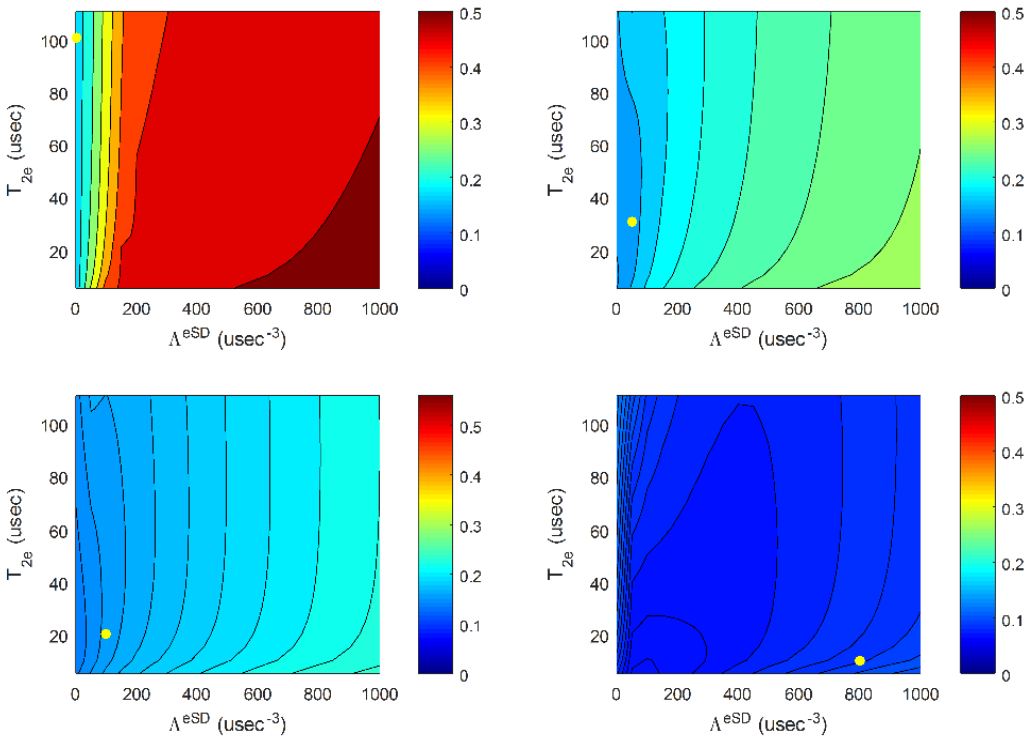

Figure 4.4. Contour plots of σ_{DNP} as a function of T_{2e} and Λ^{eSD} for 1.7, 10, 20, and 40 mM. The yellow circles mark the T_{2e} and Λ^{eSD} values given in Table 1 of the main text.

In order to assign a time constant to the polarization exchange process during eSD, characterized by Λ^{eSD}, an eSD exchange time, $T_{\max}^{eSD}$,[79] was introduced that describes the time it takes for two neighboring bins, $j_{\max}$ and $j_{\max-1}$, at the maximum of the EPR line to equalize their polarizations. This time constant provides the order of magnitude of the time for the eSD process *alone* to equalize all electron polarizations, and is calculated using

$$T_{\max}^{eSD} = \frac{1}{\Lambda^{eSD}} \frac{2(\nu_{j_{\max}} - \nu_{j_{\max-1}})^2 (2\pi)^2}{(f_{\max} - f_{\max-1})^2} \tag{4.4}$$

.

In table 4.1, the calculated value of $T_{\max}^{eSD}$ was included for each radical concentration, which has a unique Λ^{eSD} value that is assumed to be constant for the entire EPR line. As can be seen, $T_{\max}^{eSD}$ is much shorter than T_{1e}, which enables a partial depolarization of the entire EPR spectrum depending on the frequency of the μw irradiation. It should be noted that the eSD parameter, Λ^{eSD}, defining the polarization exchange rate between the electrons in different bins represents all possible mechanisms that influence this rate, including direct dipolar interactions, spin-lattice and possible cross relaxations and spin fluctuations. It is thus apparent the assumption that the Λ^{eSD} value is constant for all electrons across the EPR line should be further investigated.

Even though experimental electron spin polarization profiles are not available, one can compare experimental and simulated DNP lineshapes at different C_e by introducing a parameter, Δw_{DNP}, that is defined as the maximal difference between irradiation frequencies where the DNP spectrum equals to $\varepsilon = 0.5$ and $\varepsilon = -0.5$. Figure 4.5 illustrates the experimental and simulated Δw_{DNP} values as a function of C_e, which is used as a measure of the DNP spectral lineshape. Inspection reveals that the simulated DNP spectra are somewhat broader than the experimental DNP spectra. While the simulated values at C_e = 1.7, 10, and 40 mM deviate from the experimental values by less than 5%, the deviation at C_e = 20 mM is about 14%. The decrease in Δw_{DNP} for increasing concentration in the range of C_e = 1.7 - 20 mM is the result of the DNP mechanism changing from ^{1}H-SE to ^{1}H-iCE, as predicted also by the simulations. The deviation between the experimental and simulated values of Δw_{DNP} is a result of the mismatch between the shapes of the experimental and simulated DNP spectral

lineshapes, as can be clearly observed in figure 4.3. Confirmation that Δw_{DNP} is a valid parameter to describe DNP spectral lineshapes was determined by investigating the spectral linewidth at various absolute ε, which produced the same trends as observed for ε=±0.5 (Appendix E.2). The cause for deviations between the simulated and experimental lineshapes require further investigation.

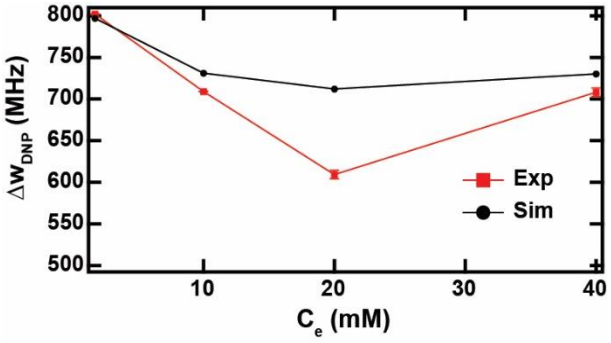

Figure 4.5. Δw_{DNP} of normalized experimental and simulated DNP spectra were plotted versus radical concentration, where the Δw_{DNP} is determined by the span of the spectrum when the normalized NMR signal is at 50% (positive to negative). Error bars were included to replicate data sets.

4.2. Temperature influence on DNP mechanisms and simulations

In order to investigate the impact of electron spin relaxation rates on DNP spectra, the 40 mM 4AT sample was analyzed at multiple cryogenic temperatures: 4, 6, 8, 10, and 20 K, where lowering the temperature will lengthen both T_{1e} and T_{2e} as well as nuclear relaxation rates. This was verified by measuring T_{1e} at 240 GHz as a function of temperature, as summarized in table 4.2. The normalized DNP spectra at the five temperatures are shown in figure 4.6a, and the enhancements obtained at 197.7 GHz of μw irradiation are listed in table 4.2. The decrease in experimental DNP enhancement with increasing temperature is expected,

considering the shortening of T_{1e}. Furthermore, increasing the temperature clearly results in the narrowing of the simulated ELDOR spectra as can be seen in figure 4.6c, and thus would alter the polarization gradients for electrons matching the iCE condition. Whether this change increases or decreases the overall iCE enhancement is not clear as the polarization gradient affects the overall enhancement, and this gradient depends on the width and shape of the electron depolarization profiles and the nuclear Larmor frequency.

The overall DNP lineshapes shown in figure 4.6a are relatively invariant with temperature, with identical Δ_{DNP}'s observed at all temperatures. However, the Δw_{DNP} display small, but systematic changes with temperature. As the temperature dependence was studied with a 40 mM sample and the SE effect is negligible at concentrations larger than 10 mM, the small changes in Δw_{DNP} as a function of temperature can be modeled by only considering the iCE mechanism with eSD. The value of T_{2e} is not changed during these simulations, since previous work has shown that slight modifications of T_{2e} do not significantly influence the ELDOR line shape.[98] With this method, the Δ_{DNP} and Δw_{DNP} temperature dependence can be replicated solely by changing the temperature and T_{1e}, while assuming that Λ^{eSD} is constant, given that C_e is constant (Appendix E.3). In figure 4.6b the (normalized) simulated DNP spectra are plotted using the experimental T_{1e} values, while the other parameters are kept the same as those used to simulate the 40 mM DNP spectrum at 4 K, as described previously. These simulated spectra agree well with the experimental DNP spectra, where both experimental and simulated DNP have identical Δ_{DNP}'s and their enhancements decrease by approximately an order of magnitude (table 4.2), while Δw_{DNP} is reduced by ~10% going from 4 to 20 K (figure 4.6d and Appendix E.3). This indicates that the absolute enhancement

strongly depends on T_{1e} as both experimental and simulated absolute enhancements vary significantly with temperature. Below 10 K there is an overall increase in Δw_{DNP} with decreasing temperature; however, there is a small decrease observed experimentally between 8 and 10 K, which is within the day-to-day average experimental error of ~13 MHz (figure 4.6d). Interestingly, the observed drop in Δw_{DNP} is also captured in the simulated Δw_{DNP}, indicating that even this small dip is captured by our model that solely adjusts T_{1e} with changing temperature. It is worth noting that the extent of spectral broadening due to T_{1e} and temperature is more sensitive for the simulated electron spin depolarization (ELDOR) spectra than the DNP spectra (figure 4.6b,c). Taken together, the modeled effects of T_{1e} alone can qualitatively reproduce the temperature dependence of the experimental DNP spectra, in terms of enhancement, overall lineshape, and spectral width, without invoking changes in Λ^{eSD}. This suggests that the eSD effect may be independent of temperature in the $\leq 20\,K$ regimes; however, systematic ELDOR experiments must be conducted to verify this hypothesis.

Table 4.2. Experimentally derived temperature dependent T_{1e} and maximum positive NMR signal enhancement (Exp ε) for a 40 mM 4AT sample in a water/glycerol glass. Experimental and simulated ε with respect to their respective enhancements at 20 K are shown for comparison, where the simulated ε at 20 K was 11.40 x10^{-5}.

Temperature (K)	T_{1e} (ms)	Exp ε	Exp ε *	Sim ε *
4	30.3	524	7.5	18.9
6	18.5	201	2.9	11.0
8	13.2	141	2.0	6.8
10	10	81	1.2	4.5
20	4.4	70	1.0	1.0

**Taken with respect to 20 K*

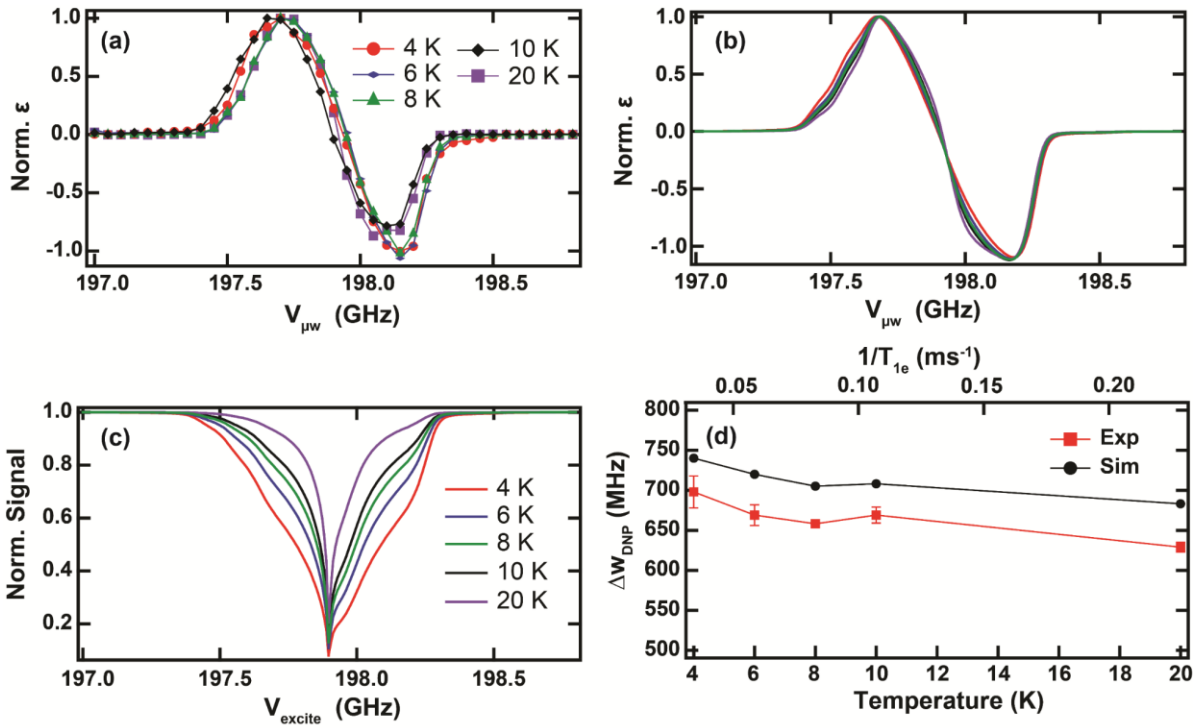

Figure 4.6. (a) Normalized experimental DNP profiles for 40 mM 4-amino TEMPO at various temperatures as defined inside the figure. (b) Normalized DNP profiles simulated for the corresponding experimental data in (a). (c) Simulated ELDOR curves for the temperatures studied with ν_{detect} *= 197.9 GHz. The parameters used in the simulations are defined in Table 2, and the rest of the parameters are:* T_{2e}*=10 μs,* $A^{\pm}$*=0.5MHz,* Λ^{eSD}*=800* μs^{-3}*,* T_{max}^{eSD} *=0.04 ms,* ν_1*=0.5 MHz,* Δ_{bin}*=2MHz.* ***(d)*** *Normalized simulated and experimental* Δw_{DNP} *were plotted vs. temperature and* $1/T_{1e}$*. Error bars were provided for replicated data sets. Lines are drawn to guide the eye.*

4.3. Microwave power influence on DNP

As has been discussed in chapter 1 and 2, there is much debate in the DNP community over the ideal μw-source – high power gyrotrons that are expensive or low cost and low power solid state source that are more flexible in their frequency and power outputs. The choice is mainly determined by the user's end goal; however, we will now evaluate the effect of $P_{\mu w}$ on DNP performance, as it has been previously shown that DNP enhancements are dependent on $P_{\mu w}$ at high radical concentrations and low temperatures.[43]

4.3.1. Simulation to account for $P_{\mu w}$

DNP spectra were taken at three μw irradiation strengths from 0.21 MHz (25 mW) to 0.46 MHz (116 mW) for a 40 mM 4AT sample at 4 K. These spectra show broadening of Δw_{DNP} by 83 MHz with increasing μw intensity from 0.21 MHz to 0.46 MHz, while Δ_{DNP} remains unchanged (figure 4.7a). As the temperature and concentration were held constant, the DNP spectra were simulated *solely* as a function of the μw irradiation strength, ν_1, while holding all other simulation parameters the same as those used in the initial simulation of the 40 mM 4AT sample at 4 K (Appendix E.4). The simulated Δw_{DNP} values as a function of ν_1 show effectively no change with increasing ν_1, whereas the experimental Δw_{DNP} was observed to increase by 15% (figure 4.7c). This increase is not due to sample heating, since no change in the NMR signal intensity is observed under off-resonant μw irradiation at full power compared to no μw irradiation. Additionally, this increase in Δw_{DNP} by an average of 85 $\pm$ 5 MHz with increasing ν_1 is consistently observed for different samples and freezing conditions. Therefore, some factor not considered in our current model is not included or must be changing concurrently with ν_1, when $P_{\mu w}$ is varied.

Thus far, the experimental DNP spectra inform us that Δw_{DNP} increases with decreasing temperature and increasing $P_{\mu w}$. The question is whether the broadening of Δw_{DNP} by decreasing temperature or increasing $P_{\mu w}$ is rooted in the same origin. If temperature or $P_{\mu w}$ are turning the same parameter "knob", then the effect on Δw_{DNP} by changing temperature can be reverted by changing $P_{\mu w}$, and vice versa. Indeed, when comparing two normalized experimental DNP spectra at vastly different experimental conditions, namely 20 K and

$\nu_1 = 0.46MHz$ versus 4 K and $\nu_1 = 0.36MHz$, the DNP spectra are essentially identical (figure 4.7b). Although experimentally $P_{\mu w}$ and temperature are very different physical factors, the similarity between these experimental DNP spectra suggests that the effects of $P_{\mu w}$ (through electron saturation effects and ν_1) and temperature (through change in polarization and relaxation rates) may be related to each other in adjusting Δw_{DNP} by altering a common factor, such as the electron saturation or spectral diffusion effects.

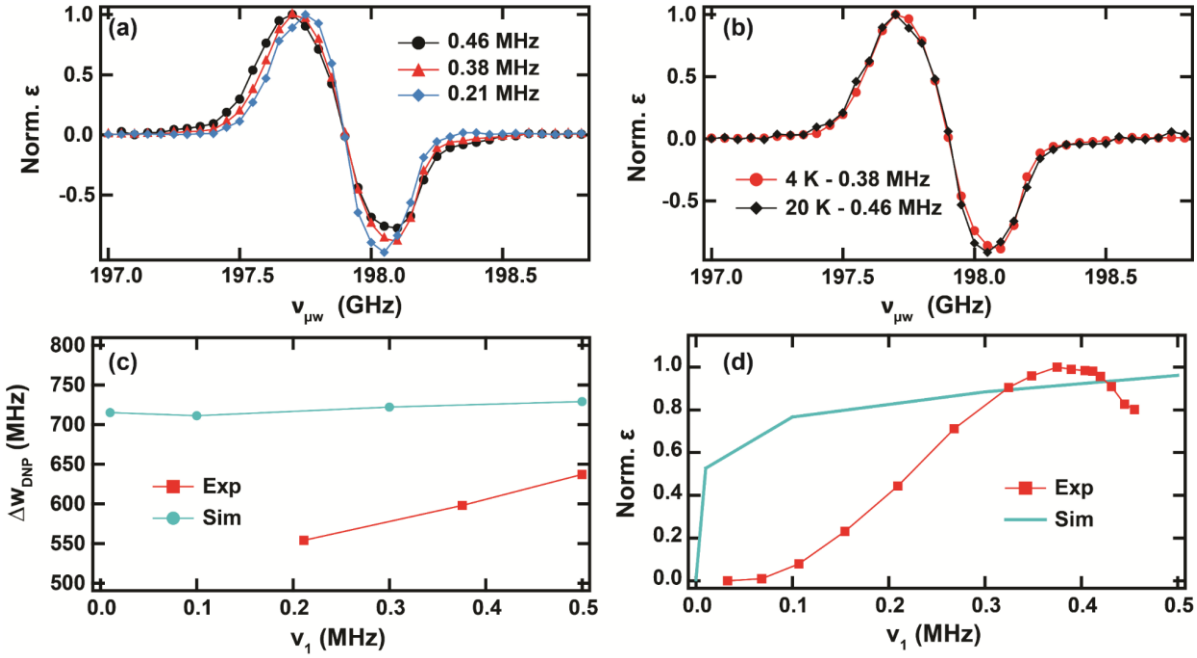

Figure 4.7. Experimental DNP spectra of 40 mM 4-amino TEMPO at 4K taken with different μw irradiation strengths (a). (b) Experimental DNP spectra taken at 4 K and 0.38 MHz of μw irradiation (red) and at 20 K and 0.46 MHz of μw irradiation. (c) Δw_{DNP} *vs.* ν_1 *are plotted for the experimental and simulated DNP profiles. (d) Experimental and simulated power curves, where the maximum positive DNP enhancement is plotted vs.* ν_1*. The parameters for the simulations are:* T_{2e}*=10 μs,* $A^{\pm}$*=0.5 MHz,* Λ^{eSD}*=800* μs^{-3}*,* Δ_{bin}*=2 MHz for* $\nu_1 \geq 0.3$ *MHz and* Δ_{bin}*=0.1MHz for* $\nu_1 < 0.3$ *MHz. All experimental data was collected after 60 sec of μw irradiation. The line associated with the experimental data is to guide the eye.*

Finally, the NMR signal enhancement as a function of ν_1 ($P_{\mu w}$ dependence) at a single $\nu_{\mu w}$, referred to as the DNP power curve, was examined. When a the DNP power curve was measured for a previous sample of 40 mM 4AT from 4 to 90 K at 197.7 GHz, the nuclear enhancement initially increased with ν_1 and then reached a plateau at temperatures > 6 K or began to decrease above a threshold ν_1 at temperatures ≤ 6 K.[110] This decrease in nuclear enhancement with increasing ν_1 has been termed 'oversaturation' by Siaw and coworkers.[43,110] Here the experimental μw intensity dependence a 4 K is presented, where the onset of oversaturation occurs at $\nu_1 = 0.37 MHz$ (figure 4.7d). When comparing the experimental power curve with the simulated one, no oversaturation effect is observed in the simulated curve (solid line, figure. 4.7d). Additionally, the experimental DNP power curve shows a qualitatively different shape, displaying a gradual increase in the experimental enhancement, in contrast to the sharp initial increase seen in the simulated DNP power curve. A partial explanation for the discrepancy between the experimental and simulated power dependent data is that the spin diffusion to the bulk of the sample is not accounted for in the theoretical model. Because of that, computing DNP signal enhancements that underlie the simulation of the DNP power curve is challenging. Whatever the exact cause, the current model fails to capture some key features of this process.

It should note that oversaturation can still be observed in the simulated spectrum when $\nu_1 \geq 2 MHz$, corresponding to a power of 2.24 W, which is experimentally inaccessible with our solid-state diode μw source (figure 4.8). This exercise informs us that there is merit in further exploring the physical basis for the dependence of DNP enhancement and spectra on ν_1, and accordingly modifying the model to reflect these findings. The effect of spin bath quenching may play a role in the observation of DNP oversaturation through their effect on

the electron spin phase memory time, but this has not been confirmed theoretically or experimentally at present. These combined $P_{\mu w}$ dependent simulations, showcase that the current model is lacking some component at high fields such that we cannot qualitatively fit the experimental results. Initial work to modify the current model to represent the $P_{\mu w}$ dependent experimental results has been made by myself and our collaborators in the Vega group by also considering power dependent ELDOR profiles. This work will be discussed further in section 4.3.3.

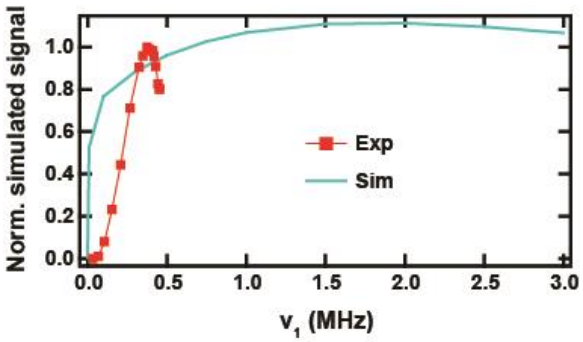

Figure 4.8. Experimental (red – symbols) and simulated power curvs with constant ΛeSD (aqua –solid line). The maximum experimentally relevant μw irradiation strength for our instrumentation is 0.5 MHz.

4.3.2. DNP oversaturation

As discussed in the previous section, DNP oversaturation was previously hypothesized to be due to strong eSD effects that can cause electron spin depolarization beyond optimal conditions for DNP.[43] The implementation of 2-source ELDOR in the static system enabled power dependent ELDORs to be acquired, such that I can directly test this hypothesis. A 40 mM 4-hydroxy TEMPO sample in 6:3:1 d_8-glycerol:D_2O:H_2O at 4 K was chosen since DNP oversaturation has been observed for years in the Han lab at these experimental conditions.

The DNP power curve was initially acquired to provide a basis for which μw irradiation strengths should be used for the ELDOR acquisitions as indicated by the arrows in figure 4.9a. Electron depolarization profiles were then acquired, where the power of the saturation or excitation pulse was varied to correspond to each of the μw powers determined from the DNP power curve. The electron spin depolarization profiles are shown in figure 4.9b, where the extent of electron spin depolarization (the width and depth) burnt into the EPR spectrum increases with higher μw irradiation strengths (more $P_{\mu w}$). The extent of electron spin depolarization continues to increase beyond the conditions that are optimal for maximal positive DNP enhancement (red and green traces, respectively). This provides direct evidence that DNP oversaturation is caused by electron spin depolarization beyond optimal for DNP, where the broader and deeper electron spin depolarization reduces the polarization difference between electron spins that meet the CE condition. This subsequently reduces the amount of polarization that can be transferred from electrons to nuclei during CE DNP and reduces the observed DNP enhancement values – i.e. DNP oversaturation.

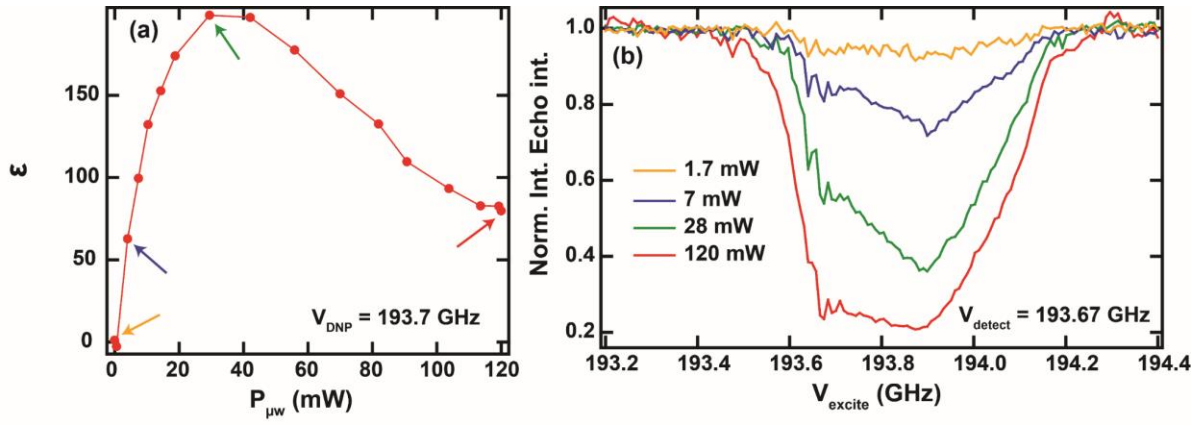

Figure 4.9. (a) DNP power curve for 40 mM 4-hydroxy TEMPO in 6:3:1 d_8-glycerol:D_2O:H_2O at 4 K. The colored arrows indicate the relative ε and $P_{\mu w}$ for each of the electron depolarization profiles shown in (b). Experimental parameters: $t_{build\text{-}up}$ = 60 sec, t_{sat} = 100 ms, t_p = 750 ns, t_d = 10 μs, τ = 500 ns, 1 scan, recycle delay = 600 ms.

The electron spin depolarization profiles not only can explain the DNP oversaturation process, but they can directly relate DNP oversaturation to eSD effects. This is because the extensive electron spin depolarization observed with DNP oversaturation is only observed in samples with significant eSD effects. As a reminder eSD is the process by which electron spin polarization is transferred between electron spins of different resonant frequencies – caused by different microenvironments, orientation in the glassy matrix, orientation with respect to the magnetic field, ect.[165,192] However, if eSD does not occur, the electron spins cannot depolarize across a sufficient bandwidth to cause a reduction in electron-nuclear polarization transfer in CE DNP, and thus no DNP oversaturation will be observed. This explains why samples with low global radical concentrations do not exhibit DNP oversaturation – because there is not enough eSD. However, if the μw irradiation is manipulated to increase the effective excitation bandwidth, then DNP oversaturation can be induced when it was previously not observed or it is initiated at lower μw irradiation powers. This can overcome conditions where there is insufficient eSD to induce DNP oversaturation. The increase in μw irradiation bandwidth can be achieved with chirp excitation pulses as described in section 2.5.3 and section 3.4, through the use of the 194 GHz system's AWG capabilities. Figure 4.10 showcases DNP profiles and power curves for chirp and cw- excitation pules as well as their corresponding electron spin depolarization profiles for a 20 mM 4-amino TEMPO sample in 6:3:1 d_8-glycerol:D_2O:H_2O at 4 K. From these, it is clear that the chirp excitation pulses have a broader electron spin depolarization profile and DNP profile compared to the cw-excitation pulses. In the DNP power curve, the threshold at which DNP oversaturation begins is 26 mW lower for the chirp pulses compared to the cw-pulses. The bandwidth of the chirp pulses,

$\Delta\omega_{chirp}$, will influence the amount of DNP enhancement observed as shown by figure 4.10d. Here the maximum DNP enhancement occurs when $\Delta\omega_{chirp}$ is equal to ω_I. This will cause the maximal number of electron spins to depolarize that meet the CE condition, such that the CE efficiency has been optimized.[193] These results illustrate the power of μw manipulation to select particular electron spin dynamics over others and reduces the necessary $P_{\mu w}$ requirements, which can be especially desirable for systems that have limited access to μw power.

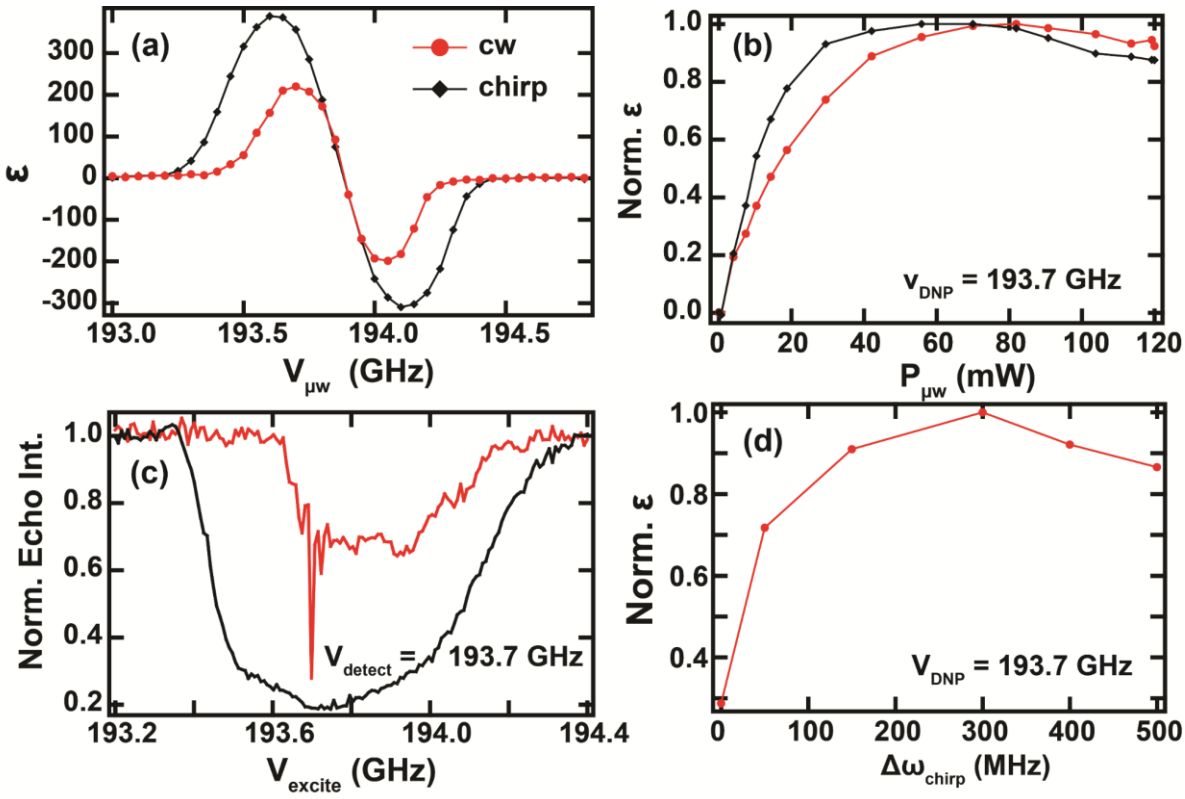

Figure 4.10. (a) Electron depolarization profiles of 20 mM 4-amino TEMPO in 6:3:1 d_8-glycerol:D_2O:H_2O at 4 K with cw and chirped μw irradiation applied during the saturation pulse. The corresponding DNP profiles (b) and power curves (c) are provided to compare the influence chirp μw manipulation has on DNP ε. (d) The normalized DNP enhancement as a function of $\Delta\omega_{chirp}$ is shown, where the maximal ε corresponds to ω_I. The ELDOR and DNP profiles were acquired with the respective optimal $P_{\mu w}$ for cw-irradiation (83 mW) and chirp-irradiation (56 mW). Experimental parameters: $t_{build\text{-}up}$ = 60 sec, $\Delta\omega_{chirp}$ = 300 MHz, t_{sat} = 100 ms, t_p = 750 ns, t_d = 10 μs, τ = 500 ns, recycle delay = 600 ms.

DNP oversaturation has currently only been reported at very low cryogenic temperatures, < 15 K. This is because at higher temperatures, T_{1e} becomes short enough that the electron spins will relax faster than eSD based *e-e* polarization transfers can establish a broad enough electron spin depolarization to induce DNP oversaturation. Therefore, a long longitudinal relaxation rate relative to the rate of eSD is necessary for DNP oversaturation to occur. A study of DNP power curves for a sample of 40 mM 4-amino TEMPO sample in 6:3:1 d_8-glycerol:D_2O:H_2O at temperatures between 4 K and 80 K, where done to evaluate the

influence of temperature on the DNP oversaturation effect (figure 4.11a). These DNP power curves show that DNP oversaturation occurs at approximately the same temperature at 4 and 6 K (30 mW), while a slightly higher power of 60 mW is required to induce DNP oversaturation at 10 K. At higher temperatures DNP oversaturation is not observed; although, it is important to note that at 25 K a plateau is reached at high $P_{\mu w}$, while at 80 K the 120 mW maximum power output of our solid-state μw-source is unable to even reach a plateau of DNP enhancement. These results correlate with shorter electron relaxation rates as has been previously noted in table 4.2 and shorter nuclear relaxation rates as shown by figure 4.11b. Work by another graduated student in the lab used ELDOR profiles of different radicals and concentrations at 25 K to show that at higher temperatures, T_{1e} dictates the extent of electron depolarization in an ELDOR profile.[194] This confirms that at higher temperatures (~ >15 K), the T_{1e} rate becomes fast enough that the eSD process is unable to efficiently spread polarization across the entire span of the electron spin spectral density, which is why eSD appears to be independent of the radical type used at 25 K, but it is still dependent on the radical concentration.[194] However, the influence of μw manipulation via chirp DNP or other shaped excitation pulses at higher temperatures than 10 K have not yet been performed.

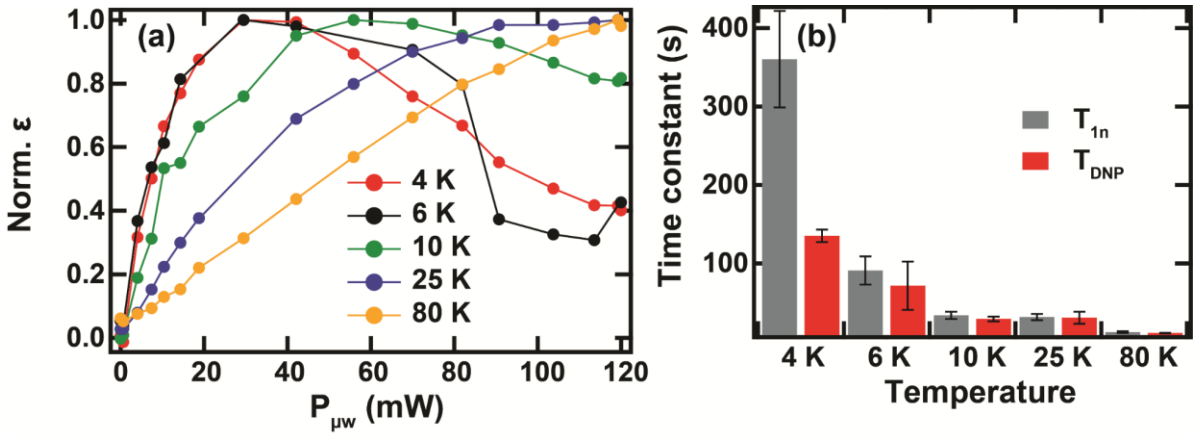

Figure 4.11. (a) Temperature dependent power curves for a 40 mM 4-amino TEMPO sample in d_8-glycerol:D_2O:H_2O at 4 K and at 7 T for 4, 6, 10, 25, and 80 K. The corresponding nuclear relaxation rates: T_{1n} and T_{DNP} are given in (b) with the errors from fitting the experimental data to a mono-exponential shown by the error bars.

4.3.3. Modifications to simulation method: improving the fit of $P_{\mu w}$ dependence

As discussed in section 4.X, the current model to simulate DNP spectra and ELDOR profiles is insufficient to reproduce the $P_{\mu w}$ dependent experimental results. First, we acquired the corresponding ELDOR spectra for the DNP power curves, which was made possible by the implementation of the 2-sourcce ELDOR hardware as discussed in section 3.3. The simulations greatly benefit from obtaining experimental electron depolarization profiles to be directly fitted instead of basing them solely off the EPR spectrum, as was done in the simulation method presented in section 4.1. However, these results were still unable to reproduce DNP oversaturation and were unable to fit the experimentally obtained ELDOR profiles with low $P_{\mu w}$. Therefore, to further modify the simulation method, we decreased the Δ_{bin} size from 2 MHz to 10-25 kHz. This allowed for the low $P_{\mu w}$ ELDOR profiles to reproduce the overall shape of the experimental ELDOR profiles. The reason why decreasing the Δ_{bin} improved the quality of the ELDOR fits is because when low $P_{\mu w}$ are applied the effective

spectral diffusion has decreased and smaller Δ_{bin} are required to capture the spectral diffusion between different spin packets. However, this improvement does not work across the whole electron spectral density, as shown by the unequal quality of fit of experimental ELDOR profiles at different ν_{detect} (figure 4.12). Here the same simulation parameters are used and fairly good agreement is observed between simulated and experimental ELDOR at ν_{detect} of 193.67 GHz, while poor fits are observed at ν_{detect} of 194.06 GHz. One possible explanation is that the electron relaxation rates (T_{1e} and T_m) are dependent on the electron spectral density – i.e. position along the EPR spectrum. Therefore, if the electron relaxation rates depend on ν_{detect}, then the extent of electron depolarization will change at different ν_{detect}. Our collaborators at 95 GHz do not see this problem, due to the much smaller electron spectral dentistry range for a nitroxide radical. However, at 194 GHz, the nitroxide has spectral dentistry over 1 GHz broad. Thus, the current simulation method that assumes singular electron relaxation rates is a poor choice at high magnetic fields when considering power dependent measurements. Work is in progress to develop a simulation method that incorporates frequency dependent T_{1e} and T_m into the current model, which should mitigate the discrepancies observed in figure 4.12.

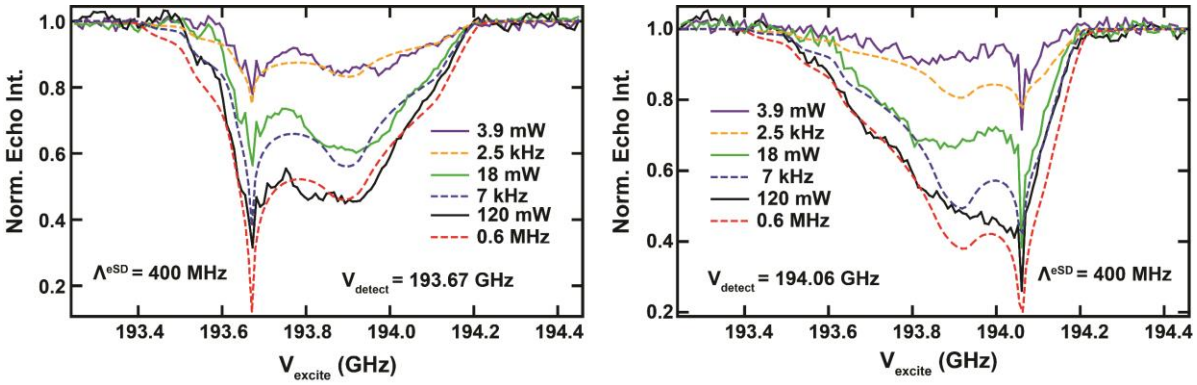

Figure 4.12. Simulated (dashed) and experimental (solid) ELDOR profiles at ν_{detect} of 193.67 GHz (left) and 194.06 GHz (right) as the applied $P_{\mu w}$ was varied for a 40 mM 4-hydroxy TEMPO in 1:1 DMSO:H_2O at 4 K and at 7 T. The applied $P_{\mu w}$ and input parameter for power in the simulation, ν_1, are given in the figure. Simulations parameters: T_{1e} = 39 ms, T_{1n} = 153 s, $A^{\pm}$ = 0.8 MHz, T_{2e} = 60µs, temperature = 4 K, Λ^{eSD} = 400 μs^3, Δ_{bin} = 0.25 MHz, and C_e = 40 mM.

4.4. Conclusion

From this chapter, the eSD effect has been found to be present in sample compositions typically used for DNP experiments and significantly impact the DNP performance at 7 T and low temperatures. This shows that the spin dynamics of many coupled electron spins greatly influences the DNP spectra and performance. The DNP spectra were successfully modeled with the incorporation of eSD theory to capture the radical concentration and temperature dependence on DNP spectra. By varying the monoradical concentration, we were able to rationally transition between the SE-DNP and CE-DNP mechanisms, as verified through simulations. We also were able to show that the temperature dependence of Δw_{DNP} can be qualitatively accounted for solely by changing T_{1e} values, while T_{2e} and Λ^{eSD} were kept constant, implying that T_{1e} has a larger influence on Δw_{DNP} than T_{2e}. The power dependence of Δw_{DNP} and DNP enhancement could not be modeled straightforwardly with the theoretical

model and parameters described in here. The observed broadening of Δw_{DNP} with increasing $P_{\mu w}$ and the overall shape of the DNP power curves could not be reproduced with simulations if ν_1 is set as the sole variable. These discrepancies are reduced by shortening Δ_{bin} in the simulation and by directly fitting experimental ELDOR profiles. The simulation method should benefit from incorporation of frequency dependent T_{1e} and T_m. Through these studies, we find that the current theory and model for DNP requires some refinement to fully capture the DNP process under static conditions, at high magnetic fields and low temperatures, of samples containing high concentrations of radicals (> 10 mM) or radical clusters.

Secondly, this chapter provides experimental results that can fully explain the DNP oversaturation effect through the acquisition of $P_{\mu w}$ dependent ELDOR profiles. From these and temperature dependent studies, we find that electron depolarization beyond optimal conditions will reduce the DNP enhancement and cause DNP oversaturation. The extent of electron depolarization is primarily modulated by T_{1e} and eSD effects, where higher temperatures will limit the effect of eSD due to faster T_{1e}. The extent of eSD in a sample is largely dominated by the radical concentration.

5. OCCURRENCE OF RADICAL HETEROGENEITY AND CLUSTERING

In chapter 4, the influence of radical concentration, temperature, and $P_{\mu w}$ and μw bandwidth on DNP were discussed. However, it was assumed that the radical concentration was homogeneous throughout the glassy matrix for all the systems. In general, this is a poor assumption to make unless the samples are flash frozen in liquid nitrogen to capture the liquid state in a moment of time, which is not feasible in the instrumental design for the 194 GHz dual DNP/EPR system described in chapter 2. Thus, this chapter makes an effort to elucidate if a heterogenous radical distribution or even radical clustering is induced by the available freezing methods for this instrumental design. Additionally, the occurrence of radical heterogeneity and clustering inherent to some radicals themselves or caused by additives typically used (here – Gd^{3+} complexes to shorten T_{1n}) are also investigated.

5.1. Induced by glass polymorphism

As DNP is most commonly applied to frozen aqueous glasses at cryogenic temperatures under magic angle spinning (MAS) or static conditions,[51,138,195,196] it is important to understand the impact vitrification has on DNP performance. The solvent type, sample composition, and freezing conditions will directly impact the type of glass formed, and thus the radical distribution throughout the sample.[197–199] Freed and co-workers have shown that the quality of the glass formed affects the EPR echo intensity, with better glasses producing stronger EPR signals.[199] In EPR studies of nitroxides, Kirilina and co-workers found that the size and structure of mono-radicals did not significantly influence the electron spin relaxation rates, while the solvent glass greatly influenced the electron spin relaxation rates.[200] In fact, the radical distribution in a sample can change the DNP mechanism and the maximum

achievable NMR signal enhancement.[43,96] As such is it important to investigate the influence of the quality and property of vitrified glasses and their radical distribution on DNP and EPR performance.

The DNP community commonly uses water/glycerol solvent systems to form amorphous glasses upon freezing, with glycerol content ranging from 40-72% by volume, while the trademark DNP juice™ specifically refers to 60:30:10% d_8-glycerol:D_2O:H_2O.[24,201] In water/glycerol glasses, the sample volume dictates the minimum required water to glycerol ratio for effective vitrification,[197] where larger water concentrations is expected to yield inhomogeneities in the solvent system.[198] Although water/glycerol is a commonly used solvent for DNP studies, there is contention in the vitrification literature on the degree of heterogeneity occurring at the mesoscopic scale upon formation of water/glycerol glasses.[202–207] Murata and Tanka argue a liquid-liquid transition occurs, which does not affect the homogeneous macroscopic distribution of water and glycerol molecules – i.e. no macroscopic phase separation occurs, but alters their hydrogen bonding network, and thus the density of the glass formed, at the mesoscopic scale, and the system's glass transition temperature.[202,208] Feldman group proposes that at glycerol concentrations ≤ 55% vol water-water interactions prevail in addition to water-glycerol and glycerol-glycerol interactions that result in the formation of ice crystals on the mesoscopic scale with some interfacial water connecting the ice crystals and the water/glycerol domains.[209,210] The Giovambattista group agrees with the Feldman group regarding the formation of ice at low glycerol concentrations, but they disagree over the range of glycerol concentrations that this micro-phase separation occurs. They further state that the glycerol content will factor into whether the ice formed will have cubic or hexagonal structures – thus influencing the density and glass transition temperature.[211,212] The

contention in the literature regarding the conditions, resultant products, and mechanism of water/glycerol vitrification are significant, but they all suggests that polymorphism exists to some degree in water/glycerol solvents, which will impact how the radicals essential for DNP and EPR are distributed in the sample. Therefore, the quality of the glass formed and the radical distribution in the glass must be known to accurately predict the ideal sample formulations to achieve large DNP enhancements, or simply consistent DNP enhancements by mitigating or utilizing solvent polymorphism.

Before the start of this study, the DNP enhancement for a single sample at 7 T and 4 K under static conditions varied significantly from day-to-day, with variations up to 40% for a water/glycerol solution of 50:40:10 by volume d_8-glycerol/D_2O:H_2O. Thus, the glass forming conditions (freezing history and sample composition) of water/glycerol samples under static DNP conditions at 4 K were investigated, with the aim to improve the consistency and predictability of DNP enhancements. The findings of this study are relevant for other low temperature DNP operations, including MAS-DNP at 80-100 K with a commercial DNP instrument, as most water/glycerol glasses have formed by 150 K.

5.1.1. Experimental results indicate polymorphism in water/glycerol glasses

The effect of sample composition and freezing conditions were evaluated on the DNP and EPR performance and the day-to-day consistency for the commonly used water/glycerol mixture-based solvents. Two different solvent compositions of water/glycerol were tested: 541 (50:40:10) versus 631 (60:30:10) by volume of d_8-glycerol:D_2O:H_2O to make 40 mM 4-amino TEMPO (4AT; Cambridge Isotopes) solutions. The EPR and DNP properties of each solvent composition were compared under two different freezing conditions: fast cool (FC) and thermally controlled (TC), with the two freezing histories depicted in figure 5.1.

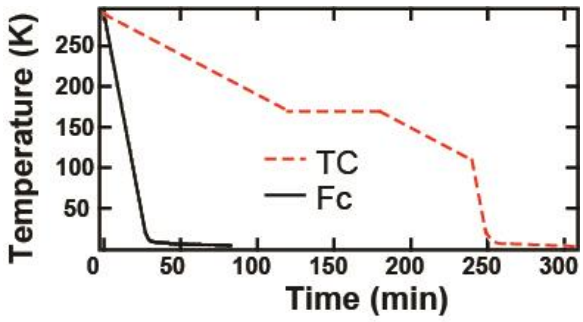

Figure 5.1. Time versus temperature depiction of the two freezing conditions: fast cool (FC) 10 K/min from 290 K to 4 K [black - solid] and thermally controlled (TC) 1 K/min from 290 K to 10 K above T_g, then 1 K/min to 100 K followed 12 K/min to 4 K [red - dashed]. Temperature was monitored with a Lake Shore Cernox® temperature sensor.

5.1.1.1. Glass transition temperatures

In order to understand the glassing behavior of the solvents under different freezing conditions, differential scanning calorimetry (DSC) analyses between 100 and 300 K were completed to determine their glass transition temperatures, T_g. The T_g values were determined from the second heating cycle and are shown in table 5.1, while the raw DSC curves are shown in figure 5.2, where the difference in heat flow between the FC and TC freezing methods is a consequence of the cooling rate - slower cooling rates induce less heat flow. All four systems form a glass, and the glass forming transition is symmetrically observed in both the cooling and heating cycles. From this, the T_g for 631-FC, 631-TC, and 541-FC was found to be ~167.7$\pm$1.5 K, and for 541-TC the T_g is 180.4 $\pm$ 1.7 K. In the heating DSC curve of 541-FC, a crystallization and subsequent melting peaking is observed above the T_g. The finding that 631-FC, 631-TC, and 541-FC have similar T_g suggests that similar glassy matrices are ultimately formed. Only 541-TC yielded a T_g that is statistically an outlier, implying 541-TC forms a different type of glass compared to the other systems.

The differing T_g between the TC and FC freezing methods observed only for the 541 solvent agrees with the literature that suggests at ≤ 55% glycerol content, non-negligible water-water interactions prevail in addition to water-glycerol and glycerol-glycerol interactions.[209,213] We postulate that persistent water-water interactions in the 541 solvent leads to the formation of minute ice particles depending on the freezing condition, while water-water interactions are non-dominant for the 631 solvent. The crystallization and melting peaks observed in the 541-FC DSC curve support the idea that ice crystals in the 541 solvent form due to the reorganization of the hydrogen bonding network between water and glycerol above the T_g that subsequently melted — similar DSC data have been reported by Popov and colleagues.[210] Since this thermodynamic transition is not symmetric on cooling and heating and was only observed on the heating cycle, we can say that the overall heterogeneity of the glass that formed upon cooling, according to DSC, is similar between the 631-FC/TC and 541-FC samples. However, this also shows that although 541-FC forms a similar glass as the 631 samples on cooling, there are fundamental differences in the 541 sample that allows for polymorphism to occur. This observation reiterates the influence and importance of the thermal history on water/glycerol glasses.

The reproducibility of polymorphism in frozen glasses needs to be verified in addition to the influence polymorphism has on the EPR and DNP results. If a different glassy matrix is formed with 541-TC, it is reasonable to expect that the radical distribution in the matrix would be different. This difference should be reflected in the EPR lineshape, phase memory times (T_m), and DNP spectra. These combined techniques provide insight into the bulk and local electron spin environments, where detailed descriptions of the methods and sample preparation are available in Appendix D.

Table 5.1. T_g values as determined by DSC analysis of the second cycle heating curve, maximum DNP enhancements after 60 s of irradiation, ε_{60}, at 197.7 GHz of μw irradiation, and maximum EPR echo intensity for 40 mM 4-amino TEMPO when irradiated at 197.925 GHz when t_p and tau = 500 ns at 7 T and at 4 K for the different solvent compositions and freezing conditions. The echo intensities were normalized to the highest signal (631-FC). Both the DNP enhancements and the EPR echo intensities represent the average of triplicated data sets and the errors correspond to day-to-day variations, where echo intensities were not corrected for T_m.

Sample	T_g (K)	ε_{60}
631		
TC	168.05	220 ± 20
FC	169.95	181 ± 24
541		
TC	180.35	125 ± 85
FC	164.85	143 ± 32

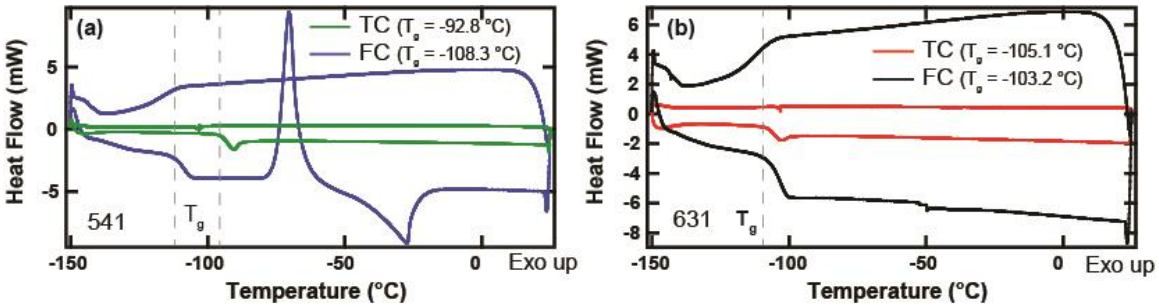

Figure 5.2. DSC plots of the different freezing conditions fast cool (FC) and thermally controlled (TC) for 40 mM 4AT in 5:4:1 (a) and 6:3:1 (b) d_8-glycerol:D_2O:H_2O. The T_g from each of the heating curves are noted in the plots by dashed grey vertical lines. The cooling curves are the top curves, while the heating curves are the bottom curves. Exothermic events are up. A TA Instruments Q2000 DSC with a 50 position autosampler, sensitivity < 0.2 μW, and a baseline drift of < 10 μW was used to collect the heating and cooling curves. An indium-sapphire standard was used for calibration of the heat capacity.

5.1.1.2. Electron spin dynamics: spectra and phase memory time

The EPR lineshapes were measured to study the bulk electron spin environment, both by continuous wave (cw-) and field-swept echo detection, of the different glassing conditions and solvent compositions at 8.56 T and 240 GHz. At high magnetic fields, the lineshape of a nitroxide EPR spectrum is dictated by the g-factor anisotropy, where the principle axis system can be determined from the spectrum with g_{xx} on the low field side and g_{zz} on the high field side. The anisotropy of the hyperfine interaction between the electron spin and ^{14}N of the nitroxide will further delineate the EPR lineshape; however only the z-component of the hyperfine coupling for nitroxides is easily observable at 240 GHz. In figure 5.3, the 631 samples present consistent EPR lineshapes acquired by cw- and field swept echo detection for both freezing conditions. The 541 samples EPR lineshapes differ in the g_{xx} region of the spectra, where the 541-TC sample has a lower intensity g_{xx} peak that is shifted slightly lower in field by ~250 ppm, as indicated in the inset of figure 5.3a. The cw- EPR spectra were simulated via EasySpin by varying the relative ratio of two populations that differ only by their g_{xx} values: 2.00839 and 2.00787, as shown in the figure 5.4, where the simulation parameters are given in table 5.2 (notes all strains are substantially smaller than their corresponding values). It was found that the 631 and 541-FC samples all favorably populate the high field species, while 541-TC favorably populates the low field species. Independent of the solvent choice, the TC freezing method displays a slightly higher population for the low field species relative to the solvent's FC counterparts. This indicates that some (small) difference exists between the 631-TC and 631-FC systems, but that the 631 solvent is more resistant to variations in the freezing method. The consistent favoring of the high field species by 541-FC and both 631 samples corroborates the T_g data that the glass properties and radical

distributions are more similar between these three samples. In contrast, there is a clear difference in the g_{xx} peak of the 541-TC sample, where differences in the radical or proton distribution due to inhomogeneities in the bulk sample would plausibly cause a shift in the g_{xx} peak (figure 5.3). It has been shown that the number of hydrogen bonds to the nitroxide moiety can shift the position of the g_{xx} peak and A_{zz}, where more hydrogen bonds shifts the g_{xx} peak to lower g-factors and smaller A_{zz}.[214,215] Thus, we speculate that the shift in the g_{xx} of 541-TC towards a lower magnetic field is caused by 541-TC having fewer average hydrogen bonds compared to the other three systems, where the observed shift of ~250 ppm is slightly larger than the loss of a single hydrogen bond – 205 ppm.[215] The difference in nitroxide-hydrogen bonds is likely due to differences in the mesoscopic structure of the glass caused by glass polymorphs; however, a rationale analysis of the hydrogen bonding network within the water/glycerol glass is outside the scope of this paper. Differences in A_{zz} could not be identified given inhomogeneous broadening of the spectra, and thus were not considered further. To determine if the change in 541-TC's g_{xx} is affected by inhomogeneities in the radical distribution, in addition to differences in the hydrogen bond network, the local electron spin concentration was evaluated for all four samples. One such method is the measurement of electron spin phase memory time, T_m, that is sensitive to the local electron spin concentration above a threshold radical concentration.[118]

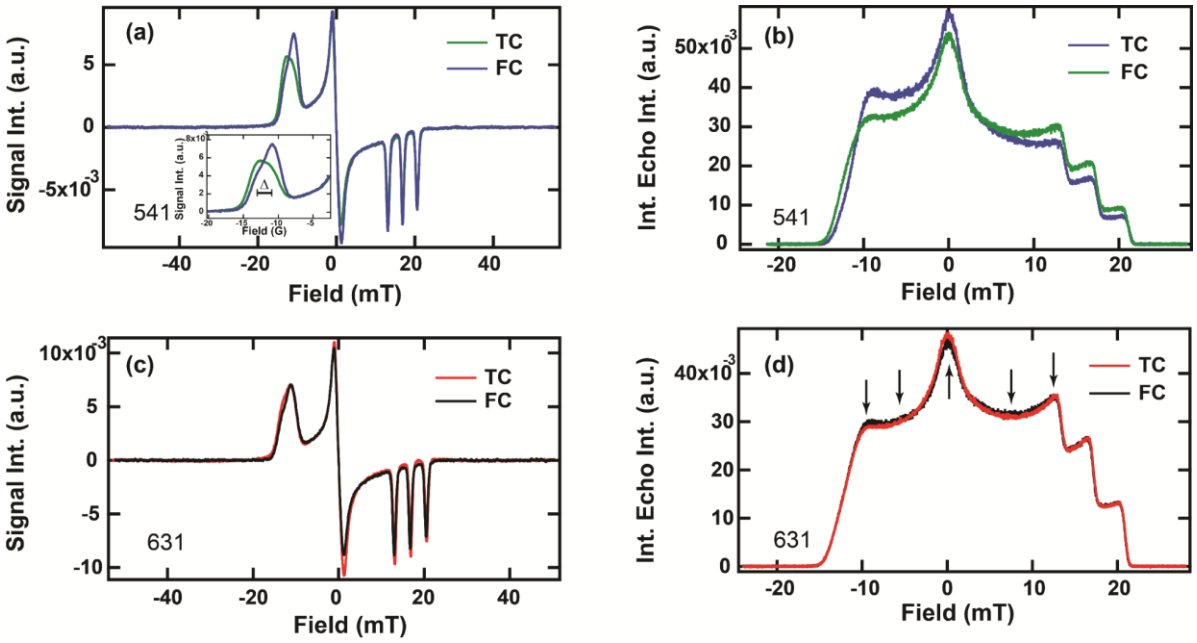

Figure 5.3. EPR lineshapes of 40 mM 4AT in 5:4:1 (a,b) and 6:3:1 (c,d) d_8-gylcerol:D_2O:H_2O at 8.56 T and 4.5 K. cw-EPR (a,c) and field swept echos (b,d) are shown for both freezing conditions: fast cool (FC) and thermally controlled (TC). The inset in (a) shows the shift in g_{xx} annotated by Δ, corresponding to 250 ppm, where g_{xx} shifts from 2.00839 to 2.00787. All spectra have been normalized to the double integral. The arrows in (d) are to show the relative position of the T_m measurements in figure 5.5.

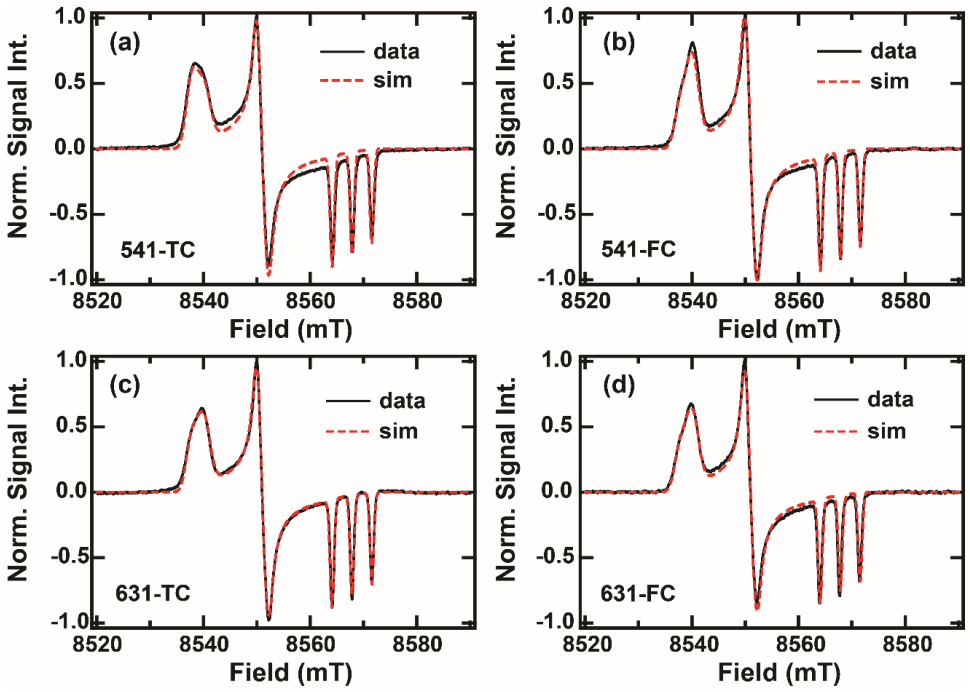

Figure 5.4. Simulated cw-EPR spectra (red-dashed) of 40 mM 4-amino TEMPO for the four systems are compared to the experimental spectra (black-solid) at 8.5 T. The weighting of the two components for the simulations are shown in table 5.2 with the other simulation parameters.

Table 5.2. Relative populations of the two components for the simulated cw-EPR spectra for each of the four systems. Parameters for EasySpin simulations are the following: S=1/2, nucleus = ^{14}N, g_{yy} = 2.00527, g_{zz} = 2.001375, A = [18 18 105], g_{Strain} = [0.00032 0 0], A_{Strain} = [4 0 0], H_{Strain} = [40 40 20], lw = 0.5, $\nu_{\mu w}$= 240 GHz, temperature = 4.5 K, and method = matrix.

Sample	% of population	
	Low field (g_{xx}=2.00839)	High field (g_{xx}=2.00787)
541-TC	55	44
541-FC	33	67
631-TC	44	56
631-FC	37	63

T_m was measured at five points across the EPR line (see arrows in figure 5.3d) for the different solvent compositions and freezing histories to get an overview of the local radical distributions for the entire EPR line, as T_m is sensitive to the local electron concentration. T_m

measured across the EPR line accounts for distortions in the EPR spectra due to differing relaxation effects that becomes more anisotropic at high magnetic fields [216]. At 8.56 T, the T_m was found to be approximately 9.5 µs across the whole EPR line for the 631-FC, 631-TC, and 541-FC samples (figure 5.5a). The 541-TC sample had distinctly shorter T_m values across the EPR line, as well as the largest anisotropy, with the shortest value of T_m, ~7.5 µs, found at the center of the EPR spectrum. T_m was also measured at 7 T to see if the trend at these two fields are consistent, and thus determine whether EPR data at 8.56 T can be used to rationalize DNP data at 7 T. To compare the T_m data at the two fields, the data was acquired at the same relative positions along the EPR line for both fields. At 7 T, 541-FC, 631-FC, and 631-TC yield slightly smaller average T_m values compared to at 8.56 T, while 541-TC has distinctly shorter T_m (figure 5.5b). However, at 7 T all T_m values were somewhat dependent on the EPR frequency, which could be due to experimental data being fit with a bi-exponential curve ($y = Aexp^{-2t/T_{m1}} + Bexp^{-2t/T_{m2}} + C$, where C is a constant, T_{m2} is very short (<500 ns) and T_{m1} is reported) to extract the T_m time constant compared to a stretched exponential fit for the T_m measurements taken at 8.56 T ($y = Aexp\left(-\left(2t/T\right)^x\right) + C$, where C is a constant, $x = 3/2$, and the T_m reported in the main text is the average decay rate, given by $T_m = \Gamma\left(1 + 1/x\right)T \approx 0.90T$).[217] The reason for the different fits at the two magnetic fields is due to the different dead times for the two spectrometers, where the dead time at 7 T is ~ 300 ns due to incorporation of phase cycling, while the dead time at 8.56 T is ~2 µs without phase cycling. T_m is expected to lengthen with decreasing magnetic field strength, as was observed.[216] Since similar trends in T_m are observed at 7 T and 8.56 T, the EPR lineshape analysis completed at 8.56 T can be used to support the DNP results at 7 T. The similar T_m values for 631-TC, 631-FC, and 541-FC across the entire EPR line for both magnetic fields

suggest that relaxation effects did not distort the EPR spectra. The congruence between these three samples at each position implies that the average local radical distribution for each system is similar, and thus glasses with similar radical heterogeneity are formed.[218] The anisotropy observed for the 541-TC system suggests a heterogeneous glass was formed, since different glass types can alter relaxation rates.[219] Analysis of T_m can be taken a step further as stated by Edwards et al, who show that the temperature dependence of T_m below the Zeeman temperature – here 9.7 K – is modulated by the electron flip-flop rate above a threshold radical concentration (~1 mM).[118] This electron flip-flop rate is dependent on the electron-electron dipolar interactions between the non-irradiated electron spins, which follow an r^3 dependence.[118] The radical concentration is extracted based on the average inter-radical distance for a given concentration. Therefore, longer T_m values correlate to shorter electron flip-flop rates and longer average distances between nearest neighboring radicals.[118] Thus, the finding that the 541-TC system at 4 K yields shorter T_m values across the entire EPR line at 7 T and 8.56 T, specifically around the center of the EPR line, where the electron spin population is greatest, implies the presence of regions with higher effective radical concentrations compared to the other three systems.[118] In other words, the radicals in the 541-TC system are clustering, resulting in a more heterogeneous radical distribution than in the other three samples, which is likely caused by 541-TC forming different glass polymorphs.

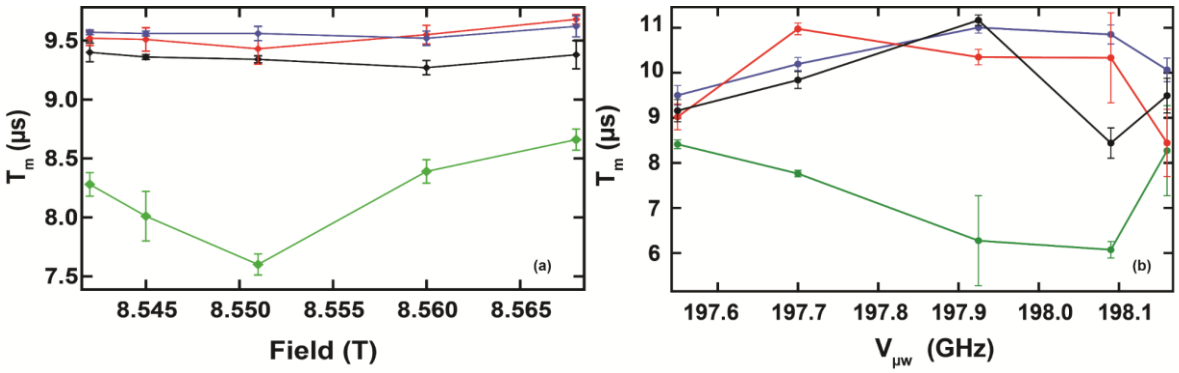

Figure 5.5. T_m was plotted as a function of the relative position along the EPR line as indicated in figure 5.3d for the different freezing conditions and model solutions of 40 mM 4AT as defined by the color code inside the plot, where (a) indicates T_m measured at 4.5 K and at 8.56 T (240 GHz) and (b) indicates T_m measured at 4 K and at 7 T (198 GHz). Lines are drawn to guide the eye.

5.1.1.3. DNP performance and consistency

The effect of glass polymorphism on the DNP performance was examined through the maximum NMR signal enhancement ($\varepsilon_{60}=S_{on,60}/S_{off,eq}$) and the DNP spectra—DNP enhancement as a function of the µw irradiation frequency. DNP spectra were taken in triplicates to compare the average enhancements in the different glassy matrices of the samples. Their consistency over multiple days is shown as error bars in figure 5.6. The 631-FC and 631-TC DNP spectra are similar to each other, with the measurable NMR signal enhancements occurring within the frequency span of the allowed EPR transitions and a peak-to-peak frequency difference of ~400 MHz. The 631-FC DNP spectrum is slightly broader than the 631-TC spectrum. The 541-TC spectrum differed significantly from the 541-FC spectrum with a broader spectrum near the baseline and a peak-to-peak frequency difference of ~500 MHz compared to the ~400 MHz of the 541-FC spectrum, as well as a ~ 20% smaller negative enhancement. In fact, the 541-TC sample displayed such large variations in the day-to-day signal enhancements that I cannot conclude whether the 541-TC yields larger or

smaller enhancements relative to 541-FC sample, even after comparing more than six data sets, where ε_{60} ranged from 40 to 210. The ε_{60} were determined in reference to steady state NMR signal without μw irradiation, where T_{1n} was assumed to be the same for all systems as the global radical concentration is the same. This effectively means that all ε_{60} were scaled equally, but it does not account for any differences in nuclear relaxation rates due to radical clustering. The 631-TC sample showed the least day-to-day variability and yielded the largest overall ε_{60} by 15-20% relative to the 181 signal enhancement observed for 631-FC as noted in table 5.1, where the reported values are the average ε_{60} and the error represents the standard deviation of the day-to-day variation. The 631-FC sample was the second best in terms of yielding large and consistent signal enhancements. Even though the distribution of radicals between the 631-FC and 631-TC systems is similar according to T_m, and the overall glass property is similar according to the T_g from DSC, DNP studies illuminate the existence of heterogeneities even between 631 samples with different freezing histories, although simulated EPR spectra did hint at this. These results show that DNP is sensitive to the arrangement of the nuclear spins, as well as the electron spins in the glassy matrix as dictated by glass polymorphism, but differentiating between the different factors is beyond the scope of this study. It becomes clear that predicting DNP enhancement values is significantly more challenging than rationalizing the EPR lineshapes, T_m data, or the shape of the DNP profile, as explaining DNP enhancements will require an in-depth understanding of the entire nuclear and electron spin ensemble of the sample.[96] Notably, 631-TC yields the highest DNP enhancement but also the weakest EPR signal intensity and requires ~4 hours to freeze the sample, while 631-FC yields both good DNP enhancements and EPR echo intensities, and only takes ~2 hours to freeze the sample.

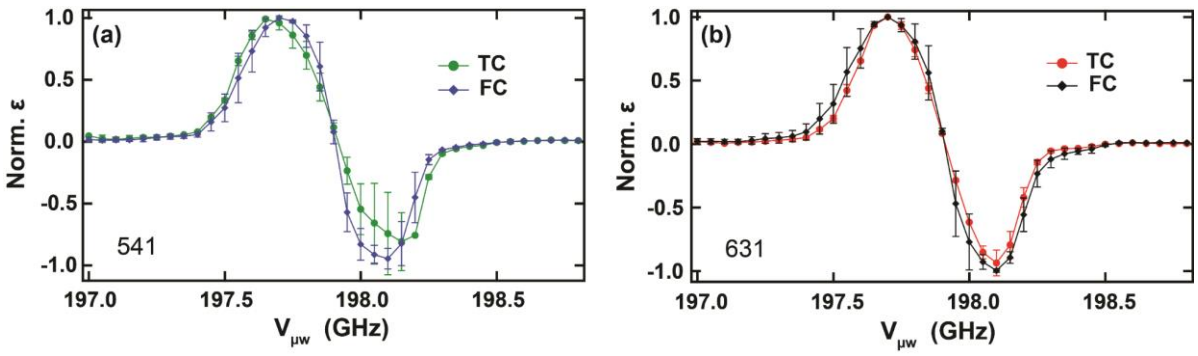

Figure 5.6. Normalized average DNP profiles comparing the freezing conditions (FC and TC) of 40 mM 4AT in 5:4:1 (a) and 6:3:1 (b) d_8-gylcerol:D_2O:H_2O taken at 7 T and 4K. All spectra were normalized to the maximum signal intensity and standard deviations are shown to indicate the variability from day-to-day for the triplicated datasets. Lines are drawn to guide the eye.

5.1.1.4. DNP mechanism confirms radical clustering

The variability of the 541-TC sample and the larger DNP signal enhancement found with the 631-TC sample is consistent with the TC freezing resulting in clustering of the radicals, which is partially mitigated by the 631-TC sample forming a better glass. In order to test this hypothesis, I evaluated a sample that contains a low radical concentration of 5 mM, where a homogeneous distribution of the radicals would yield an average inter-radical distance of 3.75 nm. A sample with this range of inter-radical separation should yield a distinct DNP spectrum and DNP power curve (DNP signal enhancement as a function of applied μw irradiation power) corresponding to the solid effect (SE) DNP mechanism. If radical clustering occurs during glass formation of the 541 solvent with a TC freezing history, then the DNP profiles of 5 mM 4AT should no longer be purely dominated by the SE. Indeed, the influence of the freezing history on the radical distribution in water/glycerol glasses can be observed in the DNP spectra of 5 mM 4AT with a 541 solvent composition. The 541-FC sample shows a

broader DNP spectrum near the baseline with a peak-to-peak DNP frequency of 450 MHz compared to 400 MHz observed for the 541-TC sample (figure 5.7a). Neither sample exhibits a classic SE DNP spectral lineshape; however, the differences in the DNP spectra are consistent with 541-FC having a larger SE contribution than that of the 541-TC sample.[43,96] (See section 4.2 for discussion on the effect of the DNP mechanism on the DNP spectra.) The larger CE contribution observed in the DNP spectrum of 541-TC shows that radical clustering must be present, effectively increasing the local radical concentration induced by glass polymorphism in the 541 solvent above the nominal 5 mM. This hypothesis is corroborated by the T_m measured for the 5 mM 4AT samples at 7 T to be 9.2 µs and 14.5 µs in the 541-TC and 541-FC samples, respectively. As discussed, the shorter T_m for TC implies a higher local radical concentration compared to FC. The DNP power curves show that the 541-TC yielded larger signal enhancements than the 541-FC sample (figure 5.7b). This is consistent with the hypothesis of radical clustering and glass polymorphism occurring in 541-TC, given that the CE is more efficient than the SE in polarizing nuclei, which results in larger signal enhancements.[43,96]

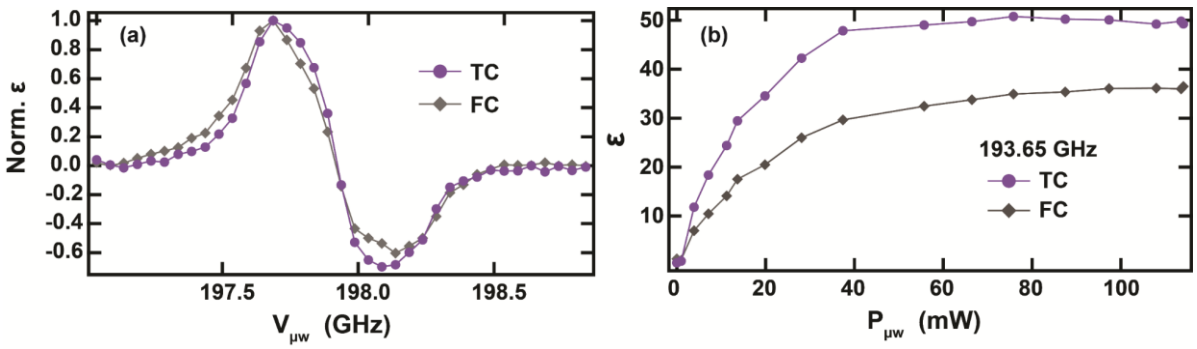

Figure 5.7. Normalized DNP profiles comparing the freezing conditions (FC and TC) of 5 mM 4AT in 5:4:1 (a) and the power curves of the same sample obtained at 193.65 GHz of μw irradiation (b) at 4 K and 6.95 T. The DNP profiles were normalized to the maximum of the signal intensity and the frequency was scaled by 4 GHz to represent data acquired at 7 T for comparison to the rest of the data presented here. Lines are drawn to guide the eye.

5.1.2. Summary of polymorphism induced heterogeneity

The analysis of DSC, EPR lineshape, T_m, and DNP spectral data shows that water/glycerol glasses with < 60 %v/v of glycerol are prone to solvent polymorphism upon freezing below 150 K that affect the performance and reproducibility of the resulting DNP and EPR data. We provide a mechanistic basis for why the 631 solvent provides more consistent DNP performance from day-to-day by minimizing glass polymorphism, relatively independent of the freezing method. The TC freezing method for 631 resulted in a 15-20% (when considering day-to-day variations) improvement on ^{1}H signal enhancement by DNP for our model system at 4 K, due to a slight increase in the local radical concentration, even though this was not detectable by T_m. The TC freezing method may be beneficial for some systems where every feasible improvement on signal enhancement is necessary or desired. If maximal signal enhancement is not necessary, then a faster cooling method, such as FC is recommended to save experimental time. Although some users prepare samples via rapid

quenching in liquid nitrogen, which should improve the quality of the glass formed, not all sample or hardware systems are compatible with this vitrification method.

The consistency between the EPR lineshape, T_m, and DNP results shows that EPR is a critical evaluation metric for DNP, where variation in DNP performance can be understood and rationalized by EPR analyses, however only to a certain degree. The residual day-to-day variation, with larger variations observed for the 541 solvent composition, is a function of the freezing/thermal histories of each sample. Although the 541 solvent has a propensity to form glass polymorphs, the freezing method will determine the degree to which polymorphism and radical heterogeneity occurs. Thus, we reiterate the importance of the solvent thermal history, which can induce greater polymorphism, especially if the glycerol content in a water/glycerol glass is ≤ 55%, as in 541, and/or is combined with thermal annealing, as defined by TC in this study. Perhaps not surprisingly, the empirically optimized and widely used solvent for cryogenic DNP, DNP juice™, has glycerol content of 60%, which provides the most reproducible DNP and EPR results independent of freezing history.[220,221] For all that the 631 solvent yields consistent EPR spectra, T_m, and DNP spectral lineshapes, consistent day-to-day DNP signal enhancement persists as the hardest parameter to achieve. This is because the spatial arrangement of the *entir*e electron and nuclear spin ensemble of the sample contributes to the DNP performance that may show variation, even if globally and qualitatively comparable glasses are formed. Thus, there is still significant development efforts needed to rationalize and predict the complete DNP performance.

5.2. Radical propensity to cluster: the case study of trityl

Besides the freezing method and polymorphic glasses forming radical heterogeneity and clusters, the radical type can also influence the formation of radical clusters. Here we will

focus on another radical type besides nitroxide-based radicals: tetrathiatriarylmethyl (TAM) radicals, where trityl (OX063) is the most commonly used one for DNP applications. The structure of the trityl OX063 is shown in figure 5.8. In TAM radicals, the unpaired electron is associated with a carbon atom, resulting in a narrow-line radical with the center of the electron spin spectral density at a g-factor of 2.003, which corresponds to 193.6 GHz at our magnetic field, and with the spectral density spanning ~200 MHz. The aromatic rings with their bulky substituents can form a propeller like structure around the radical moiety. This is advantageous for DNP, because it physically separates the unpaired electron from potential nuclei to be hyperpolarized; thus, reducing paramagnetic bleaching effects on the nuclei of interest. Trityl is typically used in dissolution DNP (dDNP) experiments with concentrations ranging from 15-60 mM at 1-4 K and at 3.35 – 7 T.[30,222–224]

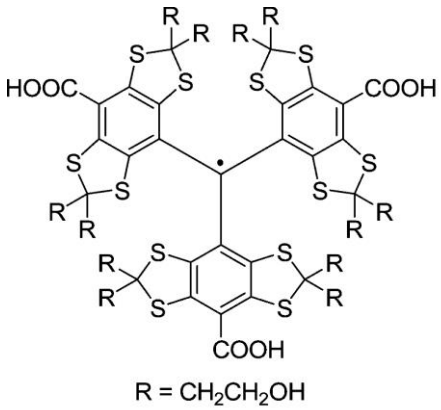

Figure 5.8. Schematic of the trityl OX063 chemical structure.

5.2.1. High trityl concentrations

For dDNP operation, trityl is routinely used at >15 mM concentrations and was originally assumed to be homogeneously distributed in the solvent as monomers.[225] However, trityl has been reported to cluster at > 1 mM concentrations in aqueous solutions.[226,227] This is significantly lower than what is typically used for DNP; therefore, the assumption that trityl is monotonic under DNP conditions is not valid. Trityl was found to form dimers, trimers, and other higher order species as the trityl concentration was increased, though monomeric trityl is still present in the liquid or frozen sample.[228] The authors suggest that the formation of trityl trimers seem to be the most stable, where stacking of the aromatic rings is the primary interaction forming these supramolecular structures.[228,229] These trimers (and dimers) will act as fast relaxing species that will increase the overall rate of nuclear hyperpolarization build-up.[230] However, the difficulty of depolarizing trimers with μw irradiation for efficient e-n polarization transfers will decrease the absolute value of possible nuclear hyperpolarization achievable for the system. As DNP performance is a combination of maximal achievable nuclear hyperpolarization in as short of a time possible, then a balancing act must be maintained between the formation of dimers and trimers and monomeric trityl.

The electronic properties of the OX063 trityl radical with 1 M urea in 6:3:1 d_8-glycerol:D_2O:H_2O at 10 K were investigated to confirm these literature results and to identify how the freezing methods available to the instrumental design presented in chapter 2 will affect the formation and presence of trityl radical clusters. This is an important designation, since the literature reported only on samples of trityl in aqueous solution that were flash frozen with liquid nitrogen. The experimental electron spin-lattice relaxation data was fit with a bi-exponential, where the fast-relaxing component was assigned to the cross-relaxation time, T_{cx},

that directly causes relaxation between the electron spin polarization and the phonons of the lattice generally via a direct one-to-one process or an Orbach-Aminov process. The slow relaxing component was assigned as the spin diffusion mediated relaxation time, T_{sd}. Here the electron spins spin diffuse via polarization conserving spin flip-flops until a fast-relaxing center can be reached, where the polarization is relaxed via interactions with the lattice phonons.[231] These time constants are reported in table 5.3. The traditional time constant for spin-lattice relaxation, T_{1e}, is typically reported as the slower time constant used here – i.e. T_{sd}. We see that as the trityl radical concentration is increased T_{sd} and T_{cx} become shorter, indicating that these processes are faster. The 2-fold larger increase of T_{cx} compared to T_{sd} between 40 mM and 10 mM trityl samples suggests more multimeric trityl complexes are present in the 40 mM sample (i.e. more trityl clusters are present at higher trityl concentrations). The overall 2-fold increase in local trityl *e-e* interactions with higher trityl concentrations between 10 mM and 40 mM is confirmed by the phase memory time, T_m, which is a measure of the local electron spin concentration.[118]

Table 5.3. Electron relaxation time constants for 10 and 40 mM trityl (OX063) with 1 M urea in 6:3:1 d_8-glycerol:D_2O:H_2O at 10 K.

[Trityl]	T_{sd} (ms)	T_{cx} (ms)	T_m (µs)
10 mM	146.3 ± 3.4	26.1 ± 1.4	2.42 ± 0.02
40 mM	84.8 ± 0.4	1.38 ± 0.05	1.61 ± 0.01

The electron relaxation properties of trityl as a function of concentration were also analyzed via ELDOR. The resulting electron spin depolarization profiles for the 10 mM and 40 mM trityl samples at 10 K are shown in figure 5.9. From these profiles, we see that the 40 mM sample has broader electron spin depolarization profiles, indicating more electron spectral diffusion and a stronger e-e interaction network. The allowed EPR transition ($\nu_{detect}=\nu_{excite}$) is annotated as 1 in figure 5.9, while the sharp peak located symmetrically 45.1 MHz from the allowed transition is assigned to the e-^{1}H forbidden transition resulting from hyperfine interactions between the electron spin and ^{1}H nuclei and is annotated as 2. The sharp peaks symmetrically located 17.1 MHz away from the allowed transition (annotated by 3) do not correspond to any possible hyperfine coupled nuclei to the electron spins. However, Marin-Montesinos et al suggest that these peaks could be attributed to well-defined e-e distances that result from multimeric trityl complexes.[228] This provides evidence that clusters of trityl radicals do form under the slower freezing conditions utilized by the 194 GHz dual DNP/EPR system at UCSB.

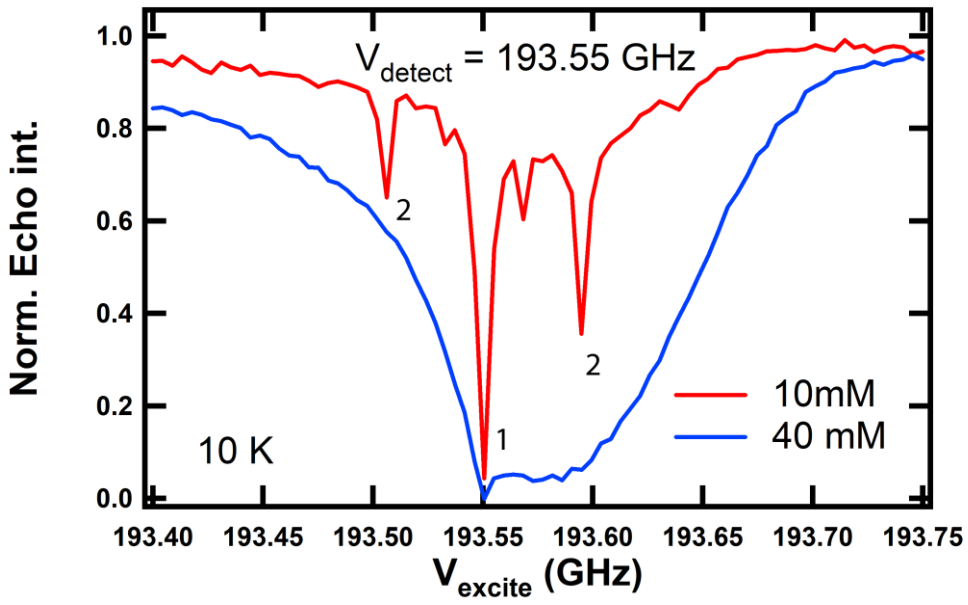

Figure 5.9. Electron depolarization profiles for 10 mM (red) and 40 mM (blue) trityl with 1 M Urea in 6:3:1 d_8-glycerol:D_2O:H_2O at 10 and at 7 T. The allowed EPR transition ($\nu_{detect} = \nu_{excite}$) is annotated by 1, while the forbidden hyperfine transitions for ^1H are annotated by 1. Experimental parameters: ν_{detect} = 193.55 GHz, t_{sat} = 100 ms, t_p = 750 ns, τ = 500 ns, t_d = 10 μs, recycle delay = 500 ms.

5.2.2. Addition of Gd-containing complexes

The current focus of dDNP research is two-fold i) applications towards *in vivo* metabolic imaging and spectroscopy of hyperpolarized [1-^{13}C]-pyruvate and its metabolites[232–235] and ii) improving DNP ε and shortening DNP build-up times.[17,236–238] Both research endeavors predominantly uses trityl radicals due to their excellent stability under biological conditions. The commercially available dDNP instrument developed by GE Healthcare for clinical applications operates at 5 T; however, higher magnetic fields would benefit from increased electron spin polarization. The challenge presented by higher magnetic fields is the significantly slower hyperpolarization build-up rates at ≥ 4.6 T,[239–243] especially for low-γ nuclei. These long DNP build-up rates become the primary constraint for experiments at

higher fields.[244,245] Attempts to mitigate the long hyperpolarization build-up time in dDNP include gating of the μw prior to NMR acquisition, μw frequency modulation, and cyclic polarization transfers between heteronuclei, with varying success.[17,238,246] Additionally, fast relaxing lanthanides have been used successfully to enhance the electron spin relaxation rate in low concentrations and nuclear relaxation rates at higher concentrations.[66,223,247,248] The exact boosting or inhibiting effects of lanthanide chelates on electron and nuclear relaxation rates is dependent on the lanthanide and chelate used, where gadolinium has the least impact on the nuclear relaxation rates, but results in the largest boost to DNP ε – by up to 4-fold.[30,223,247,249,250]

In this section, we show that by adding a high-spin $S = 7/2$ gadolinium-based endohedral metallofulleren (EMF) derivative, $Gd_3N@C_{80}$[DiPEG2000$(OH)_x$], where the three gadolinium spins are weakly coupled,[251] to a mixture of 15 mM trityl (OX063) and [1-^{13}C]-pyruvate, the ^{13}C nuclear hyperpolarization was increased up to 9-fold at 7 T and 4 K. This water-soluble derivative of $Gd_3N@C_{80}$[252] is an effective electron spin relaxation agent that causes broadening of the trityl radicals' electron spectral density, which we attribute induces the boosting effect to the DNP enhancement. We will also evaluate the effect the $Gd_3N@C_{80}$ complex has on nuclear and electron relaxation rates.

The impact of the $Gd_3N@C_{80}$ complex on DNP performance was investigated at 4 K and at 7 T for a sample of 15 mM trityl OX63 (GE Healthcare) in ^{13}C-1-pyruvic acid (Cambridge Isotopes). Three concentrations of the $Gd_3N@C_{80}$ complex were studied – 0 mM, 2 mM, and 4 mM, where 0 mM $Gd_3N@C_{80}$ complex acts as a control. The nuclear and electron spin relaxation rates and the enhancement factors for the three systems are shown in tables 5.4 and table 5.5, respectively. The equilibrium enhancements, ε_{eq}, were determined by comparing

extracted NMR signal intensities from T_{1n} (μw off) and T_{DNP} (μw on) build-up curves ($S_{\mu w\ on}/S_{\mu w\ off}$) for 0 mM, 2 mM, and 4 mM $Gd_3N@C_{80}$ complex, which were found to be 10.6, 93.7, and 25.8, respectively. This results in a 9-fold improvement in ε_{eq} with the addition of 2 mM $Gd_3N@C_{80}$ complex, while the 4 mM $Gd_3N@C_{80}$ complex only has a 2-fold improvement compared to the trityl only sample! This out-performs any previously reported boosting effects to DNP ε with the addition of gadolinium. It should be noted that although the trityl control does have lower than anticipated DNP ε compared to literature at 4 K and at 7 T, a similar lower than anticipated DNP ε is observed at 3.4 K, which allows for direct comparison to literature.[243] We attribute this difference in DNP ε for the trityl control, as being a function of our experimental design and set-up. However, from these 3.4 K results, we find that the boosting effect of the $Gd_3N@C_{80}$ complex is consistently large, such that 2 mM $Gd_3N@C_{80}$ complex continues to produce a 25-fold increase in DNP ε at 3.4 K and at 7 T. The decrease in the DNP ε boosting effects by using 4 mM instead of 2 mM $Gd_3N@C_{80}$ complex can be better understood via the electron and nuclear relaxation rates.

The nuclear spin lattice relaxation time, T_{1n}, did not significantly shorten with the addition of 2 mM $Gd_3N@C_{80}$ complex compared to the control; however, with 4 mM $Gd_3N@C_{80}$ complex, the T_{1n} is reduced by ~70%. On the other hand, the DNP build-up time, T_{DNP}, was reduced with the addition of 2 mM $Gd_3N@C_{80}$ complex by 33% compared to the control, while T_{DNP} for the 4 mM $Gd_3N@C_{80}$ complex sample is reduced by ~50%. The significant reduction in nuclear relaxation rates when doubling the concentration of the $Gd_3N@C_{80}$ complex is likely induced by three processes: i) paramagnetic relaxation enhancement (PRE) effects due to the addition of a high spin-7/2 system, ii) faster electron spin relaxation rates, which decreases the timeframe during which *e*-*n* polarization transfers

can occur, and iii) the $Gd_3N@C_{80}$ forming large aggregates, which inhibits the boosting effect of the complex on trityl DNP performance. Although PRE effects were developed specifically for T_{1n}, PRE effects will affect both the T_{1n} and T_{DNP}, since T_{DNP} is considered the reverse process to T_{1n}.[253] The electron spin lattice relaxation time, T_{1e}, was extracted by fitting the electron echo intensity as a function of the inter-pulse delay between saturation and detection pulses to a bi-exponential, where the long and short components were assigned as T_{sd} and T_{cx}, respectively, as described in section 5.2.1. T_{sd} decreases with increasing $Gd_3N@C_{80}$ concentration, while T_{cx} is essentially the same as long as the $Gd_3N@C_{80}$ complex is present in the sample, which suggests that the fast-relaxing center that directly dissipates the electron spin polarization to the lattice is the $Gd_3N@C_{80}$ complex. The relatively long T_{cx} for the trityl only sample compared to the T_{cx} for 10 and 40 mM trityl presented in section 5.2.1 suggests that trityl forms less clustered species with pyruvic acid as a solvent compared to an aqueous-based solvent. The electron spin phase memory time, T_m, which can be a measure of the local electron spin concentration, decreases slightly when the $Gd_3N@C_{80}$ complex's is added. This suggests that the overall local electron spin concentration has not drastically changed by adding $Gd_3N@C_{80}$. Although doubling the $Gd_3N@C_{80}$ concentration reduces T_m by 3-fold, which we attributed to the total number of electron spins in the sample is increasing and that the higher $Gd_3N@C_{80}$ concentration is inducing the $Gd_3N@C_{80}$ complex to form of large aggregates.

Table 5.4. Average nuclear relaxation rates and DNP signal enhancement at 60 s of μw irradiation and at steady state are listed here for 15 mM trityl with 0 mM, 2 mM, and 4 mM $Gd_3N@C_{80}$ complex in ^{13}C-pyruvic acid at 4 K and at 7 T.

Sample	T_{1n} (s)	T_{DNP} (s)	$\varepsilon_{60}/\varepsilon_{eq}$
15 mM trityl + 0 mM Gd^{3+}	2492 ± 174	1144 ± 42	76.1 / 10.6
15 mM trityl + 2 mM Gd_3	2489 ± 138	771 ± 51	297.7 / 93.7
15 mM trityl + 4 mM Gd_3	760 ± 192	576 ± 172	33.1 / 25.8

Table 5.5. Average electron spin relaxation are listed here for 15 mM trityl with 0 mM, 2 mM, and 4 mM $Gd_3N@C_{80}$ complex in ^{13}C-pyruvic acid at 4 K and at 7 T.

Sample	T_{sd} (ms)	T_{cx} (ms)	T_m (μs)	Λ^{eSD} (μs_3)
15 mM trityl + 0 mM Gd^{3+}	118.9 ± 2.8	17.6 ± 0.9	3.30 ± 0.06	0.1
15 mM trityl + 2 mM Gd_3	64.0 ± 5.5	2.99 ± 0.25	3.14 ± 0.06	6.5
15 mM trityl + 4 mM Gd_3	33.7 ± 2.6	2.77 ± 0.15	2.61 ± 0.04	4

The DNP performance with the addition of the $Gd_3N@C_{80}$ complex was analyzed via the DNP profiles (enhancement as a function of $\nu_{\mu w}$) and the DNP power curves (enhancement as a function of $P_{\mu w}$). A schematic of the DNP pulse sequence is shown in the inset of figure 5.2b; this same sequence is used to acquire the nuclear relaxation rates, where $T_{build\text{-}up}$ is varied. DNP profiles broaden with the addition of $Gd_3N@C_{80}$ compared to the trityl control as shown in figure 5.10a. In the DNP power curves, the enhancement increases with increasing applied $P_{\mu w}$ until a plateau is reached at ~90 mW for the control sample; however, the addition of the $Gd_3N@C_{80}$ complex results in minor DNP oversaturation, where the DNP enhancement will decrease at $P_{\mu w}$ higher than some threshold $P_{\mu w}$. The 4 mM $Gd_3N@C_{80}$ complex has a lower threshold $P_{\mu w}$ for DNP oversaturation – 60 mW, compared to the 2 mM $Gd_3N@C_{80}$

complex sample – 70 mW. The presence of DNP oversaturation suggests that the electron spins in the sample can be sufficiently depolarized with the available $P_{\mu w}$ and that electron spectral diffusion must be present in the system.

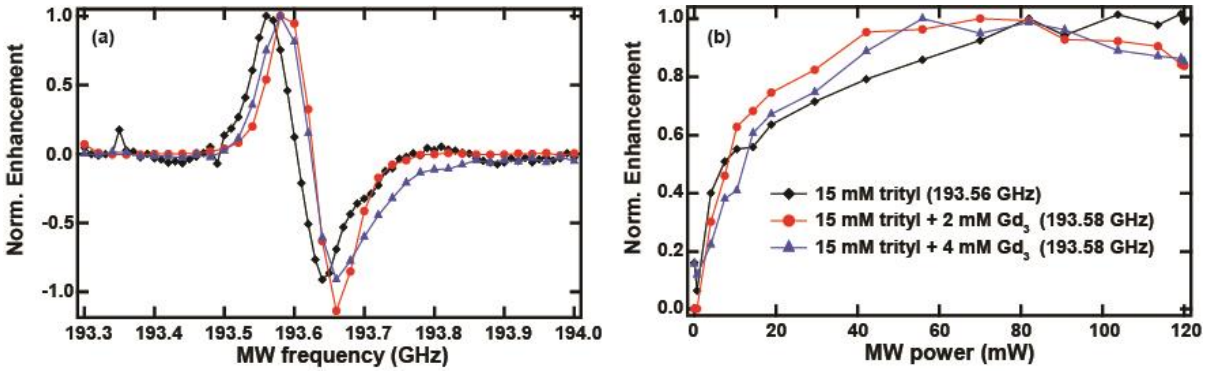

Figure 5.10. Normalized DNP profiles (a) and normalized DNP power dependent curves (b) for 15 mM trityl with 0 mM (black diamond), 2 mM (red circles), and 4 mM (blue triangles) $Gd_3N@C_{80}$ complex in ^{13}C-pyruvic acid at 4 K and at 7 T. Data was acquired after 60 s of μw irradiation.

We will now consider the electron spin spectral density and depolarization profiles, as these parameters can provide insight into the overall spin dynamics of the DNP process. The cw-EPR spectra and the electron spin depolarization profiles are presented in figure 5.11, with the ELDOR pulse sequence shown in the inset. The cw-EPR spectra were acquired on the 240 GHz EPR spectrometer at the National High Magnetic Field Laboratory, where only the trityl control and 2 mM $Gd_3N@C_{80}$ samples were acquired. The addition of the $Gd_3N@C_{80}$ complex broadens the trityl electron spectra density by 8 Gauss at the full-width-half-maximum of the EPR spectra. The electron spin depolarization profiles are similarly broader with the addition of the $Gd_3N@C_{80}$ complex. However, the 2 mM $Gd_3N@C_{80}$ electron spin depolarization profile is visibly broader than the sample containing 4 mM $Gd_3N@C_{80}$. The broader electron spectral density in the presence of $Gd_3N@C_{80}$ explains the broader DNP profiles and can

account for the significant boosting effects to the DNP ε. This is because the broader electron spectral density allows for the CE DNP mechanism to be more effectively utilized for ^{13}C. CE DNP has limited opportunity for the trityl only sample because the trityl electron spectral linewidth is ~130 MHz, while the CE condition requires the electron spins be separated by 75 MHz. This means the highest electron spectral density – i.e. the center of the trityl line, cannot participate in CE DNP and thus can only contribute to the DNP ε via the SE. The addition of the $Gd_3N@C_{80}$ complex, which broadens the trityl electron spectral density, allows more trityl electron spins to participate in CE DNP – a more efficient hyperpolarization process compared to SE DNP due to the fact that allowed EPR transitions are utilized compared to forbidden transitions.

Simulations of the ELDOR profiles that account for all experimentally recorded electron and nuclear relaxation rates were completed to extract a phenomenological electron spectral diffusion (eSD) parameter, Λ^{eSD}, as has been previously described.[98] These Λ^{eSD} are shown in table 5.5, where the following simulation parameters were chosen: $A^{\pm}$=0.8 MHz and T_{2e}=5* T_m. The trityl control was found to have negligible eSD effects, which indicates that 15 mM trityl in pyruvic acid does not effectively cluster, as suggested by T_m. This is important to note since trityl has been found to easily cluster depending on the solvent and glassing agent chosen.[228,229] Λ^{eSD} increases with the addition of $Gd_3N@C_{80}$ complex to the sample. However, the reduction of Λ^{eSD} at higher $Gd_3N@C_{80}$ concentrations may be due to the significant reduction in the systems' T_{sd} and T_{cx}, where the eSD process must complete with these relaxation processes. If the electron spin relaxation processes are more efficient than eSD, then the extent of electron spin depolarization will be reduced and the amount of polarization that can be transferred from electron spins to nuclei will be reduced. This is because the

amount of polarization that can be transferred to nuclei is dependent on the polarization difference between the electron spins that meet the CE condition. In general, the increase in Λ^{eSD} in the presence of $Gd_3N@C_{80}$ suggests that the $Gd_3N@C_{80}$ complex may increase the ability of trityl to undergo eSD processes, since only the trityl electron spin depolarization is measured in these ELDOR profiles. The ability of trityl to utilize eSD will increase the system's overall DNP efficiency, by allowing ^{13}C CE DNP to be more accessible within the relatively narrow trityl electron spectral density. Additionally, the broadening of the trityl electron spectral density with $Gd_3N@C_{80}$ will increase the probability of CE DNP in the system, and thus boost the observed DNP ε. Finally, we have not considered the effect of the high spin state of the $Gd_3N@C_{80}$ complex (3 weakly coupled S=7/2), which could directly affect the CE DNP efficiency.

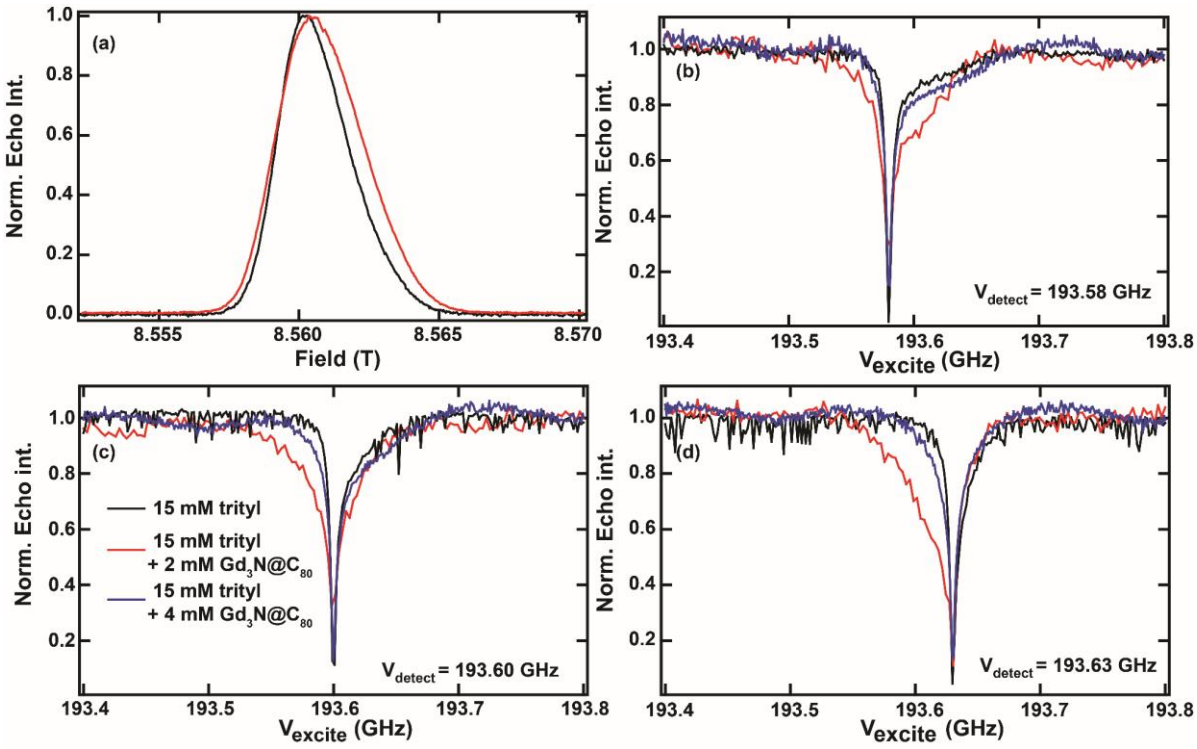

Figure 5.11. (a) Echo detected-EPR spectrum of 15 mM trityl with 0 mM (black) and 2 mM (red) $Gd_3N@C_{80}$ complex in ^{13}C-pyruvic acid at 8.57 T (240 GHz) and at 4.32 K. Electron depolarization profiles of 15 mM trityl with 0 mM (black), 2 mM (red), and 4 mM (blue) $Gd_3N@C_{80}$ complex in ^{13}C-pyruvic acid at 4 K and at 7 T at ν_{detect} = 193.58 GHz (b), 193.60 GHz (c), and 193.63 GHz (d). Experimental parameters for the EPR spectra are t_p = 1000 ns, τ = 800 ns, B_1=250 kHz, sweep rate = 0.05 mT/s, sweep range = 8.562-8.580 T, and repetition time = 3100 ns. Experimental parameters for the ELDOR profiles were t_{sat} = 100 ms, t_p = 750 ns, t_d = 10 μs, τ = 500 ns, and repetition time = 600 ms.

5.3. Summary of radical clustering

In this chapter we have shown that radical clustering and heterogeneity can occur through polymorphism of the glassy matrix and as an inherent property of the radical itself. The degree of radical heterogeneity and the formation of clusters is dependent on a multitude of factors such as the radical type and concentration, solvent, solute, added relaxing agents ($Gd_3N@C_{80}$ complex), and the freezing history. We found that by increasing the cryoprotectant concentration in water/glycerol glasses the degree of polymorphism decreased, resulting in

more consistent DNP ε from day-to-day. For trityl radicals, the formation of multimeric species was confirmed in aqueous solvents; however, their presence in pyruvic acid was greatly reduced. Finally, the addition of a $Gd_3N@C_{80}$ complex caused a surprising 25-fold improvement to DNP ε. It was through analysis of both the electron and nuclear spin dynamics that we can understand the clustering effect of radicals on DNP; however, a more systematic approach is necessary to extract the direct affect strong *e-e* interactions that result from clustering will have on DNP. The systematic analysis of *e-e* interactions on DNP in general and on nuclear spin relaxation rates specifically will be addressed in the next chapter.

6. EFFECT OF LOCAL RADICAL CONCENTRATION ON DNP AND SPIN RELAXATION RATES

In DNP, it is generally desired to have both maximal enhancement, ε, and fast build-up rates to maximize the NMR signal accumulated in the shortest time possible. To date designer bi-radicals have been synthesized with specific properties to increase *only* DNP ε via long T_{1e} and fixed orientations to maximize the CE efficiency.[44,220,254–256] However, the DNP build-up time should be an explicit design criterion for sample formulations. This is especially necessary for dDNP, where signal build-up can takes hours to maximally hyperpolarize a single sample,[257,258] and for MAS-DNP, where experimental time can be saved when signal averaging.[259] The *e*-*n* transfer rate reduces at high fields leading to a longer T_{DNP}, which becomes a limiting factor for high field DNP. The nuclear polarization build-up time constant in DNP (T_{DNP}) depends on a number of factors including the underlying DNP mechanism, strength of electron-nuclear (*e*-*n*) interactions,[260] nuclear spin-diffusion rates,[66] electron and nuclear relaxation rates,[13,261] and the applied μw bandwidth.[15] Pulsed DNP has been used to successfully shorten T_{DNP} under static conditions at low magnetic fields.[244,245] Other attempts to mitigate the long T_{DNP} in dDNP include gating of the μw prior to NMR acquisition, μw frequency modulation, and cyclic polarization transfers between heteronuclei, with varying success.[17,238,246] Additionally, the CE has faster build-up rates than the SE,[16,43] where the radical concentration modulates the effective DNP mechanism between SE and CE.[43,96] However, these studies assume a homogeneous radical distribution, while in reality the local radical concentration can vary significantly with the quality of the glassy matrix.[99] Therefore, the effect of the local radical concentration on the DNP mechanism and T_{DNP} needs to be evaluated.

Since T_{DNP} is seen as the reverse process of nuclear spin lattice relaxation, T_{1n},[253] the impact of paramagnetic relaxation enhancement (PRE) effects on nuclear relaxation processes must also be considered. PRE effects on T_{1n} have been extensively studied and utilized in NMR to determine structural constrains.[262–264] However, the existing PRE theories are valid under high temperature conditions where the *e-n* spin correlation time is very short, and the effect of electron-electron (*e-e*) interactions can be ignored.[80,81,265] Under DNP conditions both assumptions, short *e-n* correlation time and negligible *e-e* interactions, are invalid due to cryogenic temperatures and the presence of high radical concentrations that lead to strong *e-e* interactions. The electron longitudinal relaxation time, T_{1e}, is critical in determining the extent of PRE effects on T_{1n} under the high temperature condition.[266] The effect of *e-e* coupling on T_{1n} has been observed in crystals of copper Tutton salts[267,268]and in frozen solution of copper histidine;[269] however, the two presented mechanisms differ. Recently, the effect of μw irradiation on the PRE effect has been demonstrated experimentally under DNP conditions, but a complete theoretical understanding has yet to be developed.[100] This study indicates that *e-e* interactions, which are heavily influenced by the local radical concentration, play a significant role in determining T_{1n}, T_{2n}, and T_{DNP}. Therefore, a comprehensive analysis of the local radical concentration on T_{1n}, T_{DNP}, and ε is critical.

In this work, we experimentally analyze the role of *e-e* dipolar coupling on the DNP mechanism, T_{1n}, T_{DNP}, and ε using a series of radicals with a systematic increase in their local electron spin concentration (mono-radical, bi-radicals, tri-radical, and a dendrimer with 9 nitroxide moieties), while keeping the global electron spin concentration constant. The results unambiguously demonstrate that a significant shortening in both T_{1n} and T_{DNP} can be achieved by increasing the local electron spin concentration under both static and MAS conditions. This

can be used in the development of new designer radicals given the limiting effect T_{1n} and T_{DNP} will have on DNP as it is driven to higher and higher magnetic fields. We discuss the calculation of effective signal enhancement to compare the net sensitivity gain for systems having different T_{DNP}. From these we show that the dendrimer sample, with high local electron spin concentration, provides maximum sensitivity enhancement per unit time under the presented static DNP conditions. Finally, to explain the effect of a strong *e-e* coupling network on the DNP mechanism and its efficiency, we use electron double resonance (ELDOR) experiments to observe the effect of μw irradiation on electron spins.

6.1. Materials and Methods

4-amino TEMPO (4AT, Sigma-Aldrich), TOTAPOL (TOT, DyNuPol), AMUpol (AMU, CortecNet), DOTOPA-ethanol (DOT-et, provided by Tycko), HZ4_68-3 dendrimer (provided by Rajca), deuterium oxide (Cambridge Isotopes), and d_8-glycerol (Cambridge Isotopes) were used as received. DOT-et was synthesized according to Yau et al and is a tri-radical,[270] and the HZ4_68-3 dendrimer was synthesized according to Rajca et al,[271] consisting of a G3 dendrimer decorated with spirocycle-nitroxides and polyethylene glycol chains to increase water solubility. The dendritic radical has an average of 9-electron spins per radical according to spin counting at X-band. The structures for the radicals are shown in figure 6.1. Each nitroxide radical was dissolved in a stock solution of 6:3:1 by volume of d_8-glycerol : D_2O : H_2O and diluted to 10 mM electron spins, where the radical concentrations of 4AT was 10 mM, TOT and AMU were 5 mM, DOT-et was 3.33 mM, and HZ4_68-3 was 1.11 mM. Water was purified with a μ-Pure water system (Pure Power, Korea; 12.5 MΩ) prior to use. 40 μL of sample was pipetted into a cylindrical Teflon sample holder (6 mm i.d. and 7 mm height with 1 mm wall thickness) and was cooled to 4 K by continuous helium flow.

The hardware for static DNP and EPR based experiments were described in chapter 2, where all static DNP, NMR, and EPR experiments were conducted at 7 T and at 4 K.[110] MAS-DNP experiments were conducted on a Bruker 400 MHz ASCEND DNP-NMR spectrometer for solids at 92 K, where a 263 GHz gyrotron was the μw source, and a HNC probe was used for all data acquisitions. All static ^{1}H experiments were obtained with a saturation recovery pulse sequence followed by a 60 s delay and a solid echo detection (90x-t-90y), with the pulse sequence shown in the inset of figure 6.2b. Electron and nuclear relaxation rates were acquired and analyzed via the standard methods described in Appendix D. Electron spin depolarization profiles were measured via ELDOR. The pulse sequence for ELDOR experiments is shown in the inset of figure 6.7d. ELDOR experimental parameters were t_{sat} = 100 ms, t_p = 750 ns, τ = 500 ns, t_d = 10 μs, and a repetition time of 600 ms.

MAS DNP experiments utilized a saturation recovery pulse sequence followed by a standard cross polarization from ^{1}H to ^{13}C. MAS DNP experiments at 92 K were acquired with a saturation recovery pulse sequence followed by a standard CP (^{1}H to ^{13}C) pulse program. No attempts to optimize the CP condition were made for either the dendrimer or AMUpol samples. An 8 kHz spinning speed was used for MAS, while a 20 Hz rate was noted for the 'static' experiments at 92 K. The T_{1n}, T_{DNP}, and signal averaging experiments were acquired while spinning at 8 kHz. When signal averaging, a 2 sec build-up time was used with 150 scans for a total acquisition time of 5 min for both radical systems tested. For acquisition of nuclear relaxation times 8 scans were averaged together. The experimental parameters are the following: $t_p(^{1}H_{90})$ = 2.5 μs, t_p(CP) = 3 ms, $t_p(^{1}H_{decoupling})$ = 5.5 μs, P_{1H} = 29 W, and P_{13C} = 50 W.

6.2. Effects on DNP

The influence of local radical concentration effects on DNP were investigated by using radicals with differing number of electron spins per radical with the same global electron spin concentration. A global electron spin concentration of 10 mM was chosen to limit the strength of the inter-radical interactions for the radical with the highest radical concentration – the monoradical. The nitroxide-based radicals chosen for this study include a monoradical (10 mM 4-amino TEMPO (4AT)), a flexible and rigid bi-radical (5 mM TOTAPOL (TOT) and AMUpol (AMU), respectively), a tri-radical (3.33 mM DOTOPA-ethanol (DOT-et)), and a G3 dendrimer decorated with an average of 9 nitroxide moieties per radical (1.1 mM HZ4_68-3). The radicals are depicted in figure 6.1. As the biradicals were designed to have an intra-radical separation that favors CE DNP, the next nearest neighbor distributions for the different radicals were determined by equation 6.1 and are shown in figure 6.1:

$$w(r) = 4\pi r^2 C_r \, exp\left(-4\pi r^3 C_r/_3\right), \qquad (6.1)$$

where C_r is the radical concentration, $w(r)$ is the distribution of distances between nearest neighboring radicals, and r is the distance between radicals.[272] We can see from nearest neighbor distributions and the dashed line representing the ~1.3 nm distance between the electron spins on both TOT and AMU in figure 6.1 that the majority of radicals should be far enough apart to minimize inter-radical interactions. This enables the study of intra-radical interactions without significant influence from the inter-radical interactions.

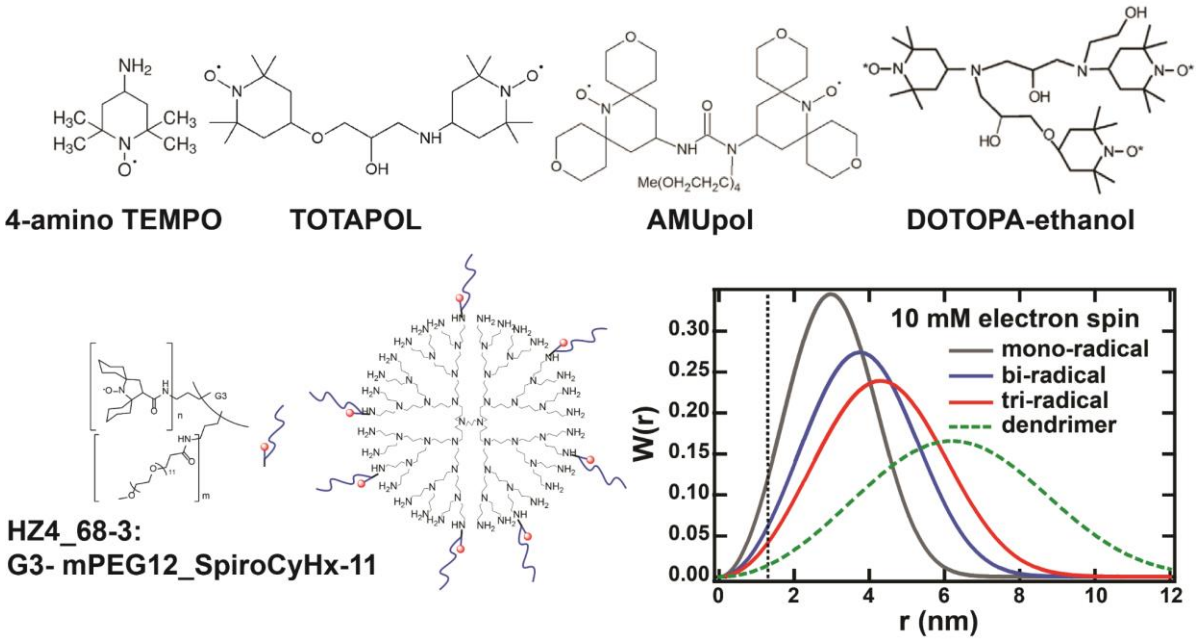

Figure 6.1. The radicals used in this study and their next nearest neighbor distributions. It was assumed the dendrimer had an average of 9 electron spins per radical from spin counting experiments at X-band, where 10 mM of electron spins would correspond to 1.11 mM dendritic radicals.

We start by examining the active DNP mechanisms for these 10 mM electron spin systems via line-shape analysis of the DNP profiles. In CE, the peak-to-peak distance (Δ_{DNP}) is less than $2\nu_n$ and the whole DNP profile falls within the range of the allowed EPR spectrum of the radical.[16,66,93] For the SE mechanism, the Δ_{DNP} is equal to $2\nu_n$, and the wings of the DNP profile extended beyond that of the allowed EPR spectrum.[67,189,273] A system with both CE and SE contributions will display attributes of both mechanisms in the DNP profile lineshape.[96]

In figure 6.2a, DNP profiles, using a build-up time ($t_{build\text{-}up}$) of 60 sec and $P_{\mu w}$ corresponding to the maximum ε from the DNP power curves in figure 6.2b, are shown to determine the mechanistic contributions for all of the radicals. The mono-radical, 4AT, has a Δ_{DNP} of 550 MHz, and the wings of the profile extended beyond the allowed EPR spectrum

(black trace, figure 6.2a), which is a manifestation of mixed SE and CE contributions. All the other radicals studied here have DNP profiles with primarily CE contributions, with a Δ_{DNP} of 450 MHz and the whole DNP profiles fits within the range of the allowed EPR spectrum. This means that the intra-radical *e-e* interactions were sufficient to achieve primarily CE DNP using radicals with 2 or more electron spins per radical. If the mono-radical had no inter-radical interactions the DNP profile should be solely influenced by the SE; however, the 4AT DNP profile has mixed SE and CE contributions, indicating inter-radical coupling. Note that since we have fixed the global electron spin concentration, an increase in the local electron spin concentration will decrease the strength of the inter-radical interactions, given the increase in the inter-radical distances (figure 6.1).

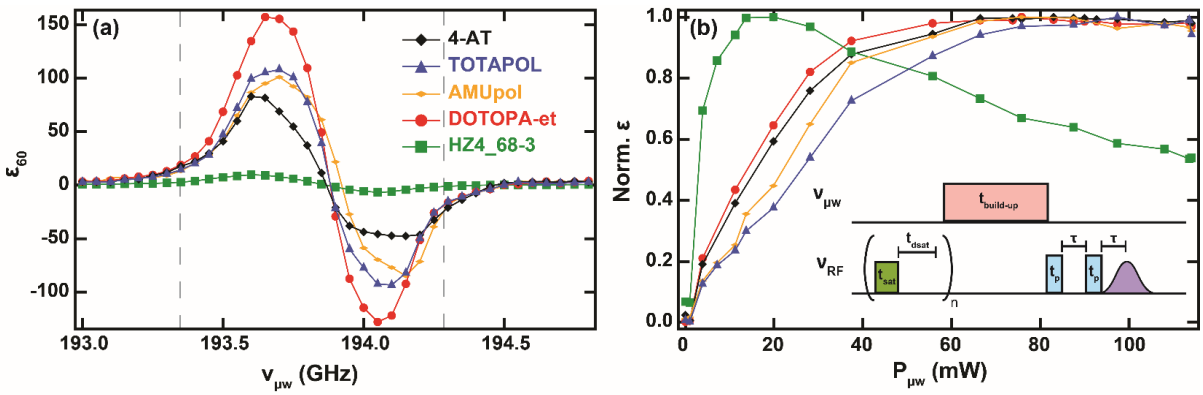

Figure 6.2. DNP profiles (a) and normalized DNP power curves (b) at 4K and at 7 T for 10 mM 4-amino TEMPO (black diamond), 5 mM TOTAPOL (blue triangle), 5 mM AMUpol (purple small diamond), 3.33 mM DOTOPA-ethanol (red circle), and 10 mM electron spin dendrimer (green square) in 6:3:1 d_8-glycerol:D_2O:H_2O. The dashed lines represent the width of the allowed EPR spectrum. The DNP power curves were acquired while irradiated at 193.65 GHz. All data was acquired with a saturation recovery solid echo pulse sequence as shown in the inset of (b) with t_p = 2.5 μs, τ = 110 μs, t_{sat} = 2.4 μs, t_{dsat} = 380 μs, n = 10, and $t_{build\text{-}up}$ = 60 s.

To compare the performances of the radicals at different $P_{\mu w}$, normalized DNP power curves with enhancements at 60 s of build-up, ε_{60}, and $\nu_{\mu w}$ selected for the positive maximal

condition are plotted in figure 6.2b. All of the radicals reach a plateau at around 65 mW of power except for the dendrimer. For the dendrimer, ε_{60} instead increases up to ~20 mW and decreases at higher $P_{\mu w}$, where ε_{60} was reduced by 45% when irradiating with 120 mW versus 20 mW. Such behavior is known as oversaturation, which has been observed for high global radical concentrations at very low temperatures, and was hypothesized to result from electron spectral diffusion (eSD) achieving beyond optimal electron spin depolarization, with experimental evidence proving this theory provided in section 4.3.2.[43] This suggests that the dendrimer has high intra-radical *e-e* coupling to cause effective eSD at much lower global electron spin concentrations, here 10 mM, than previously reported to cause oversaturation.

The optimal positive DNP enhancement with 60 s $t_{build\text{-}up}$, ε_{60}, are reported in table 6.1, and ε_{60} increases from the mono-radical, ~ 80, through the tri-radical, ~175. The dendrimer has lower DNP ε_{60} than even 4AT, ~18. To evaluate these results, we need to specify how DNP enhancement is defined. The z-component magnetization *without* and *with* μw irradiation at equilibrium is based off the classic Bloch equations according to equations 6.2 and 6.3 respectively, where equation 6.3 represents the typical T_{DNP} curve.

$$M_{z,off}(t) = M_{z,off_{eq}}\left[1 - e^{-t/T_{1n}}\right] \tag{6.2}$$

$$M_{z,on}(t) = \frac{M_{z,on_{eq}}}{M_{z,off_{eq}}}\left[1 - e^{-t/T_{DNP}}\right] \tag{6.3}$$

$M_{z,off_{eq}}$, $M_{z,on_{eq}}$, T_{1n}, and T_{DNP} are determined by fitting this equation to experimental data, where t is the $t_{build\text{-}up}$ (from the inset of figure 6.2b) and is varied *without* and *with* μw irradiation. Here we have assumed the magnetization at $t=0$ is zero in both the cases. We

derive $M_{z,off_{eq}}$, $M_{z,on_{eq}}$, and the equilibrium enhancement, i.e. $\varepsilon_{eq} = M_{z,on_{eq}}/M_{z,off_{eq}}$, values by fitting T_{1n} and T_{DNP} models to the experimental enhancement data.[274] We also report another common value, the enhancement at a specific $t_{build\text{-}up}$, ε_t, which is distinct from ε_{eq} and is defined by equation 6.4:

$$\varepsilon_t = \frac{M_{z,on_{eq}}\left[1-e^{-t/T_{DNP}}\right]}{M_{z,off_{eq}}\left[1-e^{-t/T_{1n}}\right]} \tag{6.4}$$

where the enhancement is relative to the off signal with the same $t_{build\text{-}up}$.[18] These different calculated enhancement terms for the 10 mM 4AT sample are shown as a function of $t_{build\text{-}up}$ in figure 6.3, where experimental values were used for T_{1n} and T_{DNP}. As ε_{eq} is a constant value, a horizontal line is depicted in figure 6.3. $M_{z,on}(t)$ and $M_{z,off}(t)$ rise exponentially as expected for T_{DNP} and T_{1n}, where the two traces plateau at $M_{z,on_{eq}}$ and $M_{z,off_{eq}}$ respectively. At long enough $t_{build\text{-}up}$'s, $M_{z,on}(t)$ should be equal to ε_{eq}, which occurs by 5000 s for 10 mM 4AT at 4 K. Finally, ε_t is shown to be very large at short $t_{build\text{-}up}$'s and decrease until ε_{eq} is reached with longer $t_{build\text{-}up}$'s, where ε_t takes four times longer to reach ε_{eq} than $M_{z,on}(t)$. This is due to the residual effects of non-equilibrium values of $M_{z,off}(t)$. Besides differences in sample formulations, care should be taken when comparing enhancement values from the literature because if the $t_{build\text{-}up}$ is short enough that ε_t does not equal ε_{eq}, then the reported values will be dependent on the system's T_{1n} and T_{DNP}.

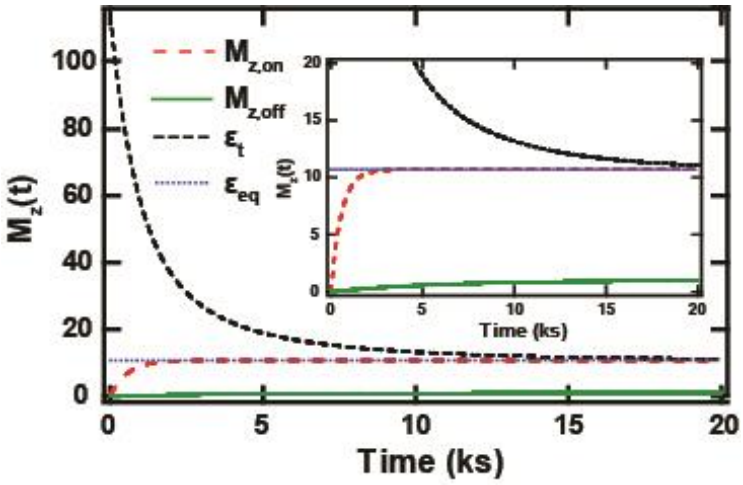

Figure 6.3. Simulated $M_z(t)$ with (red) and without (green) μw irradiation ($M_{z,on}$ and $M_{z,off}$) and the associated enhancement at each time, ε_t, (black) and at equilibrium, ε_{eq}, (blue) of 10 mM 4-amino TEMPO in 6:3:1 d_8-glycerol:D_2O:H_2O as a function of time at 4 K. $M_z(t)$ was simulated from $M_z(t)=M_{zeq}*[1-\exp(-t/T_x)]$, where T_x was 560 for T_{1n} and represents no μw irradiation and 5987 s for T_{DNP} represents DNP with μw irradiation. The values for T_{1n} and T_{DNP} were experimentally measured. The inset shows a zoom in of the y-axis.

The ε_t and ε_{eq} for the five radicals studied here are reported in table 6.1, and in general increase from mono- to tri-radical, but both decrease for the dendrimer. Oddly, TOT has the lowest ε_{eq}. The higher ε_{eq} of AMU is consistent with the literature, where more rigid radical architectures can provide higher DNP enhancement values.[275–280] The ε_t values are modulated by T_{1n} and T_{DNP}. The DNP performance between radicals with distinctly different T_{DNP} can be compared via the enhancement per unit time, $\varepsilon_T = \varepsilon_{eq}/\sqrt{T_{DNP}}$. ε_T increases with more electron spins per radical, such that the dendrimer provides the largest ε_T given its short T_{DNP} (table 6.1). This is relevant if signal averaging is employed, as the dendrimer system can outperform the other radicals studied here when delays < approximately 10-times the dendrimer T_{DNP} ~ 15 s are used. This is shown by calculating the resultant NMR signals for 1 hr and 120 sec total timeframes of signal averaging based on equation 6.4 (figure 6.4). As T_{1n} and T_{DNP} modulate DNP enhancement, the enhancement values themselves depend on the

radical, the electron spin concentration, the solvent, and the quality of the glassy matrix. This makes comparing enhancement values between different DNP systems challenging, and it must be carried out with care.

Table 6.1. Signal enhancement, TDNP and nuclear relaxation times for different radicals with 10 mM global concentration in DNP juice at 7 T magnetic field and 4 K temperature.

Sample	ε_{60} / ε_{eq}	T_{DNP} (s)	T_{1n} (s)*	ε_T
4AT	83 / 10.7	560.25 ± 10.1	5987.0 ± 172	0.45
TOTAPOL	117 / 7.6	287.95 ± 6.14	4511.6 ± 67.8	0.45
AMUpol	105 / 10.9	286.36 ± 2.78	2951.1 ± 34.6	0.64
DOTOPA-et	173 / 13.8	153.41 ± 5.67	3213.8 ± 129	1.11
HZ4_68-3	17.7 / 8.7	15.06 ± 0.23	106.26 ± 1.21	2.24

*T_{1n} of solvent only is 9789.5 $\pm$ 367 s

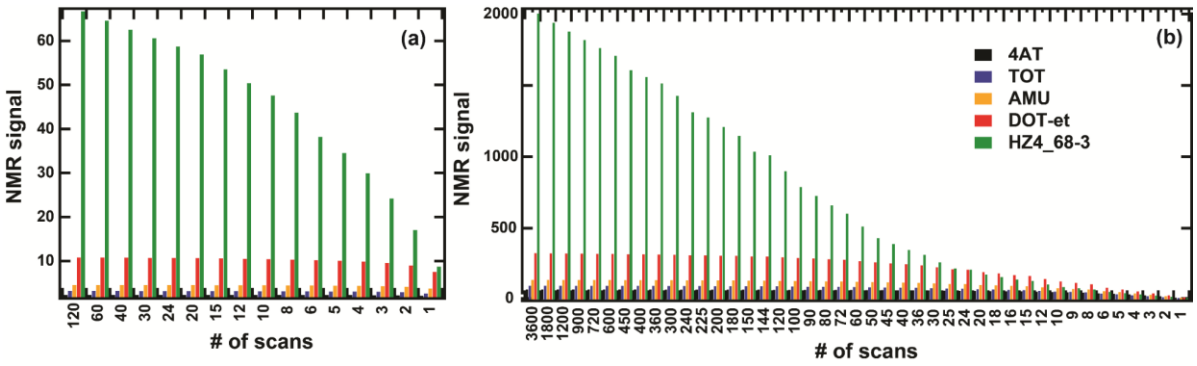

*Figure 6.4. Simulated NMR signal enhancements after signal averaging for a total timeframe of 120 sec (a) and 3600 sec (b), where the $t_{build\text{-}up}$*number of scans = total timeframe. Equation 6.4 was used and for this simulation with each radicals' respective ε_{eq} and T_{DNP}.*

6.3. Spin relaxation effects

As nuclear relaxation rates modulate DNP enhancement, specifically ε_T, we will now consider the effects that the local electron spin concentration have on both the nuclear and electron spin relaxation processes. We observe that T_{1n} and T_{DNP} both shorten with increasing

local electron spin concentrations – i.e. increasing *e-e* dipolar coupling, as shown in table 6.1 and figure 6.5. The dendrimer has 37-fold and 60-fold faster T_{1n} and T_{DNP} than the monomer (figure 6.5). However, it is not obvious why these time constants show such dramatic variation, given the constant global electron spin concentration. Interestingly, the T_{DNP} values of the two bi-radicals are comparable, but their T_{1n} values are distinctly different, which is attributed to differences in the rigidity of their underlying architecture.

In the presence of paramagnetic species, T_{1n} is thought to be dictated by PRE effects, which are assumed to be proportional to the electron spin concentration, where incoherent *e-n* fluctuations modulate T_{1n} relaxation. In existing PRE theories, the *e-e* interactions are typically not considered explicitly, as the PRE theory was originally developed for samples containing low concentrations of paramagnetic species at high temperatures.[81,262,265] As the global electron spin concentration is kept constant for all sample systems, the dramatic shortening of T_{1n} with increasing local electron spin concentration cannot be explained by existing PRE theories.[80,81,265]

The T_{DNP} value is dependent on the rate of polarization transfer from electron to nuclei and the nuclear spin diffusion rate, while the upper limit of T_{DNP} is T_{1n}.[253] At higher temperatures T_{DNP} is dominated by T_{1n}, and thus, T_{DNP} typically equals T_{1n} at > 20 K.[70] As T_{1n} is sufficiently long at < 10 K, the *e-n* polarization transfer and nuclear spin diffusion processes will determine the value of T_{DNP}. In light of this, we examine the observation that the T_{DNP} values of the two bi-radicals are comparable, but their T_{1n} values are distinctly different (table 6.1). As the same freezing procedure was used for all cases, we assume that differences in the glassy matrices are negligible, and thus the nuclear spin diffusion rates for all of the systems presented here are nominally the same. This suggests that the two bi-radicals, independent of

their conformational flexibility that alter their T_{1n} values, have similar *e-n* polarization transfer rates, as seen by their similar T_{DNP} values.

To understand the impact of *e-e* dipolar coupling on the T_{1n} and T_{DNP} times, it is important to analyze the DNP mechanism in greater detail. We showed earlier that CE DNP is active in all cases, with partial SE DNP observed only with the monoradical, 4AT, at 10 mM. In CE DNP, the polarization difference of two electron spins that meet the CE condition is transferred to a hyperfine coupled nuclear spin at the rate given by equation 6.5. The derivation of this equation is provided in Appendix F using average Hamiltonian theory and can also be found in literature using a slightly different approach as presented by Thankamony and coworkers:[260]

$$t_{en} \propto \frac{2\pi}{\Delta B\, s_\theta} \; or \; \frac{2\pi\omega_{0I}}{(B_{e_1 n} - B_{e_2 n})(d+2J)} \tag{6.5}$$

In other words, the *e-n* polarization transfer time depends on the nuclear Larmor frequency, ω_{0I}, *e-e* interactions strengths for both dipolar coupling, *d*, and J-coupling (through bond *e-e* interactions), *J*, and the difference of the hyperfine couplings between each of the two electron spins and the nuclear spin, $\Delta B = B_{e_1 n} - B_{e_2 n}$.[260] From this relation, it is clear that stronger *e-e* coupling leads to a faster *e-n* polarization transfer, t_{en}. Furthermore, if there are multiple electron spin pairs fulfilling the CE condition, then the effective DNP polarization transfer rate is a cumulative sum of these rates for each electron spin pair at the CE condition. Thus, at higher local and constant global electron spin concentration, the greater *e-e* coupling strength and the higher number of CE-fulfilling electron spin pairs will speed up the total *e-n*

polarization transfer in CE DNP and shorten T_{DNP}. However, it is important to note that the *e-n* polarization transfer is also scaled by κ,

$$\kappa = \frac{\Omega_{S_1} - \Omega_{S_2}}{\sqrt{(d+2J)^2 + \left(\Omega_{S_1} - \Omega_{S_2}\right)^2}} \tag{6.6}$$

where Ω_S is the electron spin g-anisotropy, d is the *e-e* dipolar interaction strength, and J is the *e-e* J-coupling (through bond) interaction strength. This means that the DNP ε for a single *e-n* polarization transfer is defined by $\varepsilon_s = |P_{e1}\text{-}P_{e2}|\kappa\text{-}P_n$, and that the DNP ε_s will inherently decrease as the total *e-e* interaction strength increases (i.e. as d and J increase). Thus, a balance must be maintained between having strong enough *e-e* interactions to have sufficient DNP *e-n* polarization transfers rates without having too strong *e-e* interactions such that the cumulative DNP ε over time is reduced. It is also important to note that larger *e-n* polarization transfer rates may increase the nuclear spin diffusion rate by generating larger nuclear spin polarization differentials in the system.

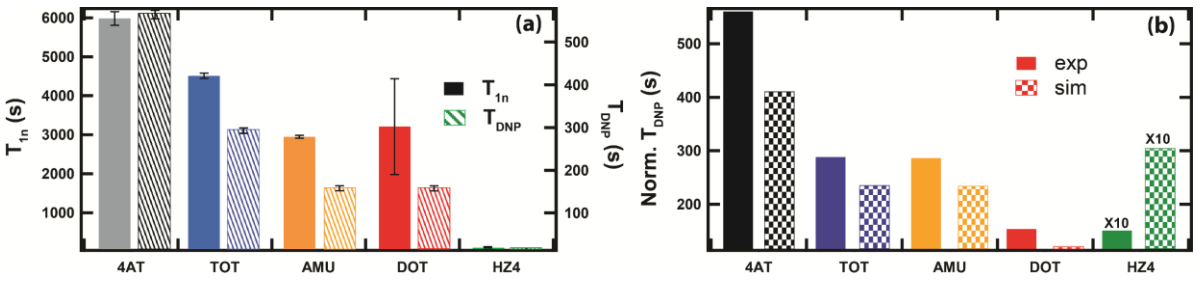

Figure 6.5. (a) Experimentally determined T_{1n} and T_{DNP} for each radical, where HZ4 represents the dendritic HZ4_8-3 radical. (b) Experimental and calculated T_{DNP} for each radical. All HZ4 (dendrimer) in (b) are 10x to ease visualization. Here the simulated T_{DNP} is extracted from the monoexponential fit of the total nuclear spin polarization shown in figure 6.6, where k_{sd} = 0.1 Hz, ΔB = 2 kHz, and the values of ten are extracted from equation 6.5 for each radical.

Simulations to determine T_{DNP} based on the t_{en} of equation 6.5 were conducted and shown in figure 6.5b. In order to showcase the effect of CE interactions on the nuclear relaxation rate, we consider a simplified model of one electron spin and seven spheres of nuclear spins (N_n) as shown in figure 6.6. The rate equations for each type of spin can be written as

$$\frac{dP_e}{dt} = -\sum_{i=1}^{Nn} k_{en_i}(P_e - P_{n_i}) \tag{6.7}$$

$$\frac{dP_{n_1}}{dt} = k_{en_1}\left(P_e - P_{n_1}\right) - k_{n_1 n_2}(P_{n_1} - P_{n_2}) \tag{6.8}$$

$$\frac{dP_{n_i}}{dt} = k_{en_i}\left(P_e - P_{n_i}\right) + k_{n_{i-1} n_i}(P_{n_{i-1}} - P_{n_i}) - k_{n_i n_{i+1}}(P_{n_i} - P_{n_{i+1}}) \tag{6.9}$$

$$\frac{dP_{n_{Nn}}}{dt} = k_{en_1}\left(P_e - P_{n_{Nn}}\right) + k_{n_{Nn-1} n_{Nn}}(P_{n_{Nn-1}} - P_{n_{Nn}}) \tag{6.10}$$

P_e is used to represent the transferable electron spin polarization, and P_{n_i} is the nuclear polarization for the nuclear spins in the i^{th} sphere. The rate constants for the *e-n* polarization transfer, k_{en_i}, were approximated to be $1/t_{en}$, as determined by equation 6.5 for each electron pair and nuclear spin system. To determine ω_{ee}, we assume $\omega_{ee} \propto \frac{k_{intra}C}{r_{intra}^3} + \frac{k_{inter}C}{r_{inter}^3}$, where k_i is the number of intra- or inter- radical interactions for each radical type and $C=\frac{\mu_0}{4\pi}\frac{\gamma_1\gamma_2}{r^3}$, where γ are the gyromagnetic ratios for each electron spin, r is the distance between the dipolar coupled electron spins, and μ_0 is the Bohr magneton. We assume ΔB of equation 6.5 is 2 kHz, ω_{0I} is 294.026 MHz, and that all possible *e-e* interactions meet the CE condition. This means that the rate of *e-n* polarization transfer is significantly overestimated, since in reality not all *e-e* interactions will meet the CE condition.

The inter-radical average distances were determined using the average values for the nearest neighbor distributions from figure 6.1. For intra-radical distances, 1.3 nm was used

for bi- and tri- radicals,[101,281] whereas 2.9 nm was assumed for the dendrimer, which was determined by finding the average distance between 9 uniformly located electron spins on a sphere of radius 2 nm using the spiral method presented by Rakhmanov, Saff, and Zhou.[282] We considered two interacting radicals and all of their possible interactions, where mono-radicals have 1 inter-radical interaction, bi-radicals have 4, tri-radicals have 9, and the dendrimer (9 electron spins per radical) has 81 interactions. The number of possible inter-radical interactions is given by (N-1)(n*n), where N is the number of radicals, and n is the number of electron spins per radical. Thus, the bi-radical has 1 intra-radical interaction, while the tri-radical has 3, based on n*(n-1)/2. From this equation the total possible intra-radical interactions for the dendrimer will be 36.

Also note that the difference in hyperfine coupling was assumed to be proportional to $1/r_{en_i}^3$, which will scale down $k_{en_i}$for nuclear spins further away from the electron spin. We considered polarization will only flow in one direction by spin-diffusion with rate constant $k_{sd} = k_{n_i n_{i+1}} \forall\, i\epsilon(1,6)$. This assumes that the nuclear spins near paramagnetic centers always have higher polarization compared to the ones that are further away, but that the rate of spin diffusion is constant, where k_{sd} is 0.1 Hz or 10 sec. Therefore, in the rate equations 6.8 and 6.10 the first and last nuclear spins are described and all the nuclear spins in between (nuclei on spheres 2 to 5) are described by equation 6.9. Finally, the total P_n is the sum of $P_{n,i}$, where we assume each sphere of nuclear spins will contain more spins, thus $P_{n,i}$ is scaled by the number of nuclear spins in the sphere according to the surface area of the sphere, ~r^2 from figure 6.6a/b.

From these calculated values of P_n (figure 6.6c), T_{DNP} was extracted via a mono-exponential fit, which are shown in comparison to the experimental T_{DNP} in figure 6.5b. We

can see that T_{en} determines the observed experimental trend of T_{DNP} shortening with increasing ω_{ee}. It is important to note that we assumed a constant nuclear spin diffusion for all of the radicals; however, the nuclear spin diffusion can vary for each radical and sample formulation and will also modulate T_{DNP}. If K_{sd} is very fast (<10 ms), then T_{DNP} for all of the radicals will converge to a single value, while if K_{sd} is very slow (> 1000 s), then T_{DNP} will also converge to a single value for all radicals. Therefore, from the experimental T_{DNP} values, we know that K_{sd} must be moderate (100 ms to 100 s) to reflect the range of experimental T_{DNP} values. A significant assumption made in these calculations is that all of the *e-e* interactions meet the CE condition, which causes an overestimation of t_{en} and subsequently of T_{DNP}, where the given simulations assume a K_{sd} that is too short, except for the dendritic radical case. These calculations demonstrate that although t_{en} is a significant contributor in determining T_{DNP} under theses experimental conditions, there are many other factors that must also be considered such as nuclear spin diffusion, electron spin pairs meeting the CE condition, the full distribution of *e-e* interaction distances for both inter- and intra- radical interactions, and accounting for all interactions in a sample instead of considering only two interacting radicals.

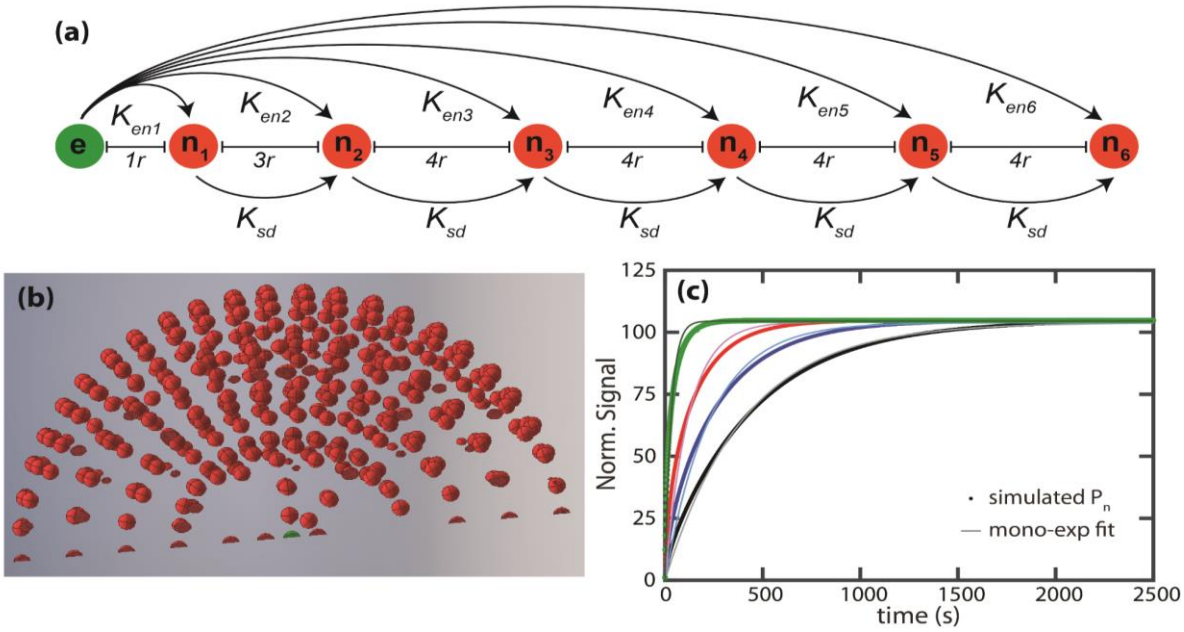

Figure 6.6. (a) Schematic model used the for simulation of nuclear spin polarization build-up. Note each nuclear spin represents a sphere of nuclei, which are illustrated in (b). The total P_n build-up is shown in (c), where a mono-exponential is used to extract T_{DNP}, which are compared to the experimental T_{DNP} in figure 6.5b.

From analysis of T_{DNP}, we determined that increased CE mediated *e-e-n* transitions caused the shortening of T_{DNP} due to stronger *e-e* interactions. These same strong *e-e* couplings also shortened T_{1n}, which is the reverse process of T_{DNP}, where the polarization flows back from the bulk nuclear spins to core nuclear spins located in proximity to the paramagnetic centers that are rapidly relaxed by PRE.[253] The primary difference between these two processes is that T_{DNP} is driven by μw irradiation to generate an enhancement of nuclear spin polarization, whereas T_{1n} is dictated by intrinsic spin dynamics that relax the system to thermal equilibrium – i.e. it is a self-driven process. The observation that T_{1n} shortens dramatically with increasing local electron spin concentration demonstrates that the *e-e* dipolar coupling strength strongly influences T_{1n} as well! This means that *intrinsic e-e* interactions meeting the CE condition can undergo a *e-e-n* transition mediated by the CE. These nuclei hyperfine

coupled to the *e-e* spin system will inherently act as a sink for nuclear spin polarization to relax faster even without μw irradiation. In other words, the CE can be operational in shortening T_{1n} without μw irradiation. Therefore, systems with higher local electron spin concentrations, such as the dendrimer radical, will have more electron spin pairs that inherently fulfill the CE condition, which induces faster nuclear relaxation. Here it is important to mention that the effect of *e-e* interactions on T_{1n} has been observed and analyzed earlier by Houten et. al. and Stoll et. al., where the studies were performed at low magnetic fields, 1.13 T and 3.34 T, respectively.[267–269] Houten et. al. rationalize the shortening of T_{1n} as an enhanced cross-relaxation induced by dipolar coupled electron spins separated by ω_{0n} (i.e. CE condition), while Stoll et. al. utilize a T_{1e}-driven mechanism to explain the shortening of T_{1n}. Our findings agree and expand upon those presented by Houten et. al., where the shortening of T_{1n} and T_{DNP} is also observed under MAS conditions at 92 K (see Appendix G, figure 15.1). Here the dendrimer radical was found to shorten both nuclear relaxation rates by 2-fold compared to AMU (the gold-standard for MAS-DNP at ~100 K), where the $^{13}C_{\alpha}$ of glycine had a T_{DNP} of 1.97±0.33 s for dendrimer and 4.02±0.35 s for AMU, while T_{1n} was 2.12 ± 0.55 s for dendrimer and 4.25 ± 0.46 s for AMU. An interesting side note is that the dendrimer radical had significantly less "depolarization"[194] compared to the AMU sample (2-fold compared to 10-fold reduction of the μw off NMR signal with spinning at 8 kHz compared to under static conditions).

To further investigate the role of *e-e* coupling in modulating T_{1n}, the electron spin relaxation rates were determined, since PRE theory typically represents the *e-n* hyperfine correlation time that modulates PRE effects with the electron spin lattice relaxation time, T_{1e}. T_{1e} was found to increase with increasing local electron spin concentration, and the phase

memory time, T_m, decreases with increasing local electron spin concentration, as shown in table 6.2. The T_{1e} for AMU is longer than TOT or the tri-radical, likely due to the rigidity of molecule compared to the other radical systems and is consistent with the shorter T_{1n} of AMU compared to TOT. However, the standard Redfield theory is not valid under the current conditions, and thus, the exact effect of T_{1e} on the PRE effect is not clear. Longer T_{1e} will aid the probability that *e-n* transfers occur by allowing spins with weaker *e-e* dipolar interactions (i.e. longer distances between coupled electrons) to participate in the CE due to the increased timeframe during which the electron spins are depolarized and can effectively interact via dipolar coupling.[242] Furthermore, an increase in the local electron spin concentration decreases T_m, which is a measure of local electron spin concentration, under conditions of high electron spin concentration and low temperature, as it applies to the bi-, tri-, and dendritic radicals in this study.[118] The observed trend for the bi-, tri-, and dendritic radicals suggests higher local electron spin concentrations, which agrees with their radical structures. The shorter T_m for the mono-radical is likely due to inter-radical interactions, while the inter-radical interactions decreases for the clustered radical species studied here, given that the global concentration is kept constant, as previously stated.

Table 6.2. Electron relaxation times and spectral diffusion rates for different radicals with 10 mM global concentration in DNP juice at 7 T magnetic field and 4 K temperature.

Sample	T_{1e} (ms)	T_m (µs)	Λ^{eSD} (µs^3)
4AT	94.2 ± 7.2	12.7 ± 1	10
TOTAPOL	86.0 ± 2.0	15.7 ± 0.3	25
AMUpol	138.5 ± 4.9	13.2 ± 0.5	25
DOTOPA-et	88.6 ± 16.6	11.9 ± 1	50
HZ4_68-3	151.81 ± 7.5	7.2 ± 0.1	1400

6.4. Electron spin depolarization

Although the electron and nuclear relaxation rates provide insight into the role of *e-e* dipolar coupling in modulating T_{DNP} and T_{1n}, it is desirable to directly measure the *e-e* interactions of the different radical systems at constant global electron spin concentration. Electron depolarization profiles can determine the extent of electron spectral diffusion (eSD), a process facilitated by *e-e* interactions, where polarization is transferred between dipolar coupled electron spins at different resonant frequencies. The acquisition of these profiles via ELDOR was is discussed in chapter 3, whereby the depth of the hole burnt into the EPR spectrum is influenced by the combined effects of T_{1e}, eSD, and $P_{\mu w}$,[165] and the width is determined primarily by eSD and μw irradiation bandwidth.

The ELDOR profiles for each radical system are shown in figure 6.7, where four ν_{detect} were chosen to sample the eSD effect across the EPR spectrum and the pulse sequence is shown in the inset of figure 6.7d. As the local electron spin concentration is increased, the depth and width of the ELDOR profile increases to the point where the dendrimer shows depolarization beyond that of its allowed EPR spectral density (figure 16.1, Appendix H). The mono-radical, and to some extent the bi-radicals, do not display significant eSD – as seen by the limited depolarization in the center of the ELDOR spectrum. The ELDOR profiles of 4AT and TOT reveal forbidden transitions due to *e-n* hyperfine interactions (i.e. SE for each nuclei hyperfine coupled to the electron spin) as sharp symmetric peaks positioned the nuclear Larmor frequency away from the allowed EPR transition ($\nu_{detect}=\nu_{excite}$, annotated as peak 1 in figure 6.7c). The hyperfine coupled peaks for ^{14}N, ^{2}H, and ^{1}H forbidden transitions are identified in figure 6.7c by 2, 3, and 4. It is only with ≥ 3-electron spins per radical that

consistently large eSD effects are observed in the ELDOR profiles at all ν_{detect}. Simulations of these profiles that account for differences in electron and nuclear relaxation rates allow for a phenomenological eSD parameter (Λ^{eSD}) to be determined, which are shown in table 6.2, and follow the theory and simulation method described by Shimon et al.[96,191] A comparison of the simulations and experimental ELDOR profiles are presented in Appendix I, with the simulation parameters reported in table 17.1. There is generally good agreement between the experimental and simulated ELDOR profiles; although the width of the dendrimer's experimental profile was difficult to reproduce. The Λ^{eSD} determined from simulations increases with more electron spins per radical, where both rigid and flexible biradicals yield the same Λ^{eSD}. Thus, we can conclude that eSD, as reflected by Λ^{eSD}, increases with higher local electron spin concentrations, independent of T_{1e}. This demonstrates that higher local electron spin concentrations directly increase eSD, which is responsible for shortening T_{DNP} and T_{1n} by facilitating the *e-n* CE transfer through enhanced *e-e* dipolar coupling. This is especially noteworthy for the bi-radicals, since they have nearly identical Λ^{eSD} and T_{DNP}. The ELDOR profiles also explain why the ε_{eq} of the dendrimer system is low—the electron spin population across the whole EPR spectrum is so broadly depolarized that it obliterates the polarization differential between the dipolar coupled electron spins that is essential for the transfer of polarization from the electrons to the nuclei.

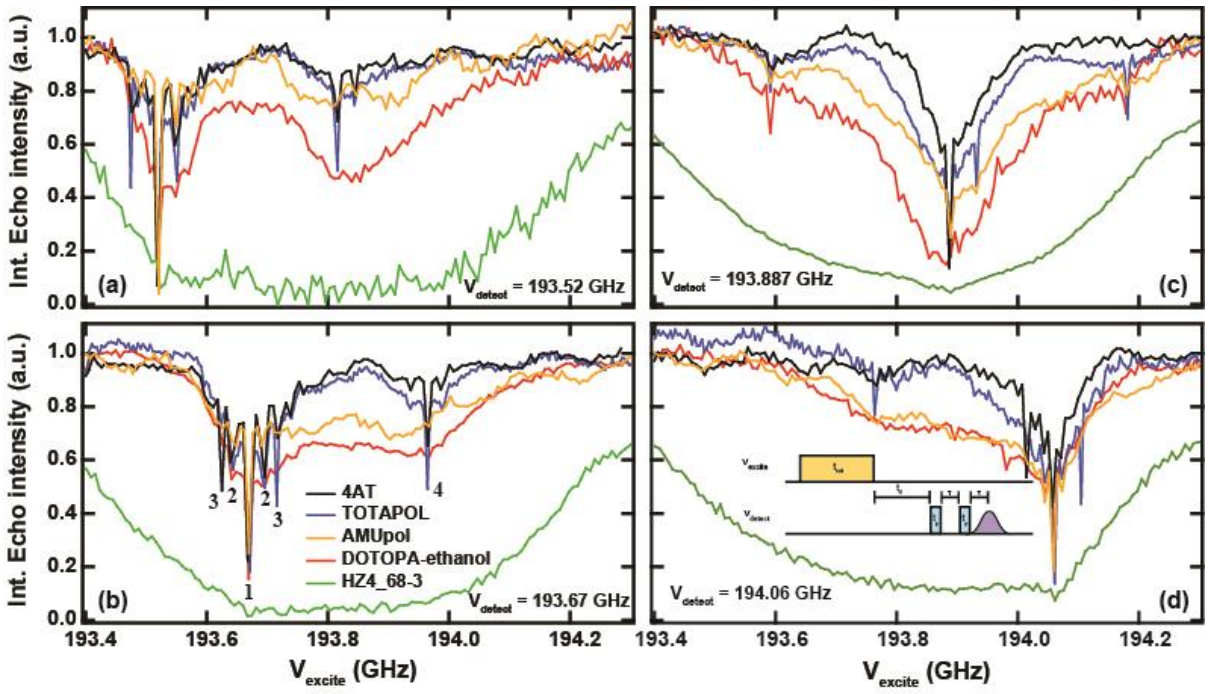

Figure 6.7. Electron spin depolarization profiles measured via ELDOR at 4K with V_{detect} of 193.52 GHz (a), 193.67 GHz (b), 193.887 GHz (c), and 194.06 GHz (d) for 10 mM 4-amino TEMPO (black), 5 mM TOTAPOL (blue), 5 mM AMUpol (purple), 3.33 mM DOTOPA-ethanol (red), and 10 mM electron spin dendrimer (green) in 6:3:1 d_8-glycerol:D_2O:H_2O. Allowed EPR transitions are denoted by 1, while 2,3, and 4 denote the forbidden ^{14}N, ^{2}H, and ^{1}H transition, respectively. The ELDOR pulse sequence is shown as an insert in (d), where t_{sat} = 100 ms, t_p = 750 ns, t_d = 10 μs, and τ = 500 ns, with a recycle delay of 600 ms.

6.5. Case study of a strong *e-e* network

If we consider the system with a strong *e-e* network, the dendritic radical reveals three outlying results: the power curve displaying DNP oversaturation (figure 6.2b), short T_{DNP} (figure 6.5/table 6.1), and extensive electron spin depolarization according to ELDOR profiles (figure 6.7). A second batch (HZ5_78-3) of the same dendritic radical with 10 mM and 1.7 mM electron spin concentrations were made to confirm these results. The two concentrations were chosen, given that 1.7 mM of a monomer nitroxide radical would display a pure SE DNP profile (see section 4.2).[96] The DNP profiles of both concentrations (figure 6.8a) confirm that only CE DNP is active, even at the lower radical concentration. As the intra-radical distance

for 1.7 mM electron spin dendrimer is > 11 nm on average, the observed CE DNP must solely originate from intra-radical *e-e* dipolar couplings within a *single* dendritic radical.

For all that the two different radical concentrations yield similar DNP profiles, T_{DNP} is drastically lengthened for 1.7 mM electron spin versus the 10 mM electron spin dendrimer samples, as expected for a lower global electron spin concentration (figure 6.8b). In both the cases T_{DNP} shortens with increasing $P_{\mu w}$. Fitting the power dependent T_{DNP} data yields an approximate square dependence between T_{DNP} and the applied $P_{\mu w}$ for both concentrations. As no sample heating is observed with our instrument's maximum $P_{\mu w}$, the T_{1n} and nuclear spin diffusion rates will not inherently change with $P_{\mu w}$. Therefore, the shortening of T_{DNP} with increasing $P_{\mu w}$ is due to an increase in the *e-n* polarization transfer rate (according to equation 6.5), which results from increased electron spin depolarization with more applied $P_{\mu w}$ as shown by the ELDOR profiles in figure 6.8c. ELDOR profiles of the 10 mM electron spin dendrimer sample were acquired at three $P_{\mu w}$ corresponding to the maximum $P_{\mu w}$ (120mW), the $P_{\mu w}$ for optimum enhancement (50mW), and the $P_{\mu w}$ yielding the same enhancement as full power (20mW) as indicated by the arrows in figure 6.8d. Clearly, the extent of electron spin depolarization increases with increasing $P_{\mu w}$, and at maximum power the ELDOR profile has broader and deeper electron spin depolarization compared to optimal conditions.

The DNP power curve of the 10 mM electron spin dendrimer system has decreased DNP enhancement above ~60 mW of $P_{\mu w}$ – termed oversaturation (figure 6.2b). It was proposed back in 2014, that DNP oversaturation is caused by broad depolarization across the EPR spectrum; however, experimental electron spin depolarization profiles were not available at the time.[43] The power dependent ELDOR profiles in figure 6.8c provide direct evidence that

this hypothesis is valid, and that at $P_{\mu w}$ higher than optimal for DNP, the electron spins are depolarized beyond the optimal-DNP ELDOR profile. This means that under oversaturation conditions, the effective polarization differentials between electron spins meeting the CE condition have been reduced, which correspondingly reduces the polarization that can be transferred to the surrounding nuclei, and thus reduces the DNP enhancement – as discussed in section 4.3.2. The large eSD found only for the dendrimer sample can explain why of all the radicals only the dendrimer sample exhibited DNP oversaturation. Unlike the 10 mM electron spin dendrimer sample, the power curve for the 1.7 mM electron spin dendrimer sample plateaus at 80 mW of $P_{\mu w}$ with no oversaturation effects (red trace, figure 6.8d). This could be due to an insufficient total number of electron spins in the system to cause oversaturation.

The relaxation and enhancement terms for the 1.7 mM and 10 mM electron spin dendrimer are shown in table 6.3, where ε_T and ε_{eq} decreases, T_{DNP} and T_{1n} lengthen, and T_{1e} and T_m shorten with decreasing dendrimer concentration. The ε_{60} does increase with the lower total electron spin concentration due to the lengthened T_{DNP}, as discussed earlier. These results are similar to other global radical concentration studies, except for T_m, which normally should be longer for lower electron spin concentrations.[43] The lengthened nuclear relaxation rates are attributed to the fewer total number of electron spins in the sample, which would also decrease ε_{eq} and ε_T.

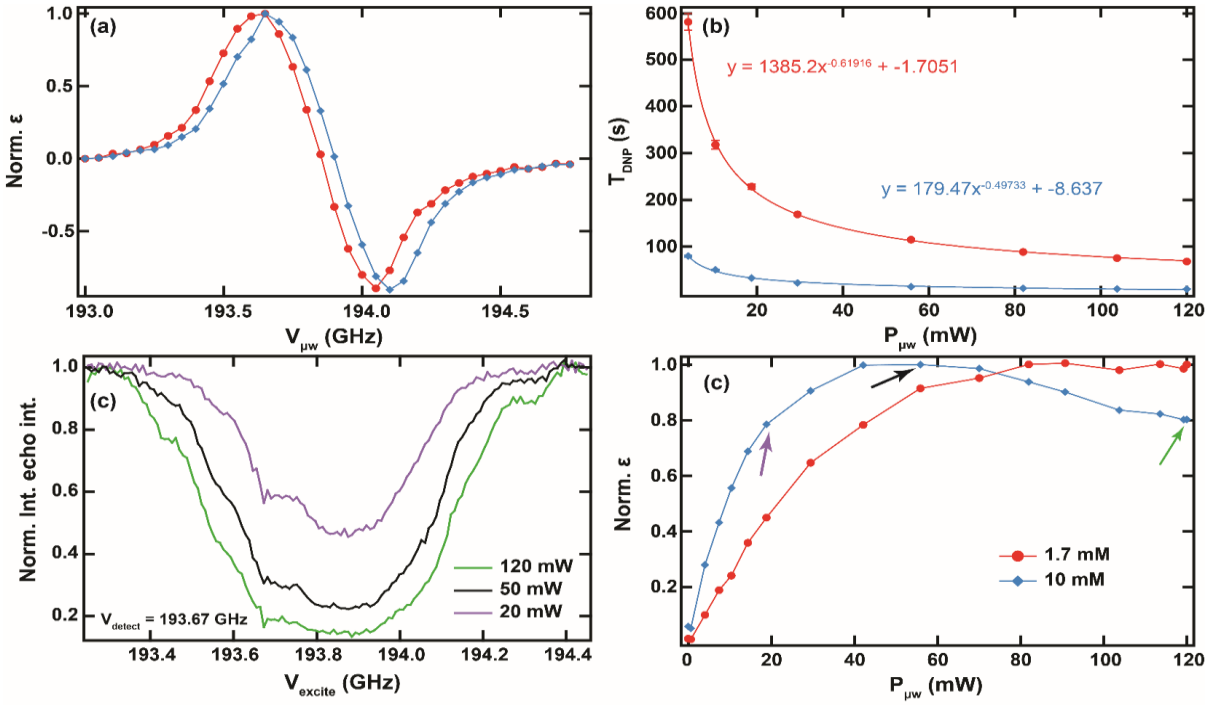

Figure 6.8. DNP profiles (a) and DNP power dependent curves (b) for 1.7 mM (red - circles) and 10 mM (blue - diamonds) electron spin of HZ5_78-3 in 6:3:1 d_8-glycerol:D_2O:H_2O at 4 K and at 7 T. Data was acquired after 60 s of MW irradiation and normalized for ease of comparison. (c) Electron depolarization profiles of the 10 mM electron spin sample at different MW irradiation strengths for the saturation pulse: 120 mW (green), 20 mW (black), and 5 mW (red), as indicated by the arrows in (d). In the ELDOR pulse sequence, ν_{detect} = 193.67 GHz, t_{sat} = 100 ms, t_p = 750 ns, t_d = 10 μs, and τ = 500 ns, with a recycle delay of 600 ms. (d) T_{DNP} as a function of the applied MW power for 1.7 mM (red-circles) and 10 mM (blue-diamonds) electron spins of HZ5_78-3 and 5 mM TOTAPOL (black triangles) in 6:3:1 d_8-glycerol:D_2O:H_2O at 4 K and at 7 T when irradiated at 193.65 GHz. T_{DNP} was determined at each MW power by fitting experimental results to $M_z(t) = M_{z_{eq}}\left(1 - e^{\frac{-t}{T_{DNP}}}\right)$, with the resultant fitting error shown in the figure. The power dependence of T_{DNP} for each concentration was fit with a power function, with the fits (slid lines) and their corresponding equations shown inside the figure in the associated color for each HZ5_78-3 and TOTAPOL concentration.

Table 6.3. Average electron and nuclear relaxation rates and DNP signal enhancement at 60 s of μw irradiation, at steady state, and per until time are lister here for 1.7 mM and 10 mM electron spin of HZ5_78-3 dendrimer in 6:3:1 d_8-glycerol:D_2O:H_2O at 4 K and at 7 T. The T_{DNP} listed here was obtained under optimal conditions for positive DNP enhancement.

[HZ5_78-3]	$\varepsilon_{60}/\varepsilon_{eq}$	T_{DNP} (s)	T_{1n} (s)	T_{1e} (ms)	T_m (μs)	ε_T
1.7 mM	78.8 / 5.8	68.3 ± 1.1	983.19 ± 27.7	102.3 ± 2.8	4.6 ± 0.1	0.70
10 mM	19.1 / 7.5	14.6 ± 0.2	113.61 ± 1.3	151.8 ± 7.5	7.2 ± 0.1	1.96

The dendrimer radical does not have a strong enough paramagnetic quenching factor from the average 9-electron spins per radical to completely eliminate the ^{1}H signal from the dendritic structure itself. This was observed by dissolving a 10 mM electron spin of HZ4_68-3 dendrimer radical in 6:4 of d_8-glycerol:D_2O – i.e. a fully perdeuterated solvent. Thus, any observed NMR signal will result from the ^{1}H on the dendritic radical itself. Not only was ^{1}H NMR signal observed, but T_{1n} and T_{DNP} (at $P_{\mu w}$ corresponding to optimal DNP enhancement – 20 mW and maximum power output – 114 mW) were measured for the dendrimer in the perdeuterated solvent. A comparison of the NMR signal between the partially protonated (6:3:1) versus fully perdeuterated solvents (6:4:0), shows that the ^{1}H from the dendrimer produce ~23% of the total ^{1}H NMR signal for the 6:3:1 solvent system. This means that the paramagnetic quenching for this dendritic radical is limited and will not completely quench the signal from a potential solute of interest. Additionally, when comparing the T_{1n} and T_{DNP} results, the contribution from the dendrimer ^{1}H should be accounted for since 23% of the total signal is not negligible. Both the 6:3:1 and 6:4:0 solvent systems' T_{1n} and T_{DNP} measurements were fit with a mono-exponential as previously described for the other radicals and are reported in table 6.4. Between the mono-exponential fits the T_{DNP} at optimal DNP conditions were effectively identical for both solvents. However, T_{1n} shortened and T_{DNP} at 114 mW

lengthened by deuterating the solvent. The shorter T_{1n} conceptually makes sense because the ^{1}H on the dendrimer are close to the electrons (closer on average compared to the solvent bulk ^{1}H), which will have a larger PRE effect and cause the magnetization to relax faster compared to solvent ^{1}H in addition to the CE mediated nuclear spin relaxation. To understand why the T_{DNP} at $P_{\mu w}$ higher than optimal for DNP lengthens will require an analysis to separate the dendrimer and solvent ^{1}H.

In order to account for the dendrimer ^{1}H in the 6:3:1 solvent, a bi-exponential fit was applied with a fit equation of $y = M_{z,on/off_{eq}}\left(1 - Ae^{-t/T_{x1}} - e^{-t/T_{x2}}\right)$, where the T_{x1} were the experimentally determined T_{1n} and T_{DNP} values from the 6:4:0 solvent system, representing the ^{1}H of the radical, A is the difference in NMR signal intensity (A=0.23), and T_{x2} can be either T_{1n} or T_{DNP} for the solvent ^{1}H. The extracted solvent only ^{1}H T_{1n} and T_{DNP} values are reported in table 6.4 as bi-exponential fit component two. The solvent only ^{1}H resulted in longer T_{1n}, effectively the same T_{DNP} at optimal DNP conditions, and shorter T_{DNP} at 114 mW relative to the mono-exponential fit of the 6:3:1 system. This suggests that the solvent and radical ^{1}H build-up rates are equal under optimal DNP conditions; however, at higher applied $P_{\mu w}$, then the solvent ^{1}H will have significantly faster T_{DNP}s' – here by a factor of 2. The combination of longer T_{1n} and shorter T_{DNP} at high applied $P_{\mu w}$ for solvent ^{1}H, suggests that DNP is more efficient for solvent ^{1}H compared to ^{1}H on the radical itself under these conditions. Here the ^{1}H spin diffusion of the whole solvent network can spread the nuclear polarization from each dendrimer radical, while for the ^{1}H of the dendrimer can only by hyperpolarized by the electron spins on the radical itself, which will be limited by the total number of electron spin pairs that meet the CE condition, thus decreasing some of the CE efficiency for dendrimer ^{1}H compared to ^{1}H solvent.

Table 6.4. T_{1n} and T_{DNP} were extracted from build-up curves without and with μw irradiation at 193.65 GHz, respectively for 10 mM electron spin dendrimer radical HZ4_68-3 in 6:3:1 and 6:4:0 d_8-glycerol:D_2O:H_2O at 4K and at 7 T. The raw experimental data of both solvent systems were fitted with a mono-exponential ($y = M_{z,on/off_{eq}}\left(1 - e^{-t/T_x}\right)$, where the T_x can be either T_{1n} or T_{DNP} and M_{zeq} is the signal at equilibrium). The 6:3:1 solvent system was also fitted with a bi-exponential ($y = M_{z,on/off_{eq}}\left(1 - Ae^{-t/T_{x1}} - e^{-t/T_{x2}}\right)$, where the T_{x1} were the T_{1n} and T_{DNP} values from the 6:4:0 solvent system, representing the ^1H of the radical, A is the difference in NMR signal intensity (A=0.23), and T_{x2} can be either T_{1n} or T_{DNP} for the solvent ^1H).

Solvent	T_{1n} (s)	T_{DNP} 20 mW (s)	T_{DNP} 114 mW (s)	Fit Type
6:3:1	106.26 ± 1.21	15.06 ± 0.23	7.39 ± 0.08	Mono-exp
6:4:0	65.19 ± 2.21	15.36 ± 0.63	12.91 ± 0.39	Mono-exp
6:3:1	65	15	13	Bi-exp comp 1
	124.5 ± 2.01	15.07 ± 0.03	6.40 ± 0.14	Bi-exp comp 2

6.6. Conclusions

Higher local electron spin concentrations induced by either radical clustering or multi-mer radicals results in shorter T_{1n} and T_{DNP} and larger ε_T due to the increased probability of *e-e-n* transitions that meet the CE condition. For T_{DNP} and ε_T, this increases the rate of *e-n* polarization transfer, and for T_{1n}, these inherent transitions act as a sink for nuclear relaxation. Thus, the nuclear spin relaxation rates under static and MAS conditions are modulated by the *e-e* interaction strength of *e-e-n* transitions mediated by the CE independent of μw irradiation. Therefore, *e-e* interaction strength, the number of *e-e* interactions, and T_{DNP} should be design criterion for the next generation of designer radicals for DNP. T_{DNP} is further influenced by the $P_{\mu w}$ applied to the system, where the signal builds-up faster with higher $P_{\mu w}$ independent of whether DNP oversaturation occurs or not. We provide further evidence that DNP oversaturation is due to electron spin depolarization beyond optimal conditions, as shown for the dendrimer sample. This is attributed to the presence of strong *e-e* dipolar couplings that

result in extensive eSD. Although eSD does increase with higher local electron spin concentrations, eSD does not appear to be very effective until at least 3-electron spins are dipolar coupled, as suggested by the electron spin depolarization profiles; this will require further study.

Higher local radical concentrations are beneficial for faster DNP acquisitions due to the large ε_T or if a very low global radical concentration is desired – such that the more efficient CE DNP can be selected. This is especially noticeable for the dendrimer system where simulations of signal averaging resulted in larger NMR signals for the dendrimer system as long as the delay was < 10*T_{DNP}. The shortened T_{DNP} for clustered electron spins is also beneficial for high magnetic fields, given that nuclear relaxation will lengthen with stronger fields. The dendrimer is especially useful, as the T_{2n} does not appreciably change even though T_{DNP} has drastically shorted, which allows for easy acquisitions of NMR echoes. From this study we have found that nuclear spin relaxation rates are strongly influenced by the *e-e* interaction strength and that these same *e-e* interactions may aid in improving DNP efficiency at higher magnetic fields.

7. CONCLUSIONS AND PROSPECTIVES

This work showcases the instrument developments that have successfully been implemented in the dual DNP/EPR system operating at 194 GHz in the Han lab at UCSB. The versatile capabilities of this instrument enabled acquisition of both electron and nuclear spin dynamics that have elucidated the underlying DNP mechanisms for a sample as well as the effect strong *e-e* interactions have on eSD, DNP, and nuclear relaxation processes. This chapter will recap the major findings presented in the preceding chapters in addition to providing a prospective for future research endeavors in relation to instrument development, DNP relevant spin dynamics, and applications that can benefit from DNP.

7.1. Summary of preceding research

Versatile and agile dual DNP/EPR spectrometers are necessary to broaden the scope of DNP experiments for a range of applications, and to understand the underlying physics and mechanisms for DNP processes, especially when new sample formulations or odd results are to be explored. The instrument and experimental designs outlined in chapters 2 and 3 enables the reader to build a modular two ss-μw source design for an AWG-capable dual DNP/EPR instrument. The advantage of a modular design allows the instrument to be easily modified to accommodate exactly what is needed for the desired experiments or available budget, while also providing easy access for upgrading one module at a time or adding new modules. Although alternative μw sources were mentioned, the ss-μw source is the heart of a versatile dual capability instrument owing to its wide bandwidths (~10 GHz) and tunability that allows the user to access a range of g-factors found with atypical radicals or paramagnetic transition metals for DNP and EPR experiments. The AWG capability provides the agility necessary for precise μw pulse shaping and broadening the excitation bandwidth for DNP and EPR, while

the addition of a second μw source improves the performance and eliminates artifacts for pump-probe type ELDOR experiments.

A versatile instrument is necessary to fully explore the DNP experimental conditions. To begin this endeavor, the effect of the radical concentration, experimental temperature, and $P_{\mu w}$ were considered on a standard sample with an assumed homogeneous radical distribution. A simulation model that incorporates eSD into the SE and CE DNP mechanisms successfully reproduced the transition from SE to CE with increasing radical concentrations. This same method was able to model the temperature dependence by varying only T_{1e}; however, this model was unable to reproduce DNP oversaturation with increasing $P_{\mu w}$. Acquisition of $P_{\mu w}$ dependent electron spin depolarization profiles proved that DNP oversaturation is caused by electron spin depolarization beyond the optimal conditions – i.e. those yielding maximal DNP enhancement. While decreasing the Δ_{bin} in the simulation model improved the fits with respect to the experimental $P_{\mu w}$ dependent DNP and ELDOR profiles, the models were unable to fit ELDOR profiles well across multiple ν_{detect}.

The assumption that radicals were homogeneously distributed in DNP samples was disproven in chapter 5. Here the effects glass polymorphism had on radical distributions was analyzed via EPR spectra, electron and nuclear spin relaxation rates, and DNP performance. It was found that faster freezing methods and high cryoprotectant concentrations could help mitigate radical heterogeneity throughout the sample. The inherent propensity of some radicals to cluster was also investigated for the case of trityl, where trityl forms dimers and trimers above a 1 mM concentration. It was interesting to see that the proclivity of trityl to cluster is dependent on the solvent choice, where pyruvic acid greatly reduced the formation of clusters compared to aqueous solvents. The addition of lanthanide additives to boost DNP

enhancements are generally in low enough concentrations that they do not cluster and seem to have a negligible effect on whether trityl will cluster or not. One interesting finding was that three weakly interacting gadolinium high spin systems (S=7/2) boosted the DNP enhancement by 25-fold, where other gadolinium-based additives have only reported ≤ 4-fold boosting effect.

The finding that radicals are not homogeneously distributed through a DNP sample (as previously assumed) led me to investigate the impact of the local electron spin concentration on DNP and the electron and nuclear spin dynamics. As the local electron spin concentration was increased, the *e*-*e* interaction strength also increased. We found that more *e*-*e* interactions (even if they have weaker interaction strengths) will result in very efficient eSD, and the probability of these *e*-*e* interactions meeting the CE will also increase. This causes the T_{1n} and T_{DNP} to shorten significantly because the nuclear spins can undergo an *e*-*e*-*n* CE mediated transition that will build-up hyperpolarization faster and act as a sink for nuclear relaxation. This effect is a coherent process that occurs concurrently with incoherent nuclear spin relaxation pathways such as PRE effects. The dendritic radical used in this study not only had a 3-orders of magnitude reduction in T_{1n}, the T_{2n} was not significantly affected. This means that the echo detected NMR signal is not influenced by the CE mediated relaxation pathway, which has potential applications for high field DNP, since T_{1n} will increase at higher fields. Therefore, radical clustering will increase the number of *e*-*e* interactions to mitigate this effect via the CE mediated nuclear relaxation, enabling a faster build-up of hyperpolarization and saving acquisition time when signal averaging.

These combined findings illustrate the importance of the spin dynamics that dictate DNP, where the experimental conditions modulate the spin dynamics. Therefore, the

experimental conditions can be manipulated to optimize the spin dynamics for maximum DNP enhancement across a wide range of sample formulations. This will broaden the scope of possible applications for DNP and make DNP more accessible and user friendly to the scientific community as a robust characterization technique for biosolids, materials, and for hyperpolarized liquid-state NMR via dDNP.

7.2. Prospective outlook to DNP-based research

The results presented in section 7.1 can act as a stepping stone to future research endeavors that continue the process of developing more versatile instrumentation and improving our understanding of the underlying spin dynamics that drive the DNP process. These results can also be used in applications to better understand material properties, functions, and dynamics. A brief overview of the prospective future in DNP-based research is presented in the following sections.

7.2.1. Prospective of instrumental developments

I will first touch on a few instrument developments that are underway across the DNP field and specifically on three instrument developments that will soon be implemented in the 194 GHz dual DNP/EPR system in the Han lab. Efforts to improve the $P_{\mu w}$ output of μw-sources, both solid-state and gyrotron-based sources are underway, where gyrotron-based sources also need improved flexibility in terms of frequency modulation and bandwidth.[283–286] Due to the expensive nature of cryogenic cooling and limited access to funding, optimization of cryogenic cooling efficiency is in progress as is the development of cryogen-free solutions.[221,287] For dual DNP/EPR based instruments, incorporating pump-probe type experiments, such as ELDOR and electron-nuclear double resonance (ENDOR)[117,124,288]

enables acquisition of multi-spin dynamics. Finally, moving single and dual mode instruments to higher magnetic fields is desired due to the increased resolution of g-factors for electron spins, higher resolution of nuclear spin systems under MAS, decreased quadrupolar effects for nuclear spins, and the increased electron and nuclear polarizations according to Boltzmann statistics.

The dual DNP/EPR instrument operating at 194 GHz will soon receive the following up-grades: i) magnetic field sweep coil, ii) helium refrigeration system for sample cooling, and iii) a new dual DNP/EPR probe with sample exchange capabilities. The magnetic field sweep coil (Bridge 12 Technologies) will allow for field swept and frequency stepped EPR spectra to be acquired on the same instrument. The sweep coil will fit inside the 89 mm bore of our Bruker superconducting NMR magnet, but outside of the sample cryostat. This sweep coil has a field homogeneity of $\pm$ 1 ppm over a 10 mm length and should provide up to a 30 mT shift in the magnetic field. The major advantage of this up-grade is that it will enable us to acquire EPR spectra via the traditional field-swept method and will eliminate the standing wave issue that can occur when acquiring frequency-stepped EPR spectra (both pulsed and cw).

The helium refrigeration up-grade to the 194 GHz system will significantly reduce our helium consumption, which will positively impact the environment and our budget due to the extremely high cost of liquid helium. The refrigeration system (Janis Research Co.) will replace the cryostat we currently are using (it will fit inside the soon to be installed sweep coil). The current cryostat uses ~100 L of liquid helium for 40 hours of operation at 4 K, which roughly equates to $800 of liquid helium for only two days of operation. The new refrigeration system can operate down to 3.5 K with only 0.5 L of helium gas (< $1 for helium) consumed for over a week of continuous operation. This will greatly reduce the operational cost of

consumables for the dual DNP/EPR instrument and will not limit experimental time to the consumption of 100 L of liquid helium (the amount of liquid helium available at our facility is limited to 100 L at a time), where higher temperatures will have even slower consumption rates.

The final up-grade of a new dual DNP/EPR probe is under development by me. This probe is required in order to install the previous two upgrades, since the ID of the new refrigeration system (42 mm) is smaller than our current probe's OD (65 mm), and the current cryostat OD (89 mm) is larger than the sweep coil's ID (69 mm). The new probe is based on our current design, where the μw transmission and use of inductively coupled NMR coils has not changed. In the new probe, the μw will be coupled from the quasi optical bridge into a corrugated waveguide located at the center of the probe for direct transmission of the μw to the sample. The corrugated waveguide is in the process of being manufactured by Bridge 12 Technologies, where we have integrated the waveguide taper and extension pieces mentioned in section 2.7 as a single piece to prevent misalignments and to provide corrugations to the waveguide extension (the current one is just a smooth-walled copper tube). The addition of corrugations to the waveguide extension component, where the ID of the waveguide is reduced to 5.0 mm from 12.7 mm, requires that the OD of the extension be 7.5 mm instead of the current 6.6 mm. This requires the NMR inductively coupled coils to be resized to accommodate the increase in OD by 0.9 mm. As such all the NMR coil diameter dimensions listed in Appendix B.2 have been increased by 0.9 mm.

The key component of this new probe will be the sample exchanging capability. Since the waveguide will be positioned in the center of the probe insert, the traditional method of exchanging samples via direct insertion into the sweet spot of the magnet will *not* work.

Therefore, I have developed a mechanism of inserting the sample down the side of the probe insert and rotating the sample into the sweet spot of the magnet from below. As the only access point is from the top of the refrigeration system, the sample must be inserted past the NMR coil, rotated to the center of the probe, and then lifted up into the NMR circuitry, which couples to the waveguide extension and is shown in figure 7.1a. This sample exchange mechanism is still in the process of being manufactured; an illustration of this system is shown in figure 7.1b, where the angle of rotation and the distance the sample can be lifted has been limited to prevent damage to the NMR circuitry and μw waveguide. Sample exchanging will reduce the time to switch between samples significantly, since the entire system can remain at temperature between samples. This process currently takes a total of ~ 5 hours to switch between samples, where it takes ~3 hours to warm up and ~ 2 hours to cool to 4 K. It is anticipated that the new probe will be able to exchange samples in just 30 min if the same temperature is used, which will save hours of operational time.

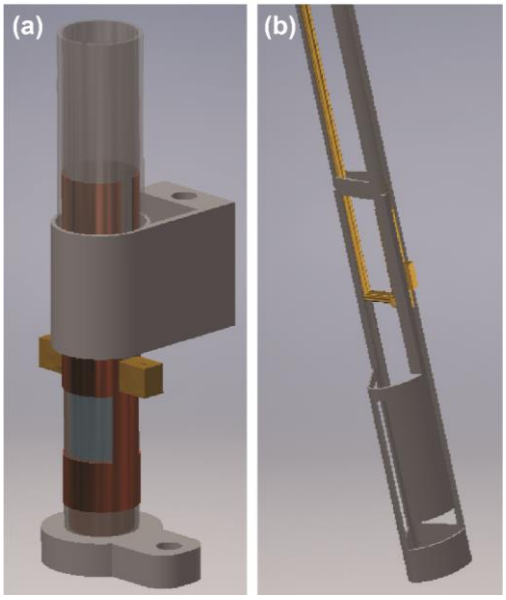

Figure 7.1. Graphic rendering of the inductively coupled NMR coil design (a) and the sample exchanger design (b) to be used in the new dual DNP/EPR probe.

7.2.2. Prospective for spin dynamic relevant to DNP

There are still many unknowns when considering DNP mechanisms and the underlying spin dynamics that dictate the relaxation processes modulating DNP. While this work showcases the effect *e-e* interactions have on nuclear spin relaxation pathways, it is unknown how differences in the core and bulk nuclear relaxation rates will affect DNP. This is further complicated by *n-n* spin diffusion, where these spin diffusion rates are unknown. There has been some discussion in literature regarding the presence of a spin diffusion barrier that can exist between core and bulk nuclei.[13,70] What is not known is the size of these spin diffusion barriers and what energetic cost is needed to overcome said barrier. Additionally, we do not know at what distance *e-e* interactions should *not* be considered, and how the *e-n* polarization transfer efficiency is dependent on distance – i.e. is it cubic like the relationship between distance and interaction strength for *e-e* interactions or is it exponential like typical relaxation

processes, etc. Finally, we do not know the impact that delocalization of the unpaired electron spin will have on DNP. The radicals traditionally used to study DNP are localized, which limits the electron spin dynamics. However, the Rajca group from the University of Nebraska, Lincoln has recently developed a series of paramagnetic organic radicals that feature delocalization of the unpaired electron spin and strong exchange coupling between the electron spins on these multi-meric radicals, where an example radical from this series is shown in figure 7.2. These types of radicals and their effect on DNP will be very interesting radical systems to investigate.

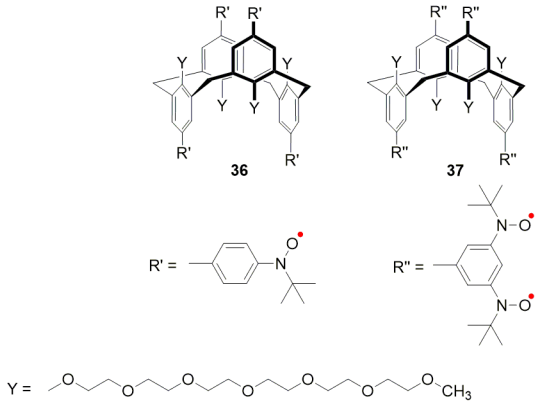

Figure 7.2. Structures of exotic tetra- and octameric nitroxide radicals. The double bonds between the radical species will delocalize the electron spins and allow for strong exchange coupling. Figure provided by Andrzej Rajca.[289]

The simulation method to fit DNP and ELDOR profiles presented in chapter 4 was unable to fully reproduce the $P_{\mu w}$ dependent experimental results. Some improvements to this method were mentioned in section 4.3.3, but incorporation of $\nu_{\mu w}$ dependent T_{1e} and T_{2e} should be completed to improve the performance of this simulation method. Additionally, this method assumes a single eSD rate for the entire electron spin spectral density. This is generally a poor assumption to make when considering an inhomogeneously broadened EPR spectrum at high

fields, which can easily span over a 1 GHz bandwidth. This assumption is valid if a narrow line radical – trityl – is used, but this is limited to low magnetic fields (<140 GHz). Future iterations of this simulation method should consider $\nu_{\mu w}$ dependent eSD rates or a distribution of eSD rates to better represent the physical spin system of an inhomogeneously broadened electron spin spectral density at high magnetic fields.

7.2.3. Prospective DNP applications

Finally, I will consider three applications of DNP. The nuclear hyperpolarization build-up times will scale to longer times with higher magnetic fields. This effect can become prohibitively slow at very high fields. Therefore, the ability of the dendritic radical introduced in chapter 6 to shorten T_{DNP} should help mitigate this effect; however, we have yet to test this hypothesis. It would be very interesting to study the effect of strong or numerous *e-e* interactions at higher fields than 7 T, such as at 18.8 T (800 MHz). Furthermore, the mechanism behind the significant DNP enhancement boosting effects produced by the $Gd_3N@C_{80}$ complex presented in chapter 5 is not known. If the mechanism behind this boosting effect was better understood, then a wider range of additives to boost DNP enhancement could be developed. Secondly, these complexes can be used to help hyperpolarize pyruvic acid for metabolic imaging in patients, such as for cardiac and neurological conditions via MRI.[52,290] Lastly, I present the case of DNP to study heterogeneous catalysts. In general, the distribution of catalytically active species across the surface of the supporting structure in heterogeneous catalysts is unknown. If the active species is paramagnetic, such as vanadium (V), then ED-NMR and DNP could help elucidate the surface structure surrounding the active species via *e-n* hyperfine interactions and determine if the active species form clusters or are homogeneously distributed. Additional magnetic

resonance techniques that could aid in the analyses of *e-n* hyperfine interactions are electron-nuclear double resonance (ENDOR) and hyperfine interaction spectroscopy (HYSCORE).[116,124,165,288,291,292] Vanadium (III and IV) are ideal starting points for this type of application because both oxidation states are paramagnetic – i.e. can be used in DNP as an inherent source for hyperpolarization and directly studied via EPR-based studies, and because vanadium is already a commonly used catalytic species.[293] In heterogeneous catalysts with metal oxides as the support structure, vanadium is primarily used to catalyze oxidation reactions, such as SO_2 to SO_3, polymerization of olefins, ammoxidation of aromatics, and the direct conversion of methane to aromatics.[293–295] These organic compounds can then be used in numerous applications including the manufacture of plastics and the fixation of pollutants from power plants. The paramagnetic oxidation states of vanadium (III and IV) are generally formed during the mechanism of these catalytic oxidation cycles, which makes them ideal to study to determine the catalytic mechanisms and isolate intermediate species via *e-n* correlated magnetic resonance. These studies can then be used to optimize the catalytic efficiency of these systems, improving performance, and reducing costs for these industrial applications.

References

1 A. Samoson, E. Lippmaa and A. Pines, *Mol. Phys.*, 1988, **65**, 1013–1018.

2 M. Pannier, V. Schadler, M. Schops, U. Wiesner, G. Jeschke and H. W. Spiess, *Macromolecules*, 2000, **33**, 7812–7818.

3 I. V. Sergeyev, L. a. Day, A. Goldbourt and A. E. McDermott, *J. Am. Chem. Soc.*, 2011, **133**, 20208–20217.

4 F. Deng, J. Yang and C. Ye, in *Modern Magnetic Resonance*, ed. G. A. Webb, Springer, Dordrecht, 2008, pp. 205–211.

5 M. J. N. Junk, H. W. Spiess and D. Hinderberger, *J. Magn. Reson.*, 2011, **210**, 210–217.

6 J. Song, O. H. Han and S. Han, *Angew. Chemie Int. Ed.*, 2015, **54**, 1–7.

7 S. Abbrent and S. Greenbaum, *Curr. Opin. Colloid Interface Sci.*, 2013, **18**, 228–244.

8 C. Bonhomme, C. Gervais and D. Laurencin, *Prog. Nucl. Magn. Reson. Spectrosc.*, 2014, **77**, 1–48.

9 M. M. Britton, *Chem. Soc. Rev.*, 2010, **39**, 4036.

10 F. W. Lancaster and W. Gordy, *J. Chem. Phys.*, 1951, **19**, 1181–1191.

11 F. Bloch, W. W. Hansen and M. Packard, *Phys. Rev.*, 1946, **69**, 127.

12 E. Purcell, H. Torrey and R. Pound, *Phys. Rev.*, 1945, **69**, 37–38.

13 C. T. Farrar, D. A. Hall, G. J. Gerfen, S. J. Inati and R. G. Griffin, *J. Chem. Phys.*, 2001, **114**, 4922–4933.

14 Y. Hovav, A. Feintuch and S. Vega, *J. Magn. Reson.*, 2010, **207**, 176–189.

15 Y. Hovav, A. Feintuch and S. Vega, *J. Magn. Reson.*, 2012, **214**, 29–41.

16 D. Shimon, Y. Hovav, A. Feintuch, D. Goldfarb and S. Vega, *Phys. Chem. Chem.*

Phys., 2012, **14**, 5729–5743.

17 S. Jannin, A. Bornet, S. Colombo and G. Bodenhausen, *Chem. Phys. Lett.*, 2011, **517**, 234–236.

18 A. W. Overhauser, *Phys. Rev.*, 1953, **92**, 411–415.

19 T. R. Carver and C. P. Slichter, *Phys. Rev.*, 1953.

20 R. a. Wind, M. J. Duijvestijn, C. van der Lugt, A. Manenschijn and J. Vriend, *Prog. Nucl. Magn. Reson. Spectrosc.*, 1985, **17**, 33–67.

21 V. A. Atsarkin, G. A. Vasneva and E. A. Novikov, *Sov. Phys. JETP*, 1975, 746–751.

22 A. Abragam and M. Goldman, *Reports Prog. Phys.*, 1978, **41**, 395–467.

23 M. L. Seely, M. R. Bergström, S. K. Dhawan, V. W. Hughes, R. F. Oppenheim, K. P. Schüler, P. A. Souder, K. Kondo, S. Miyashita, S. J. St. Lorent and Y.-N. Guo, in *High-Energy Physics with Polarized Beams and Polarized Targets*, eds. C. Joseph and J. Soffer, Birkhäuser, Basel, 38th edn., 1981, vol. 38.

24 D. A. Hall, D. C. Maus, G. J. Gerfen, S. J. Inati, L. R. Becerra, F. W. Dahlquist and R. G. Griffin, *Science (80-.).*, 1997, **276**, 930–932.

25 B. J. Wylie, B. G. Dzikovski, S. Pawsey, M. Caporini, M. Rosay, J. H. Freed and A. E. McDermott, *J. Biomol. NMR*, 2015, **61**, 361–367.

26 A. Pavlova, R. McCarney, Evan, W. Peterson, Dylan, W. Dahlquist, Frederick, J. Lew and S. Han, *Phys. Chem. Chem. Phys.*, 2009, **11**, 6833–6839.

27 M. Lelli, A. J. Rossini, G. Casano, O. Ouari, P. Tordo, A. Lesage and L. Emsley, *Chem. Commun.*, 2014, **50**, 10198–201.

28 F. A. Perras, T. Kobayashi and M. Pruski, *J. Am. Chem. Soc.*, 2015, **137**, 8336–8339.

29 V. K. Michaelis, E. Markhasin, E. Daviso, J. Herzfeld and R. G. Griffin, *J. Phys. Chem.*

Lett., 2014, **3**, 2030–2034.

30 E. Ravera, D. Shimon, A. Feintuch, D. Goldfarb, S. Vega, A. Flori, C. Luchinat, L. Menichetti and G. Parigi, *Phys. Chem. Chem. Phys.*, 2015, **17**, 26969–26978.

31 E. Miclet, D. Abergel, A. Bornet, J. Milani, S. Jannin and G. Bodenhausen, *J. Phys. Chem. Lett.*, 2014, **5**, 3290–3295.

32 L. Protesescu, A. J. Rossini, D. Kriegner, M. Valla, A. De Kergommeaux, M. Walter, K. V. Kravchyk, M. Nachtegaal, J. Stangl, B. Malaman, P. Reiss, A. Lesage, L. Emsley, C. Copéret and M. V. Kovalenko, *ACS Nano*, 2014, **8**, 2639–2648.

33 Ü. Akbey, B. Altin, A. Linden, S. Özçelik, M. Gradzielski and H. Oschkinat, *Phys. Chem. Chem. Phys.*, 2013, **15**, 20706–16.

34 M. P. Conley, A. J. Rossini, A. Comas-Vives, M. Valla, G. Casano, O. Ouari, P. Tordo, A. Lesage, L. Emsley and C. Copéret, *Phys. Chem. Chem. Phys.*, 2014, **16**, 17822–7.

35 A. Lund, M. F. Hsieh, T. A. Siaw and S. Han, *Phys. Chem. Chem. Phys.*, 2015, **17**, 25449–25454.

36 P. Wolf, M. Valla, A. J. Rossini, A. Comas-Vives, F. Núñez-Zarur, B. Malaman, A. Lesage, L. Emsley, C. Copéret and I. Hermans, *Angew. Chemie - Int. Ed.*, 2014, **75**, 10179–10183.

37 A. J. Rossini, A. Zagdoun, M. Lelli, A. Lesage, C. Copéret and L. Emsley, *Acc. Chem. Res.*, 2013, **46**, 1942–51.

38 S. Smeets, Z. J. Berkson, D. Xie, S. I. Zones, W. Wan, X. Zou, M. F. Hsieh, B. F. Chmelka, L. B. McCusker and C. Baerlocher, *J. Am. Chem. Soc.*, 2017, **139**, 16803–16812.

39 G. Mollica, D. Le, F. Ziarelli, G. Casano, O. Ouari, T. N. T. Phan, F. Aussenac, P.

Thureau, D. Gigmes, P. Tordo and S. Viel, *ACS Macro Lett.*, 2014, **3**, 922–925.

40 A. C. Pinon, J. Schlagnitweit, P. Berruyer, A. J. Rossini, M. Lelli, E. Socie, M. Tang, T. Pham, A. Lesage, S. Schantz and L. Emsley, *J. Phys. Chem. C*, 2017, **121**, 15993–16005.

41 T. C. Ong, W. C. Liao, V. Mougel, D. Gajan, A. Lesage, L. Emsley and C. Copéret, *Angew. Chemie - Int. Ed.*, 2016, **55**, 4743–4747.

42 W. R. Gunther, V. K. Michaelis, M. a. Caporini, R. G. Griffin and Y. Román-Leshkov, *J. Am. Chem. Soc.*, 2014, **136**, 6219–6222.

43 T. A. Siaw, M. Fehr, A. Lund, A. Latimer, S. A. Walker, D. T. Edwards and S. Han, *Phys. Chem. Chem. Phys.*, 2014, **16**, 18694–18706.

44 A. Zagdoun, G. Casano, O. Ouari, M. Schwarzwälder, A. J. Rossini, F. Aussenac, M. Yulikov, G. Jeschke, C. Coperet, A. Lesage, P. Tordo and L. Emsley, *J. Am. Chem. Soc.*, 2013, **135**, 12790–12797.

45 Ü. Akbey, A. H. Linden and H. Oschkinat, *Appl. Magn. Reson.*, 2012, **43**, 81–90.

46 A. J. Rossini, A. Zagdoun, M. Lelli, D. Gajan, F. Rascón, M. Rosay, W. E. Maas, C. Copéret, A. Lesage and L. Emsley, *Chem. Sci.*, 2012, **3**, 108–115.

47 M. Lelli, D. Gajan, A. Lesage, M. A. Caporini, V. Vitzthum, P. Miéville, F. Héroguel, F. Rascón, A. Roussey, C. Thieuleux, M. Boualleg, L. Veyre, G. Bodenhausen, C. Copéret and L. Emsley, *J. Am. Chem. Soc.*, 2011, **133**, 2104–7.

48 K. R. Thurber, A. Potapov, W.-M. Yau and R. Tycko, *J. Magn. Reson.*, 2013, **226**, 100–106.

49 K. R. Thurber and R. Tycko, *J. Chem. Phys.*, 2012, **137**, 84508–84514.

50 D. Shimon, Y. Hovav, A. Feintuch, D. Goldfarb and S. Vega, *Phys. Chem. Chem.*

Phys., 2012, **14**, 5729–5743.

51 B. Vuichoud, J. Milani, A. Bornet, R. Melzi, S. Jannin and G. Bodenhausen, *J. Phys. Chem. B*, 2014, **118**, 1411–1415.

52 A. Flori, M. Liserani, F. Frijia, G. Giovannetti, V. Lionetti, V. Casieri, V. Positano, G. D. Aquaro, F. a. Recchia, M. F. Santarelli, L. Landini, J. H. Ardenkjaer-Larsen and L. Menichetti, *Contrast Media Mol. Imaging*, 2015, **10**, 194–202.

53 J. Wolber, F. Ellner, B. Fridlund, A. Gram, H. J??hannesson, G. Hansson, L. H. Hansson, M. H. Lerche, S. M??nsson, R. Servin, M. Thaning, K. Golman and J. H. Ardenkj??r-Larsen, *Nucl. Instruments Methods Phys. Res. Sect. A Accel. Spectrometers, Detect. Assoc. Equip.*, 2004, **526**, 173–181.

54 J. H. Ardenkjaer-Larsen, B. Fridlund, A. Gram, G. Hansson, L. Hansson, M. H. Lerche, R. Servin, M. Thaning and K. Golman, *Proc. Natl. Acad. Sci. U. S. A.*, 2003, **100**, 10158–63.

55 R. W. Schurko, *Acc. Chem. Res.*, 2013, **46**, 1985–1995.

56 D. A. Hirsh, A. J. Rossini, L. Emsley and R. W. Schurko, *Phys. Chem. Chem. Phys.*, 2016, **18**, 25893–25904.

57 M. P. Hildebrand, H. Hamaed, A. M. Namespetra, J. M. Donohue, R. Fu, I. Hung, Z. Gan and R. W. Schurko, *CrystEngComm*, 2014, **16**, 7334–7356.

58 D. A. Hirsh, A. J. Rossini, L. Emsley and R. W. Schurko, *Phys. Chem. Chem. Phys.*, 2016.

59 A. M. Namespetra, D. A. Hirsh, M. P. Hildebrand, A. R. Sandre, H. Hamaed, J. M. Rawson and R. W. Schurko, *CrystEngComm*, 2016, **18**, 6213–6232.

60 C. D. Jeffries, *Dynamic Nuclear Orientation*, John Wiley, New York, 1963.

61 C. D. Jeffries, *Phys. Rev.*, 1957, **106**, 164–165.

62 A. Abragam and W. G. Proctor, *C. R. Hebd. Seances Acad. Sci.*, 1958, **246**, 2253–2256.

63 A. V. Kessenikh, V. I. Lushchikov and A. A. Manenkov, *Sov. Physics- Solid State*, 1963, **5**, 321–329.

64 C. F. Hwang and D. a. Hill, *Phys. Rev. Lett.*, 1967, **19**, 1011–1014.

65 D. S. Wollan, *Phys. Rev. B*, 1976, **13**, 3671–3685.

66 Y. Hovav, A. Feintuch and S. Vega, *J. Chem. Phys.*, 2011, **134**, 74509.

67 Y. Hovav, O. Levinkron, A. Feintuch and S. Vega, *Appl. Magn. Reson.*, 2012, **43**, 21–41.

68 Y. Hovav, A. Feintuch and S. Vega, *Phys. Chem. Chem. Phys.*, 2013, **15**, 188–203.

69 Q. Z. Ni, E. Daviso, T. V. Can, E. Markhasin, S. K. Jawla, T. M. Swager, R. J. Temkin, J. Herzfeld and R. G. Griffin, *Acc. Chem. Res.*, 2013, **46**, 1933–1941.

70 A. A. Smith, B. Corzilius, A. B. Barnes, T. Maly and R. G. Griffin, *J. Chem. Phys.*, 2012, **136**, 15101.

71 K. R. Thurber and R. Tycko, *Isr. J. Chem.*, 2014, **54**, 39–46.

72 K. R. Thurber and R. Tycko, *J. Chem. Phys.*, 2014, **140**.

73 A. Karabanov, G. Kwiatkowski and W. Köckenberger, *Appl. Magn. Reson.*, 2012, **43**, 43–58.

74 A. Karabanov, A. van der Drift, L. J. Edwards, I. Kuprov and W. Köckenberger, *Phys. Chem. Chem. Phys.*, 2012, **14**, 2658–68.

75 A. Karabanov, D. Wiśniewski, I. Lesanovsky and W. Köckenberger, *Phys. Rev. Lett.*, 2015, **115**, 20404.

76 T. Maly, G. T. Debelouchina, V. S. Bajaj, K.-N. Hu, C.-G. Joo, M. L. Mak-Jurkauskas,

J. R. Sirigiri, P. C. a van der Wel, J. Herzfeld, R. J. Temkin and R. G. Griffin, *J. Chem. Phys.*, 2008, **128**, 52211.

77 M. Bennati, *eMagRes*, 2017, **6**, 271–282.

78 D. Banerjee, D. Shimon, A. Feintuch, S. Vega and D. Goldfarb, *J. Magn. Reson.*, 2013, **230**, 212–219.

79 Y. Hovav, D. Shimon, I. Kaminker, A. Feintuch, D. Goldfarb and S. Vega, *Phys. Chem. Chem. Phys.*, 2015, **17**, 6053–6065.

80 I. Solomon, *Phys. Rev.*, 1955, **99**, 559–565.

81 R. V. P. E.M. Purcell, *Phys. Rev.*, 1948, 679–746.

82 F. Mentink-Vigier, Ü. Akbey, Y. Hovav, S. Vega, H. Oschkinat and A. Feintuch, *J. Magn. Reson.*, 2012, **224**, 13–21.

83 W. T. Wenckebach, *J. Magn. Reson.*, 2017, **277**, 68–78.

84 S. C. Serra, A. Rosso and F. Tedoldi, *Phys. Chem. Chem. Phys.*, 2012, **14**, 13299–13308.

85 A. G. Redfield, *Phys. Rev.*, 1955, **98**, 1787.

86 B. Provotorov, *Zh. Exsp. Teor. Fiz*, 1962, **14**, 1126–1131.

87 I. Solomon, in *Magnetic and Electric Resonance and Relaxation*, ed. J. Smidt, Amsterdam: North-Holland, 1963, p. 25.

88 M. Goldman, *Spin temperature and nuclear magnetic resonance in solids*, Clarendon Press, Oxford, 1970.

89 V. A. Atsarkin and A. V. Kessenikh, *Appl. Magn. Reson.*, 2012, **43**, 7–19.

90 K. Kundu, A. Feintuch and S. Vega, *J. Phys. Chem. Lett.*, 2018, **9**, 1793–1802.

91 Y. Hovav, I. Kaminker, D. Shimon, A. Feintuch, D. Goldfarb and S. Vega, *Phys. Chem.*

Chem. Phys., 2014, 17, 226–44.

92 I. Kaminker, D. Shimon, Y. Hovav, A. Feintuch and S. Vega, *Phys. Chem. Chem. Phys.*, 2016, **18**, 11017–11041.

93 W. T. Wenckebach, *J. Magn. Reson.*, 2017, **284**, 104–114.

94 D. Shimon, A. Feintuch, D. Goldfarb and S. Vega, *Phys. Chem. Chem. Phys.*, 2014, **16**, 6687–99.

95 D. Banerjee, D. Shimon, A. Feintuch, S. Vega and D. Goldfarb, *J. Magn. Reson.*, 2013, **230**, 212–219.

96 A. Leavesley, D. Shimon, T. A. Siaw, A. Feintuch, D. Goldfarb, S. Vega, I. Kaminker and S. Han, *Phys. Chem. Chem. Phys.*, 2017, **19**, 3596–3605.

97 A. Equbal, Y. Li, A. Leavesley, A. Rajca and S. Han, *J. Phys. Chem. Lett.*

98 Y. Hovav, I. Kaminker, D. Shimon, A. Feintuch, D. Goldfarb and S. Vega, *Phys. Chem. Chem. Phys.*, 2015, **17**, 226–244.

99 A. Leavesley, C. B. Wilson, M. S. Sherwin and S. Han, *Phys. Chem. Chem. Phys.*, 2018, **20**, 9897–9903.

100 S. K. Jain, T. A. Siaw, A. Equbal, C. B. Wilson, I. Kaminker and S. Han, *J. Phys. Chem. C*, 2018, **122**, 5578–5589.

101 K. N. Hu, C. Song, H. H. Yu, T. M. Swager and R. G. Griffin, *J. Chem. Phys.*, 2008, **128**, 52302.

102 H. Takahashi, C. Fernández-De-Alba, D. Lee, V. Maurel, S. Gambarelli, M. Bardet, S. Hediger, A. L. Barra and G. De Paëpe, *J. Magn. Reson.*, 2014, **239**, 91–99.

103 A. A. Smith, B. Corzilius, O. Haze, T. M. Swager and R. G. Griffin, *J. Chem. Phys.*, 2013, **139**, 214201.

104 A. Feintuch, D. Shimon, Y. Hovav, D. Banerjee, I. Kaminker, Y. Lipkin, K. Zibzener, B. Epel, S. Vega and D. Goldfarb, *J. Magn. Reson.*, 2011, **209**, 136–141.

105 P. A. S. Cruickshank, D. R. Bolton, D. A. Robertson, R. I. Hunter, R. J. Wylde and G. M. Smith, *Rev. Sci. Instrum.*, 2009, **80**, 103012.

106 J. Leggett, R. Hunter, J. Granwehr, R. Panek, A. J. Perez-Linde, A. J. Horsewill, J. McMaster, G. Smith and W. Kockenberger, *Phys. Chem. Chem. Phys.*, 2010, **12**, 5883–5892.

107 J. Granwehr, J. Leggett and W. Köckenberger, *J. Magn. Reson.*, 2007, **187**, 266–276.

108 A. A. Smith, B. Corzilius, J. A. Bryant, R. Derocher, P. P. Woskov, R. J. Temkin and R. G. Griffin, *J. Magn. Reson.*, 2012, **223**, 170–179.

109 L. R. Becerra, G. J. Gerfen, B. F. Bellew, J. A. Bryant, D. A. Hall, S. J. Inati, R. T. Weber, S. Un, T. F. Prisner, A. E. Mcdermott, K. W. Fishbein, K. E. Kreischer, R. J. Temkin, D. J. Singel and R. G. Griffin, *J. Magn. Reson. Ser. A*, 1995, **117**, 28–40.

110 T. A. Siaw, A. Leavesley, A. Lund, I. Kaminker and S. Han, *J. Magn. Reson.*, 2016, **264**, 131–153.

111 B. D. Armstrong, T. Edwards, Devin, J. Wylde, Richard, A. Walker, Shamon and S. Han, *Phys. Chem. Chem. Phys.*, 2010, **12**, 5920–5926.

112 G. W. Morley, L. C. Brunel and J. van Tol, *Rev. Sci. Instrum.*, 2008, **79**, 64703.

113 T. Dubroca, J. Mckay, X. Wang and J. van Tol, *IEEE Int. Microw. Symp.*, 2017, 1400–1403.

114 F. H. Cho, V. Stepanov, C. Abeywardana and S. Takahashi, in *Methods in Enzymology*, Elsevier Inc., 1st edn., 2015, vol. 563, pp. 95–118.

115 F. H. Cho, V. Stepanov and S. Takahashi, *Rev. Sci. Instrum.*, 2014, **85**, 75110.

116 M. Bennati, C. T. Farrar, J. A. Bryant, S. J. Inati, V. Weis, G. J. Gerfen, P. Riggs-Gelasco, J. Stubbe and R. G. Griffin, *J. Magn. Reson.*, 1999, **138**, 232–243.

117 M. M. Hertel, V. P. Denysenkov, M. Bennati and T. F. Prisner, *Magn. Reson. Chem.*, 2005, **43**, 248–255.

118 D. T. Edwards, S. Takahashi, M. S. Sherwin and S. Han, *J. Magn. Reson.*, 2012, **223**, 198–206.

119 D. T. Edwards, Z. Ma, T. J. Meade, D. Goldfarb, S. Han and M. S. Sherwin, *Phys. Chem. Chem. Phys.*, 2013, **15**, 11313–11326.

120 E. Reijerse, P. P. Schmidt, G. Klihm and W. Lubitz, *Appl. Magn. Reson.*, 2007, **31**, 611–626.

121 K. A. Earle and J. H. Freed, *Appl. Magn. Reson.*, 1999, **16**, 247–272.

122 Bruker, 2018.

123 H. Blok, J. A. J. M. Disselhorst, S. B. Orlinskii and J. Schmidt, *J. Magn. Reson.*, 2004, **166**, 92–99.

124 H. Blok, J. A. J. M. Disselhorst, H. Van Der Meer, S. B. Orlinskii and J. Schmidt, *J. Magn. Reson.*, 2005, **173**, 49–53.

125 Y. A. Grishin, M. R. Fuchs, A. Schnegg, A. A. Dubinskii, B. S. Dumesh, F. S. Rusin, V. L. Bratman and K. Möbius, *Rev. Sci. Instrum.*, 2004, **75**, 2926–2936.

126 K. Möbius, A. Savitsky, A. Schnegg, M. Plato and M. Fuchst, *Phys. Chem. Chem. Phys.*, 2005, **7**, 19–42.

127 K. Thurber and R. Tycko, *J. Magn. Reson.*, 2016, **264**, 99–106.

128 K. R. Thurber, A. Potapov, W. M. Yau and R. Tycko, *J. Magn. Reson.*, 2013, **226**, 100–106.

129 K. R. Thurber, W. M. Yau and R. Tycko, *J. Magn. Reson.*, 2010, **204**, 303–313.

130 A. Carroll and K. Zilm, *Priv. Commun.*, 2017, **July**.

131 A. Leavesley, I. Kaminker and S. Han, in *DNP Handbook*, eds. V. K. Michaelis, R. G. Griffin, S. Vega and B. Corzilius, Wiley&Sons, 1st edn., 2018.

132 I. Kaminker, R. Barnes and S. Han, *J. Magn. Reson.*, 2017, **279**, 81–90.

133 H. Y. Chen, Y. Kim, P. Nath and C. Hilty, *J. Magn. Reson.*, 2015, **255**, 100–105.

134 K. Takeda, *J. Magn. Reson.*, 2008, **192**, 218–229.

135 M. Lelli, S. R. Chaudhari, D. Gajan, G. Casano, A. J. Rossini, O. Ouari, P. Tordo, A. Lesage and L. Emsley, *J. Am. Chem. Soc.*, 2015, **137**, 14558–14561.

136 M.-A. Geiger, M. Orwick-Rydmark, K. Märker, W. T. Franks, D. Akhmetzyanov, D. Stöppler, M. Zinke, E. Specker, M. Nazaré, A. Diehl, B.-J. van Rossum, F. Aussenac, T. Prisner, Ü. Akbey and H. Oschkinat, *Phys. Chem. Chem. Phys.*, 2016, **18**, 30696–30704.

137 M. Rosay, L. Tometich, S. Pawsey, R. Bader, R. Schauwecker, M. Blank, P. M. Borchard, S. R. Cauffman, K. L. Felch, R. T. Weber, R. J. Temkin, R. G. Griffin and W. E. Maas, *Phys. Chem. Chem. Phys.*, 2010, **12**, 5850–5860.

138 D. Lee, E. Bouleau, P. Saint-Bonnet, S. Hediger and G. De Paëpe, *J. Magn. Reson.*, 2016, **264**, 116–124.

139 Y. Matsuki, T. Idehara, J. Fukazawa and T. Fujiwara, *J. Magn. Reson.*, 2016, **264**, 107–115.

140 B. E. Sturgeon and R. D. Britt, *Rev. Sci. Instrum.*, 1992, **63**, 2187–2192.

141 C. E. Davoust, P. E. Doan and B. M. Hoffman, *J. Magn. Reson. - Ser. A*, 1996, **119**, 38–44.

142 B. Biospin, 2018.

143 A. V. Astashkin, J. H. Enemark and A. Raitsimring, *Concepts Magn. Reson. Part B Magn. Reson. Eng.*, 2006, **35**, 125–136.

144 C. and P. Industries, 2018.

145 A. E. I. Systems, 2018.

146 Bruker, 2018.

147 M. Rosay, L. Tometich, S. Pawsey, R. Bader, R. Schauwecker, M. Blank, P. M. Borchard, S. R. Cauffman, K. L. Felch, R. T. Weber, R. J. Temkin, R. G. Griffin and W. E. Maas, *Phys. Chem. Chem. Phys.*, 2010, **12**, 5850–5860.

148 C. and P. Industries, 2018.

149 V. D. Inc, 2018.

150 Elva-1, 2018.

151 A. I. Smirnov and A. Nezerov, *High powered W-Band sources to boost high frequency power output*, 2017.

152 T. Kaufmann, T. J. Keller, J. M. Franck, R. P. Barnes, S. J. Glaser, J. M. Martinis and S. Han, *J. Magn. Reson.*, 2013, **235**, 95–108.

153 I. Kaminker, R. Barnes and S. Han, *J. Magn. Reson.*, 2017, **279**, 81–90.

154 K. A. Earle, D. S. Tipikin and J. H. Freed, *Rev. Sci. Instrum.*, 1996, **67**, 2502.

155 P. F. Goldsmith, *Quasioptical Systems: Gaussian Beam Quasioptical Propagation and Applications*, IEEE Press, New York, 1998.

156 B. Marsden, V. Lim, B. Taber and A. Zens, *J. Magn. Reson.*, 2016, **268**, 25–35.

157 B. Taber and A. Zens, *J. Magn. Reson.*, 2015, **259**, 114–120.

158 B. Epel, 2018.

159 E. L. Hahn, *Phys. Rev.*, 1950, **80**, 580–594.

160 S. A. Self, *Appl. Opt.*, 1983, **22**, 658.

161 E. J. Kowalski, D. S. Tax, M. a. Shapiro, J. R. Sirigiri, R. J. Temkin, T. S. Bigelow and D. a. Rasmussen, *IEEE Trans. Microw. Theory Tech.*, 2010, **58**, 2772–2780.

162 R. Abrams, *IEEE J. Quantum Electron.*, 1972, **8**, 838–843.

163 M. K. Thumm and W. Kasparek, *IEEE Trans. Plasma Sci.*, 2002, **30**, 755–786.

164 T. A. Siaw, M. Fehr, A. Lund, A. Latimer, S. A. Walker, D. T. Edwards and S.-I. Han, *Phys. Chem. Chem. Phys.*, 2014, **16**, 18694.

165 A. Schweiger and G. Jeschke, *Principles of Pulsed Electron Paramagnetic Resonance Spectroscopy*, Oxford University Press, New York, 2001.

166 A. Nalepa, K. Möbius, W. Lubitz and A. Savitsky, *J. Magn. Reson.*, 2014, **242**, 203–213.

167 A. Potapov, B. Epel and D. Goldfarb, *J. Chem. Phys.*, 2008, **128**, 52320.

168 P. Schosseler, T. Wacker and A. Schweiger, *Chem. Phys. Lett.*, 1994, **224**, 319–324.

169 M. Florent, I. Kaminker, V. Nagarajan and D. Goldfarb, *J. Magn. Reson.*, 2011, **210**, 192–199.

170 A. Nalepa, K. Möbius, W. Lubitz and A. Savitsky, *J. Magn. Reson.*, 2014, **242**, 203–213.

171 N. Cox, W. Lubitz and A. Savitsky, *Mol. Phys.*, 2013, **111**, 2788–2808.

172 N. Cox, W. Lubitz and A. Savitsky, *Mol. Phys.*, 2013, **111**, 2788–2808.

173 J. Baum, R. Tycko and A. Pines, *Phys. Rev. A*, 1985, **32**, 3435–3447.

174 J. M. Bohlen, M. Rey and G. Bodenhausen, *J. Magn. Reson.*, 1989, **84**, 191–197.

175 D. Kunz, *Magn. Reson. Med.*, 1986, **3**, 377–384.

176 A. Doll, S. Pribitzer, R. Tschaggelar and G. Jeschke, *J. Magn. Reson.*, 2013, **230**, 27–39.

177 A. Doll, M. Qi, S. Pribitzer, N. Wili, M. Yulikov, A. Godt and G. Jeschke, *Phys. Chem. Chem. Phys.*, 2015, **17**, 7334–7344.

178 P. E. Spindler, S. J. Glaser, T. E. Skinner and T. F. Prisner, *Angew. Chemie - Int. Ed.*, 2013, **52**, 3425–3429.

179 P. E. Spindler, I. Waclawska, B. Endeward, J. Plackmeyer, C. Ziegler and T. F. Prisner, *J. Phys. Chem. Lett.*, 2015, **6**, 4331–4335.

180 P. Schöps, P. E. Spindler, A. Marko and T. F. Prisner, *J. Magn. Reson.*, 2015, **250**, 55–62.

181 M. Tseitlin, R. W. Quine, G. A. Rinard, S. S. Eaton and G. R. Eaton, *J. Magn. Reson.*, 2011, **213**, 119–125.

182 T. Kaufmann, T. J. Keller, J. M. Franck, R. P. Barnes, S. J. Glaser, J. M. Martinis and S. Han, *J. Magn. Reson.*, 2013, **235**, 95–108.

183 M. A. Smith, H. Hu and A. J. Shaka, *J. Magn. Reson.*, 2001, **151**, 269–283.

184 T. E. Skinner, T. O. Reiss, B. Luy, N. Khaneja and S. J. Glaser, *J. Magn. Reson.*, 2003, **163**, 8–15.

185 K. Kobzar, T. E. Skinner, N. Khaneja, S. J. Glaser and B. Luy, *J. Magn. Reson.*, 2008, **194**, 58–66.

186 S. C. Serra, A. Rosso and F. Tedoldi, *Phys. Chem. Chem. Phys.*, 2013, **15**, 8416–8428.

187 A. De Luca, I. R. Arias, M. Müller and A. Rosso, *Phys Rev B*, 2016, **94**, 14203.

188 A. Karabanov, G. Kwiatkowski and W. Köckenberger, *Mol. Phys.*, 2014, **112**, 1838–1854.

189 D. Wišniewski, A. Karabanov, I. Lesanovsky and W. Köckenberger, *J. Magn. Reson.*, 2016, **264**, 30–38.

190 D. Shimon, Y. Hovav, I. Kaminker, A. Feintuch, D. Goldfarb and S. Vega, *Phys. Chem. Chem. Phys.*, 2015, **17**, 11868–11883.

191 D. Shimon, Y. Hovav, I. Kaminker, A. Feintuch, D. Goldfarb and S. Vega, *Phys. Chem. Chem. Phys.*, 2015, **17**, 11868–11883.

192 E. Bordignon, H. Brutlach, L. Urban, K. Hideg, A. Savitsky, A. Schnegg, P. Gast, M. Engelhard, E. J. J. Groenen, K. Möbius and H. J. Steinhoff, *Appl. Magn. Reson.*, 2010, **37**, 391–403.

193 I. Kaminker and S. Han, *J. Phys. Chem. Lett.*, 2018, **In Press**.

194 A. Lund, 2017.

195 D. Sezer, M. J. Prandolini and T. F. Prisner, *Phys. Chem. Chem. Phys.*, 2009, **11**, 6626–6637.

196 R. E. Hurd, Y. F. Yen, A. Chen and J. H. Ardenkjaer-Larsen, *J. Magn. Reson. Imaging*, 2012, **36**, 1314–1328.

197 V. Berejnov, N. S. Husseini, O. A. Alsaied and R. E. Thorne, *J. Appl. Crystallogr.*, 2006, **39**, 244–251.

198 D. Banerjee and S. V. Bhat, *J. Non. Cryst. Solids*, 2009, **355**, 2433–2438.

199 E. R. Georgieva, A. S. Roy, V. M. Grigoryants, P. P. Borbat, K. A. Earle, C. P. Scholes and J. H. Freed, *J. Magn. Reson.*, 2012, **216**, 69–77.

200 E. P. Kirilina, I. A. Grigoriev and S. A. Dzuba, *J. Chem. Phys.*, 2004, **121**, 12465.

201 D. Lee, S. Hediger and G. De Paëpe, *Solid State Nucl. Magn. Reson.*, 2015, **66**–**67**, 6–20.

202 K. Murata and H. Tanaka, *Nat. Mater.*, 2012, **11**, 436–443.

203 K. Murata and H. Tanaka, *Nat. Commun.*, 2013, **4**, 1–8.

204 Y. Hayashi, A. Puzenko, I. Balin, Y. E. Ryabov and Y. Feldman, *J. Physcial Chem. B*, 2005, **109**, 9174–9177.

205 I. Popov, A. Greenbaum (Gutina), A. P. Sokolov and Y. Feldman, *Phys. Chem. Chem. Phys.*, 2015, **17**, 18063–18071.

206 D. A. Jahn, J. Wong, J. Bachler, T. Loerting and N. Giovambattista, *Phys. Chem. Chem. Phys.*, 2016, **18**, 11042–11057.

207 J. Bachler, V. Fuentes-Landete, D. A. Jahn, J. Wong, N. Giovambattista and T. Loerting, *Phys. Chem. Chem. Phys.*, 2016, **18**, 11058–11068.

208 K. Murata and H. Tanaka, *Nat. Commun.*, 2013, **4**, 1–8.

209 Y. Hayashi, A. Puzenko, I. Balin, Y. E. Ryabov and Y. Feldman, *J. Physcial Chem. B*, 2005, **109**, 9174–9177.

210 I. Popov, A. Greenbaum (Gutina), A. P. Sokolov and Y. Feldman, *Phys. Chem. Chem. Phys.*, 2015, **17**, 18063–18071.

211 D. A. Jahn, J. Wong, J. Bachler, T. Loerting and N. Giovambattista, *Phys. Chem. Chem. Phys.*, 2016, **18**, 11042–11057.

212 J. Bachler, V. Fuentes-Landete, D. A. Jahn, J. Wong, N. Giovambattista and T. Loerting, *Phys. Chem. Chem. Phys.*, 2016, **18**, 11058–11068.

213 A. Puzenko, Y. Hayashi, Y. E. Ryabov, I. Balin, Y. Feldman, U. Kaatze and R. Behrends, *J. Phys. Chem. B*, 2005, **109**, 6031–6035.

214 E. Bordignon, A. I. Nalepa, A. Savitsky, L. Braun and G. Jeschke, *J. Physcial Chem. B*, 2015, **119**, 13797–13806.

215 E. Bordignon, H. Brutlach, L. Urban, K. Hideg, A. Savitsky, A. Schnegg, P. Gast, M. Engelhard, E. J. J. Groenen, K. Möbius and H. J. Steinhoff, *Appl. Magn. Reson.*, 2010, **37**, 391–403.

216 E. P. Kirilina, T. F. Prisner, M. Bennati, B. Endeward, S. A. Dzuba, M. R. Fuchs, K. Möbius and A. Schnegg, *Magn. Reson. Chem.*, 2005, **43**, 119–129.

217 M. N. Berberan-Santos, E. N. Bodunov and B. Valeur, *Chem. Phys.*, 2005, **315**, 171–182.

218 H. Sato, V. Kathirvelu, G. Spagnol, S. Rajca, A. Rajca, S. S. Eaton and G. R. Eaton, *J. Phys. Chem. B*, 2008, **112**, 2818–2828.

219 E. P. Kirilina, I. A. Grigoriev and S. A. Dzuba, *J. Chem. Phys.*, 2004, **121**, 12465.

220 G. Mathies, M. A. Caporini, V. K. Michaelis, Y. Liu, K. Hu, D. Mance, J. L. Zweier, M. Rosay, M. Baldus and R. G. Griffin, *Angew. Chemie - Int. Ed.*, 2015, **54**, 11770–11774.

221 A. B. Barnes, M. L. Mak-Jurkauskas, Y. Matsuki, V. S. Bajaj, P. C. A. van der Wel, R. DeRocher, J. Bryant, J. R. Sirigiri, R. J. Temkin, J. Lugtenburg, J. Herzfeld and R. G. Griffin, *J. Magn. Reson.*, 2009, **198**, 261–270.

222 F. Jähnig, G. Kwiatkowski, A. Däpp, A. Hunkeler, B. H. Meier, S. Kozerke and M. Ernst, *Phys. Chem. Chem. Phys.*, 2017, **19**, 19196–19204.

223 L. Lumata, M. E. Merritt, C. R. Malloy, A. D. Sherry and Z. Kovacs, *J. Phys. Chem. A*, 2012, **116**, 5129–38.

224 A. Flori, M. Liserani, S. Bowen, J. H. Ardenkjaer-Larsen and L. Menichetti, *J. Phys. Chem. A*, 2015, **119**, 1885–93.

225 L. Lumata, Z. Kovacs, A. D. Sherry, C. Malloy, S. Hill, J. van Tol, L. Yu, L. Song and

M. E. Merritt, *Phys. Chem. Chem. Phys.*, 2013, **15**, 9800.

226 I. Marin-Montesinos, J. C. Paniagua, A. Peman, M. Vilaseca, F. Luis, S. Van Doorslaer and M. Pons, *Phys. Chem. Chem. Phys.*, 2016, **18**, 3151–3158.

227 I. Marin-Montesinos, J. C. Paniagua, M. Vilaseca, A. Urtizberea, F. Luis, M. Feliz, F. Lin, S. Van Doorslaer and M. Pons, *Phys. Chem. Chem. Phys.*, 2015, **17**, 5785–5794.

228 I. Marin-Montesinos, J. C. Paniagua, M. Vilaseca, A. Urtizberea, F. Luis, M. Feliz, F. Lin, S. Van Doorslaer and M. Pons, *Phys. Chem. Chem. Phys.*, 2015, **17**, 5785–5794.

229 I. Marin-Montesinos, J. C. Paniagua, A. Peman, M. Vilaseca, F. Luis, S. Van Doorslaer and M. Pons, *Phys. Chem. Chem. Phys.*, 2016, **18**, 3151–3158.

230 H. Chen, A. G. Maryasov, O. Y. Rogozhnikova, D. V. Trukhin, V. M. Tormyshev and M. K. Bowman, *Phys. Chem. Chem. Phys.*, 2016, **18**, 24954–24965.

231 H. Chen, A. G. Maryasov, O. Y. Rogozhnikova, D. V. Trukhin, V. M. Tormyshev and M. K. Bowman, *Phys. Chem. Chem. Phys.*, 2016, **18**, 24954–24965.

232 S. J. Nelson, J. Kurhanewicz, D. B. Vigneron, P. E. Z. Larson, A. L. Harzstark, M. Ferrone, M. Van Criekinge, J. W. Chang, R. Bok, I. Park, G. Reed, L. Carvajal, E. J. Small, P. Munster, V. K. Weinberg, J. H. Ardenkjaer-Larsen, A. P. Chen, R. E. Hurd, L.-I. Odegardstuen, F. J. Robb, J. Tropp and J. A. Murray, *Sci Transl Med*, 2013, **5**.

233 C. H. Cunningham, J. Y. C. Lau, A. P. Chen, B. J. Geraghty, W. J. Perks, I. Roifman, G. A. Wright and K. A. Connelly, *Circ. Res.*, 2016, **119**, 1177–1182.

234 A. P. Chen, J. Y. C. Lau, R. D. A. Alvares and C. H. Cunningham, *Magn. Reson. Med.*, 2015, **73**, 2087–2093.

235 C. Guglielmetti, C. Najac, A. Didonna, A. Van der Linden, S. M. Ronen and M. M. Chaumeil, *Proc. Natl. Acad. Sci.*, 2017, **114**, E6982–E6991.

236 S. Jannin, A. Bornet, R. Melzi and G. Bodenhausen, *Chem. Phys. Lett.*, 2012, **549**, 99–102.

237 A. Bornet, A. Pinon, A. Jhajharia, M. Baudin, X. Ji, L. Emsley, G. Bodenhausen, J. H. Ardenkjaer-Larsen and S. Jannin, *Phys. Chem. Chem. Phys.*, 2016, **18**, 30530–30535.

238 A. Bornet, J. Milani, B. Vuichoud, A. J. Perez Linde, G. Bodenhausen and S. Jannin, *Chem. Phys. Lett.*, 2014, **602**, 63–67.

239 H. Jóhannesson, S. Macholl and J. H. Ardenkjaer-Larsen, *J. Magn. Reson.*, 2009, **197**, 167–175.

240 L. L. Lumata, R. Martin, A. K. Jindal, Z. Kovacs, M. S. Conradi and M. E. Merritt, *Magn. Reson. Mater. Physics, Biol. Med.*, 2015, **28**, 195–205.

241 H. A. I. Yoshihara, E. Can, M. Karlsson, M. H. Lerche, J. Schwitter and A. Comment, *Phys. Chem. Chem. Phys.*, 2016, **18**, 12409–12413.

242 S. a Walker, D. T. Edwards, T. A. Siaw, B. D. Armstrong and S. Han, *Phys. Chem. Chem. Phys.*, 2013, **15**, 15106–20.

243 F. Jähnig, G. Kwiatkowski, A. Däpp, A. Hunkeler, B. H. Meier, S. Kozerke and M. Ernst, *Phys. Chem. Chem. Phys.*, 2017, **19**, 19196–19204.

244 G. Mathies, M. A. Caporini, V. K. Michaelis, Y. Liu, K. N. Hu, D. Mance, J. L. Zweier, M. Rosay, M. Baldus and R. G. Griffin, *Angew. Chemie - Int. Ed.*, 2015, **54**, 11770–11774.

245 S. K. Jain, G. Mathies and R. G. Griffin, *J. Chem. Phys.*, 2017, **147**, 164201.

246 A. Bornet, A. Pinon, A. Jhajharia, M. Baudin, X. Ji, L. Emsley, G. Bodenhausen, J. H. Ardenkjaer-Larsen and S. Jannin, *Phys. Chem. Chem. Phys.*, 2016, **18**, 30530–30535.

247 J. Gordon, I. Rowland, E. Peterson and S. Fain, *Proc. 19th Sci. Meet. Int. Soc. Magn.*

Reson. Med., 2011, **19**, 2011.

248 D. T. Peat, A. J. Horsewill, W. Köckenberger, A. J. P. Linde, D. G. Gadian and J. R. Owers-Bradley, *Phys. Chem. Chem. Phys.*, 2013, **15**, 7586.

249 A. Kiswandhi, B. Lama, P. Niedbalski, M. Goderya, J. Long and L. Lumata, *RSC Adv.*, 2016, **6**, 38855–38860.

250 D. T. Peat, A. J. Horsewill, W. Köckenberger, A. J. P. Linde, D. G. Gadian and J. R. Owers-Bradley, *Phys. Chem. Chem. Phys.*, 2013, **15**, 7586.

251 J. Zhang, P. P. Fatouros, C. Shu, J. Reid, L. S. Owens, T. Cai, H. W. Gibson, G. L. Long, F. D. Corwin, Z. J. Chen and H. C. Dorn, *Bioconjug. Chem.*, 2010, **21**, 610–615.

252 S. Stevenson, J. P. Phillips, J. E. Reid, M. M. Olmstead, P. Rath and A. L. Balch, *Chem. Commun.*, 2004, 2814–2815.

253 C. Ramanathan, *Appl. Magn. Reson.*, 2008, **34**, 409–421.

254 D. J. Kubicki, G. Casano, M. Schwarzwälder, S. Abel, C. Sauvée, K. Ganesan, M. Yulikov, A. J. Rossini, G. Jeschke, C. Copéret, A. Lesage, P. Tordo, O. Ouari and L. Emsley, *Chem. Sci.*, 2016, **7**, 550–558.

255 C. Sauvée, M. Rosay, G. Casano, F. Aussenac, R. T. Weber, O. Ouari and P. Tordo, *Angew. Chemie - Int. Ed.*, 2013, **52**, 10858–10861.

256 C. Sauvée, G. Casano, S. Abel, A. Rockenbauer, D. Akhmetzyanov, H. Karoui, D. Siri, F. Aussenac, W. Maas, R. T. Weber, T. Prisner, M. Rosay, P. Tordo and O. Ouari, *Chem. - A Eur. J.*, 2016, **22**, 5598–5606.

257 J. H. Ardenkjaer-Larsen, A. M. Leach, N. Clarke, J. Urbahn, D. Anderson and T. W. Skloss, *NMR Biomed.*, 2011, **24**, 927–932.

258 S. Reynolds and H. Patel, *Appl. Magn. Reson.*, 2008, **34**, 495–508.

259 A. B. Barnes, B. Corzilius, M. L. Mak-Jurkauskas, L. B. Andreas, V. S. Bajaj, Y. Matsuki, M. L. Belenky, J. Lugtenburg, J. R. Sirigiri, R. J. Temkin, J. Herzfeld and R. G. Griffin, *Phys. Chem. Chem. Phys.*, 2010, **12**, 5861–5867.

260 A. S. Lilly Thankamony, J. J. Wittmann, M. Kaushik and B. Corzilius, *Prog. Nucl. Magn. Reson. Spectrosc.*, 2017, **102**–**103**, 120–195.

261 S. Stoll, B. Epel, S. Vega and D. Goldfarb, *J. Chem. Phys.*, 2007, **127**.

262 J. Clore, G. Marius; Iwahara, *Chem. Rev.*, 2009, **109**, 4108–4139.

263 J. Iwahara, C. D. Schwieters and G. M. Clore, *J. Am. Chem. Soc.*, 2004, **126**, 5879–5896.

264 C. P. Jaroniec, *J. Magn. Reson.*, 2015, **253**, 50–59.

265 W. E. Blumberg, *Phys. Rev.*, 1960, **119**, 79–84.

266 C. P. Jaroniec, *J. Magn. Reson.*, 2015, **253**, 50–59.

267 J. Van Houten, W. T. Wenckebach and N. J. Poulis, *Physica*, 1977, **92B**, 201–209.

268 J. Van Houten, W. T. Wenckebach and N. J. Poulis, *Physica*, 1977, **92B**, 210–220.

269 S. Stoll, B. Epel, S. Vega and D. Goldfarb, *J. Chem. Phys.*, 2007, **127**.

270 W. M. Yau, K. R. Thurber and R. Tycko, *J. Magn. Reson.*, 2014, **244**, 98–106.

271 A. Rajca, Y. Wang, M. Boska, J. T. Paletta, A. Olankitwanit, M. A. Swanson, D. G. Mitchell, S. S. Eaton, G. R. Eaton and S. Rajca, *J. Am. Chem. Soc.*, 2012, **134**, 15724–15727.

272 S. Chandrasekhar, *Rev. Mod. Phys.*, 1943, **15**, 1–89.

273 B. Corzilius, *Phys. Chem. Chem. Phys.*, 2016, **18**, 27190–27204.

274 G. Mathies, S. Jain, M. Reese and R. G. Griffin, *J. Phys. Chem. Lett.*, 2016, **7**, 111–116.

275 M. K. Kiesewetter, B. Corzilius, A. A. Smith, R. G. Griffin and T. M. Swager, *J. Am. Chem. Soc.*, 2012, **134**, 4537–40.

276 Y. Matsuki, T. Maly, O. Ouari, H. Karoui, F. Le Moigne, E. Rizzato, S. Lyubenova, J. Herzfeld, T. Prisner, P. Tordo and R. G. Griffin, *Angew. Chemie*, 2009, **121**, 5096–5100.

277 E. L. Dane, B. Corzilius, E. Rizzato, P. Stocker, T. Maly, A. A. Smith, R. G. Griffin, O. Ouari, P. Tordo and T. M. Swager, *J. Org. Chem.*, 2012, **77**, 1789–97.

278 A. Zagdoun, G. Casano, O. Ouari, M. Schwarzwälder, A. J. Rossini, F. Aussenac, M. Yulikov, G. Jeschke, C. Copéret, A. Lesage, P. Tordo and L. Emsley, *J. Am. Chem. Soc.*, 2013, **135**, 12790–12797.

279 K. R. Thurber, W.-M. Yau and R. Tycko, *J. Magn. Reson.*, 2010, **204**, 303–313.

280 W.-M. Yau, K. R. Thurber and R. Tycko, *J. Magn. Reson.*, 2014, **244**, 98–106.

281 P. Gast, D. Mance, E. Zurlo, K. L. Ivanov, M. Baldus and M. Huber, *Phys. Chem. Chem. Phys.*, 2017, **19**, 3777–3781.

282 E. A. Rakhmanov, E. B. Saff and Y. M. Zhou, *Math. Res. Lett.*, 1994, **1**, 647–662.

283 D. E. M. Hoff, B. J. Albert, E. P. Saliba, F. J. Scott, E. J. Choi, M. Mardini and A. B. Barnes, *Solid State Nucl. Magn. Reson.*, 2015, **72**, 79–89.

284 A. B. Barnes, E. a. Nanni, J. Herzfeld, R. G. Griffin and R. J. Temkin, *J. Magn. Reson.*, 2012, **221**, 147–153.

285 Y. Matsuki, T. Idehara, J. Fukazawa and T. Fujiwara, *J. Magn. Reson.*, 2016, **264**, 107–115.

286 V. D. Inc, 2018.

287 A. H. Linden, W. T. Franks, Ü. Akbey, S. Lange, B. J. Van Rossum and H. Oschkinat,

J. Biomol. NMR, 2011, **51**, 283–292.

288 L. Kulik, B. Epel, J. Messinger and W. Lubitz, *Photosynth. Res.*, 2005, **84**, 347–353.

289 A. Rajca, S. Mukherjee, M. Pink and S. Rajca, *J. Am. Chem. Soc.*, 2006, **128**, 13497–13507.

290 C. Guglielmetti, C. Najac, A. Didonna, A. Van der Linden, S. M. Ronen and M. M. Chaumeil, *Proc. Natl. Acad. Sci.*, 2017, **114**, E6982–E6991.

291 D. Goldfarb, Y. Lipkin, A. Potapov, Y. Gorodetsky, B. Epel, A. M. Raitsimring, M. Radoul and I. Kaminker, *J. Magn. Reson.*, 2008, **194**, 8–15.

292 I. Kaminker, H. Goldberg, R. Neumann and D. Goldfarb, *Chem. - A Eur. J.*, 2010, **16**, 10014–10020.

293 A. Dinse, A. Ozarowski, C. Hess, R. Schomäcker and K. P. Dinse, *J. Phys. Chem. C*, 2008, **112**, 17664–17671.

294 G. Deo, I. E. Wachs and J. Haber, *Crit. Rev. Surf. Chemsitry*, 1994, **4**, 141–187.

295 B. M. Weckhuysen and D. E. Keller, *Catal. Today*, 2003, **78**, 25–46.

296 M. Rosay, M. Blank and F. Engelke, *J. Magn. Reson.*, 2016, **264**, 88–98.

297 Q. Z. Ni, E. Daviso, T. V. Can, E. Markhasin, S. K. Jawla, T. M. Swager, R. J. Temkin, J. Herzfeld and R. G. Griffin, *Acc. Chem. Res.*, 2013, **46**, 1933–1941.

298 V. S. Bajaj, M. K. Hornstein, K. E. Kreischer, J. R. Sirigiri, P. P. Woskov, M. L. Mak-Jurkauskas, J. Herzfeld, R. J. Temkin and R. G. Griffin, *J. Magn. Reson.*, 2007, **189**, 251–279.

299 V. S. Bajaj, C. T. Farrar, M. K. Hornstein, I. Mastovsky, J. Vieregg, J. Bryant, B. Eléna, K. E. Kreischer, R. J. Temkin and R. G. Griffin, *J. Magn. Reson.*, 2003, **160**, 85–90.

300 S. Jawla, E. Nanni, M. Shapiro, I. Mastovsky, W. Guss, R. Temkin and R. Griffin, in

2011 International Conference on Infrared, Millimeter, and Terahertz Waves, IEEE, 2011, pp. 1–2.

301 T. Idehara, K. Kosuga, L. Agusu, I. Ogawa, H. Takahashi, M. E. Smith and R. Dupree, *J. Infrared, Millimeter, Terahertz Waves*, 2010, **31**, 763–774.

302 N. Kumar, U. Singh and A. K. Sinha, *Infrared Phys. Technol.*, 2015, **68**, 44–51.

303 L. Becerra, G. Gerfen, R. Temkin, D. Singel and R. Griffin, *Phys. Rev. Lett.*, 1993, **71**, 3561–3564.

304 Y. Matsuki, K. Ueda, T. Idehara, R. Ikeda, I. Ogawa, S. Nakamura, M. Toda, T. Anai and T. Fujiwara, *J. Magn. Reson.*, 2012, **225**, 1–9.

305 T. Idehara, Y. Tatematsu, Y. Yamaguchi, E. M. Khutoryan, a. N. Kuleshov, K. Ueda, Y. Matsuki and T. Fujiwara, *J. Infrared, Millimeter, Terahertz Waves*, 2015, **36**, 613–627.

306 J. Leggett, R. Hunter, J. Granwehr, R. Panek, A. J. Perez-Linde, A. J. Horsewill, J. McMaster, G. Smith and W. Kockenberger, *Phys. Chem. Chem. Phys.*, 2010, **12**, 5741–5751.

307 A. A. Smith, B. Corzilius, J. A. Bryant, R. DeRocher, P. P. Woskov, R. J. Temkin and R. G. Griffin, *J. Magn. Reson.*, 2012, **223**, 170–179.

308 A. Feintuch, D. Shimon, Y. Hovav, D. Banerjee, I. Kaminker, Y. Lipkin, K. Zibzener, B. Epel, S. Vega and D. Goldfarb, *J. Magn. Reson.*, 2011, **209**, 136–141.

309 A. Zens, *Pers. Commun.*, 2016, January.

310 P. Bowyer, J. Finnigan, B. Marsden, B. Taber and A. Zens, *J. Magn. Reson.*, 2015, **261**, 190–198.

311 T. A. Siaw, S. A. Walker, B. D. Armstrong and S.-I. Han, *J. Magn. Reson.*, 2012, **221**,

5–10.

312 P. F. Goldsmith, in *Quasioptical Systems*, IEEE Press, 1998, pp. 168–170.

313 J. L. Doane, in *Infrared and Millimeter Waves*, ed. K. J. Button, Academic Press Inc., New York, 1985, pp. 123–170.

314 F. Mentink-Vigier, S. Paul, D. Lee, A. Feintuch, S. Hediger, S. Vega and G. De Paëpe, *Phys. Chem. Chem. Phys.*, 2015, **17**, 21824–21836.

315 M.-A. Geiger, M. Orwick-Rydmark, K. Märker, W. T. Franks, D. Akhmetzyanov, D. Stöppler, M. Zinke, E. Specker, M. Nazaré, A. Diehl, B.-J. van Rossum, F. Aussenac, T. Prisner, Ü. Akbey and H. Oschkinat, *Phys. Chem. Chem. Phys.*, 2016, **18**, 30696–30704.

316 D. T. Edwards, Y. Zhang, S. J. Glaser, S. Han and M. S. Sherwin, *Phys. Chem. Chem. Phys.*, 2013, **15**, 5707–19.

317 E. Bordignon, A. I. Nalepa, A. Savitsky, L. Braun and G. Jeschke, *J. Physcial Chem. B*, 2015, **119**, 13797–13806.

8. Appendix A: Currently available hardware world-wide

An overview of the current capabilities in DNP systems is provided in table 9.1, where a more detailed review of current DNP instrumentation – both commercial and home-built – is provided in the reviews by Siaw et. al.,[110] Thankamony et. al.,[260] Rosay et. al.,[296] and Ni et. al.[297] This list is by no means exhaustive and does not list where commercial systems have been installed, but it is provided to showcase the broad range of instrument capabilities that are currently available. It is important to note that this quick overview presents both MAS and static based DNP instrumentation as well as those specialized towards dDNP. The μw-sources in these modern systems are primarily either gyrotron- or diode-based sources. A key difference is that gyrotron, while outputting larger $P_{\mu w}$ have much smaller frequency bandwidths of ~3 GHz, while a solid-state μw source can easily have over a 10 GHz bandwidth; however, these sources only produce $P_{\mu w}$ in the milliwatts. This is discussed further in section 2.5, while chapter 2 overall focuses on solid-state μw sources.

Table 8.1. Summary of primary modern ssDNP spectrometers and their current capabilities.

System	Field	Temperature	MW source output	Current system capabilities
Gyrotron-powered DNP	9.4 T 14 T 18.8 T	> 90 K	5-35 W	MAS acquisition, field swept DNP[109,221,284,298–303]
	9.4 T[304] 14 T[138] 16.4 T[285,305]	30 K	5-35 W	MAS acquisition, field swept DNP spectra
Dissolution DNP	3.35 T/94 GHz[54] 5 T/140 GHz 6.7 T/180 GHz[238]	1.2 K	90 mW (diode)	Field/Frequency modulation, Frequency swept DNP, MRI metabolic imaging, dDNP, commercial 5 T system: SPINlab^{TM} by GE Healthcare
Nottingham Kockenberger lab dissolution DNP/EPR	3.35 T/94 GHz polarization /9.4 T NMR detection	1-2 K	180 mW (diode)	Frequency swept DNP spectra, dDNP (polarize at 3.35 T and detect solution NMR at 9.4 T), frequency swept cw-EPR, quasi optical system[107]
	3.35 T / 94 GHz	1.5 K	200 mW (diode)	Pulsed/cw-EPR, frequency & amplitude modulation, frequency swept DNP (650 MHz bandwidth), dDNP, ELDOR[306]
MIT Griffin lab DNP/EPR	5 T / 140 GHz	1.4-290 K	120 mW (diode)	Pulsed & field swept echo-EPR, frequency swept DNP, ELDOR, ENDOR, static NMR acquisition[307]
Weizmann Institute Vega and Goldfarb DNP/EPR	3.34 T / 94 GHz	2.5-290 K	1 W (diode)	Pulsed/cw-EPR, frequency modulation, frequency swept DNP, ELDOR, static NMR acquisition[291,308]
NIH Tycko lab DNP	9.4 T / 263 GHz	20-290 K	0.8 W (EIO) 30 mW (diode)	MAS acquisition, frequency swept DNP (diode source only), field sweep, quasi optical system, cooling via helium and spinning with nitrogen[48,129]
UCSB Han lab DNP/EPR	7 T / 194 GHz	3-290 K	140 mW x2 (diode) & 400 mW (diode)	Pulsed and cw-EPR, frequency swept DNP, static and MAS NMR acquisition, quasi optical system, AWG functionality, 2-source ELDOR[110,111,131,153]

9. Appendix B: Hardware components

B.1. Theory behind inductively coupled NMR coils

The signal to noise ratio (SNR) in NMR is partially determined by the quality of the radio frequency (RF) coil used and the overall circuity of the RF probe. For high resolution NMR, probe designs require high fidelity, robustness, and efficiency, while idealized probes need to be versatile such that multiple nuclei can be manipulated simultaneously. In most commercial probe designs, elements of original probes dating back to the birth of NMR can be seen. For all that we have increased the number of possible resonances and improved the probe efficiency through impressive engineering feats, not many significant advances to RF probe design have happened in recent or even not so recent years. However, circuit design is quite different now than it was in the 1960's and 1970's. Back then the common practice was to implement many ground points into the design, while current circuit designs tend to minimize ground points.[309] The reason behind minimizing the number of ground points is because not all ground points are the same and in some cases, there can even be no common ground point. These pseudo-ground points act as additional resistors in the circuit.[309] It was based on this paradigm shift that resulted in Zens and coworkers to re-design the basic circuitry behind the NMR probe in the past five years.

To minimize the number of grounding points in the probe, Zens and coworkers switched from capacitively coupled coils to inductively coupled coils. In capacitive probes, additional ground points are required, which complicates the return path to the absolute ground, where erroneous ground points add resistance to the probe and reduce the efficiency of acquiring NMR signal.[157] An inductively coupled probe minimizes the ground points, such that only the 50 Ω ports for the matching circuits are grounded.

In order to compare the efficiency of NMR coils, Zens and coworkers developed a method to describe the efficiency of circuits called circuit filling factor (CFF), which is described by

$$CFF_{k,a} = \frac{L_a i_a^2}{\sum_{j=1}^{N} L_j i_j^2} \qquad (9.1)^{157}$$

Here *L* is the inductance and *i* is the current in the inductor, where the *j* indices indicate specific inductors in the circuit. This is complementary to the traditionally used sample filling factor (SFF), where the SFF specifically utilizes the transverse component of the *B* field and its influence on the sample, while the CFF looks at the total field for each inductor in the circuit. The two filling factors are complementary to each other.[157] In an experiment, the SNR is proportional to the square of the composite of both the SFF and CFF. One key feature of the CFF is that the sum of each individual inductors' CFF in a circuit equals one, which means that each of the inductors in the circuit will also follow an energy sum rule.[157] The energy sum of the CFF directly shows that each additional inductor in the circuit will degrade the performance of the original circuit; therefore, careful thought is required to assess the need and use for each inductor and to be wary of additional inductors.[157] Zens notes that this concept is not unknown to the NMR community, as additional resonances introduced into a system, such as ^{2}H, will degrade the performance of ^{1}H. The additional ground points in traditional circuits, which create grounding loops can act as inductors and degrade the circuit's performance even further. It is important to point out that the number of resonances in a circuit cannot exceed the number of inductors in the circuit.

To further reduce the number of ground points when using magnetically coupled circuits, inductively coupled circuits can be used instead of capacitively coupled circuits.[156] The authors specify that in inductively coupled circuits, the circuit can be broken into two components the sample resonator insert (SRI), which is a simple ungrounded LC circuit, and a parent inductor circuit. The parent circuit has the tuning and matching circuitry, while the SRI surrounds the sample. The SRI can be inside the parent circuit or not; when inside the parent circuit, the natural resonances of the SRI will be shifted. For a double resonant circuit, the lower frequency resonance will be redshifted and the higher frequencies will be blueshifted.[3] Another reason to favor inductive coupling over capacitive coupling, is that inductively coupled circuits require less wires and leads, which will lower the overall resistance of the probe's circuit.[310]

The reduction of ground points and the versatility of inductively coupled NMR coils presented by Toby Zens and coworkers prompted their use in the 194 GHz system in the Han group at UCSB. The ability to tune these inductively coupled coils robustly and easily at cryogenic temperatures is an added benefit. The design of our system's inductively coupled NMR coils (developed in collaboration with Toby Zens and Ting Ann Siaw (formerly a Han lab member and now in the employ of Jeol)) are easy to construct and use detailed descriptions of the construction are provided in Appendix B.2.

B.2. Construction of inductively coupled NMR coils

Although NMR has been around for over 60 years, the lack of commercially available NMR probes that can access cryogenic temperatures below 100 K has motivated the construction and use of inductively coupled NMR coils. This design has robust tuning, with a wide tuning range, allowing acquisition of experiments operating from room temperature to 4

K. The use of inductive coupling also simplifies the circuitry so that only one ground point is defined, eliminating spurious resonances that are a result of grounding loops. Due to cryogenic cooling, the Q of the coil improves significantly, resulting in less rf power needed to obtain short 90 pulses < 3 μs for the ^{1}H coil. Additionally, the cheap and simple probe construction allows dedicated probes for each nuclei for single frequency operation. The basic design and underlying circuitry are shown in figure 10.1, where the only ground point is located on the pick-up loop or coupling loop.

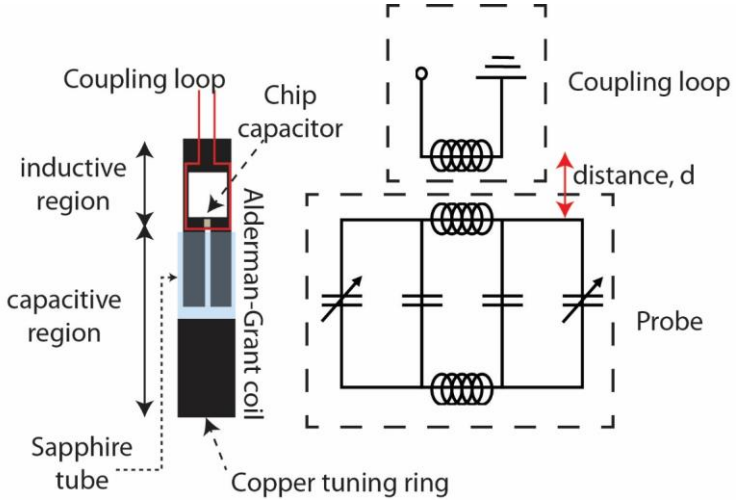

Figure 9.1. (left) Schematic of coupling loop and Alderman-Grant coil and (right) circuit diagram representing the schematic. The circuitry for the coupling loop and probe are zoned according to the dotted line boxes.

The materials needed to construct inductively coupled NMR probes are simple: copper wire, copper foil, ceramic chip capacitors, and sapphire tubes. The flat shape of the NMR coil is designed according to figure 10.2 for either Alderman-Grant (left) or saddle (right) coils and printed out on paper. In the case of the Alderman-Grant coil, the printed shape is taped onto a 0.001" bare copper foil (McMaster-Carr) and cut with a sharp pair of scissors to ensure accurate corners. The resulting copper shape is wrapped around an aluminum

mandrel and then soldered at the vertical seam (left edge to right edge in figure 10.2). Ceramic chip capacitors (American Technical Ceramics) are added to the vertical gaps right below the coil window to pre-tune the coil to the correct frequency range. In the case of the saddle coil, the printed shape is wrapped and taped around an 8.7 mm outside diameter (OD) aluminum mandrel, and a length of 20 AWG bare copper wire (McMaster-Carr) is wound according to the printed design with the aid of pliers. The wound saddle coil is then soldered onto two 0.001" thick copper foil tabs as shown below in figure 10.2. The gaps between these two tabs can then be used to solder a capacitor to pre-tune the coil to the desired frequency range. The completed coils, Alderman-Grant or saddle, are transferred to a permanent coil former, which is an 8.7 mm OD x 7.7 mm ID x 60 mm length sapphire tube (San Jose Delta Associates, Inc.). Inside the sapphire formers, copper guard rings (as shown in figure 10.3) are inserted to help define the radiofrequency (rf) region of the coil, such that the rf field is confined to the window of the coil where the sample will be located. When working with lower NMR frequencies, it is important that the copper guard rings are as flush as possible on the sapphire former, since the combination of the copper sheets and the sapphire create a tuning capacitor that functions at cryogenic temperatures. The sapphire former acts as the dielectric for this tuning capacitor. This tuning capacitor is not shown in the circuit diagram in figure 10.1 but can be thought of as additional capacitance that is in series to each of the inductive elements.

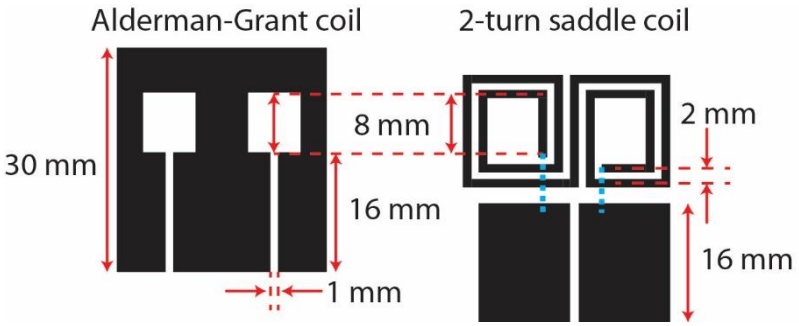

Figure 9.2. Flat printout designs used to construct an Alderman-Grant coil (> 250 MHz) or saddle coil (< 250 MHz). The blue dotted lines are connections to from the saddle coil to the copper tabs (black squares below the saddle coil).

Once the coils have been completed and secured on the sapphire former, the capacitive region can now be completed. This is done by inserting the 'skirt' of the Alderman-grant or saddle coil into a larger diameter (10 mm OD x 9 mm ID) sapphire tube. Lastly, a movable tuning ring machined from copper is slid over the 10 mm OD sapphire tube. This tuning ring is secured onto a G-10 rod with a set screw so that it can be controlled externally to provide vertical motion (figure 10.3).

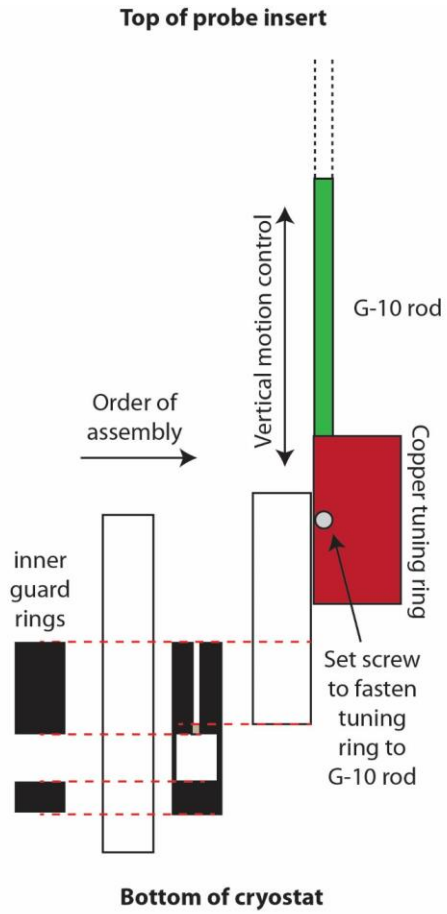

Figure 9.3. Exploded view sketch of ^{1}H probe assembly. Parts are assembled from left to right according to the arrow indicated in the figure. The components from left to right are: Copper inner guard rings, inner sapphire tube, Alderman-Grant coil, Outer sapphire tube, copper tuning ring attached to a G-10 rod using a set screw for external (room temperature) tuning.

B.3. Intermediate frequency stage for heterodyne EPR detection

All the μw electronic components used in the heterodyne detection intermediate frequency stage to generate a reference 3 GHz signal are shown in figure 10.3. The 12 GHz synthesizer outputs of the VDI transmitter and slave sources are shown on the top left corner. The frequencies of the two synthesizers are inherently offset by 187.5 MHz as described in the main text. Consequently a 187.5 MHz frequency is produced after the first mixer (Marki M10616NA). This 187.5 MHz frequency is then amplified and multiplied x16 to 3 GHz (with

filters applied to maintain spectral purity). This signal is used to drive the IQ mixer's LO channel. A 3 GHz signal originating from the sub-band mixer of the VDI receiver system is fed into the RF input of the same IQ mixer as described in the main text. Between the receiver system and the RF channel of the IQ mixer, an amplifier, an isolator, and a filter are used to provide a clean 3 GHz signal at the appropriate amplitude for the IQ mixer and protect the receiver system from reflected μw power. The outputs of the IQ mixer provide real and imaginary quadrature DC signals of the EPR signal arising from the sample.

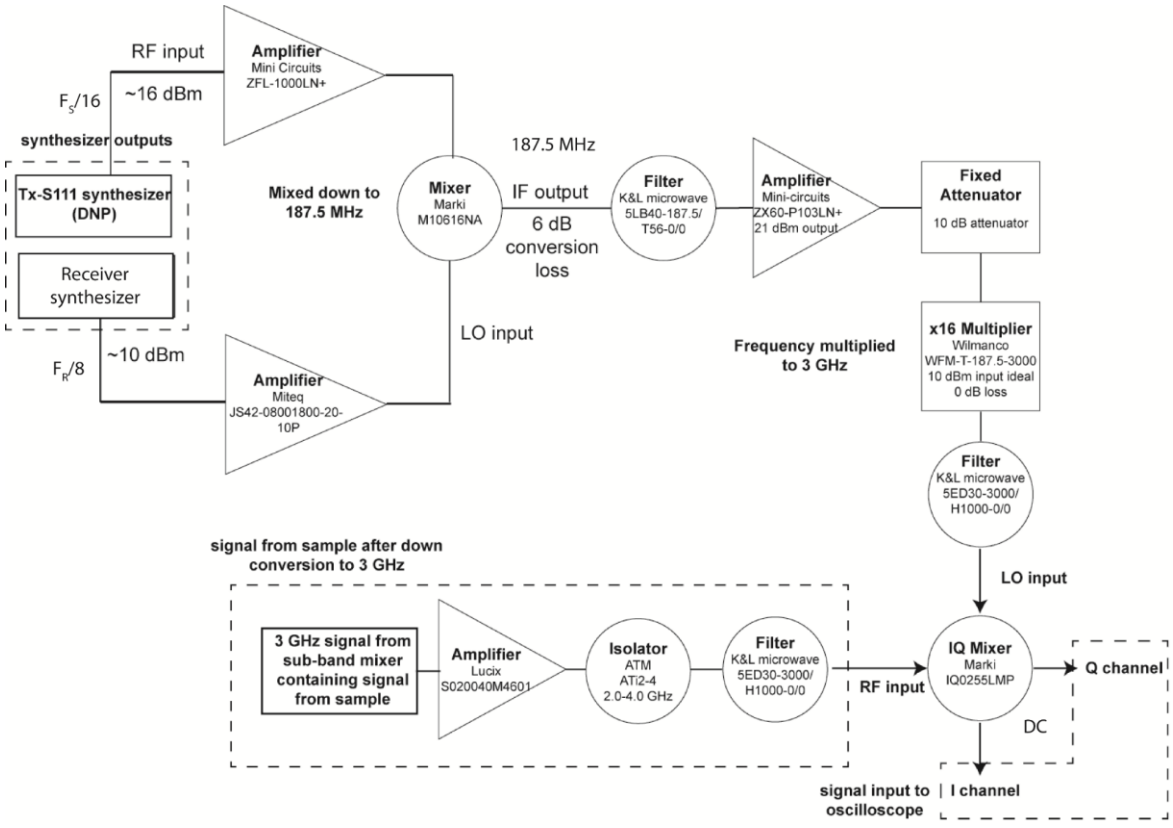

Figure 9.4. Detailed list of IF stage components for 194 GHz heterodyne detection scheme. The components shown here are used to generate a 3 GHz reference signal that is eventually fed into the LO input of the IQ Mixer.

10. Appendix C: Hardware diagnostics

Power analyses of the transmission system (μw source, quasi optics, waveguide, and waveguide extension) were performed by comparing the direct μw power output of the source to the resulting μw power after passing through each transmission system component. In this section, we will also discuss the alignment process of the μw bridge in relation to the corrugated waveguide of the DNP probe as measured by the pyroelectric detector within the magnet (see details below), where the μw bridge alignment is critical for minimizing μw loss due to imperfect coupling of the μw beam into the waveguide.

C.1. μw source performance: $P_{\mu w}$ vs. $\nu_{\mu w}$ and time

The μw power profile over (i) frequency, and (ii) time, was determined as these are the two important hardware operation parameters for characterizing μw performance for typical DNP and EPR experiments. For example, a typical nitroxide-based experiment will span over a 1-2 GHz bandwidth and will last 10 minutes to multiple hours long. This means that during such an experiment, the μw power across frequency and throughout the entire experimental time should have as little variation as possible. Using a photoacoustic power meter (Thomas Keating), the power output as a function of μw frequency (figure 11.1a) and as function of time at a set μw frequency (figure 11.1b) were measured. The μw power stability of the solid state source at a set frequency is excellent, with power fluctuations below 0.05% over > 30 hrs of continuous measurement time. This offers confidence in the quality of the data that requires long measurement times such as ^{13}C samples at liquid helium temperatures with T_{1n} values typically of a few hours.

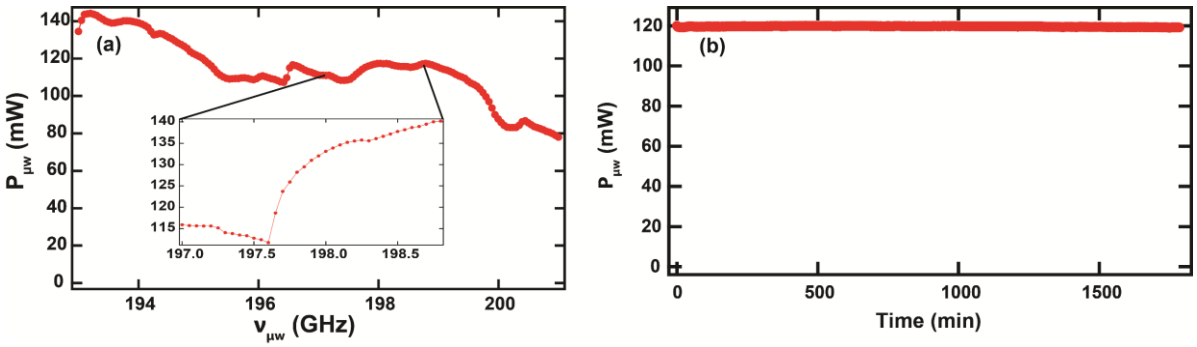

Figure 10.1. $P_{\mu w}$ output for the low power AMC a) across the full 8 GHz frequency range. The inset shows the power output across the frequency range used for obtaining DNP spectra of nitroxides between 197. 0 – 198.8 GHz (before the magnetic field was changed from 7.05 T to 6.905 T). Lines are to guide the eye. b) Source power stability at 197.7 GHz with no applied attenuation taken over 32 hours of operation. An average power output of 119.6 mW was observed with a variation of power over time < 0.05 %.

C.2. Insertion losses of quasi optical components

Three quasi optical circuits depicted in figure 11.2 (dual DNP/EPR, low-loss DNP, and Martin-Puplett DNP) are examined in detail where the measured insertion losses of all the QO components (including the μw waveguide) are tabulated in table 11.1, while the theoretical and measured total loss of the different circuits are presented in table 11.2. The procedure for determining the insertion loss for each quasi optical component, whereby all insertion loss measurements are performed with the power meter. For accurate testing of the losses associated with these components it is imperative that the E-field is parallel to the plane of the bridge and at Brewster's angle (55.5°) to the detection film of the photoacoustic power meter to minimized reflections, which allows for a frequency independent absolute power calibration. This is why additional Faraday rotators or the angle of the source itself was altered in order to achieve the required orientation of the E-field. The power losses for each

configuration are shown in figure 11.3b-e and is then compared to the power measured for the reference configuration figure 11.3a to arrive at the loss associated with each component.

When analyzing the insertion losses of the quasi optic components, the loss associated with the Martin-Puplett interferometer when linear polarization is chosen is largest (3.3 dB) compared to the other components (table 11.2), confirming that the μw beam distortion captured by the pyrocam (section 2.10.2) contributes significantly to the μw power loss, given that the interferometer components (roof mirrors, wire grid polarizer) have negligible losses (<0.05 dB). The insertion loss is only measured for linear polarization since the rotated polarization induced by the interferometer makes it very difficult to obtain polarization parallel to the bridge for an accurate power reading (i.e. the power meter cannot measure circularly polarized μw accurately). The loss associated with the flat mirror was experimentally determined to be dependent on the placement of the mirror, which corresponds to positions where the μw beam is diverging or converging. This is contrary to the theory that flat mirrors should have negligible loss, which indicates that there could be imperfections in the smoothness of the flat mirror. The observation of this position-dependent power loss associated with the flat mirror is also present in the different quasi optical circuits. Aside from these losses that are not intrinsic but solvable, the isolator and waveguide have losses of 1.3 dB and 0.45 dB, respectively, which is consistent given the expected losses of ~1 dB for a Faraday rotator that is part of the isolator. The measured power losses for each quasi optical component will allow the total loss for each circuit to be determined.

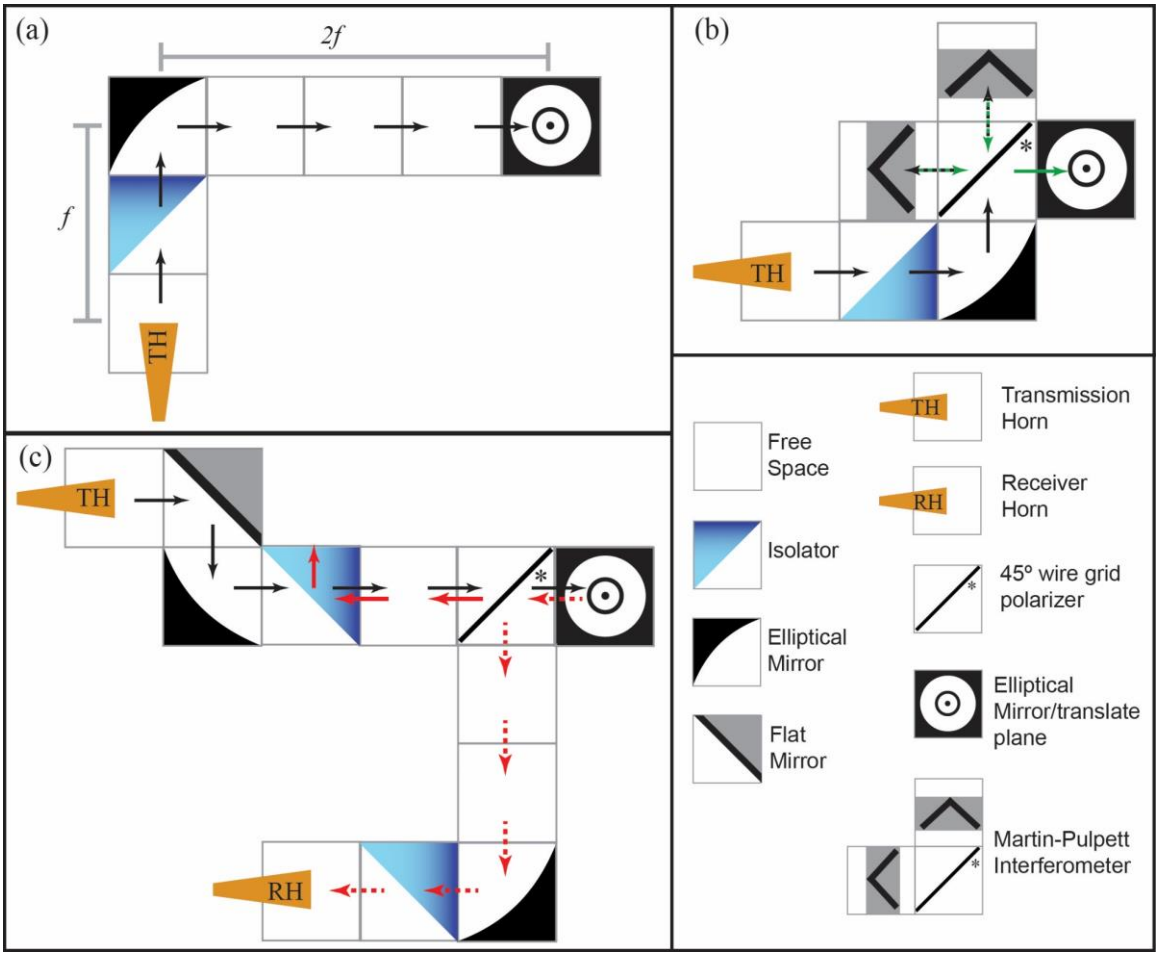

Figure 10.2. Schemes of different quasi optical circuits: (a) low-loss DNP circuit (b) Martin-Puplett DNP circuit, (c) dual DNP/EPR circuit. Each tile represents a distance of 12.5 cm (f/2). The dark portion of isolator indicates the position of the 45° Faraday rotator. Black arrows represent the incident μw beam; green arrows represent the MW beam after recombining in a Martin-Puplett interferometer; solid red arrows indicate the reflected beam not carrying the EPR signal, which are directed to a MW absorber; dashed red arrows represent the reflected beam carrying the EPR signal that is directed to the receiver horn.

*Table 10.1. Comparative loss analysis at 197.7 GHz of individual quasi optical components based on the quasi optical circuits depicted in figure 11.3(a-e). All quasi optical components were purchased from Thomas Keating Ltd. *The loss for the flat mirror is position dependent, as explained in the text above.*

Component	Insertion Loss (dB)
isolator	1.3 ± 0.2
flat mirror*	1.9 ± 0.3
waveguide	0.45 ± 0.05
Interferometer	3.3 ± 0.3

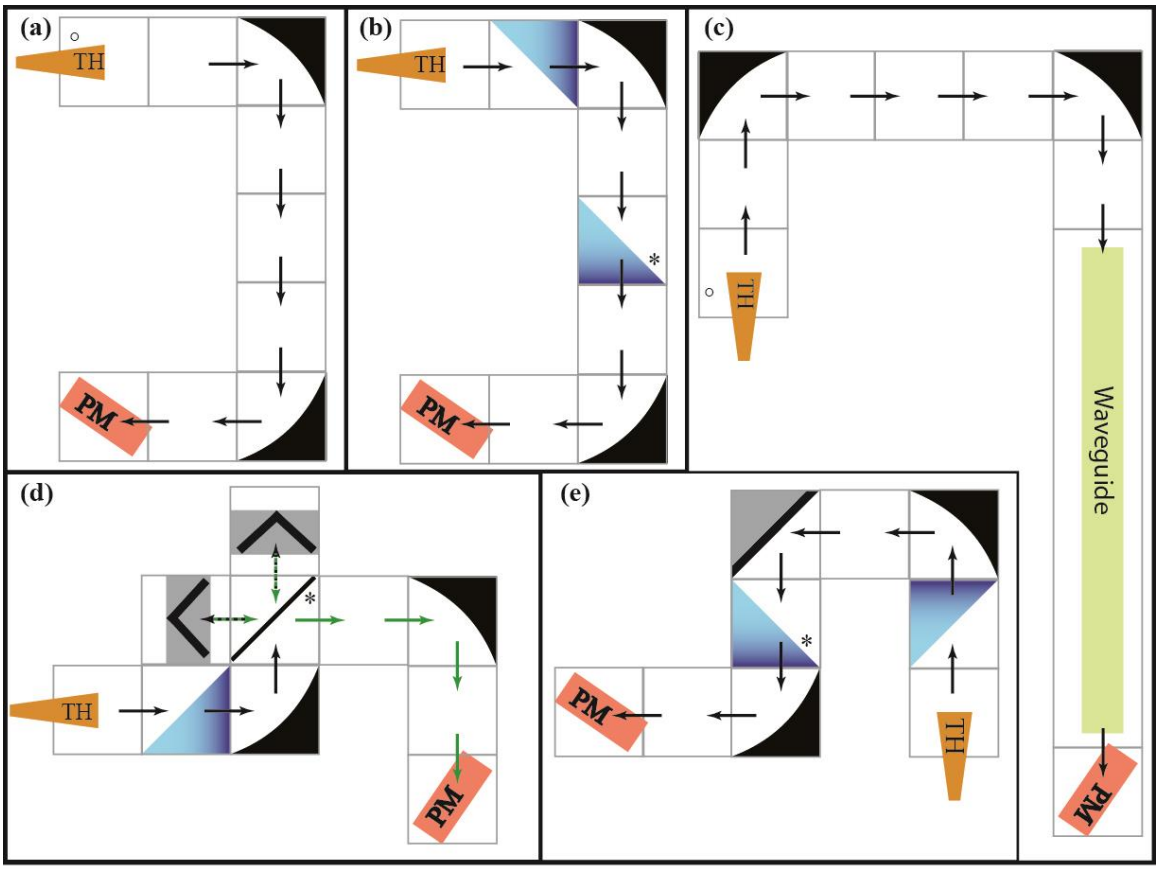

*Figure 10.3. Schematics of quasi-optical set-ups for power analysis. a) A simple 2-mirror set-up; reference configuration. b) A simple 2-mirror set-up with two isolators; for measurement of isolator insertion loss c) Simple 2-mirror set-up with waveguide; for measurement of waveguide insertion loss d) 2-mirror set-up with isolator and interferometer; for measurement of Martin-Puplett interferometer insertion loss e) Three mirror set-up with a flat mirror between the two ellipsoid mirrors; for measurement of flat mirror insertion loss. ° indicates the source is oriented such that the E-field is horizontal; otherwise, the source is oriented for a vertical E-field. Each tile represents a distance of 12.5 cm (f/2). * indicates a 45° wire grid polarizer. PM denotes the power meter.*

In table 11.2, the theoretical loss associated with all circuits were calculated from the measured insertion losses (Table 11.1) and compared to the measured power loss values obtained with the pyroelectric detector mounted at the sample position inside the magnet. The μw source is digitally modulated at 20 Hz with a SR830 lock-in amplifier (Stanford Research Systems) so that the power detected by the pyroelectric detector can be converted into a

voltage response measured by the same lock-in amplifier. In order to obtain an accurate comparison between the voltage reading of the pyroelectric and the direct μw power reading of the photoacoustic power meter, a linear calibration curve correlating the two values was made. For the dual DNP/EPR QO circuit, the power meter was used to obtain the actual loss at the position of the EPR detector.

From the theoretical loss calculations, the low-loss DNP circuit provides the least total μw power loss (2 dB) compared to the Martin-Puplett circuit (5 dB) or the dual DNP/EPR circuit (3.7 dB) at the sample position. When the insertion loss through the entire circuit is measured, the measured values are consistent with the predicted theoretical values within error. Taken together, the dual DNP/EPR QO circuit is the best compromise between low power loss and access to combined DNP and EPR capabilities (prior to transitioning to a 2-AMC configuration).

Table 10.2. Loss analysis of QO circuits. Theoretical and actual loss of the systems are provided.

QO Design	Theoretical loss (dB)	Actual loss (dB)
Martin-Pulpett	5	7 ± 1
Low-loss DNP	2	2.5 ± 0.3
Dual DNP/EPR	3.7	3.1 ± 0.05

C.3. μw bridge alignment and characterization of probe insert

The alignment between the μw bridge and the waveguide is an extremely important parameter, as this critically determines the amount of μw power loss through the waveguide. With good alignment, the total μw loss can be kept to 2% due to the coupling efficiency from

free space to the HE_{11} mode of the waveguide, as there is virtually no loss through the waveguide. To perform μw alignment, I found that maximizing the reading of the pyroelectric detector (described in Section 2.10) mounted at the sample position inside the magnet is the most efficient and accurate empirical method. To optimize μw alignment, the position of the μw bridge is varied vertically, laterally, and angularly with respect to the waveguide. The pyroelectric detector reading also provides a relative measure of μw power incident at the sample, in conjunction with the photoacoustic power meter calibration.

The pyroelectric detector mounted at the sample position can also measure the losses of different waveguide components. As such four different waveguide extensions were tested: a smooth-walled magnesium-stabilized Zirconia (International Ceramic Engineering/Thomas Keating Ltd.), a smooth-walled copper, and a corrugated thin film of gold epoxied onto CTFE or a plastic support. The insertion losses for these four extensions are tabulated in table 11.3. For the smooth walled extensions, the zirconia waveguide extension incurs a surprisingly large insertion loss of 7.46 dB (82 % μw power loss), while the simple copper waveguide extension transmits the μw power with no measurable loss. The performance of the easy-to-machine smooth copper waveguide is comparable to a corrugated waveguide extension optimized for μw transmission, and was ultimately used to acquire all data presented here. However, strong radiofrequency NMR pulses may cause eddy currents when the NMR coil is positioned too close to the solid copper waveguide extension—a problem that we did not encounter in our setup so far. With the same test, we were able to verify that one of our corrugated waveguide extensions, which had previously been shown to be low-loss [111,164,242,311] had been damaged as there was a measurable insertion loss of 1.46 dB (20 % loss in μw power). To verify the visible damage to the corrugated gold thin film was responsible

for the loss, the μw loss through this damaged waveguide extension was compared with a pristine waveguide extension with the same construction, except on a plastic support with a high ^{1}H NMR background signal. Indeed, the pristine waveguide extension did not exhibit any insertion loss, verifying our hypothesis that the discussed insertion loss was caused by mechanical damage to the thin film corrugation of the waveguide extension. The function of the waveguide extension is to contain the μw before arriving at the sample without interfering with the NMR probe performance. Since, the NMR probe is situated at the end of the waveguide extension, it is important to consider the effect of NMR background signal from the plastic support and material used to fabricate the waveguide extension. Of the four waveguide extensions examined here, the smooth copper waveguide provides the best μw containment and lowest ^{1}H background NMR signal.

Here, it is important to consider the effect of substituting a corrugated waveguide extension with a smooth walled waveguide extension. By changing from a corrugated waveguide to a smooth walled waveguide, the wavefront of the HE_{11} mode transmitted in the corrugated waveguide will be distorted.[312,313] In addition to the power losses induced by the coupling efficiency between perfectly aligned smooth walled and corrugated waveguides, any misalignment of the waveguide and the waveguide extension can result in mode conversions, such as axial offsets, tilts, and abrupt changes in radius.[163,313] The abrupt change in radius becomes significant if one was to minimize modal mismatching between the two waveguide types, where the smooth walled waveguide would have to have a radius that is 0.842 times smaller than the corrugated waveguide (see discussion in 2.7). Besides the mode conversions this would cause, there would also be significant back reflections due to the discontinuity in the waveguide radius,[313] which is extremely disadvantageous for EPR operation. The

attenuation caused by using a smooth walled waveguide extension is considered negligible over the 43 mm length of the extension. Thus in order to maximize power transmitted through the waveguide extension and minimize reflections for EPR operation, a 5.3 mm ID was used for both corrugated and smooth walled waveguide extensions. The slight power loss due to mode conversions between corrugated and smooth walled waveguides will have a minimal impact on DNP operation, since at this time we are primarily interested in the power transmitted and not the wavefront or mode transmitted. However, this will have a more significant impact for EPR operation due to the power losses from the modal mismatches by switching between corrugated and smooth walled guides becomes more relevant for the inherently low EPR signal. Finally, the distorted wavefront may not uniformly irradiate the sample's surface area, which would have the greatest impact on EPR detection. Considering μw transmission and low ^{1}H background NMR signal, the smooth walled copper waveguide was used for the rest of data presented here. In the future, we will employ a thin metal corrugated waveguide mounted on a ^{1}H background free dielectric support, or a corrugated copper waveguide.

Table 10.3. Insertion losses for four different types of waveguide extensions, calculated from the pyroelectric readings before and after the waveguide extensions.

Waveguide extension type	Insertion loss from waveguide extension, dB/%	NMR ^{1}H Background Signal
smooth copper waveguide	0/0	No background signal
gold corrugated waveguide with plastic support	0/0	Plastic support causes huge background signal
damaged gold corrugated waveguide with CTFE support	1.46/20	Epoxy resin adds small amount of background signal
zirconia waveguide	7.46/82	No background signal

C.4. Description of the Martin-Puplett based DNP quasi optics

In the Martin-Puplett based DNP circuit the vertically polarized beam exits the source transmission horn and passes through the isolator system, both described earlier, where the polarization is rotated by 45° counter-clockwise. The Gaussian beam diverges after leaving the transmission horn, but is reflected as a collimated beam off an elliptical mirror and sent through a Martin-Puplett interferometer, consisting of a vertical wire grid polarizer (labeled with *) that acts as a beam splitter and two roof mirrors that rotate the polarization by 90°. One of the roof mirrors is attached to a micrometer that provides lateral movement to adjust the pathlength between the wire grid polarizer and the movable roof mirror. The polarization of the recombined beam after the interferometer changes as a function of the pathlength difference, so that linear, circular, or elliptical polarization can be selected. The μw beam is then refocused by a second elliptical mirror into the waveguide in the probe insert.

11. Appendix D: Methods for experimental acquisition

DNP enhancements are the NMR signal with μw irradiation relative to the NMR signal without μw irradiation (S_{MWon}/S_{MWoff}). DNP profiles and power curves were obtained by measuring the DNP enhancement as a function of μw frequency ($\nu_{\mu w}$) and power ($P_{\mu w}$), respectively. Nuclear relaxation rates were measured by incrementing the delay between the rf-saturation pulse sequence and the echo-forming pulses with and without μw irradiation for T_{DNP} (DNP build-up time) and T_{1n} (spin-lattice relaxation) respectively. The integrated NMR peaks were then fitted to $M_Z(t) = M_{eq}\left[1 - \exp\left(-{}^{t}/_{T_x}\right)\right]$, where T_x is T_{DNP} and T_{1n}, respectively. Phase memory time (T_m) and electron spin lattice relaxation (T_{1e}) measurements were obtained by producing an echo with two short pulses (500 ns) that was digitized to Specman4EPR. In T_m measurements the delay between the pulses is incremented, and the resulting echo intensities are fitted to a mono-exponential. In T_{1e} measurements, a 50 ms saturation pulse proceeds the detection pulses, where the delay between the saturation and detection pulses, t_d, is incremented, and the resulting echo intensities are fitted to a bi-exponential. Electron relaxation rates were extracted by fitting the data to bi-exponential curves according to $M(t) = Aexp\left(-{bt}/_{T_{x1}}\right) + Bexp\left(-{bt}/_{T_{x2}}\right) + C$, where b was 1 for T_{1e} measurements and 2 for T_m measurements. The T_{x1} and T_{x2} were the long and short T_{1e} and T_m values, where the long terms were reported in the main text.

12. Appendix E: Chapter 4

E.1. Differentiating between eSD and ^{1}H hyperfine interaction

ELDOR spectra are the reduction of the echo intensity as a function of excitation frequency (ν_{excite}) and provide insight into the electron depolarization profile when irradiated with microwaves (μw). Experimental ELDOR spectra of the 10 mM and 40 mM 4-amino TEMPO (4AT) samples in a d_8-gylcerol/D_2O/H_2O glass at 4 K and 7 T are shown in figure 13.1 at a variety of detection frequencies (ν_{detect}) that span the entire nitroxide EPR line. Each ELDOR spectrum has a sharp strong peak that corresponds to ν_{detect}=ν_{excite}, which is the allowed transition. Additional side peaks can be identified as the forbidden single quantum transitions due to hyperfine interactions with the surrounding nuclei (these are the sharp but weaker peaks generally offset by ≤ 50 MHz for ^{14}N and 300 MHz for ^{1}H) as discussed by Florent et al.[169] In the 10 mM 4AT sample, the ^{1}H forbidden transition is seen to shift as ν_{detect} is shifted and that little to no depolarization is seen at the center of the EPR line, which was attributed to electron spectral diffusion (eSD) in higher concentration samples such as 40 mM 4AT (see main text). It is interesting to note that the large depolarization assigned as eSD in the 40 mM 4AT sample is observed independently of ν_{detect}. The central depolarization that is independent of ν_{detect} is a hallmark of significant eSD effects in a system.

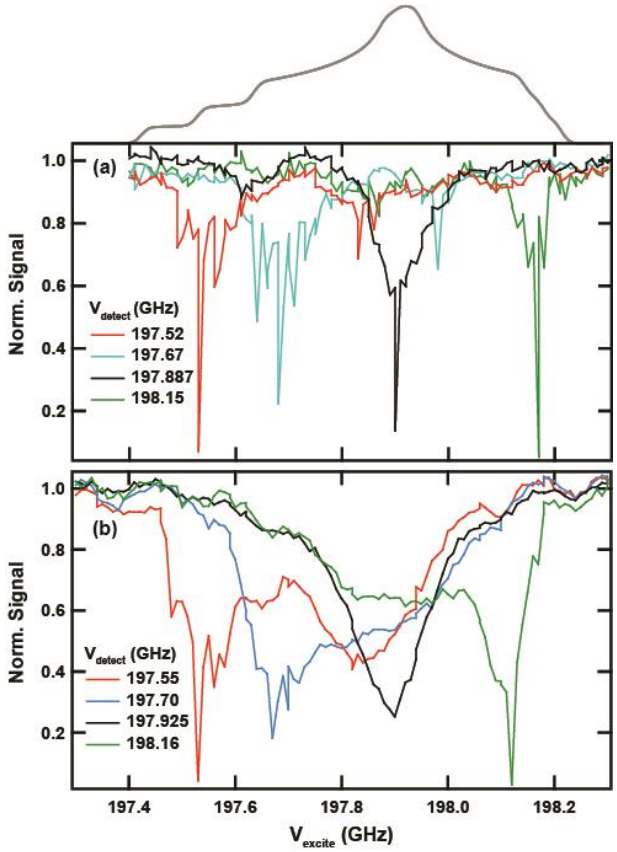

Figure 12.1. ELDOR spectra of 10 mM (a) and 40 mM (b) 4-amino TEMPO in a d_8-gylcerol/D_2O/H_2O glass at 4 K and 7 T for varying ν_{detect} as defined inside the figure. The nitroxide EPR line is above the ELDOR spectra as a reference of the relative electron populations. Experimental parameters are t_{sat} = 100 ms, repetition time = 400 ms, t_p = 500 ns, t_d = 10 μs, and τ = 500 ns.

E.2. Analysis of Δw_{DNP}

The parameter describing the width of the DNP spectrum, Δw_{DNP}, is used as a general descriptor of the overall breadth of the DNP spectra. However, to make sure that the Δw_{DNP} is an accurate representation of the DNP profiles overall lineshape, specifically its breadth, the span of experimental and simulated DNP spectra at relative signal intensities were plotted as a function of radical concentration for 12.5, 25, 50, and 75% of the signal intensity, where the span from positive to negative was considered (figure 13.2). A pictorial representation of these

spans at different signal intensities is shown in figure 13.2a, while the actual spans for simulated and experimental DNP profiles at the different signal intensities as a function of radical concentration are shown in figure 13.2b. As a function of concentration, all of the different signal intensities, except for 100% (Δ_{DNP}), show similar results, suggesting the use of Δw_{DNP} is a valid descriptor of the overall DNP spectral lineshape breadth.

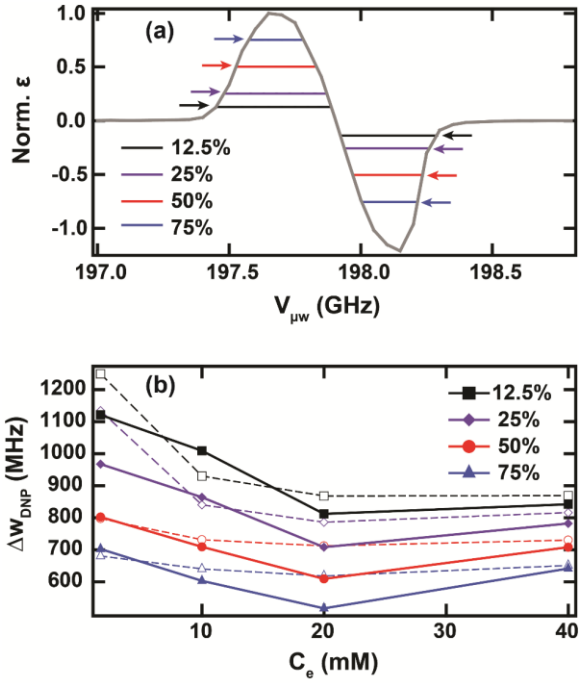

Figure 12.2. The span of the spectrum at 12.5%, 25%, 50%, and 75% is depicted in (a). Normalized experimental and simulated DNP profile widths according to the span of the profile at 12.5%, 25%, 50%, and 75% of the normalized NMR signal intensity were plotted versus radical concentration. Simulated spectra are depicted with dashed lines and experimental data is represented with solid lines, where the lines are to guide the eye. Specifically, Δw_{DNP} is when the signal intensity is 50%.

E.3. Simulation of temperature dependent DNP profiles

Simulated ELDOR curves were used to make electron depolarization profiles for a single excitation frequency, which were then used to calculate the temperature dependent simulated DNP (figure 13.3). Each ELDOR curve represents the electron depolarization spectrum as function of the excitation frequency for a single detection frequency. Compiled ELDOR curves can then be used to extract the depolarization profile for the excitation frequencies that are used for the calculation of the DNP spectrum. Three representative ELDOR curves are shown for each temperature in figure 13.3. The normalized simulated DNP spectra are in good qualitative agreement with the experimental temperature dependent data. The negative enhancement peak of the normalized simulated ELDOR spectra are consistently slightly less than one. For the experimental DNP spectra there is a slight reduction of the negative enhancement peak in the DNP spectra with increasing temperature.

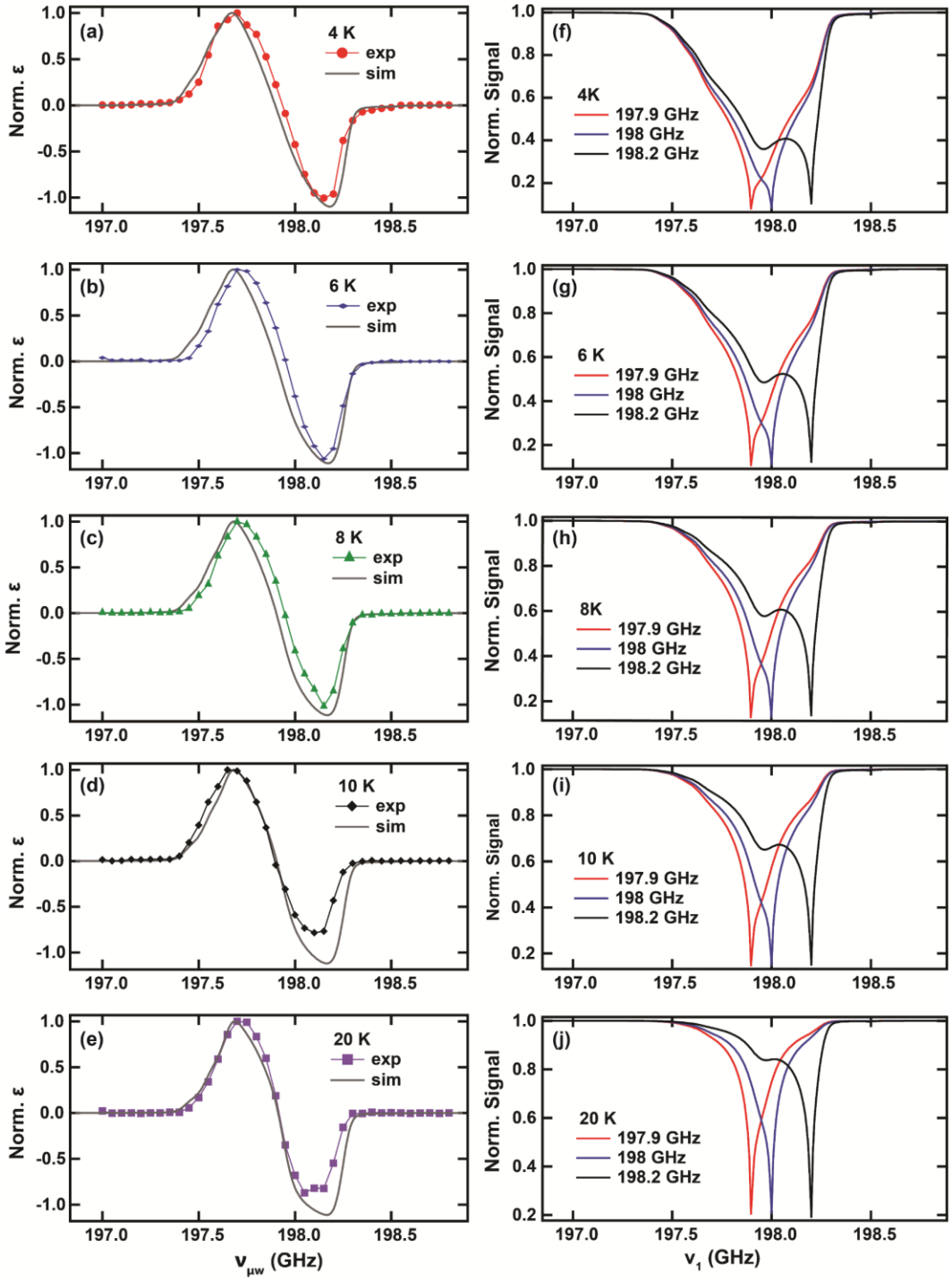

Figure 12.3. Normalized experimental and simulated DNP profiles for 40 mM 4-amino TEMPO were compared across multiple temperatures (a-e). The temperatures and designation of experimental or simulation are defined inside the figures. (f-j) Corresponding simulated ELDOR curves for the different temperatures 4K, 6K, 8K, 10K, and 20K are shown at detection frequencies ν_{detect} = 197.9 GHz (red), ν_{detect} = 198 GHz (blue), ν_{detect} = 198.2 GHz (black). The parameters used for the simulations are given in table 4.2 of the main text.

E.4. Simulated $P_{\mu w}$ dependent DNP profiles

When considering the power dependence of the 40 mM 4AT sample at 4 K, simulations where only ν_1 are varied need to be considered (figure 13.4). The simulated ELDOR curves have a minimal broadening effect with increasing ν_1. This is also reflected in the simulated DNP spectra, where the simulated DNP spectra have almost no discernible difference at low ν_1. It is interesting to note that at high enough powers, the simulated spectra result in DNP signal intensity that spans more than 1.8 GHz.

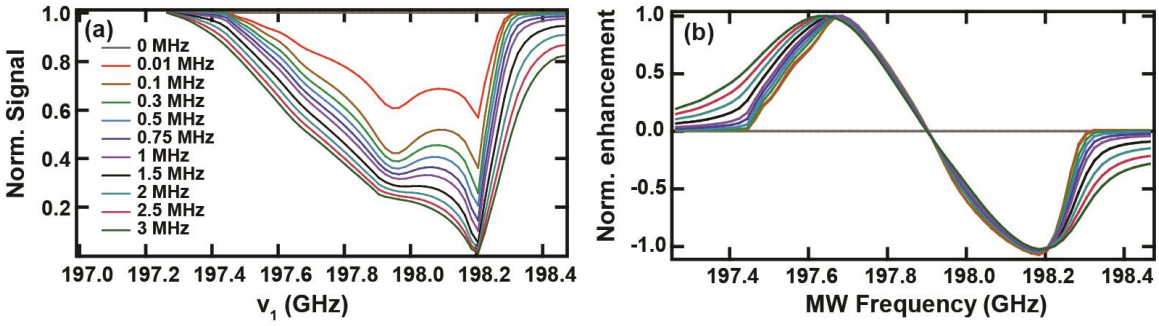

Figure 12.4. Simulated ELDOR (a) and DNP profiles (b) of 40 mM 4-amino TEMPO at 4K for varying μw irradiation strengths as defined inside the figure. The simulation assumes a constant Λ^{eSD} of 800 μs3 for each irradiation strength, ν_1, and the ELDOR curves have a detection frequency of νdetect = 198.2 GHz. The parameters used for the simulations are given in table 4.1 of the main text.

13. Appendix F: Derivation of t_{en}

In the CE, the polarization difference of two electrons, at the CE condition, gets transferred to the hyperfine coupled nuclear spin at the rate given by equation 6.5 in the main text.[260] Here we derive the effective CE Hamiltonian using average Hamiltonian theory. Note that the CE has been analyzed in detail using a three spin system by several groups as summarized in the review by Thankamony.[260] This is our perspective that results in similar predictions as those made earlier.

A three-spin system with 2 electron and 1 nuclear spins can be described by following Hamiltonian:

$$H = \Omega_{S1}S_{1z} + \Omega_{S2}S_{2z} + \omega_{0I}I_z + B_1S_{1z}I_x + B_2S_{2z}I_x + A_1S_{1z}I_z$$
$$+A_2S_{2z}I_z + d\left(2S_{1z}S_{2z} - S_{1x}S_{2x} - S_{1y}S_{2y}\right) - 2JS_1.S_2 \qquad (13.1)$$

Here Ω_{Si}, B_i, A_i and J are electron g-anisotropies, pseudo-secular, and secular hyperfine couplings with the nuclear spin and *e-e* dipole-dipole coupling respectively, and ω_{0I} is the nuclear Larmor frequency. The Hamiltonian can be rewritten in terms of zero and double quantum bases as:

$$H = (\Omega_{S1} - \Omega_{S2})\frac{(S_{1z} - S_{2z})}{2} + (\Omega_{S1} + \Omega_{S2})\frac{(S_{1z} + S_{2z})}{2} + \omega_{0I}I_z$$
$$+(B_1 - B_2)\frac{(S_{1z} - S_{2z})}{2}\ I_x + (B_1 + B_2)\frac{(S_{1z} + S_{2z})}{2}I_x + (A_1 - A_2)\frac{(S_{1z} - S_{2z})}{2}\ I_z$$
$$+(A_1 + A_2)\frac{(S_{1z}+S_{2z})}{2}I_z + (d - J)(2S_{1z}S_{2z}) - (d + 2J)(S_{1x}S_{2x} + S_{1y}S_{2y}) \qquad (13.2)$$

Using notations $\Sigma x = x_1 + x_2$ and $\Delta x = x_1 - x_2$ for $x = \Omega_s, B, A$, $S_p^{\Sigma} = (S_{1p} + S_{2p})/2$, $S_p^{\Delta} = (S_{1p} - S_{2p})/2$ for $p = x, y, z$, and $D_d = d - J$ and $D_0 = d + 2J$ equation (2) can be expressed as

$$H = \Delta\Omega_S S_z^{\Delta} + \omega_{0I} S^{\Delta} I_z + \Delta B S_z^{\Delta} I_x + \Delta A S_z^{\Delta} I_z - D_0 S_x^{\Delta} - D_d S^{\Delta}$$
$$+\Sigma\Omega_S S_z^{\Sigma} + \omega_{0I} S^{\Sigma} I_z + \Sigma B S_z^{\Sigma} I_x + \Sigma A S_z^{\Sigma} I_z + D_d S^{\Sigma} \qquad (13.3)$$

Note that we have used $S_x^{\Delta} = (S_{1x} S_{2x} + S_{1y} S_{2y})$ and $S^{\Sigma} + S^{\Delta} = 2 S_{1z} S_{2z}$. Consider the zero quantum part i.e. the terms with Δ in equation (3)

$$H^{\Delta} = \Delta\Omega_S S_z^{\Delta} + \omega_{0I} S^{\Delta} I_z + \Delta B S_z^{\Delta} I_x + \Delta A S_z^{\Delta} I_z - D_0 S_x^{\Delta} - D_d S^{\Delta} \qquad (13.4)$$

The Hamiltonian in equation (4) can be seen as a two spin Hamiltonian with one electron and one nuclear spin, which can be transformed to a tilted frame such that the *e-e* coupling and differential g-anisotropy terms can be combined to give an effective field along "*z*".

$$H^{\Delta'} = \omega_{Seff} S_{z'}^{\Delta} + \omega_{0I} S^{\Delta} I_z + \Delta B\left(S_{z'}^{\Delta} c_\theta + S_{y'}^{\Delta} s_\theta\right) I_x + \Delta A\left(S_{z'}^{\Delta} c_\theta + S_{y'}^{\Delta} s_\theta\right) I_z - D_d S^{\Delta}$$

(13.5)

Here $\omega_{Seff} = \sqrt{\Delta\Omega_S^2 + D_0^2}$, $tan\theta = D_0/\Delta\Omega_S$, and c_θ and s_θ represent cosθ and sinθ. One more frame transformation is needed to analyze the Hamiltonian in the interaction frame of nuclear Zeeman and effective electron nutation field.

$$\widetilde{H}^{\Delta\prime} = e^{-i\Omega_S S_{z'}^{\Delta} t} e^{-i\omega_{0I} S^{\Delta} I_z t} \left[\Delta B c_\theta S_{z'}^{\Delta} I_x + \Delta B s_\theta S_{y'}^{\Delta} I_x + \Delta A c_\theta S_{z'}^{\Delta} I_z + \Delta A s_\theta S_{y'}^{\Delta} I_z - D_d S^{\Delta} \right] e^{i\Omega_S S_{z'}^{\Delta} t} e^{i\omega_{0I} S^{\Delta} I_z t} \quad (13.6)$$

Now we will use the average Hamiltonian theory to determine the effective time independent Hamiltonian that can be used in the Liouville-van Neumann equation to calculate the density matrix at any given time. The only term that survives in the average Hamiltonian and leads to polarization transfer is $\Delta B s_\theta S_{y'}^{\Delta} I_x$, so we will consider this term only

$$\widetilde{H}^{\Delta\prime} = e^{-i\omega_{Seff} S_{z'}^{\Delta} t} e^{-i\omega_{0I} S^{\Delta} I_z t} \left[\Delta B s_\theta S_{y'}^{\Delta} I_x \right] e^{i\omega_{Seff} S_{z'}^{\Delta} t} e^{i\omega_{0I} S^{\Delta} I_z t} \quad (13.7)$$

This can be rearranged as follows:

$$\widetilde{H}^{\Delta\prime} = \frac{\Delta B s_\theta}{2} \begin{bmatrix} \left(S_{y'}^{\Delta} I_x + S_{x'}^{\Delta} I_y \right) c_{(\omega_{Seff} - \omega_{0I})t} - \left(S_{y'}^{\Delta} I_x - S_{x'}^{\Delta} I_y \right) c_{(\omega_{Seff} + \omega_{0I})t} \\ -\left(S_{y'}^{\Delta} I_y - S_{x'}^{\Delta} I_x \right) s_{(\omega_{Seff} - \omega_{0I})t} + \left(S_{y'}^{\Delta} I_y + S_{x'}^{\Delta} I_x \right) s_{(\omega_{Seff} + \omega_{0I})t} \end{bmatrix} \quad (13.8)$$

The effective Hamiltonian is given by

$$\bar{H}^{\Delta\prime} = \frac{1}{\tau} \int_0^{\tau} \widetilde{H}^{\Delta\prime} dt \quad (13.9)$$

The matching condition at which the effective Hamiltonian in equation (9) is non-zero is given in equation (10).

$$\omega_{Seff} \pm \omega_{0I} = 0 \tag{13.10}$$

$$\Rightarrow \sqrt{\Delta\Omega_S^2 + D_0^2} \pm \omega_{0I} = 0 \tag{13.11}$$

Assuming that $\Delta\Omega_S \gg D_0$ we get the well-known CE condition

$$\Omega_{s1} - \Omega_{s2} \pm \omega_{0I} = 0 \tag{13.12}$$

The effective Hamiltonian on the matching condition is given as follows:

$$\bar{H}^{\Delta\prime} = \frac{\Delta B s_\theta}{2}\left[\left(S_{y'}^{\Delta} I_x + S_{x'}^{\Delta} I_y\right)\right] \tag{13.13}$$

The initial density matrix can be written as

$$\rho_0 = \varepsilon_{e1} S_{1z} + \varepsilon_{e2} S_{2z} + \varepsilon_n I_z \tag{13.14}$$

Here ε_{ei} and $\varepsilon_n$are the polarizations for the two electrons and the nuclear spin, respectively. We can rewrite this in terms of the zero and double quantum operators.

$$\rho_0 = (\varepsilon_{e1} - \varepsilon_{e2}) S_z^{\Delta} + (\varepsilon_{e1} + \varepsilon_{e2}) S_z^{\Sigma} + \varepsilon_n I_z \tag{13.15}$$

The effective Hamiltonian is in a tilted frame, so the density matrix written in the same frame can be expressed as:

$$\rho_0' = \Delta\varepsilon(S_{z'}^{\Delta}c_\theta + S_{y'}^{\Delta}s_\theta) + \Sigma\varepsilon S_z^{\Sigma} + \varepsilon_n I_z \tag{13.16}$$

$$\rho_0' = (\Delta\varepsilon c_\theta - \varepsilon_n)\frac{\left(S_{z'}^{\Delta} - I_z\right)}{2} + (\Delta\varepsilon c_\theta + \varepsilon_n)\frac{\left(S_{z'}^{\Delta} + I_z\right)}{2} + S_{y'}^{\Delta}s_\theta + \Sigma\varepsilon S_z^{\Sigma} \tag{13.17}$$

The time evolution of this can be given as follows:

$$\rho_t = e^{-i\bar{H}^{\Delta'}t}\rho_0' e^{i\bar{H}^{\Delta'}t} \tag{13.18}$$

$$\rho_t = (\Delta\varepsilon c_\theta - \varepsilon_n)\left[\frac{\left(S_{z'}^{\Delta} - I_z\right)}{2}\cos\left(\frac{\Delta B s_\theta}{2}t\right) + \frac{\left(S_{x'}^{\Delta}I_x - S_{y'}^{\Delta}I_y\right)}{2}\sin\left(\frac{\Delta B s_\theta}{2}t\right)\right]$$

$$+(\Delta\varepsilon c_\theta + \varepsilon_n)\frac{\left(S_{z'}^{\Delta} + I_z\right)}{2} + S_{y'}^{\Delta}s_\theta + \Sigma\varepsilon S_z^{\Sigma} \tag{13.19}$$

At time $t = \frac{2\pi}{\Delta B s_\theta}$ the density matix is given as

$$\rho_t = -(\Delta\varepsilon c_\theta - \varepsilon_n)\frac{\left(S_{z'}^{\Delta} - I_z\right)}{2} + (\Delta\varepsilon c_\theta + \varepsilon_n)\frac{\left(S_{z'}^{\Delta} + I_z\right)}{2} + S_{y'}^{\Delta}s_\theta + \Sigma\varepsilon S_z^{\Sigma} \tag{13.20}$$

$$\rho_t = \varepsilon_n S_{z'}^{\Delta} + \Delta\varepsilon c_\theta I_z + S_{y'}^{\Delta}s_\theta + \Sigma\varepsilon S_z^{\Sigma} \tag{13.21}$$

So the polarization on the nuclear spin becomes $\Delta\varepsilon c_\theta$ as opposed to ε_n at t=0, giving a net enhancement of $(\Delta\varepsilon c_\theta - \varepsilon_n)$ at the time given in equation (22).

$$t_{en} \propto \frac{2\pi}{\Delta B\, s_\theta} \; or \; \frac{2\pi\omega_{0I}}{(B_{e_1 n} - B_{e_2 n})(d+2J)} \tag{13.22}$$

The above analysis indicates that the *e-n* polarization transfer time shortens as ΔB increases and the sum of dipolar and exchange interaction strengths and it elongates as the nuclear Larmor frequency increases. Therefore, CE is less efficient at high magnetic fields and can be affected more severely by the electron relaxation rates. Furthermore, the net polarization transfer is less than or equal to the difference of the electron spin polarizations. Note that μw irradiation was not considered in this analysis; therefore, if $\Delta\varepsilon c_\theta < \varepsilon_n$and the electron spins are at the CE condition, then nuclear depolarization can occur as has been reported in literature.

14. Appendix G: Shortening nuclear relaxation rates: MAS DNP at 92 K

The nuclear relaxation rates of 1.33 M $^{13}C_{\alpha}$-glycine in d_8-glycerol:D_2O:H_2O at 92 K under 8 kHz MAS conditions were acquired with 10 mM electron spin concentration for AMUpol (5 mM) and the dendritic radical (1.11 mM). The acquisition parameters were discussed in section 6.1 and Appendix D. The raw experimental curves for nuclear relaxation with and without μw irradiation at 263 GHz are presented in figure 15.1, where the time constants (T_{DNP} and T_{1n}, respectively) were extracted with a mono-exponential fit. The dendrimer radical was found to shorten both nuclear relaxation rates by 2-fold compared to AMU, where the $^{13}C_{\alpha}$ of glycine had a T_{DNP} of 1.97±0.33 s for dendrimer and 4.02±0.35 s for AMU, while T_{1n} was 2.12 ± 0.55 s for dendrimer and 4.25 ± 0.46 s for AMU. The shortening of nuclear relaxation rates is consistent with the experimental results obtained under static conditions and at 4 K (see section 6.3). This means the basic principles of the CE mediated *e-e-n* relaxation pathway for nuclear spins holds across wide temperature ranges and vastly different experimental conditions (spinning versus not spinning).

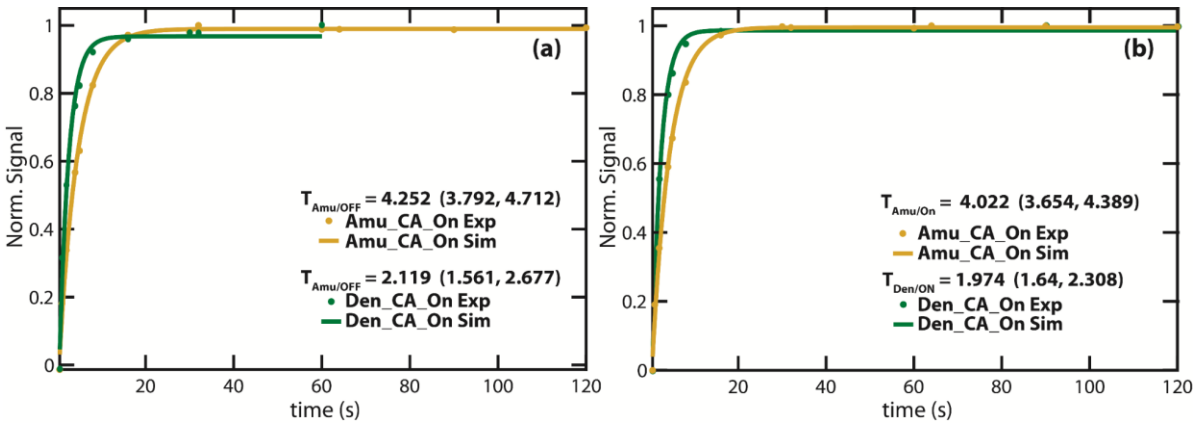

Figure 14.1. T_{1n} (a) and T_{DNP} (b) of 1.33 M ^{13}C-glycine in d_8-glyercol:D_2O:H_2O with 5 mM AMU or 1.11 mM dendrimer radical under 8 kHz MAS at 92 K with a 263 GHz gyrotron for μw irradiation. Extracted time constants are reported in the figure.

Under MAS conditions, DNP depolarization occurs, where the NMR signal without μw irradiation will decrease as the spinning speed increases. This effect causes the DNP ε to be artificially enhanced beyond reality with increasing spinning speed due to the smaller reference (off) signal. DNP depolarization with MAS has been studied by Lund[194] and the de Päepe group.[314,315] The simple normalized DNP ε ($S_{\mu won}/S_{\mu woff}$) for the dendrimer and AMU samples containing glycine at various spinning speeds and at 92 K and 400 MHz are shown in figure 15.2. Here we see that the AMU sample has a significant reduction of ε by 10-fold by reducing the spinning speed, while the dendrimer sample only had a reduction of ε by 2-fold. This is a very interesting finding, since it is generally proposed in DNP depolarization literature that strong *e-e* interactions between wide-line radicals causes more extensive DNP depolarization. The fact that we see no change in the extent of DNP depolarization with increasing spinning speed (besides the initial onset), suggests that the extensive eSD of the dendrimer system mitigates the effects of fast spinning speeds, which could be advantageous for ultra-fast MAS-DNP based experiments. This is a preliminary result, where a more thorough study of *e-e* interactions on MAS-DNP must be conducted.

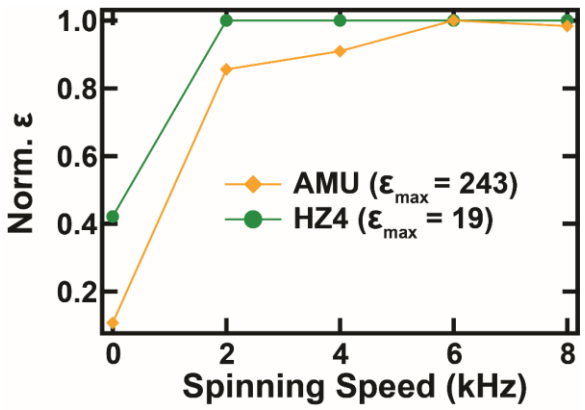

Figure 14.2. Normalized ε for 1.33 M 13C-glycine in d8-glyercol:D2O:H2O with 5 mM AMU or 1.11 mM dendrimer radical (10 mM electron spin) under 8 kHz MAS at 92 K with a 263 GHz gyrotron for μw irradiation. The maximum ε for each radical are shown inside the figure.

15. Appendix H: Rapid Passage spectra of multi-mer radicals at 8.5 T

EPR spectra normalized to the maximum signal intensity for the five radical systems in this study are presented in figure 15.1. The rapid passage EPR spectra were taken at 4.5 K and at 8.56 T on a home-built 240 GHz EPR spectrometer with heterodyne detection as has been previously described.[118,316] For each sample 10 µL of solution was placed inside a Teflon sample cup and frozen to 4.5 K via continuous flow of helium at atmospheric pressures. The spectra were acquired with a scan rate of 1 mT/min and 20 kHz modulation of the B_0 field. The resultant EPR signals were demodulated by two synchronized lock-in amplifiers – one for each output from the IQ mixer in the detection scheme. A zero-order phase correction was applied to transfer all of the signal from the two quadratures produced by each lock-in amplifier into one trace. The two traces from each lock-in amplifier were then phase corrected (zero-order) to obtain the absorption and derivative EPR signals. The monoradical (4AT) and flexible biradical (TOT) had very similar spectral lineshapes, while the rigid biradical's (AMU) g_{xx} was shifted to lower fields. The tri-radical (DOT-et) also had a shifted g_{xx} to lower field, but not to the extent of AMU. The dendrimer had the broadest EPR spectra compared to the other four radicals and the largest difference to its spectral lineshape. The g_{xx} is similar to that of the mono- and bi-radicals; however, the strong electron-electron interactions distort the shape between the principle axes of the g-tensor. The g_{zz} of the dendrimer has been shifted to higher fields compared to the other radical systems. The slight shifts in g_{xx} can be attributed to either strong electron-electron dipolar coupling broadening the spectral width and/or to slightly different glassy matrices surrounding the radicals, where a different hydrogen bonding network can shift the g_{xx} of a nitroxide radical.[215,317] The dramatic shift in the g_{xx} of AMU is a combination of the strong electron-electron interactions (both dipolar and through bond J-

coupling), the glassy matrix, and the more rigid architecture of the AMU radical compared to all of the other radical systems studied here. The differences in the dendrimer EPR spectral lineshape has been attributed to the clustered effected of the electron spins on the dendrimer, which results in strong electron-electron interactions.

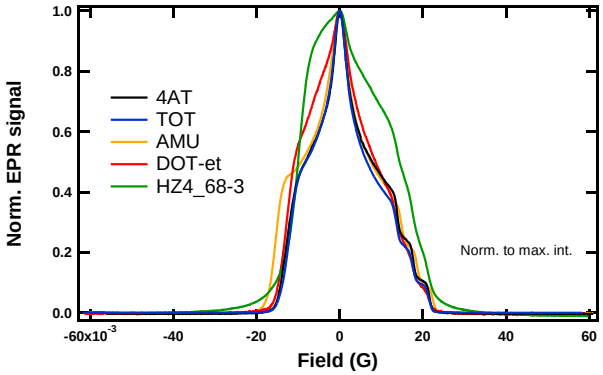

Figure 15.1. Rapid passage cw-EPR spectra of 10 mM electron spin concentration of 4-amino TEMPO, TOTAPOL, AMUpol, DOTOPA-ethanol, and the dendrimer HZ4_68-3. Spectra were acquired on an 8.56 T home-built 240 GHz EPR spectrometer at 4.5 K. All spectra were normalized to the maximum EPR signal intensity.

16. Appendix I: Simulations of ELDOR profiles dependent on the local electron spin concentration

The ELDOR profiles for the five radicals have been simulated, and the comparison between the radicals and the experimental ELDOR profiles is shown in figure 16.1. The ELDOR profile simulation theory incorporates electron spectral diffusion (eSD) and was originally developed by Hovav and Shimon.[79,98] The simulation parameters are provided in table S1, where experimental values were used as much as possible for electron and nuclear relaxation rates. T_{2e} was chosen to be ~10x T_m for each of the five radicals, and $A^{\pm}$ was chosen to fit the peaks resulting from forbidden electron-^{1}H transitions due to the hyperfine interaction between the two spins. Two detection frequencies were used to compare the experimental and simulated results for each frequency, where the fit at one frequency is better than the other, where generally the lower frequency simulation has better agreement with the experimental data (except for AMUpol). The dendrimer simulation was challenging to fit due to its extremely broad electron spin depolarization profiles. The overall good agreement between simulated fits and experimental data allowed the phenomenological eSD parameter, Λ^{eSD}, to be extracted in order to compare the relative eSD between with different radicals independently of the radicals' electron relaxation rates.

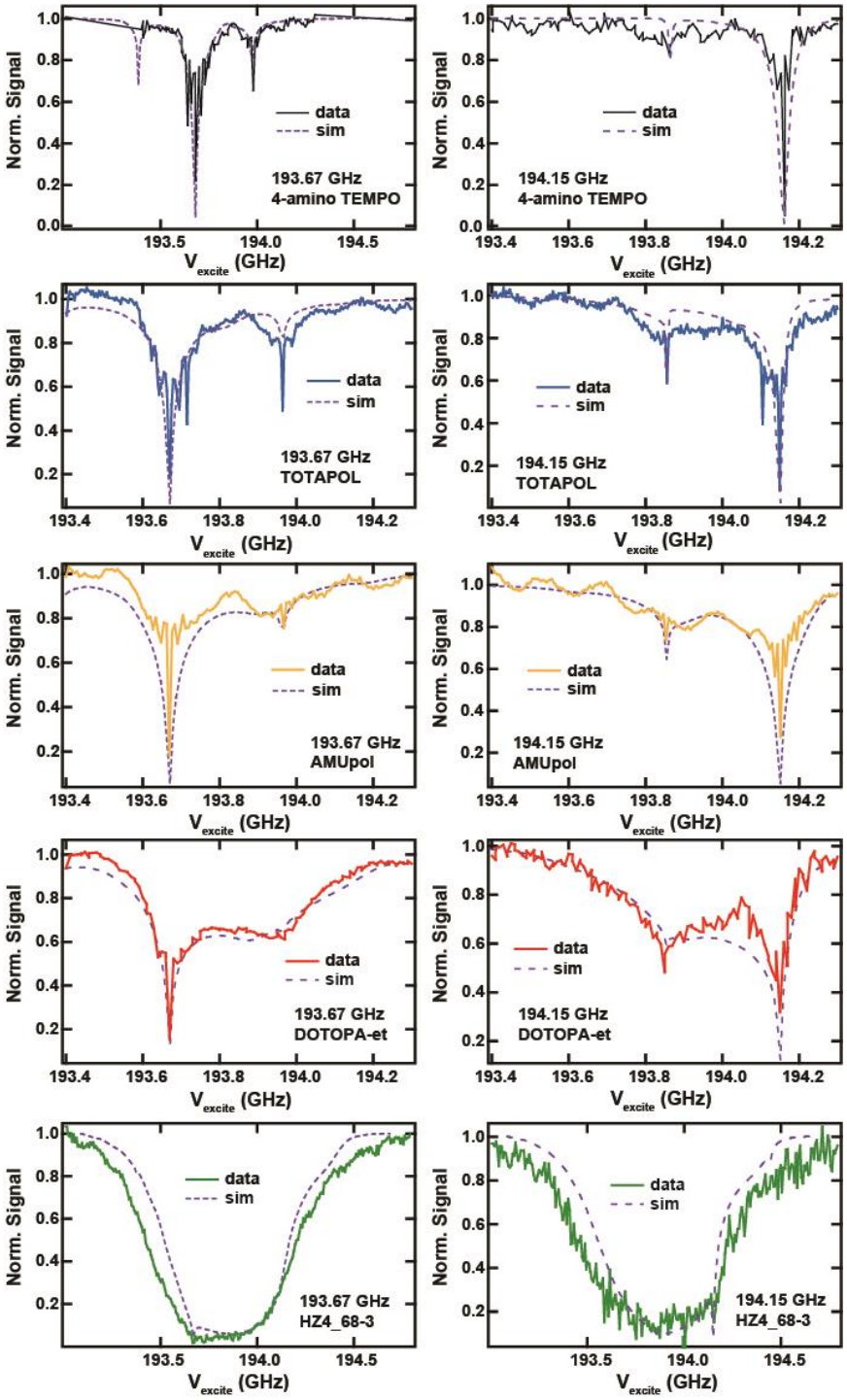

Figure 16.1. Experimental and simulated ELDOR profiles for 10 mM e- of 4-amino TEMPO (black – top), TOTAPOL (blue – second from top), AMUpol (yellow – middle), DOTOPA-ethanol (red – second from bottom), HZ4_68-3 [dendrimer (green – bottom)] in 6:3:1 d_8-glycerol:D_2O:H_2O at 4 K and at 7 T. Two ν_{detect} are shown 193.67 GHz (left) and 194.15 GHz (right) with t_p = 750 ns, t_{sat} = 100 ms, t_d = 10 μs, τ = 500 ns, and a repetition time of 600 ms. Simulations parameters are listed in table 16.1.

Table 16.1. Simulation parameters for fitting of the experimental electron depolarization profiles. All samples had C_n = 11 M, C_e = 10 mM, temperature = 4 K, and $P_{\mu w}$ = 0.6 MHz. Here 'T_{DNP}' is used as 'T_{1n}' in the simulation and T_{2e} was selected to be ~10 x T_m, except for the dendrimer, which was ~2 x T_m due to very poor fits with 10 x T_m.

Sample	T_{1e} (ms)	T_{2e} (µs)	Λ^{eSD} (μs^3)	$A^{\pm}$ (MHz)	T_{1n} (s)
4AT	94.2	120	10	7	560
TOTAPOL	86.0	150	25	10	288
AMUpol	138.5	130	25	10	286
DOTOPA-et	88.6	120	150	10	153
HZ4_68-3	151.8	20	1400	10	15